ANALYSIS OF THIN LIQUID FILMS DRIVEN BY SURFACE ACOUSTIC WAVES

Analyse von getriebenen dünnen Flüssigkeitsfilmen
durch akustische Oberflächen Wellen

Dissertation

zur Erlangung des Grades
Doctor rerum naturalium (Dr. rer. nat.)
am Institut für Theoretische Physik
der Westfälischen Wilhelms-Universität Münster

vorgelegt von
Kevin David Joachim Mitas
geb. am: 17.08.1991 in: Geseke

ausgegeben und betreut von
Prof. Dr. Uwe Thiele
Institut für Theoretische Physik
der Westfälischen Wilhelms-Universität Münster

Münster, 2021

Theoretische Physik

Analysis of thin liquid films driven by surface acoustic waves

Inaugural-Dissertation
zur Erlangung des Doktorgrades
der Naturwissenschaften im Fachbereich Physik
der Mathematisch-Naturwissenschaftlichen Fakultät
der Westfälischen Wilhelm-Universität Münster

vorgelegt von
Kevin David Joachim Mitas
aus Lippstadt
– 2021 –

This version is slightly revised.

Dekan: Prof. Dr. Michael Rohlfing

Erster Gutachter: Prof. Dr. Uwe Thiele

Zweiter Gutachter: Prof. Dr. Ofer Manor

Tag der mündlichen Prüfung: 13.10.2021

Tag der Promotion: 13.10.2021

”*It seems to be one of the fundamental features of nature that fundamental physical laws are described in terms of a mathematical theory of great beauty and power* “

- PAUL DIRAC, *The Evolution of the Physicist’s Picture of Nature, 1963*

Abstract

Homogeneous flat thin films of partially wetting liquids on a solid substrate have various dynamics, which depend on external forces. A common method to create a homogeneous liquid film is to withdraw a plate from a liquid bath. The formation of structures is achieved with a variation of the substrate inclination. In this case in which the film experiences a lateral component of the gravity force. Gravity and the withdrawal velocity of the substrate from the liquid meniscus support different energy levels of the substrate-liquid system, which translate to patterns of the substrate-coating liquid. This phenomenon is described by the classical Landau-Levich model. A more controlable alternative for generating ultra-thin coating liquid films of a few micrometres thickness may be obtained by using surface acoustic waves (SAW). SAW, which propagate in the solid substrate, induce a force and consequently mass transport in the liquid, which is analogous to a withdrawn plate.

In my dissertation, I particularly investigate the theoretical dyanmics and statics of thin-films, which are driven by SAW. For this purpose, a thin-film equation is derived from the Navier-Stokes equations by employing the long-wave approximation (lubrication approach). It is solved using a numerical method of pseudo-arclength continuation to investigate bifurcations in the coating film patterns when under the influence of various control parameters, such as the strength of the SAW and properties of the liquid. The resulting bifurcation diagrams provide insight into the occurring stationary and time-periodic states of the liquid films. In particular, time-periodic states correspond to occurring pattern formation, where ridges are pulled out of the liquid bath at constant time intervals. The results obtained by the continuation analysis are verified with numerical time simulations. Both methods reveals that the SAW-System contains stable time-periodic solutions.

Then, the classical Landau-Levich system is extended and analysed by including an additional immiscible liquid layer. This two-layered system is analysed by performing time simulations for flat films in subject to the wettability of the lower film and liquid properties (surface tension and contact angle), to find various symmetric as well as asymmetric droplet constellations, which form by this type of coarsening process.

Then, the model is studied for the Landau-Levich coating geometry. As in the previous analysis, time simulations are employed to determine the coarsening behaviour of the coating liquid on a moving substrate. The results reveal that droplets at the upper liquid layer are drawn out of the bath at regular intervals. These droplets appear atop of the lower liquid layer and thus provide a uniform coating of the substrate.

Kurzfassung

Glatte dünne homogene Filme partiell benetzender Flüssigkeiten auf festen Substraten, können unter dem Einfluss externer Kräfte diverse Dynamiken aufweisen. Eine bekannte Methode, um einen homogenen Flüssigkeitsfilm zu erzeugen, ist das Ziehen einer Platte aus einem Flüssigkeitsreservoir, wodurch ein dünner, großteils strukturloser Flüssigkeitsfilm auf dem Substrat zurück bleibt. Um Strukturbildungen zu begünstigen reicht es aus das Substrat anzuneigen. Dadurch wird der Flüssigkeitsfilm einer weiteren laterale Kraft der Gravitationskraft ausgesetzt. Durch die Gravitation und der Zieh-Geschwindigkeit des Substrates wirken zusätzlich unterschiedliche Energie-Stärken des Substrat-Flüssigkeitsystems auf den Meniskus des Flüssigkeitsbad, wodurch eine Flüssigkeitsbeschichtung des Substrates mit regulären Muster ausbilden kann. Dieses Phänomen wird durch das klassische Landau-Levich Modell beschrieben. Eine leichtere kontrollierbare alternative zu diesem Beschichtungsverfahren, um strukturierte ultra-dünne Flüssigkeitsfilme von wenigen Mikrometern Dicke zu erzeugen, sind sogenannte akustische Oberflächen-Wellen (surface acoustic waves – SAW). Diese SAW, welche im Substrat unterhalb des Flüssigkeitsfilms propagieren, induzieren Kräfte und in Konsequenz Massentransport in der Flüssigkeit analog zum Ziehen des Substrates.

In meiner Dissertation untersuche ich insbesondere das Verhalten von dünnen Flüssigkeitsfilmen theoretisch, die durch die SAW getrieben werden. Dazu wird eine Dünnfilm-Gleichung für SAW-getriebene Flüssigkeitsfilme mit der Langwellen-Approximation (Lubrication Ansatz) aus den Navier-Stokes Gleichungen hergeleitet. Diese Gleichung wird mit Hilfe der numerischen Methode der Pseudo-Bogenlängen Kontinuierung hinsichtlich des Bifurkationsverhalten unter Einfluß verschiedener Kontroll-Parameter, wie der SAW-Stärke und der Flüssigkeitseigenschaften, ausgiebig untersucht. Die resultierenden Bifurkationsdiagramme ermöglichen einen Einblick in die auftretenden stationären und zeitperiodischen Zustände der Flüssigkeitsfilme. Die auftretenden zeitperiodischen Zustände ensprechen auftretender Musterbildung. Dabei werden in konstanten Zeitabständen Flüssigkeitswülste aus dem Flüssigkeitsbad gezogen. Die gefundenen Kontinuierungsergebnisse zu den zeitperiodischen Zuständen werden mit Hilfe numerischen Zeit Simulationen auf ihr langzeit Verhalten überprüft. Dabei zeigt sich, dass stabile zeitperiodische Zustände in dem SAW-System existieren.

Das behandelte klassische Landau-Levich System wird nun mit einem zusätzlichen Flüssigkeitsfilm, bei dem diese Flüssigkeiten nicht mischbar sind, erweitert. Dieses Zweischicht-System wird zunächst mit Hilfe von Zeitsimulation für einen flachen Gesamt-Film in Abhängigkeit der Benetzbarkeit des unteren Filmes und weiteren unterschiedlichen Flüssigkeitseigenschaften untersucht. Dabei werden verschiedene symmetrische als auch asymmetrische Tropfen-Konstellationen, die sich nachdem Coarsening-Prozess bilden, gefunden.

Anschließend wird das Modell unter Berücksichtigung der Landau-Levich Geometrie studiert. Dieses neue Landau-Levich Modell wird dann mit Zeit Simulationen hinsichtlich des Coarsening Verhalten auf einem bewegten Substrates untersucht. Hierbei zeigt sich, dass in gleichmässigen zeitlichen Abständen Tropfen der oberen Flüssigkeitsschicht aus dem Bad gezogen werden. Diese Tropfen liegen auf dem unteren Flüssigkeitsfilm, die das gezogene Substrat gleichmässig bedeckt.

Contents

Danksagung

CHAPTER ONE

Introduction

> ” *Omnium enim rerum principia parva sunt* “
>
> – MARCUS TULLIUS CICERO,
> *De Finibus Bonorum et Malorum*
> *Book V, Chapter 58. 45 BC*

Mankind has always strived for knowledge in order to find explanations for unexplainable events. Researchers describe these natural events as realistically as possible with the use of physical and mathematical models and are defined by the laws of nature. These laws of nature and events are constantly being researched, so that the knowledge of mankind is expanded. This enables the establishment of further connections between events in nature.

More than two thirds of the surface of the earth are covered with water, which is stored in oceans, rivers and lakes. As water a central element of life, it is natural that most habitable areas are linked to water. Nevertheless, many areas with sparse supply on water are nowadays inhabited by humans. This is possible only because mankind has managed to irrigate water poor regions.

Around 3000 BC (ancient years), the Egyptians developed the concept of geometric considerations in the form of mathematical expressions. Furthermore, the Egyptians built the first fishing boats without knowing of the principle of buoyancy [137]. Many centuries later in the age of the Greeks, *Archimedes (287-217BC)* described the principle of buoyancy of objects. He postulated that anything may float in liquid as soon as the object is lighter than the displaced liquid, which is known as the Archimedes' principle [119]. This postulate was thus the first historical description of hydrostatics. With the help of his postulate, a new quantity for describing materials was discovered: The density ρ defined as the mass per unit volume.

It was not until hundreds of years later that *Blaise Pascal (1623-1662)* evolved the ideas of Archimedes by establishing the first law of hydrostatics in the 17th century. His developed law, known as Pascal's law [2, 11], has significantly influenced the entire basic physical idea of fluid mechanics. He discovered that the pressure acting on an object in water increases linearly with the vertical distance below the surface. The expression yields

$$p(x) = \rho g x + p_0 \,. \tag{1.1}$$

This equation describes the pressure p in liquids, whereas g is the gravitational constant, ρ the density of the liquid, x is the vertical distance below the surface of the object and p_0 the normal pressure above the liquid. In the same century, Isaac Newton had a major influence on physics. He was not only responsible for the discovery of gravitational acceleration but he had also influence in the field of hydrodynamics. *Isaac Newton (1642-1726)* was the first to describe the flow of incompressible (constant density) liquids [96]. To honor his discovery, these liquids carry his name: incompressible newtonian fluids. *Isaac Newton* discovered that in one dimension, the shear stress τ linearly depends on the deformation rate μ_d of the liquid times the local derivative of the velocity v. In the form of a mathematical expression, his consideration yields

$$\tau = \mu_\mathrm{d} \frac{\mathrm{d}v}{\mathrm{d}x}. \tag{1.2}$$

This linear correlation of shear stress τ and deformation rate μ_d, however, only applies to incompressible gases and newtonian liquids.
Later in 1738, *Daniel Bernoulli (1700-1782)* formulated a mathematical approach to describe the flow of incompressible fluids in a pipe [84]. Thereby, he established that the sum of the squared velocity v of liquid times pressure p and potential energy at any position remains constant. This is better known as the Bernoulli equation and describes a steady state. Several years later, in 1757, *Leonhard Euler (1707-1783)* extended Bernoulli's approach and established the Euler equation, yielding

$$\rho \left(\frac{\partial v}{\partial t} + v \frac{\partial v}{\partial x} \right) = - \frac{\partial p}{\partial x} \,. \tag{1.3}$$

This fundamental equation of fluid dynamics can be understood as a transport equation. The partial differential equation (1.3) does not take into account external forces and only describes the variation of pressure p and velocity v of a liquid in one dimension. Notice that the velocity v of a liquid always involves a negative pressure gradient, which in turn is amplified by the spatial change of liquid flow. This fundamental knowledge obtained from the Euler equation is the cornerstone of today's hydrodynamics.

The findings of hydrostatic and hydrodynamic effects are further developed in the 19th century by *Claude-Louis Navier (1785-1836)* in 1827, *Siméon Denis Poisson (1781-1840)* in 1831, *Adhémar Jean Claude Barré de Saint-Venant (1797-1886)* in 1843 and *George Gabriel Stokes (1819-1903)* in 1849 [114]. They expanded the Euler equation further and derived a transport equation that now considers external body forces acting on the incompressible newtonian liquid flow. These findings are summarised in a set of equations, the Navier-Stokes equations, see Sec. 2.1 for a detailed analysis. The Navier-Stokes equations are fundamental equations in hydrodynamics and are used to describe a wide range of related problems, see Eqs. (2.5) and (2.6). The continuity equation is divergence free due to the pressure p for incompressible liquids. This means that the associated velocity field has a constant volume and thus local mass conservation.

In 1942, *Lev Landau (1908-1968)* and *Benjamin Levich (1917-1987)* analytically investigated the transfer of a simple viscous liquid from a bath onto a continuously withdrawn plate [73]. They showed that a homogeneous macroscopic liquid layer of a well-defined thickness is deposited onto the plate. This thickness h_c (coating thickness) depends on the Capillary number $\mathrm{Ca} = \mu v_\mathrm{p}/\gamma$. It is a nondimensional measure of driven free surface liquids, where v_p corresponds to the velocity of the withdrawn plate, and μ and γ are the viscosity and surface tension of the liquid, respectively. The deposited film height h_c scales with the power $\propto \mathrm{Ca}^{2/3}$. Overall, this phenomenon is well-known as the classical Landau-Levich problem and is fundamental for investigations of transferring liquid layers.

The example mentioned above refers mainly to the effects within liquid (mass transport). It is also necessary to consider the interaction between the liquid and the solid surface, which can be classified as a wettability effect. Depending on their chemical properties, thin films on solid surfaces occasionally rupture. This results in several small droplets of liquid remaining on the substrate. The length scale of these droplets is defined by capillarity and wettability. Back in 1805, *Thomas Young (1773-1829)* and *Pierre-Simon Laplace (1749-1827)* established a formulation, see Eq. (1.4), for the pressure jump between in- and outside of droplet [142].

$$p_\mathrm{L} = \frac{2\gamma}{r_\mathrm{d}} \tag{1.4}$$

The result is expanded further by Young-Laplace for droplets on flat horizontal solid substrates, see Eq. (2.18). Then, the Laplace pressure acting on the droplet depends on the surface tension γ and the radius r_d of the droplet. In this case, the droplet adapts a spherical cap-like shape and the contact angle between the droplet surface and mass is conserved. In addition to this “deformation” pressure at the free surface of the droplet, a contact angle is formed by three phases of gas, liquid and substrate. *Boris Vladimirovich Derjaguin (1902-1994)* has established a description of a disjoining pressure, which describes the wettability of liquid at the solid-liquid interface [28, 29, 30]. In Sec. 2.3 the Derjaguin pressure is described in more detail.

The transportation of liquid is achieved in different ways. The simplest case is to make use of gravity. For instance, liquid flows down a slope, where the momentum depends on the inclination of liquid streaming, i.e. two thousand years ago, the

Romans invented aqueducts to facilitate the transport of water above ground to places where water is not accessible [62]. The aqueducts are one of the prominent examples in history, where mankind used the stored potential energy to control and manipulate the flow of liquid.
Another way of liquid manipulation has been shown by Landau and Levich. They show that withdrawing a plate from a liquid bath generates a flow of liquid. This method is a common example of liquid deposition.
A temperature gradient allows the liquid to create convection rolls. In 1855, *James Thomson (1822-1892)* found that liquids may flow under a temperature gradient [130]. Later, this phenomenon was investigated by *Carlo Maragoni (1840-1925).* He described the occurring effects and the behaviour of liquid in a temperature gradient, nowadays known as Marangoni effect [82]. Many studies have proven that the Maragoni effect creates a liquid flow within the liquid by evaporation [13, 19, 20, 23, 90, 95].

A special focus in this work is to investigate another type of liquid transfer by using surface acoustic waves (SAW). It started by *Robert Hooke (1635-1702)* and was further developed by *Ernst Florens Friedrich Chladni (1756-1827)* in 1787, who observed the behaviour of different patterns for particles influenced by sound [22]. These are termed Chladni figures. Then, in the year 1831, *Michael Faraday (1791-1867)* discovered similar behaviour in liquids, where standing waves are discovered namely Faraday waves, [40]. *John William Strutt, third Baron Rayleigh (1842-1919)* further developed the idea of Faraday waves in 1885 [110]. If an elastic surface is considered, on which mechanical surface waves propagate, vibrations are generated in the substrate, which can be interpreted as small earthquakes. These surface waves propagate within the substrate, so that a microscopically small actuation mechanism at the solid-liquid interface creates pressure in the liquid ensuring that the liquid advances over the substrate. They are called Rayleigh surface acoustic waves and the induced liquid flow is also known as *acoustic streaming. Wesley L. Nyborg (1917-2011)* layed the foundation and qualitatively characterised this as acoustic streaming starting in 1953 [93, 94] and *Amgad Rezk* (et al.) then carried out the first successful experiments with silicon oil showing that SAW of MHz frequency in a solid substrate provides dynamic wetting of surfaces through liquid films [112, 113]. The interest in SAW has grown in recent years as industry is looking for new ways and methods to control coating processes. The SAW may be a cheap and easy method to create and control a suitable pattern during a coating process where very small droplets of a few micrometers are generated, which could have an advantage over traditional dip-coating techniques.

In this work, first of all, the most important formulas to determine a thin-film equation are established. For this purpose the Navier-Stokes equations are briefly discussed and applied to the flow that occurs in a liquid film. Then, to derive a thin-film evolution equation, a long-scale approximation also known as a lubrication approach [95] is used. Subsequently, a linear approach for the SAW within the substrate is introduced, which is furthermore translated into vibrations. These vibrations influence the liquid film height and deform the liquid structure [7, 16, 88]. The determined model allows one to obtain a dimensionless thin-film evolution equation [87]. Subsequently, this equation is extended by the addition of further attributes, such as the disjoining pressure, a gravitational force and an inclination of the substrate. Together, this results in an advanced thin-film equation for a layer of partially wetting liquid driven by SAW. Subsequently, the equation is analysed by the use of a pseudo-arclength continuation approach to obtain bifurcation diagrams for one and two dimensional geometry. With the help of the bifurcation diagrams the considered system is analysed and the special characteristics of stable steady states are identified [85]. This enables the detection of very interesting states, for instance time-periodic behaviour. Then, these states are further verified with direct numerical simulations techniques, which provides insight into the temporal behaviour. The established equation provides the possibility to compare the SAW-driven system with the withdrawal of a plate in Ref. [47]. In addition, the behaviour is studied considering volatile liquids.

Then, with the gathered information so far, a two-layer liquid system is investigated in relation to the classical Landau-Levich system [105, 106]. One of the first studies of a two-layer liquid model was performed in 1869, where a droplet of oil was spreads on a water film [77]. In other words, two liquid layers are on top of each other and it is assumed that, due to the high surface tension, these liquids do not mix. The two-layer liquid film system is studied theoretically for two different cases by using time simulations. In the first case, a flat film system of two-layers of immiscible liquids is investigated for different liquid characteristics, such as ratio of surface tension and ratio of wetting strength of both liquid layers. Therefore, various compounds of droplet constellations are observed after the dewetting and coarsening process. In the second case, the two-layer system is considered in a classical Landau-Levich geometry where a plate is withdrawn out of a bath. This new model is interpreted as an enhanced Landau-Levich system and the temporal behaviour of the withdrawal films are discovered and compared to the classical Landau-Levich system (one-layer).

In the appendix, a short tutorial for the Matlab package PDE2PATH is provided [136]. It gives some insights of the treated thin-film system driven by SAW and assists interested readers to quickly reproduce and expand results of this thesis.

The contribution of this work consists of many results that can be investigated further. The presented results of this thesis are intended to serve as a basis for future studies, in a theoretical manner or for experiments in either SAW-driven thin-films or a two-layer model in a Landau-Levich geometry, regardless of whether a thin film is dragged out by a moving plate directly or indirectly via propagating SAW. Note that a PDE2PATH tutorial in this work is available in a data repository `https://doi.org/10.5281/zenodo.5595985`.

CHAPTER TWO

Fundamentals of hydrodynamics

” *Ut sementem feceris, ita metes.* “

– MARCUS TULLIUS CICERO,
De oratore II
65, 261, 55 BC

This chapter introduces the fundamentals of hydrodynamics that are necessary to derive a thin-film evolution equation with the aid of the Navier-Stokes equations. Therefore, liquid thin film and droplet states on solid substrates are explained. Here, different boundary conditions occur, i.e. force equilibria at the liquid-gas interface. Furthermore, two different descriptions for liquid wetting in hydrodynamics are considered, one for a macroscopic case and the other for mesoscopic case. On the mesoscopic length scale the wetting energy of the liquid is described by a model of Derjaguin [30], whereas the macroscopic case the model of Young-Laplace applies [142]. Both models are combined to describe a partially wetting of (non-volatile) liquid thin films. At the end of this chapter, a non-conserved flux for volatile liquids is introduced, which allows to describe evaporation and condensation for liquid films.

After introducing the fundamentals of hydrodynamics, an evolution equation to describe a thin-film model is derived in Chap. 3. This equations allows to describe two different situations, namely, a film that is pulled out of a bath by a moving plate and a meniscus or thin film that is driven by Rayleigh surface acoustic waves (SAW). Before the major hydrodynamic equations are discussed some notations are introduced.

First, a reduced representation of the partial derivative is given,

$$\frac{\partial f(x)}{\partial x} := \partial_x f(x) = \partial_x f \quad \text{and} \quad \frac{\partial^2 f(x)}{\partial x^2} := \partial_{xx} f \,. \tag{2.1}$$

Note that arguments of arbitrary functions may be dropped.
Furthermore, the thin film geometry is reduced to two dimensions (2D). Hereby, the independent variables x and z are the cartesian coordinates reflecting coordinates parallel (x) and orthogonal (z) to the substrate, see Fig. 2.1. Only in the case that considers a three dimensional geometry, the lateral component in y-direction is

introduced, which then is described by vectors in 2D and 3D

$$\vec{r}^{\,(2)} := \begin{pmatrix} x \\ z \end{pmatrix} \quad \text{and} \quad \vec{r}^{\,(3)} := \begin{pmatrix} x \\ y \\ z \end{pmatrix}, \tag{2.2}$$

respectively. In addition, the derivative and Laplace operators for both cases are defined. For the 2D case, it reads

$$\vec{\nabla}^{(2)} := \begin{pmatrix} \partial_x \\ \partial_z \end{pmatrix}, \quad \Delta^{(2)} = \left(\vec{\nabla}^{(2)}\right)^2 := \partial_{xx} + \partial_{zz} \tag{2.3}$$

while in 3D it reads

$$\vec{\nabla}^{(3)} := \begin{pmatrix} \partial_x \\ \partial_y \\ \partial_z \end{pmatrix} \quad \text{and} \quad \Delta^{(3)} = \left(\vec{\nabla}^{(3)}\right)^2 := \partial_{xx} + \partial_{yy} + \partial_{zz}. \tag{2.4}$$

When the notations of the operaters are dropped, for instance $\vec{\nabla}$, a 2D case is considered.

After discussing the geometrical considerations about liquid films, liquid droplets, boundary layers and contact lines, the effects of liquid wettability are introduced. These additional forces are described with the aid of Derjaguin's pressure or wetting energy [30]. Initially, only non-volatile liquids are considered and at the end of this chapter, a non-conserved flux is briefly introduced that allows to describe evaporation and condensation for volatile liquids, see Sec. 2.4.

2.1 Navier-Stokes equations

Hydrodynamic systems are commonly described by means of liquid flow and (mass) transport equations. For incompressible newtonian liquids, the flow is described by the Navier-Stokes equations. These are nonlinear equations and they read

$$\rho\left[\partial_t \vec{v}^{\,(2)} + \left(\vec{v}^{\,(2)} \cdot \vec{\nabla}^{(2)}\right)\vec{v}^{\,(2)}\right] = \vec{\nabla}^{(2)} \cdot \boldsymbol{T} + \vec{f}^{\,(2)}, \tag{2.5}$$

$$\text{with} \quad \vec{\nabla}^{(2)} \cdot \vec{v}^{\,(2)} = 0\,. \tag{2.6}$$

The chosen representation of the velocity field $\vec{v}^{\,(2)}$ is 2D, i.e.

$$\vec{v}^{\,(2)}(\vec{r}^{\,(2)},t) = \begin{pmatrix} u(\vec{r}^{\,(2)},t) \\ w(\vec{r}^{\,(2)},t) \end{pmatrix}. \tag{2.7}$$

For incompressible liquids the density ρ remains always constant. The arbitrary function, represented by $\vec{f}^{(2)}$, can reflect any kind of body force, that is acting on the liquid, for instance, gravitational or electromagnetic forces. The Navier-Stokes Eqs. (2.5) and (2.6) have a divergence free velocity field for incompressible liquids. Furthermore, the mass of the liquid is conserved. The stress tensor $\boldsymbol{T}$ is given by [74]

$$\boldsymbol{T} = -p(\vec{r}^{\,(2)},t)\mathbb{1} + \mu\Big[\vec{\nabla}^{(2)}\vec{v}^{\,(2)} + (\vec{\nabla}^{(2)}\vec{v}^{\,(2)})^T\Big]\,, \tag{2.8}$$

where the pressure field $p(\vec{r}^{\,(2)},t)$ is acting on the liquid and μ is the corresponding viscosity of the liquid. Here in Eq. (2.8), $\mathbb{1}$ is the unit matrix.
To further simplify calculations, the Navier-Stokes Eqs. (2.5) and (2.6) are reduced by using the introduced stress tensor from Eq. (2.8) for incompressible conditions. Subsequently, this results in

$$\rho\Big[\partial_t\vec{v}^{\,(2)} + \Big(\vec{v}^{\,(2)}\cdot\vec{\nabla}^{(2)}\Big)\vec{v}^{\,(2)}\Big] = -\vec{\nabla}^{(2)}p(\vec{r}^{\,(2)},t) + \mu\Delta^{(2)}\vec{v}^{\,(2)} + \vec{f}^{\,(2)}. \tag{2.9}$$

Due to the mass conservation of an incompressible newtonian liquid, the stress tensor is used to reduce the Navier-Stokes equation into Eq. (2.9). This equation is used, when introducing further considerations and boundary conditions for liquid films. The derivation of a thin-film evolution equation is described in detail in Chap. 3.

2.2 Boundary conditions for thin liquid films

In the following, boundary conditions for liquid films or droplets are presented in an isothermal system. These boundary conditions influence the behaviour of liquids, so that for instance droplets with dome-like shapes are formed. First, flat films on a flat, horizontal and rigid solid substrate are considered. Hereby, several boundary conditions for a liquid film are considered. One is the no-slip and no-penetration condition. It implies, that the liquid has zero relative velocity U at the solid substrate at $z = 0$ and has no penetration into the substrate. In this thesis a moving thin liquid film on a rigid solid substrate with speed U along the x-direction is considered and applying these condition then leads to

$$\vec{v}^{(2)} = (U,0)^T \quad \text{at} \quad z = 0\,. \tag{2.10}$$

The next boundary condition is the kinematic condition at the free surface of the liquid

$$\partial_t h = w - u\partial_x h \quad \text{at} \quad z = h(\vec{r}^{\,(2)},t)\,. \tag{2.11}$$

The time evolution of the height profile of the liquid depends on the liquid velocity components. The last boundary condition is a force equilibrium condition at the free surface of the liquid. Here, an isothermal case is considered and it is written as

$$\boldsymbol{T}\cdot\vec{n}^{\,(2)} = \gamma K\vec{n}^{\,(2)}\,, \tag{2.12}$$

where γ is the surface tension, K is the mean curvature of the free surface and the stress tensor $\boldsymbol{T}$ is applied for the liquid. In particular, the term $\gamma K \vec{n}^{\,(2)}$ is interpreted as a Laplace pressure and acts orthogonal to the liquid surface [26].
Next, the mean curvature K of the liquid-gas interface as well as the normal $\vec{n}^{\,(2)}$ the tangent vectors $\vec{t}^{(2)}$ are defined as

$$K = \frac{\partial_{xx} h}{\left[1 + (\partial_x h)^2\right]^{3/2}}\,, \tag{2.13}$$

$$\vec{n}^{\,(2)} = \frac{(-\partial_x h, 1)^T}{\left[1 + (\partial_x h)^2\right]^{1/2}} \tag{2.14}$$

and

$$\vec{t}^{(2)} = \frac{(1, \partial_x h)^T}{\left[1 + (\partial_x h)^2\right]^{1/2}}, \tag{2.15}$$

respectively, schematics in Fig. 2.1.

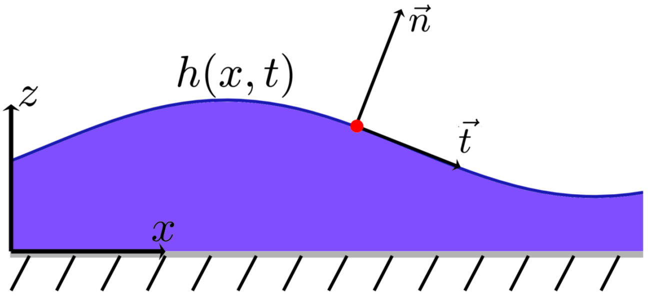

Figure 2.1: *Illustration of a non-volatile liquid film situated on a flat horizontal substrate. The profile height of the film is given by* $h(x,t)$*. At the liquid-gas interface a red point is marked which indicates the tangential vector* $\vec{t}$ *as well as the corresponding normal vector* $\vec{n}$*.*

An expression to describe the shape of the surface is determined by projecting the vectorial boundary condition (stress balance) in Eq. (2.12) onto the normal direction $\vec{n}$, leading to

$$\begin{aligned} p + \frac{2\mu}{1 + (\partial_x h)^2}\Big[- (\partial_x u)(\partial_x h)^2 - \partial_z w + (\partial_x h)(\partial_z u + \partial_x w)\Big] \\ = -\frac{\gamma \partial_{xx} h}{\left[1 + (\partial_x h)^2\right]^{3/2}} \end{aligned} \tag{2.16}$$

with the Laplace pressure $p = p_{\mathrm{L}}$ at $z = h(x,t)$, while projecting Eq. (2.12) onto the tangent vector $\vec{t}$ results in

$$\mu\Big[(\partial_z u + \partial_x w)\Big(1 - (\partial_x h)^2\Big) + 2(\partial_z w - \partial_x u)\partial_x h\Big] = 0\,. \tag{2.17}$$

Now two boundary conditions are defined in Eqs. (2.16) and (2.17). In Eq. (2.16) a relation of pressure p, viscosity μ and surface tension γ is established. The geometrical shape is only affected by the surface tension.

2.3 Macroscopic and mesoscopic description of wettability

In the following, two different models of liquid wettabilities are introduced. At first, a liquid on a macroscopic length scale is treated. For this, a liquid droplet with a constant volume V is considered to be on a flat horizontal solid substrate. Hereby, the liquid droplet takes a spherical cap-like shape, whereas around the droplet a "dry film state" with $h \to 0$ is considered. Subsequently, this leads to a geometrical form of the droplet that has two contact points at the boundaries. At each of these points, three phases, liquid, solid and gas phase meet at a triple point contact line. An equilibrium angle θ_{eq} of the liquid at the contact lines emerge. This macroscopic state is in an equilibrium state and described by the Young and Young-Laplace-laws in Eq. (1.4) [142]. At the contact lines an angle at equilibrium is defined as

$$\gamma_{\mathrm{LG}}\cos(\theta_{\mathrm{eq}}) = \gamma_{\mathrm{SG}} - \gamma_{\mathrm{SL}} \quad \text{with} \quad \gamma = \gamma_{\mathrm{LG}}\,. \tag{2.18}$$

Three surface tensions are given with γ_{LG} liquid-gas, γ_{SG} solid-gas and γ_{SL} solid-liquid. The typical equilibrium angles formed by the liquid contact lines with the substrate is in the range of $0° < \theta_{\mathrm{eq}} < 180°$. In Fig. 2.3 (b) such an equilibrium angle θ_{eq} is shown.

The shape of the spherical cap of a liquid droplet always depends on the wettability of the substrate. By varying the wettability, the radius r_d of the spherical cap is changed, because at equilibrium the angle θ_{eq} changes, while the volume of the droplet remains constant. When no wettability occurs, i.e. a non-wetting substrate, a fully spherical liquid droplet is formed. This droplet only touches the substrate at one single point, leading to a maximal contact angle of $\theta_{\mathrm{eq}} = 180°$. If the substrate is fully wettable, however, no contact angle between the liquid and the substrate is developed, so that the contact angle is $\theta_{\mathrm{eq}} = 0°$. These three different cases of non-, partially- and full wettability are presented in Fig. 2.2. This macroscopic description of a liquid droplet on a solid surface is not sufficient to describe very thin films. An additional energy must be introduced, the so-called disjoining potential $V_{\mathrm{dp}}(h)$ (wetting energy) on a mesoscopic scale. In other words, in addition to the Laplace pressure p_{L}, the disjoining pressure p_{dp} is acting on the liquid. In this work, the disjoining pressure introduced by Derjaguin is used [30].

For partially wettable liquid films in a thermodynamic equilibrium, a new equilibrium

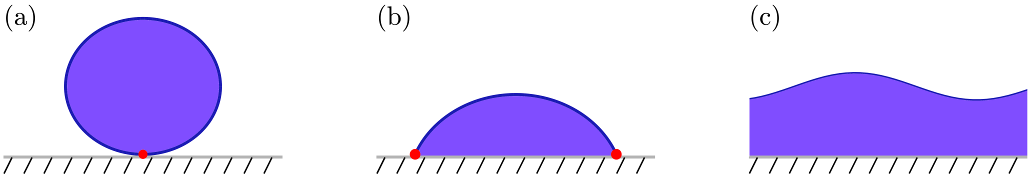

FIGURE 2.2: *Representations of three different wetting configurations on a solid and flat surface: (a) non-wetting, (b) partially wetting and (c) fully wetting. Each of these representations show a liquid (droplet) on the surface with "identical" volume. The liquids have different shapes due to the Laplace pressure* p_{L} *and the wettability of the substrate. The occurring contact points are marked by a red point. In (a) a liquid droplet is on a non-wetting substrate, which results in a complete sphere with only one contact point and an angle of* $\theta_{\mathrm{eq}} = 180^{\circ}$*, in (b) with a partial wetting substrate, the liquid droplet forms a spherical cap, or dome-like form with two contact points, so that, the angle of contact takes on a value of* $0^{\circ} < \theta_{\mathrm{eq}} < 180^{\circ}$ *and in (c) where a fully wetting substrate is considered, the solid surface is covered by a liquid film, where no contact point exists, so that* $\theta_{\mathrm{eq}} = 0^{\circ}$*.*

state was observed [12, 102, 103, 118, 126]. An ultra-thin film of liquid coexists with a liquid droplet, so that no direct contact angle is formed at the edges of the liquid droplet, opposed to the sketch in Fig. 2.2 (b). Overall, this leads to the phenomenon that the direct surrounding of a liquid droplet is always covered with such an ultra-thin film. The ultra-thin film is denoted as an absorption layer or precursor film which has a fixed height of h_{p} for droplet $r \to \infty$. This ultra-thin film is connected to the droplet at each contact line, so that the solid substrate is always covered by a ultra thin liquid film. The statement initially contradicts the sharp contact line in the case of a macroscopic perspective. Nevertheless, different experiments with liquids at microscopic level have shown that a precursor film is found in the immediate vicinity of droplets [9, 10, 55, 59, 120].
A sketch of this phenomenon is shown for a 1D droplet in Fig. 2.3.

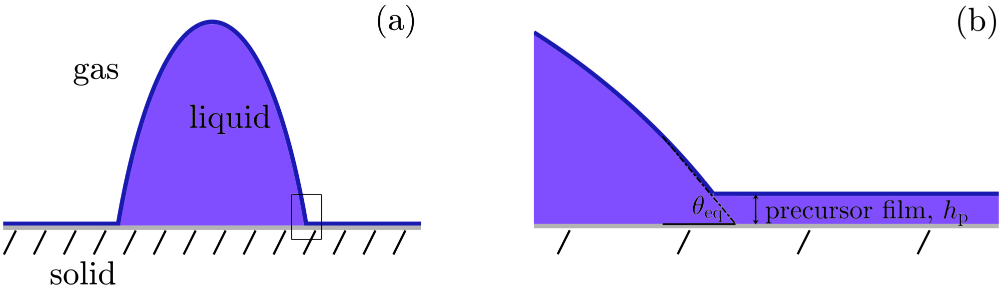

FIGURE 2.3: *In (a) a schematic representation showing a liquid droplet in equilibrium on a horizontal solid surface. The liquid droplet coexists with the precursor film due to the acting disjoining pressure. The outlined part of the figure is enlarged in (b) and highlights the contact angle* θ_{eq} *at a three phase contact region and the precursor film height* h_{p}*.*

The acting pressure $\Pi(h) = -\partial_h V_{\mathrm{dp}}(h)$ can be added in two different ways into the formalism. One is to add the pressure directly to the Laplace pressure in the corresponding boundary condition in Eq. (2.16). Then, this pressure is a sum of $p = p_{\mathrm{L}} - \Pi(h)$. The other way makes use of the Navier-Stokes Eqs. (2.5) and (2.6).

Here it is applied as an additional conservative body force [25, 95]. The body force yields

$$\vec{f}^{(2)}_{\mathrm{dp}} = -\vec{\nabla}^{(2)}\varphi_{\mathrm{dp}} \quad \text{with} \quad \varphi_{\mathrm{dp}} = \Pi(z) - \Pi(h)\,. \tag{2.19}$$

Both of these approaches lead to identical results. Here the Derjaguin pressure is used. Itis a combination of two acting forces, the long-range Van der Waals interaction $\Pi(h)_{\mathrm{VdW}}$, which is destabilising [36], and the short-range interaction $\Pi(h)_{\mathrm{sr}}$, which acts stabilising, i.e.,

$$\Pi(h) = \Pi(h)_{\mathrm{VdW}} + \Pi(h)_{\mathrm{sr}} = -\frac{A}{h^3} + \frac{B}{h^6}\,. \tag{2.20}$$

In Eq. (2.20) the parameter A corresponds to the strength of the Van der Waals interaction and B is the strength of the short-range interaction. When the Derjaguin pressure crosses zero, i.e., $\Pi(h_{\mathrm{p}}) = 0$, the wetting energy f has a minimum corresponding to the height h_{p} of the equilibrium absorption layer. Setting $\Pi(h_{\mathrm{p}}) = 0$ in Eq. (2.20), the corresponding film height is determined as

$$h_{\mathrm{p}} = \left(\frac{B}{A}\right)^{\frac{1}{3}}. \tag{2.21}$$

Next, three different configurations are derived with the Derjaguin pressure from Eq. (2.20).

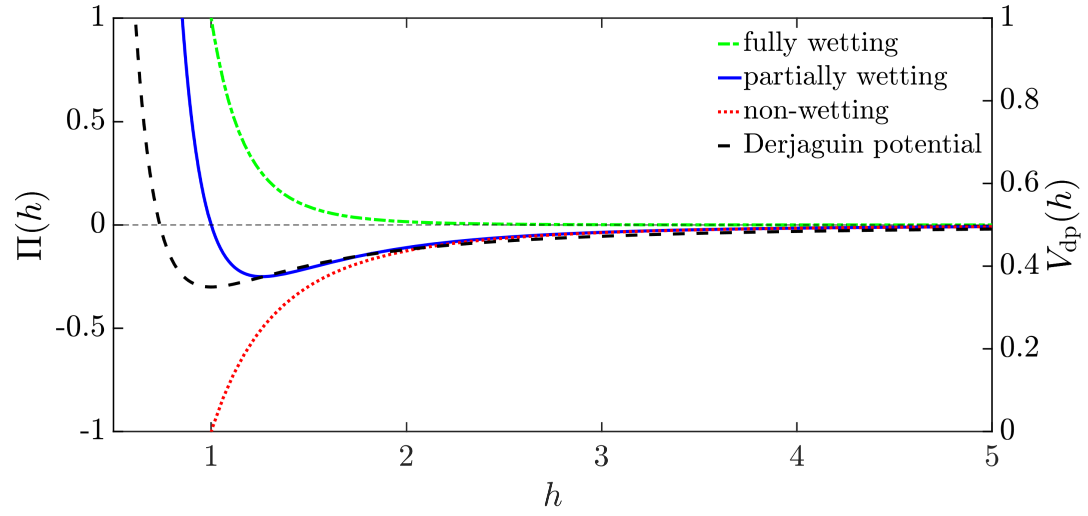

FIGURE 2.4: *Three wetting configurations, completly wetting, partial wetting and non-wetting showing as a function of the disjoining pressure $\Pi(h)$ and the Derjaguin potential $V_{\mathrm{dp}}(h)$ (black dashed line) for $A = B = 1$. The green dashed line shows completly wetting, where long-range Van der Waals forces are turned off with $A = 0$ and $B = 1$. The red dotted line indicates that the short-range forces are set to $B = 0$ and only the long-range forces are acting with $A = 1$. In the latter case, where both long- and short-range forces are acting ($A = 1$ and $B = 1$), an equilibrium is established, so that a precursor film with $h_{\mathrm{p}} = 1$ remains.*

The wettability depends on both parameters A and B. For $A \leq 0 \wedge B > 0$ a full wettability, for $A \geq 0 \wedge B > 0$ partial wettability and for $A \geq 0 \wedge B \leq 0$ no wettability are obtained, see Fig. 2.4. The case $A \leq 0 \wedge B \leq 0$ is not considered. The total surface energy $E_\gamma(h)$ of a thin film with height h, where the Derjaguin pressure is included, is then given by

$$E_\gamma(h) = \gamma_{\mathrm{SL}} + \gamma + V_{\mathrm{dp}}(h) \quad \text{with} \quad V_{\mathrm{dp}}(h) = -\int \Pi(h)\mathrm{d}h\,. \tag{2.22}$$

In the limiting case for very large film heights $h \to \infty$, results into the energy equilibrium state of a liquid film of a macroscopic case. Hereby, Derjaguin potential disappears with $V_{\mathrm{dp}}(h \to \infty) \to 0$, see Fig. 2.4.

2.4 Volatile liquids

In the previous Sec. 2.3, where two different pressures act on liquid film or liquid droplet, the initial attention was focused on Laplace pressure p_{L} and Derjaguin disjoining pressure Π in the case of non-volatile newtonian liquids. Now, the previous model of partially wetting liquids for non-volatile liquids is used for volatile liquid films or droplets [45, 89, 128, 131, 139, 141]. Hereby, Eq. (2.11) and Eq. (2.12) are revisited and evaporation is applied. Then, the kinematic boundary condition reads

$$\partial_t h = w - u\partial_x h - j_{\mathrm{evap}} \quad \text{at} \quad z = h(\vec{r}^{\,(2)},t)\,. \tag{2.23}$$

where the time evolution of the liquid height profile is dependend on the evaporation rate β_{evap}. This evaporation rate removes or adds liquid at the free surface (liquid-gas interface). As a result, the force equilibrium condition at the free surface of the liquid yields

$$(\boldsymbol{T} - \boldsymbol{T}_{\mathrm{gas}}) \cdot \vec{n}^{\,(2)} = \gamma K \vec{n}^{\,(2)} + (\partial_s \gamma)\vec{t}^{\,(2)}. \tag{2.24}$$

This force equilibrium condition has two stress tensors $\boldsymbol{T}$ and $\boldsymbol{T}_{\mathrm{gas}}$ one corresponds to the liquid and the other corresponds the gas phase.

For a non-constant surface tension, i.e temperature gradients, tangential forces occur at the surface. In particular, these forces are Marangoni forces and they are proportional to the surface gradient $\partial_s := \vec{t}^{\,(2)}\vec{\nabla}^{(2)}$ [49]. The resulting Marangoni convection exerts additional forces that cause deformations of the surface [15, 35, 124, 127].

For the isothermal system, the stress tensor is considered $\boldsymbol{T} \gg \boldsymbol{T}_{\mathrm{gas}}$, which results into the Eq. (2.12). Then, the surface tension γ is considered constant and no Maragoni forces act on the free surface.

In this way evaporation and/or condensation is introduced. In Fig. 2.25, a sketch of a volatile liquid droplet with a non-conserved flux in form of evaporation $j_{\mathrm{evap}}(x,t)$ is presented. The arrows around the liquid droplet indicate that liquid evaporates. The arrows in Fig. 2.25 point away from the liquid, meaning that the volume of the

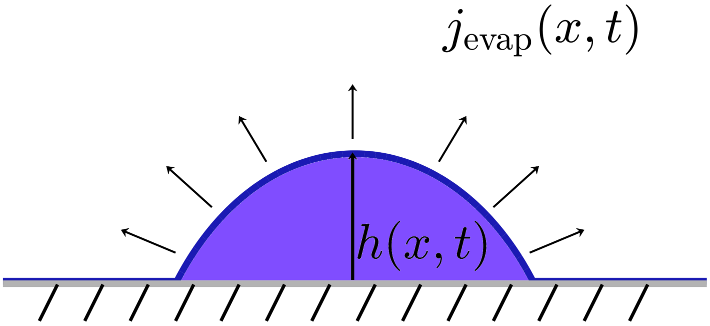

Figure 2.5: *Schematic sketch illustrating a liquid droplet on a flat substrate under the effect of evaporation. The droplet has a film height of* $h(x,t)$*. The arrows pointing away from the liquid droplet represent the direction of evaporation (non-conserved) flux* $j_{\text{evap}}(x,t)$*, which determine the loss of liquid.*

liquid droplet is decreasing.

In this thesis the non-conserved flux from Ref. [131] is used. It is defined as

$$j_{\text{evap}}(x,t) = \beta_{\text{evap}}\left(\frac{p}{\rho} - \mu_{\text{evap}}\right) \quad \text{with} \quad p = p_{\text{L}} - \Pi(h)\,. \tag{2.25}$$

Here, the non-conserved flux has an evaporation rate (or the strength of evaporation) β_{evap} and the chemical potential μ_{evap} of the vapour phase or “vapour pressure”. Note that, the non-conserved flux in Eq. (2.25) disappears exactly when the inner pressure of the liquid p/ρ is equal the external vapour pressure μ_{evap}. In other words, the liquid condensates as long as the overall pressure p in the liquid droplet is low. With Eq. (2.25) the precursor film neither evaporates nor condensates, when $\Pi(h) = \rho\mu_{\text{evap}}$, i.e., the absorption layer thickness depends on μ_{evap}.

CHAPTER THREE

Derivation of a thin-film equation with surface acoustic waves (SAW)

> ” *Non scholae, sed vitae discimus* “
>
> – LUCIUS ANNAEUS SENECA,
> *Epistulae morales ad Lucilium*
> *letter 106, section 12, 65 AD*

In order to describe a thin film mathematically, a so-called thin-film equation is derived. This thin-film equation is determined with the governing hydrodynamic equations, represented by the Navier-Stokes Eqs. (2.5) and (2.6), and the introduced boundary conditions for liquid films, see Sec. 2.2. The local film thickness of the thin film is determined by a long-wave approximation. Hereby, a lubrication ansatz is used, which is known as lubrication theory [95]. However, the main topic of this work focusses on thin films driven by Rayleigh surface acoustic waves (SAW) [87]. In addition, the SAW-theory by Nyborg is considered [93, 94]. In subsequent steps, the evolution equation is further expanded by more attributes: wettability (see Sec. 2.3), lateral forces acting on the liquid (gravity), inclination of the substrate and evaporation. Combining all of these leads to a thin-film evolution equation (nonlinear differential equation), which allows to describe and to analyse two different models: the classical Landau-Levich system, where a thin film is withdrawn by a plate from a bath and thin film driven by a propagating SAW. In the final step, a scaling for the limiting case is introduced, which allows to directly compare both models.

3.1 Geometry of SAW-driven thin-film model

The movement of liquid flow within a liquid is expressed by stream functions. The stream function Ψ is represented by the corresponding velocity field $\vec{v}^{\,(2)}$. This velocity field function also fulfills the continuity equations automatically to ensure mass conservation. The stream function Ψ defined as

$$\vec{v}^{\,(2)}(\vec{r}^{\,(2)},t) = \begin{pmatrix} u(\vec{r}^{\,(2)},t) \\ w(\vec{r}^{\,(2)},t) \end{pmatrix} = \begin{pmatrix} \partial_z \Psi \\ -\partial_x \Psi \end{pmatrix} . \tag{3.1}$$

The reduced Navier-Stokes Eq. (2.9) written in terms of the stream function Eq. (3.1) is

$$\begin{aligned} &\rho\Big\{\partial_t\Big[(\vec{\nabla}^{(2)})^2\Psi\Big] + (\partial_z\Psi)\partial_x\Big[(\vec{\nabla}^{(2)})^2\Psi\Big] - (\partial_x\Psi)\partial_z\Big[(\vec{\nabla}^{(2)})^2\Psi\Big]\Big\} \\ &= \mu(\vec{\nabla}^{(2)})^4\Psi . \end{aligned} \tag{3.2}$$

To further reduce the model, the system is considered as a two-dimensional (2D) problem using the Laplace operator from Eq. (2.3).

For this case, the geometrical consideration assumes that the liquid bath is at the right side of a domain Ω at $x = L/2$. The substrate is horizontally oriented. Then, in the resulting liquid bath a meniscus is formed. The meniscus has a constrained curvature with radius $\vec{R}$. A simple sketch of a 2D thin-film model driven by SAW is given in Fig. 3.1.

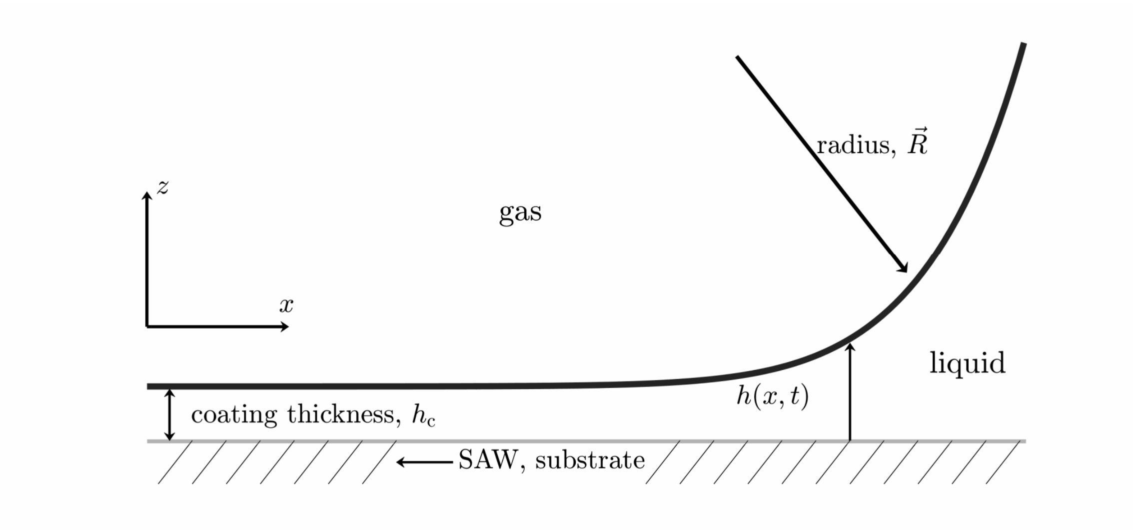

Figure 3.1: *Simplified illustration of a thin-film system in which a liquid film is deposited from a bath (situated at the right boundary) to the negative x-direction using surface acoustic waves (SAW). In the substrate, which is under the thin film the SAW propagates. A meniscus is formed at the bath side, which is defined by the arrow pointing on the curvature of the meniscus with radius* $\vec{R}$. *On the other side of the illustration at* $x = -L/2$, *a coating thickness of film height* $h(x,t) = h_c$ *is situated.*

Fig. 3.1 shows that a Rayleigh SAW propagates along the x-direction in the solid substrate. The resulting momentum causes in-plane and out-of-plane displacements of the substrate surface. These displacements, which transfer into the liquid above, also invoke a small liquid momentum parallel and orthogonal to the solid substrate. As a result, a flow within the liquid is induced by SAW. The occurring deformation of the solid substrate is described via an asymptotic series ansatz of the velocity of the displacements U_{dis} of the solid-liquid interface [60, 97]. This ansatz is only applicable if the ratio between the small displacements and a length scale of SAW is very small $\zeta \equiv U_{\text{dis}}/\omega_s k \ll 1$. Here, the angular frequency of the SAW is ω_s and k is the wave number. Based on the theory of linear elasticity only the leading order is considered [3]. As a result, the flow of the liquid above the solid substrate can be described with

$$\begin{pmatrix} u(\vec{r}^{\,(2)},t) \\ w(\vec{r}^{\,(2)},t) \end{pmatrix} = U_{\mathrm{dis}} \begin{pmatrix} \cos(\omega_s t - kx) \\ \chi \sin(\omega_s t - kx) \end{pmatrix} + \mathcal{O}(\zeta) \quad \text{at} \quad z = 0\,. \tag{3.3}$$

The parameter χ describes the ratio of the magnitude between in-plane and out-of-plane displacements [87]. In further calculations this factor $\chi \approx 1.3$ is omitted, as it does not contribute to the analytical and numerical treatment of this study.

3.2 Scaling to nondimensional quantities

In order to investigate a nonlinear partial differential equation (PDE) with physical quantities, i.e. velocity U_{dis} Eq. (3.3), by using numerical techniques, it is inevitable to use a scaling approach. This approach replaces the physical quantities with nondimensional quantities. For an evolution equation it is common to scale the system's length first. The thickness of the height profile $h(x,t)$ is scaled with the viscous penetration length of the SAW

$$\delta \equiv \sqrt{\frac{2\mu}{\rho\omega_s}}. \tag{3.4}$$

The factor $\sqrt{2}$ is introduced for convenience and simplifies further calculations. Since the thin-film model has a strong dependence on the meniscus curvature R, the characteristic length scaling of the system is given with

$$L \equiv \sqrt{\delta R}\,. \tag{3.5}$$

In the following, a ratio between the system size L and height profile $h(x,t)$ is introduced, which allows to perform a long-wave (lubrication) approximation ansatz [95]. The assumption is that the height profile through the long-wave approach is interpreted as a thin film. Therefore, the smallness parameter with $\epsilon \ll 1$ is introduced, and the corresponding system length is scaled with

$$\epsilon \equiv \frac{\delta}{L}\,. \tag{3.6}$$

The underlying idea is that far away from the meniscus position, where the coating thickness h_{c} of the thin-film should be very small in comparison to the curvature R or the height of the meniscus h_{m}. Additional dimensional quantities (with tildes) employing scales (3.4), (3.5) and scale ratio (3.6) are presented in Tab. 3.1

dimensional quantities	dimensionless quantities
x	$\tilde{x} = x\epsilon/\delta$
z	$\tilde{z} = z/\delta$
h	$\tilde{h} = h/\delta$
t	$\tilde{t} = t\omega$
k	$\tilde{k} = k\delta/\epsilon$
Ψ	$\tilde{\Psi} = \Psi/\delta U_{\text{dis}}$
p	$\tilde{p} = p\delta/\epsilon^2\gamma$

TABLE 3.1: *Scaling of the dimensional physical quantities to nondimensional ones for deriving the thin-film equation.*

From now on, the tildes from the dimensionless quantities are dropped for simplicity and in addition, two more dimensionless hydrodynamic parameters are introduced

$$\mathrm{Ca} \equiv \frac{\mu U_{\text{dis}}}{\gamma} \qquad \text{and} \qquad \mathrm{Re} \equiv \frac{\rho U_{\text{dis}}\delta}{\mu}\,. \tag{3.7}$$

The Reynold number Re describes the ratio of inertial to viscous forces and the Capillary number Ca defines the ratio of surface tension force and viscous force, respectively. All these dimensionless quantities are now substituted into Eqs. (2.11), (2.16), (3.2) and (3.3) for non-volatile liquids with $\beta_{\text{evap}} = 0$.

The dimensionless quantities are now incorporated in the Navier-Stokes Eq. (3.2). Considering that the wavelength of SAW is small compared to the film thickness with $h(x) \ll k^{-1}$, the caused effects from the pressure p are negligible. Subsequently, this allows to simplify the following expression into

$$\begin{aligned}
&\frac{\rho}{\mu}\Bigg[\frac{U_{\text{dis}}\omega_s\epsilon^2}{\delta}\partial_{xxt}\Psi + \frac{U_{\text{dis}}\omega_s}{\delta}\partial_{zzt}\Psi + \frac{U_{\text{dis}}^2\epsilon^3}{\delta^2}(\partial_z\Psi)\partial_{xxx}\Psi \\
&\quad + \frac{U_{\text{dis}}^2\epsilon}{\delta^2}(\partial_z\Psi)\partial_{zzx}\Psi - \frac{U_{\text{dis}}^2\epsilon^3}{\delta^2}(\partial_x\Psi)\partial_{zxx}\Psi - \frac{U_{\text{dis}}^2\epsilon}{\delta^2}(\partial_x\Psi)\partial_{zzz}\Psi\Bigg] \\
&= \frac{U_{\text{dis}}\epsilon^4}{\delta^3}\partial_{xxxx}\Psi + 2\frac{U_{\text{dis}}\epsilon^2}{\delta^2}\partial_{xxzz}\Psi + \frac{U_{\text{dis}}}{\delta^3}\partial_{zzzz}\Psi\,.
\end{aligned} \tag{3.8}$$

Eq. (3.8) is linearised in ϵ, so that all terms of higher order with $\mathcal{O}(\epsilon^2)$ are dropped. Furthermore, the definitions of (3.5) and (3.7) are used to obtain t

$$2\partial_{zzt}\Psi + \epsilon\mathrm{Re}\Big[(\partial_z\Psi)\partial_{zzx}\Psi - (\partial_x\Psi)\partial_{zzz}\Psi\Big] = \partial_{zzzz}\Psi + \mathcal{O}(\epsilon^2)\,. \tag{3.9}$$

Eq. (3.9) represents a scaled stream function. The streaming of the liquid, which is caused by the displacements momentum described in Eq. (3.3) is further transformed. Hereby, only the real part $\Re$ of the oscillations induced by SAW is considered. Then, the corresponding flow of liquid is expressed with exponential functions and reads

$$\begin{pmatrix} \partial_z \Psi \\ -\partial_x \Psi \end{pmatrix} = \Re \begin{pmatrix} \mathrm{e}^{\mathrm{i}(t-kx)} \\ \epsilon^{-1} \mathrm{e}^{\mathrm{i}(t-kx-\pi/2)} \end{pmatrix} \quad \text{at} \quad z = 0\,. \tag{3.10}$$

The kinematic condition of the free surface of the liquid [Eq. (2.11)] without evaporation becomes

$$2\partial_t h + \epsilon \mathrm{Re}\Big[\partial_x \Psi + (\partial_z \Psi)\partial_x h\Big] = 0 \quad \text{at} \quad z = h(x,t)\,, \tag{3.11}$$

In order to derive the expression from Eq. (3.11), Eq. (2.11) is expanded by a factor of $\delta\rho/\mu$. This allows to substitute the scaling for the Reynold number Re.
Next, Eq. (2.16), which represents the shape of the liquid surface, projected by the normal vector and Eq. (2.17) projected by the tangential vector $\vec{t}$ are scaled. The normal vector is given by

$$\begin{aligned} \frac{2\mu}{1+(\epsilon\partial_x h)^2}\Bigg[&-\left(\frac{\epsilon U_{\mathrm{dis}}}{\delta}\partial_{xz}\Psi\right)(\epsilon\partial_x h)^2 + \frac{\epsilon U_{\mathrm{dis}}}{\delta}\partial_{zx}\Psi \\ &+ (\epsilon\partial_x h)\left(\frac{\epsilon U_{\mathrm{dis}}}{\delta}\partial_{zx}\Psi - \frac{\epsilon U_{\mathrm{dis}}}{\delta}\partial_{xz}\Psi\right)\Bigg] \\ &= -\frac{\gamma\frac{\epsilon^2}{\delta}\partial_{xx}h}{\Big[1+(\epsilon\partial_x h)^2\Big]^{3/2}} - \frac{\gamma\epsilon^2}{\delta}p \quad \text{at} \quad z = h(x,t)\,. \end{aligned} \tag{3.12}$$

In the subsequent step, Eq. (3.12) is Taylor-expanded at the free surface $z = h(x,t)$ and the terms of $\mathcal{O}(\epsilon^2)$ and higher are omitted, resulting in

$$-\partial_{zx}\Psi = \frac{\epsilon}{2\mathrm{Ca}}\Big(\partial_{xx}h + p\Big) + \mathcal{O}(\epsilon^2) \quad \text{at} \quad z = h(x,t)\,. \tag{3.13}$$

The tangential component results in

$$\partial_{zz}\Psi + \mathcal{O}(\epsilon^2) = 0 \quad \text{at} \quad z = h(x,t)\,. \tag{3.14}$$

Now, the curvature of the liquid surface vector has to vanish. In other words, the tangent vector, which is always in line with the free surface $z = h(x,t)$, has to equal the curvature. This assumption leads to a flat film. On the one hand, if the first order $\mathcal{O}(1)$ of Eq. (3.13) is examined, one obtains

$$-\partial_{zx}\Psi = 0 = \partial_x u = -\partial_z w \quad \text{at} \quad h(x,t)\,. \tag{3.15}$$

Eq. (3.15) determines the flow of the liquid at the free surface. On the other hand, by looking at the following order $\mathcal{O}(\epsilon)$, the equation corresponds to the pressure at the free surface and reads

$$p = -\partial_{xx} h \quad \text{at} \quad h(x,t)\,. \tag{3.16}$$

In the next steps, the concept of liquid flow (mass transport) is extended. Here, the results from the stress tensor are applied to the reduced Navier-Stokes Eq. (2.9). In this case only the flow of liquid in the x-direction is taken into account, so that the term is simplified to

$$\rho \partial_t u = -\partial_x p + \mu(\partial_{xx} + \partial_{zz})u\,. \tag{3.17}$$

Now, the results from the normal stress tensor of Eqs. (3.15) and (3.16) are used at the boundary of the free surface and using the dimensionless quantities from (3.7) as well as scaling from Tab. 3.1, it results in

$$2\partial_{zt}\Psi = \frac{\epsilon^3}{\mathrm{Ca}}\partial_{xxx}h + \partial_{zzz}\Psi + \mathcal{O}(\epsilon^2) \quad \text{at} \quad h(x,t)\,. \tag{3.18}$$

In this way, all the gathered information obtained from the scaled projection at the free surface of the liquid is maintained in Eq. (3.18), allowing to replace Eq. (3.13) with Eq. (3.18) in the calculations.

Then, the corresponding film thickness $h(x,t)$ has to be determined. Here, it is assumed that the profile film thickness $h(x,t)$ has to develop slowly and that the temporal variation is caused by the high frequency of the propagating SAW. This results in the displacements from the solid surface, which is then further transmitted into the liquid. At the free surface these displacements have to vanish, so that the remaining liquid film height at the free surface is undisturbed.
The stream at the free surface at $z = h_0(x,t) = h_0$ is approximated with

$$\begin{aligned} \Psi|_{z=h(x,t)} &= \Psi|_{z=h_0} + (h-h_0)\partial_z\Psi|_{z=h_0} \\ &\quad + \frac{1}{2}(h-h_0)^2\partial_{zz}\Psi|_{z=h_0} + \mathcal{O}\Big((h-h_0)^3\Big) \end{aligned} \tag{3.19}$$

Furthermore, an asymptotic ansatz for the stream function Ψ and film height $h(x,t)$ is introduced. The aim is to describe the variation caused by the SAW that is transmitted from the solid surface into the liquid. The lubrication approximation of the governing equations is obtained from the first order of magnitude $\mathcal{O}$ in the asymptotic series [95]. In this way, the asymptotic approach is consistent with the parallel-local-flow assumption of the stream function Ψ up to the order of $\mathcal{O}(\epsilon)$.

The asymptotic series for the corresponding velocity field yields

$$\Psi = \epsilon^{-1}\Psi_{-1} + \Psi_0 + \epsilon\Psi_1 + \mathcal{O}(\epsilon^2) \tag{3.20}$$

and for the film height $h(x,t)$ is determined up to the second order $\mathcal{O}(\epsilon^2)$

$$h(x,t) = h_0 + \epsilon h_1(x,t) + \epsilon^2 h_2(x,t) + \mathcal{O}(\epsilon^3)\,. \tag{3.21}$$

Both Eqs. (3.20) and (3.21) are essential for the lubrication ansatz. Subsequently, they are combined into Eq. (3.19), where only the linear order in ϵ is considered, which results in

$$\begin{aligned}\Psi|_{z=h_0} =& \,\epsilon^{-1}\Psi_{-1}|_{z=h_0} + (\Psi_0 + h_1\partial_z\Psi_{-1})|_{z=h_0} \\ &+ \epsilon\Big(\Psi_1 + h_1\partial_z\Psi_0 + h_2\partial_z\Psi_{-1} + \frac{1}{2}h_1^2\partial_{zz}\Psi_{-1}\Big)\Big|_{z=h_0} + \mathcal{O}(\epsilon^2)\,.\end{aligned} \tag{3.22}$$

Eq. (3.22) is substituted into Eqs. (3.11) and (3.18), whereas the asymptotic ansatz for the stream function Ψ of Eq. (3.20) is used in Eqs. (3.9) and (3.10). Note that the boundary condition of the free surface at $z = h_0$ is matched here. In the following, the four presented expressions are in the same leading order $\mathcal{O}(\epsilon^{-1})$ and they yield

$$(3.9): \quad 2\partial_{zzt}\Psi_{-1} = \partial_{zzzz}\Psi_{-1} \tag{3.23}$$

$$(3.10): \quad \Big(\partial_z\Psi_{-1}, -\partial_x\Psi_{-1}\Big)^T = \Re\Big(0, \exp\Big[\mathrm{i}(t - kx - \pi/2)\Big]\Big)^T \qquad \text{at} \quad z = 0 \tag{3.24}$$

$$(3.18): \quad 2\partial_{zt}\Psi_{-1} = \partial_{zzz}\Psi_{-1} \qquad \text{at} \quad z = h_0\,. \tag{3.25}$$

Eq. (3.11) has no leading order in $\mathcal{O}(\epsilon^{-1})$, and it expresses an undisturbed film height. In other words, the film height stays constant in time $\partial_t h_0 = 0$. This set of three equations is interpreted as a vertical flow of liquid due to the displacement of the solid surface induced by SAW. By integrating Eq. (3.24) in x direction, the second component of the vector gives

$$\Psi_{-1}(x,t) = -k^{-1}\cos(t - kx) \quad \text{at} \quad z = 0\,. \tag{3.26}$$

Note that the leading order of the solution of the flow Ψ_{-1} in Eq. (3.26) is in phase with the x-component of the displacement momentum in Eq. (3.3). The next order of magnitude in ϵ is investigated, leading to the following set of equations in terms of order $\mathcal{O}(\epsilon)$

$$(3.9):\quad 2\partial_{zzt}\Psi_0 = \partial_{zzzz}\Psi_0 \tag{3.27}$$

$$(3.10):\quad \Big(\partial_z\Psi_0, -\partial_x\Psi_0\Big)^T = \Re\Big(\exp\Big[\mathrm{i}(t-kx)\Big], 0\Big)^T \qquad \text{at} \quad z=0 \tag{3.28}$$

$$(3.11):\quad \partial_t h_1 = -\frac{\mathrm{Re}}{2\epsilon}\partial_x\Psi_{-1} \qquad \text{at} \quad z=h_0 \tag{3.29}$$

$$(3.18):\quad 2\partial_{zt}\Psi_0 = \partial_{zzz}\Psi_0 \qquad \text{at} \quad z=h_0\,. \tag{3.30}$$

These equations of the order $\mathcal{O}(\epsilon)$ represent the Stokes boundary layers. They are created by the displacements momentum oriented horizontally in the substrate. The displacements are induced by the propagating SAW in the solid surface, creating oscillating boundary layers. Eq. (3.11) is solved by inserting the solution for Ψ_{-1} [Eq. (3.26)] and integrating once with respect to time t, leading to

$$h_1(x,t) = -\frac{\mathrm{Re}}{2\epsilon}\cos(t-kx)\,. \tag{3.31}$$

Here, $h_1(x,t)$ represents the capillary waves induced by SAW. In addition, Ψ_0 is determined by using Eqs. (3.27)-(3.30). Solving the set of equations, leads to

$$\Psi_0(\vec{r}^{\,(2)},t) = \Re\left\{\frac{(1-\mathrm{i})\sinh\Big[(1+\mathrm{i})h_0\Big] + \sinh\Big[(1+\mathrm{i})(z-h_0)\Big]}{2\cosh\Big[(1+\mathrm{i})h_0\Big]}\mathrm{e}^{\mathrm{i}(t-kx)} + g(t)\right\}. \tag{3.32}$$

Hereby, Eq. (3.14) is taken into account as an additional requirement, which is trivially solved when using the asymptotic ansatz. The solution of Ψ_0 is calculated with MATHEMATICA[1] and satisfies all boundary conditions of Eqs. (3.27)-(3.30). The arbitrary function of time $g(t)$ is neglected in further calculations, as it does not contribute to derive the evolution equation. All three time-dependent solutions for h_1, Ψ_{-1} and Ψ_0 in Eqs. (3.31), (3.26) and (3.32) represent fast oscillating frequencies and also depend on the viscous time scale [5, 6, 87]. These frequencies are connected to the vibration induced by the propagating SAW in the substrate on a fast time scale ω_s^{-1}. For the long-wave analysis of thin films, however, a slow temporal development is required. The previous time dependence is limited to the fast frequency of the SAW, which is the motion of the substrate and liquid at $z=0$. It is important to note that the occurring effects of the SAW due to the acoustic streaming in liquids takes place in two different time scales. For this reason, an additional slow hydrodynamic time scale T is introduced to quantify the slow motion of the liquid film with

$$T \equiv \frac{L}{\mathrm{Re}U_\mathrm{d}} = \frac{L}{\nu} \ll \omega^{-1}\,. \tag{3.33}$$

---

[1] MATHEMATICA Version 11.2

This scale allows to scale the dynamics of the film flow for a slow time scale. In the next step, it is necessary to average the fast oscillating frequency of the SAW over time. At this point a suitable operator is introduced [37, 93, 109] and it reads

$$\Big\langle f(t) \Big\rangle = \frac{1}{2\pi} \int_0^{2\pi} \Re f(t) \mathrm{d}t \,. \tag{3.34}$$

The arbitrary function $f(t)$ is averaged over a complete period 2π. This operator allows to determine the remaining expressions of order $\mathcal{O}(\epsilon)$ for a short time scale of the stream functions, to derive a SAW-driven thin-film evolution equation. The set of four time-averaged equations read

$$(3.9): \quad \Big\langle \partial_{zzzz}\Psi_1 \Big\rangle = -\frac{\mathrm{Re}}{\epsilon} \Big\langle (\partial_x \Psi_{-1})(\partial_{zzz}\Psi_0) \Big\rangle \tag{3.35}$$

$$(3.10): \quad \Big(\Big\langle \partial_z \Psi_1 \Big\rangle, \Big\langle -\partial_x \Psi_1 \Big\rangle \Big)^T = (0,0)^T \qquad \text{at} \quad z = 0 \tag{3.36}$$

$$(3.11): \quad \Big\langle \partial_{zz}\Psi_1 \Big\rangle = -\Big\langle h_1 \partial_{zzz}\Psi_0 \Big\rangle \qquad \text{at} \quad z = h_0 \tag{3.37}$$

$$(3.18): \quad \Big\langle \partial_{zzz}\Psi_1 \Big\rangle = -\frac{\epsilon^2}{\mathrm{Ca}} \partial_{xxx} h_0 - \Big\langle h_1 \partial_{zzzz}\Psi_0 \Big\rangle \qquad \text{at} \quad z = h_0 \,. \tag{3.38}$$

Eq. (3.38) uses $\langle 2\partial_{zt}\Psi_1 \rangle = 0$ for order $\mathcal{O}(\epsilon)$. Note that the order $\mathcal{O}(\epsilon)$ is used in Eq. (3.22) for Eqs. (3.37) and (3.38), which describe the surface of the film. In Eq. (3.38) the film height is kept constant for sufficiently small thin-films (ϵ^2). This term does not vanish with the time-average operator. In a final step, the last unknown stream function Ψ_1 is determined. Eq. (3.35) is solved by integrating it three times over z. In a subsequent step, the time-average operator from Eq. (3.34) is applied and the solutions for Ψ_0 and Ψ_{-1} are inserted. The final expression yields

$$\begin{aligned} \Psi_1(\vec{r}^{\,(2)}) = & \frac{-z\sin(2h) + z\sinh(2h)}{4[\cos(2h) + \cosh(2h)]} \\ & + \frac{\cos(z)\cosh(2h-z) + \cosh(z)\cos(2h-z)}{4[\cos(2h) + \cosh(2h)]} + c(\vec{r}^{\,(2)}) \,. \end{aligned} \tag{3.39}$$

The arbitrary function $c(\vec{r}^{\,(2)})$ contains all the remaining information such as acting pressure, surface tension and other means. Then, the flux of the liquid is approximated by the leading order of Ψ with

$$Q_{\mathrm{fl}}(x,t) = \langle \Psi \rangle|_{z=h} - \langle \Psi \rangle|_{z=0} \approx \epsilon(\langle \Psi_1 \rangle|_{z=h} - \langle \Psi_1 \rangle|_{z=0}) \,. \tag{3.40}$$

In order to find an expression for the arbitrary function $c(\vec{r}^{\,(2)})$ in Eq. (3.39) the boundary conditions of Eq. (3.36)-(3.38) are applied and inserted into Eq. (3.40), so that the flux yields

$$Q_{\text{fl}}(x,t) = \text{Re}hv_{\text{s}}(h) + \frac{\epsilon^3}{3\text{Ca}} h^3 \partial_{xxx} h \tag{3.41}$$

with the dimensionless expression for the propagating SAW

$$v_{\text{s}}(h) = \frac{1}{4h} \left(\frac{h \sinh(2h) - h \sin(2h) + 2\cos(h)\cosh(h)}{\cos(2h) + \cosh(2h)} - 1 \right). \tag{3.42}$$

Note that Eq. (3.42) becomes $v_{\text{s}}(h) \approx h^3/8 + \mathcal{O}(h^7)$ for very low film thickness $h \to 0$. Therefore, the SAW-driving and plate velocity U_0 represent different functional dependencies at small h, but become similar at large film thickness h.

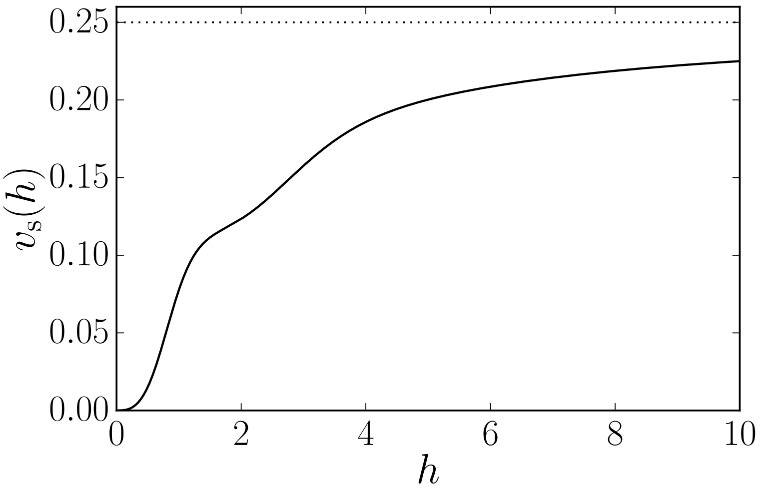

Figure 3.2: *Plot of the dimensionless propagating Rayleigh SAW-term $v_{\text{s}}(h)$ (solid black line) for growing film heights h. The SAW $v_{\text{s}}(h)$ approaches 0.25, which is marked by a dotted line. So for h $\to \infty$, the SAW reaches $v_{\text{s}}(h) \to 0.25$.*

In order to derive a dimensionless thin-film evolution equations as in Ref. [87], continuity and all dimensionless quantities from Tab. 3.1 and Eq. (3.7) are used. All tildes are dropped and the evolution equation reads

$$\partial_t h = -\partial_x Q_{\text{fl}}(x,t) = -\partial_x \left[-hv_{\text{s}}(h) + \frac{h^3}{3\text{We}_{\text{s}}} \partial_{xxx} h \right]. \tag{3.43}$$

This continuity equation describes the dynamics of the liquid film height profile on a fully wetting plate in absence of gravity and other external forces. Here, the scaled dimensionless Weber number with $\text{We}_{\text{s}} = \text{ReCa}/\epsilon^3$ combines the ratio between the convective stress, which is induced by the SAW, and the capillary stress due to the surface tension at the free surface. The minus sign of the advection term hv_{s} is introduced for convenience. The model considers that the SAW is acting towards the negative x-direction, see sketch Fig. 3.1.

Next, Eq. (3.43) is transformed back introducing a dimensional equation. This allows to expand the corresponding thin-film equation in order to add more attributes.

A typical velocity scale of the SAW v_s is given by

$$\tilde{v}_\mathrm{s}(h) = \frac{\rho\delta U_\mathrm{dis}^2}{\mu} v_\mathrm{s}(h) \equiv U_\mathrm{w} v_\mathrm{s}(h)\,. \tag{3.44}$$

The complete dimensional thin-film equation then includes the geometry of the classical Landau-Levich model where a plate under an angle α is withdrawn from a bath. The contribution of lateral forces is decisively influenced by gravity g. In addition, a partial wetting liquid is considered. The wetting potential reads

$$f(h) = \kappa\left(\frac{h_\mathrm{p}^3}{5h^5} - \frac{1}{2h^2}\right) \tag{3.45}$$

In Eq. (3.45) prefactor κ represents a typical energy density scale (wetting strength) and h_p is the height of the precursor film. Then, the Derjaguin (disjoining) pressure results

$$\Pi(h) = -\partial_h f(h) = \kappa\left(\frac{h_\mathrm{p}^3}{h^6} - \frac{1}{h^3}\right). \tag{3.46}$$

with wetting strength κ [118]. Then, the full dimensional thin-film equation is obtained and reads

$$\partial_t h = -\partial_x\left\{ - hU_\mathrm{drag} - hU_\mathrm{w} v_\mathrm{s}(h) + \frac{h^3}{3\mu}\Big[\partial_x\left(\gamma\partial_{xx}h + \Pi(h) - \rho g h\right) + \alpha\rho g\Big]\right\}. \tag{3.47}$$

Hereby, U_drag corresponds to the velocity of the withdrawn plate. By, re-introducing the scalings for time $t = L/\nu$, film thickness δ and length scale L for the x-coordinate, the nondimensional equation reads

$$\begin{aligned}\partial_t h = -\vec{\nabla}\cdot\Bigg\{ &- h\Big(D_1 + D_2 v_\mathrm{s}(h), 0\Big)^T + \frac{h^3}{3}\vec{\nabla}\cdot\Big[D_3\Delta h + D_4\Pi(h)\Big] \\ &+ D_5\frac{h^3}{3}\left[\Big(\frac{\alpha}{\epsilon}, 0\Big)^T - \vec{\nabla}h\right]\Bigg\},\end{aligned} \tag{3.48}$$

whereas Eq. (3.48) is expanded for a 2D case, where the y-component is added. Note that the velocities, dragged plate D_1 and SAW $D_2 v_\mathrm{s}(h)$ are only acting in the x-direction and the solid substrate is inclinated as well at angle α. The introduced nondimensional numbers are

$$D_1 = \frac{U_\mathrm{drag}}{\nu},\quad D_2 = \frac{U_\mathrm{w}}{\nu},\quad D_3 = \frac{\epsilon^3\gamma}{\mu\nu},\quad D_4 = \frac{\epsilon\delta\kappa}{\mu\nu},\quad \text{and}\quad D_5 = \frac{\epsilon\rho g\delta^2}{\mu\nu}\,. \tag{3.49}$$

At first, the parameter ν is kept general, so that all five nondimensional numbers in Eq. (3.48), are described as: $D_1 = U_0$ represents a velocity ratio corresponding to a plate dragging strength, $D_2 = \epsilon_\mathrm{s}$ the velocity ratio corresponding to a SAW strength

$D_3 = \mathrm{We}_\mathrm{s}^{-1}$ an inverse Capillary or Weber number, $D_4 = \mathrm{Ha}$ is called Hamaker number and $D_5 = G$ is gravity.

This particular scaling is the main parametrisation for the investigation of the thin-film system considering partially wetting liquid. This allows to compare both cases, which corresponds to the classical Landau-Levich system for partially wetting liquid in Ref. [47, 123, 132] and SAW-driven meniscus in Ref. [87]. Note that the film height h of Ref. [46] is scaled by a factor of three $\tilde{h} \to 3h$. The main focus on the thin film behaviour is investigated by the effects which occur, by plate velocity U_0 in Sec. 5.1 and SAW strength ϵ_s in Sec. 5.2. In addition, this study also allows to retain the ability to investigate the influence of We_s, which is a an important parameter in Ref. [87].

Then, the general evolution equation is obtained from Eq. (3.48) with the scaling Eq.(3.49) and reads

$$\begin{aligned}\partial_t h = -\vec{\nabla} \cdot \Bigg\{ &\underbrace{-h\Big(U_0 + \epsilon_\mathrm{s} v_\mathrm{s}(h),0\Big)^T}_{\text{advection term}} + Q_\mathrm{m} \vec{\nabla} \cdot \underbrace{\left[\frac{1}{\mathrm{We}_\mathrm{s}} \Delta h + \mathrm{Ha}\Pi(h)\right]}_{\text{Laplace and disjoining pressure}} \\ &+ Q_\mathrm{m} \underbrace{G\left[\Big(\alpha,0\Big)^T - \vec{\nabla} h\right]}_{\text{gravity and lateral forces}} \Bigg\} \quad \text{with} \quad \underbrace{Q_\mathrm{m} = \frac{h^3}{3}}_{\text{mobility factor}} \ . \end{aligned} \tag{3.50}$$

The dimensionless evolution Eq. (3.50) describes a more realistic thin-film model that either case of a thin film is drawn out by a dragged plate or SAW. Eq. (3.50) provides the possibility to investigate a thin-film problem regarding to wettability and lateral forces acting on the liquid due to gravity and or inclination of plate or substrate. In App. A.1 further scalings are introduced in order to recover different scalings employed in the literature.

3.3 Velocity field in 1D case

An advancing or flowing liquid can be described by streamlines, which provides insights to the corresponding mass transport beneath the liquid-gas interface. These streamlines have characteristic behaviours, such as locally straight and parallel flow and convection rolls, which are commonly determined in liquids [1, 24, 49]. It is possible to calculate the velocity field of liquid by using the full advection term, plate velocity and SAW, to determine the transport of liquid. This in turn allows to visualise the behaviour of a thin film withdrawn by a plate or driven by SAW. To start the derivation of streamlines, the flow of the thin-film model at the free surface $z = h(x,t)$ given by Eq. (2.11) is considered. It directly yields the conditions for the derivatives of the corresponding velocity fields for $u(\vec{r}^{\,(2)})$ and $w(\vec{r}^{\,(2)})$. The stream function is already defined in Eq. (3.1).

The liquid flow in a two-dimensional (2D) system, is determined by $\Psi_1(x,z)$ from Eq. (3.39) and combined with Eq.(3.1). Note that the liquid flow also depends on disturbances from the oscillating frequency of the SAW, which in turn depends on both coordinates x and z. This leads to

$$u(\vec{r}^{\,(2)}) = \frac{\partial}{\partial z}\Psi_1(\vec{r}^{\,(2)}) = \frac{-\cos(z)\sinh(2h-z) + \sinh(z)\cos(2h-z)}{4\Big(\cos(2h)+\cosh(2h)\Big)} + \frac{\cosh(z)\sin(2h-z) - \sin(z)\cosh(2h-z) - \sin(2h) + \sinh(2h)}{4\Big(\cos(2h)+\cosh(2h)\Big)} + \partial_z c(\vec{r}^{\,(2)}) \tag{3.51}$$

for the x-component and for the z-component

$$\begin{aligned} w(\vec{r}^{\,(2)}) &= \frac{\partial}{\partial x}\Psi_1(\vec{r}^{\,(2)}) = \frac{\partial \Psi_1}{\partial h}\frac{\partial h}{\partial x} \\ &= \Bigg\{ \frac{-z\cos(2h) + z\cosh(2h) + \cos(z)\sinh(2h-z) - \cosh(z)\sin(2h-z)}{2\Big(\cos(2h)+\cosh(2h)\Big)} \\ &\quad - \left[\frac{-z\sin(2h) + z\sinh(2h) + \cos(z)\cosh(2h-z) + \cosh(z)\cos(2h-z)}{2\Big(\cos(2h)+\cosh(2h)\Big)^2}\right] \\ &\quad \cdot \Big(\sinh(2h) - \sin(2h)\Big)\Bigg\}\partial_x h + \partial_x c(\vec{r}^{\,(2)})\,. \end{aligned} \tag{3.52}$$

It is obvious, that both Eqs. (3.51) and (3.52) show that the oscillating SAW depends on both coordinates x and z. Here, the function $c(\vec{r}^{\,(2)})$ corresponds to the occurring pressure $p(\vec{r}^{\,(2)})$ of the thin film due to the boundary conditions and is expressed as

$$\partial_x p(\vec{r}^{\,(2)}) = G\partial_x h - \partial_x\left(\frac{1}{\mathrm{We_s}}\partial_{xx}h - \Pi(h)\right)\,. \tag{3.53}$$

Due to the transport equation of the liquid flow [38], the pressure has to satisfy the following conditions

$$\partial_{zz}u = \partial_x p - G\alpha \tag{3.54}$$

$$\text{and} \quad \partial_z p = -G\,. \tag{3.55}$$

Using Eqs. (3.53) and (3.55) and integrating once, it gives

$$p(\vec{r}^{\,(2)}) = G(h-z) - \frac{1}{\mathrm{We_s}}\partial_{xx}h - \Pi(h)\,. \tag{3.56}$$

Furthermore, the streamlines in the liquid have to be in line with the solid surface at $z = 0$, so that no-slip and no-penetration occurs. It reads

$$u(x,0) = -\Big[U_0 + v_\mathrm{s}(\vec{r}^{\,(2)})\Big|_{z=0}\Big] \,. \tag{3.57}$$

where the SAW-term is determined by Eq. (3.39) with $\Psi_1 = v_\mathrm{s}$ and is further simplified to

$$v_\mathrm{s}(\vec{r}^{\,(2)})\Big|_{z=0} = \frac{1}{4} \,. \tag{3.58}$$

Eq. (3.57) has two contributions: one constant velocity U_0 corresponds to the dragged plate and one constant acting SAW v_s. Both act in the same x-direction. Furthermore, $v_\mathrm{s}(\vec{r}^{\,(2)})|_{z=h} - v_\mathrm{s}(\vec{r}^{\,(2)})|_{z=0}$ immediately results into $v_\mathrm{s}(h)$, see Eq. (3.42). Inserting Eq. (3.51) into Eq. (3.56) and integrating once with respect to z leads to the full solution of the flow in the x-direction

$$\begin{aligned} u(\vec{r}^{\,(2)}) = &\Big[G(\partial_x h - \alpha) - \partial_x\left(\frac{1}{\mathrm{We_s}}\partial_{xx}h - \Pi(h)\right)\Big]\left(\frac{z^2}{2} - hz\right) \\ &- \Big[U_0 + v_\mathrm{s}(\vec{r}^{\,(2)})\Big] \,. \end{aligned} \tag{3.59}$$

Next the velocity field in the z-direction with $w(\vec{r}^{\,(2)})$ is determined. The continuity yields

$$0 = \partial_x u + \partial_z w \,. \tag{3.60}$$

Then, the velocity for the z-direction is calculated and reads

$$\begin{aligned} w(\vec{r}^{\,(2)}) &= -\int_0^z \Big[\partial_x u(\vec{r}^{\,(2)})\Big]\,\mathrm{d}z \\ &= -\Big[\partial_{xx}p\left(\frac{z}{3} - h\right) - (\partial_x p - G\alpha)\partial_x h\Big]\frac{z^2}{2} + \partial_x v_\mathrm{s}(\vec{r}^{\,(2)}) \,. \end{aligned} \tag{3.61}$$

Eqs. (3.59) and (3.61) are used to determine the stream function of a corresponding solution of the thin-film evolution equation.

3.4 Thin-film equation including evaporation

The effects of evaporation or condensation are included in a simplified form into the dimensional thin-film equation by adding the non-conserved flux [Eq. (2.25)] to Eq. (3.48). Therefore, the general scaling in (3.1) and dimensionless quantities are used once again. Then, the full dimensionless evolution equation reads

$$\begin{aligned}\partial_t h = &- \vec{\nabla} \cdot \Bigg\{ - h\Big(U_0 + \epsilon_\mathrm{s} v_\mathrm{s}(h), 0\Big)^T + Q_\mathrm{m} \vec{\nabla} \cdot \left[\frac{1}{\mathrm{We}_\mathrm{s}} \Delta h + \Pi(h)\right] \\ &+ Q_\mathrm{m} G \left[\Big(\alpha, 0\Big)^T - \vec{\nabla} h\right]\Bigg\} + \beta_\mathrm{s} \left\{\frac{1}{\mathrm{We}_\mathrm{s}} \Delta h + \Pi(h) + \mu_\mathrm{s}\right\}\end{aligned} \tag{3.62}$$

with the mobility $Q_\mathrm{m} = h^3/3$. Thereby, two new nondimensional quantities are introduced and they are scaled with

$$\beta_\mathrm{s} \equiv \frac{\mu\nu}{\epsilon^2 \delta\rho} \beta_\mathrm{evap} \quad \text{and} \quad \mu_\mathrm{s} \equiv \frac{\epsilon\delta\rho}{\nu\mu} \mu_\mathrm{evap} \,. \tag{3.63}$$

In this way, Eq. (3.62) describes the evolution of a volatile liquid thin film. In the next chapter, the numerical methods of path continuation and time simulation are explained and introduced.

CHAPTER FOUR

Numerical and analytical techniques

> ”*Iucundi acti labores* “
>
> – MARCUS TULLIUS CICERO,
> *De Finibus Bonorum et Malorum*
> *Book II, Chapter 105, 45 BC*

When analysing nonlinear ordinary differential equations (ODEs) and partial differential equations (PDEs) it is common to use numerical as well as analytical techniques to investigate the derived problem accordingly. Two different methods are explained, which are sufficient for this numerical analysis. One is the path continuation, which is used to generate bifurcation diagrams. They are computed by changing a main control parameter of a steady state solution of the PDE or ODE. Analysing bifurcation diagrams provides insights into behaviour of occurring steady states. These allow to theoretically investigate and interpretate the system. Bifurcation diagrams are computed with the Matlab package PDE2PATH [34, 136], see Sec. 4.1 for a detailed explanation.
The second method is a numerical time simulation. This numerical approach gives information about the temporal behaviour of the system. Time simulations are conducted with OOMPH-LIB [54], see Sec. 4.2.
Both numerical methods, path continuation and time simulation, are used and allow to investigate the occurring dynamical behaviour of the corresponding system. At the end of this chapter, in Sec. 4.4, an analytical method, namely a linear stability analysis, is performed for a thin film. This method allows to predict the stability of the solutions of the system.

4.1 Path continuation approach with pde2path

One of the standard techniques to study the behaviour of a nonlinear system given by ODEs or PDEs is to analyse their bifurcation behaviour. In this work, bifurcation diagrams are constructed via a numerical approach of a path continuation and allow to investigate stable and unstable steady states of a nonlinear physical system [4, 31, 32, 33, 39, 66, 70, 85]. In the case of the derived nonlinear thin-film evolution

Eq. (3.50) a numerical approach is essential.
In order to track steady states of a bifurcation curve, several steps have to be considered. At first a main control parameter is chosen, for instance velocity or inclination of plate for the classical Landau-Levich problem. The control parameter is varied, while a steady state solution is determined. This technique allows one to track branches of the bifurcation curve consisting of steady states from any stationary ODE or PDE. The tracked branch is analysed by calculating the corresponding eigenvalues from the Jacobian matrix to obtain further information on the stability of steady states. Furthermore, it also allows to identify different types of bifurcation, i.e., Saddle-Node and Hopf bifurcations, which are useful to make conclusions concerning the behaviour of the system.

4.1.1 Pseudo-arclength continuation

There are two different path continuation methods. One is called natural path continuation and the other one is termed pseudo-arclength path continuation. Both methods are illustrated in Fig. 4.1.

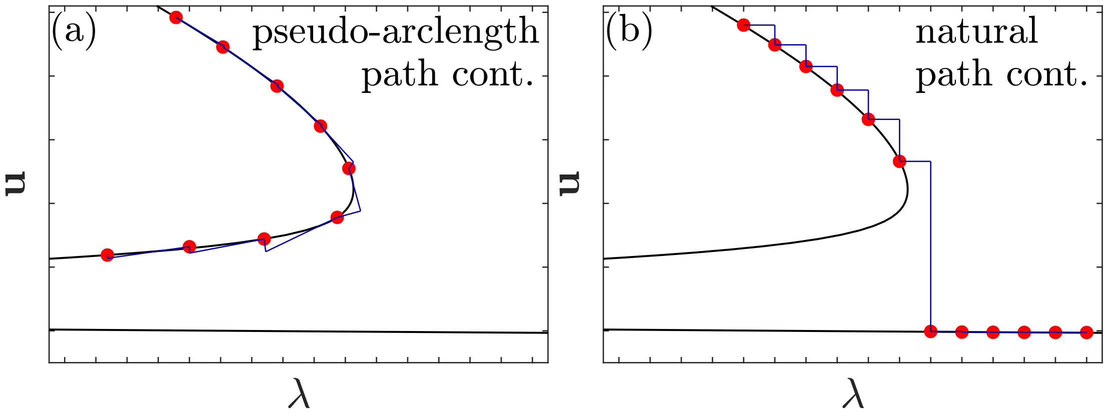

FIGURE 4.1: *Illustration of two different path continuation methods: (a) shows iteration steps of the pseudo-arclength continuation and (b) represents the natural path continuation. With the pseudo-arclength continuation in (a), changes in direction caused by the control parameter* λ *are tracked, due to a advanced tangent in parameter space, so that Saddle-Node bifurcations are detected. The natural path continuation in (b) misses this advantage, so that changes of direction cannot be covered, which results into an unintended jump from one solution branch onto another solution branch.*

Both path continuation methods allow to track a bifurcation curve in parameter space. One significant advantage of the pseudo-arclength path continuation is to fully track a solution branch. In contrast to the natural path continuation, the pseudo-arclength path continuation does not unintentionally “jump“ to another solution branch at a fold, see left panel of Fig. 4.1 (a). As a result the natural path continuation may lose information of the investigated system, so that in this thesis only the pseudo-arclength continuation is used to generate bifurcation diagrams. In the following the (pseudo-arclength) path continuation is briefly explained.
In every case of performing a pseudo-arclength path continuation, an ODE or a

PDE is denoted as $G[\boldsymbol{u},\lambda]$, where $\boldsymbol{u} = (u_1, \dots, u_{n_u})$ denotes a scalar field in $\mathbb{R}^{n_u}$, n_u corresponds to the degrees of freedom and λ presents the main control parameter. In this way, the scalar field $\boldsymbol{u}$ is spatially discretised by means of finite elements over the investigated domain Ω. By implementing an ODE or PDE in PDE2PATH, it is important to note that the occurring problem is reduced to a set of algebraic equations [136]. For this, the method of a finite element method (FEM) is used [76, 100]. For any continuation approach only stationary solutions are considered. The time derivative has to vanish and then it follows

$$0 = -G(\boldsymbol{u},\lambda) = M\dot{\boldsymbol{u}} \quad \text{with} \quad \mathrm{d}_t\boldsymbol{u} = \dot{\boldsymbol{u}}\,, \tag{4.1}$$

where M is the mass matrix with $M \in \mathbb{R}^{n_u \times n_u}$ [27]. The dynamical stability of $\boldsymbol{u}$ is then determined by the eigenvalues of the Jacobian matrix calculated in $\partial_{\boldsymbol{u}}G$.

While tracking a solution branch of steady states, two consecutive steps are always performed during this process:

The first is a prediction step where a tangential projection advances from a known solution at parameter value λ to a first initial “guess” at a new parameter value $\lambda + \Delta\lambda$. Subsequently, the determined solution is corrected via a Newton method [86] and converges to a steady solution at $\lambda + \Delta\lambda$. These two steps are iteratively repeated for any path continuation method so that a solution branch is tracked. In addition, in the pseudo-arclength path continuation method, an additional parameter during this process is considered. As the name of the pseudo-arclength path continuation suggests, the change of the arclength Δs is kept constant in $G(\boldsymbol{u},\lambda)$. The idea behind this technique is that the step size $\Delta\lambda$ and the change of field $\boldsymbol{u}$ are approximated via the arclength's change Δs with

$$|\Delta\boldsymbol{u}|^2 + (\Delta\lambda)^2 \approx (\Delta s)^2\,. \tag{4.2}$$

In order to make s an approximation of the arclength of the solution branch, a function p, here as a arclength condition, is introduced. The function $p(\boldsymbol{u},s,\lambda)$ yields

$$p(\boldsymbol{u},s,\lambda) := \xi\Big\langle \boldsymbol{u} - \boldsymbol{u}_0, \mathrm{d}_s\boldsymbol{u}_0\Big\rangle + (1-\xi)\Big\langle \lambda - \lambda_0, \mathrm{d}_s\lambda_0\Big\rangle - \Delta s \overset{!}{=} 0\,. \tag{4.3}$$

The introduced scalar product with $\Big\langle \cdot, \cdot \Big\rangle$ is in $\mathbb{R}^{n_u}$. The differential is then denoted as $\mathrm{d}_s \equiv \mathrm{d}/\mathrm{d}s$ with respect to the arclength s and ξ. Hereby, ξ corresponds to a free parameter, which denotes the weights for the field $\boldsymbol{u}$. Subsequently, this allows one to extend Eq. (4.1) by Eq. (4.3), which immediately leads to the problem

$$H(\boldsymbol{u},\lambda) = \begin{pmatrix} G(\boldsymbol{u},\lambda) \\ p(\boldsymbol{u},\lambda,s) \end{pmatrix} \overset{!}{=} \begin{pmatrix} 0 \\ 0 \end{pmatrix}\,. \tag{4.4}$$

The function H is weighted with $p(\boldsymbol{u},\lambda,s)$ and defines a hyperplane in $(\boldsymbol{u},\lambda)$-space in dependence of the normalised step size of constant arclength Δs in $G(\boldsymbol{u},\lambda)$. The

Jacobian of Eq. (4.4) for the current step k in block form yields

$$J_H(\boldsymbol{u},\lambda) = \left(\begin{array}{c|c} \partial_{\boldsymbol{u}} G & \partial_\lambda G \\ \hline \partial_s \boldsymbol{u}^{(k)} & \partial_s \lambda^{(k)} \end{array}\right) . \tag{4.5}$$

Note that every tangent direction is given with ∂_s. Subsequently, the problem is solved with the Newton method and converges from the previous steady solution k to the next approximated solution $k+1$ in ($\boldsymbol{u}$,λ)-space, which is given by

$$\left(\begin{array}{c|c} \partial_{\boldsymbol{u}} G & \partial_\lambda G \\ \hline \partial_s \boldsymbol{u}^{(k)} & \partial_s \lambda^{(k)} \end{array}\right) \begin{pmatrix} \partial_s \boldsymbol{u}^{(k+1)} \\ \partial_s \lambda^{(k+1)} \end{pmatrix} + \begin{pmatrix} \partial_s G \\ \partial_s p \end{pmatrix} = \begin{pmatrix} 0 \\ -1 \end{pmatrix} \quad \text{with} \quad k \in \mathcal{N}_1 . \tag{4.6}$$

This process is iteratively repeated to follow the solution branch of the steady states.

4.1.2 Branch switching to time-periodic states (TPS)

Detected Hopf bifurcations on a branch of steady states are an important bifurcation in this thesis. They indicate that a branch of time-periodic states (TPS) emerges. A Hopf bifurcation occurs when a complex conjugated pair of eigenvalues passes the imaginary axis. This is determined by the Jacobian matrix. In order to track these time-periodic branches, a new time scale $\tilde{t} = t\tau$ has to be adopted, where τ is the period. The periodic time τ is unknown and the time is discretised in the interval $\tilde{t} \in [0,1]$ [27, 39]. In the following, the tilde is omitted. In consequence, Eq. (4.1) is expanded, so that it covers a time-periodic solution of the form

$$M\dot{\boldsymbol{u}}(x,t) = -\tau G(\boldsymbol{u},\lambda) , \qquad \text{with} \qquad \boldsymbol{u}(x,0) = \boldsymbol{u}(x,1) . \tag{4.7}$$

It is important to note that Eq. (4.7) is time dependent. At the bifurcation, the first initial guess for the periodic time is chosen $\tau = 2\Pi/\omega$. In order to ensure a unique solution of Eq. (4.7), a phase condition with an explicit time discretisation is introduced. The phase condition has to vanish by integrating over the full time period and yields

$$q(\boldsymbol{u}) := \int_0^1 \Big\langle \boldsymbol{u}(t), M\dot{\boldsymbol{u}}_0(t) \Big\rangle \mathrm{d}t = 0 . \tag{4.8}$$

The previous step is given by $\dot{\boldsymbol{u}}_0(t)$. Then, the step length condition is defined as

$$\begin{aligned} p(\boldsymbol{u},\tau,\lambda) :=& \xi_H \int_0^1 \Big\langle \boldsymbol{u}(t) - \boldsymbol{u}_0(t), \mathrm{d}_s \boldsymbol{u}_0(t) \Big\rangle \mathrm{d}t + (1-\xi_H) \\ & \cdot \Big[w_\tau (\tau - \tau_0)(\mathrm{d}_s \tau_0) + (1 - w_\tau)(\lambda - \lambda_0)(\mathrm{d}_s \lambda_0) \Big] - \Delta s \overset{!}{=} 0 . \end{aligned} \tag{4.9}$$

Note that, in Eq. (4.9) the scalar field $\boldsymbol{u}_0(t)$, the time period τ_0 and the control parameter λ_0 are results from the previous step. The free parameters ξ_H and w_τ denote the weights of the field $\boldsymbol{u}$ at the period τ. In order to track the solution branch of time-periodic states in parameter space, Eq. (4.4) is extended once more. This allows one to formulate an extended problem which reads

$$H(\boldsymbol{u},\tau,\lambda) := \begin{pmatrix} G(\boldsymbol{u},\tau,\lambda) \\ q(\boldsymbol{u}) \\ p(\boldsymbol{u},\tau,\lambda) \end{pmatrix} \overset{!}{=} \begin{pmatrix} 0 \\ 0 \\ 0 \end{pmatrix} \quad \in \mathbb{R}^{mn_u+2}. \tag{4.10}$$

In Eq. (4.10) the steady state problem given by $G(\boldsymbol{u},\tau,\lambda) = 0$ is completed to also determine the unknown parameter τ. In contrast, in the previous case of a pseudo-arclength path continuation for a steady state, one only has $G(\boldsymbol{u},\lambda) = 0$. The field $\boldsymbol{u}$ has to be adjusted due to the time discretisation of the TPS in $\mathbb{R}^{mn_u}$. Subsequently, a Newton method on the initial guess U^k is performed . Then, the solution converges on the solution U^{k+1} with

$$U^{k+1} = U^k - \mathcal{A}(U^k)^{-1}H(U^k) \qquad \text{where} \tag{4.11}$$

$$\mathcal{A} = \begin{pmatrix} \partial_{\boldsymbol{u}}G & \partial_\tau G & \partial_\lambda G \\ \partial_{\boldsymbol{u}}q & 0 & 0 \\ \xi_H T_{\boldsymbol{u}} & (1-\xi_H)w_\tau T_\tau & (1-\xi_H)(1-w_\tau)T_\lambda \end{pmatrix}. \tag{4.12}$$

In addition, $U = (\boldsymbol{u},\tau,\lambda)$ is substituted once to reduce the governing problem and the tangent T in U is then calculated by

$$\mathcal{A}(U)T_i = (0,0,1)^T. \tag{4.13}$$

Eq. (4.11) is solved and these steps are iteratively repeated to trace the branch of time-periodic states.

4.2 Time simulation

Until now, different methods of path continuation have been discussed to determine steady states and time-periodic states of ODEs and PDEs. Next, the technique of numerical time integration is briefly explained. In this work, time simulations are performed with the tool OOMPH-LIB [54]. A numerical time simulation is widely used and allows one the time evolution of states described by ODEs and PDEs. In most cases, they allow to compare the prediction of a theoretical model with experimental results. Bifurcation diagrams obtained by path continuation only provide information of stable and unstable steady states, their bifurcations and branches of stable and unstable time-periodic states (TPS). In this work, the stability of time-periodic states is determined by time simulations and linearly stable steady states are also confirmed by time simulations. Time-periodic states correspond to the occurrence of pattern formation. Example are parallel ridges, which may be formed by thermal effects or hexagon patterns, which occur due to the Rayleigh instabilities

[21, 61, 75, 111].

When PDEs and ODEs are studied by time simulations, the investigated problem is given by $\partial_t \boldsymbol{u} = G(x_i,\boldsymbol{u}(x_i))$, where $\boldsymbol{u}$ corresponds to a scalar field in $\mathbb{R}^{n_u}$. It is discretised with a finite element method (FEM). Therefore, the function $\boldsymbol{u}(x_i,t)$ is expressed by spatially localised base functions $\psi_i(x)$. This is then written as

$$\boldsymbol{u}(x_i,t) = \sum_i u_i(t)\psi_i(x_i)\,. \tag{4.14}$$

The spatial derivatives of Eq. (4.14) only depend on $\psi_i(x)$, so that it gives

$$\partial_x \boldsymbol{u}(x_i,t) = \sum_i u_i(t)\,\partial_x\psi_i(x)\,. \tag{4.15}$$

By using a weighted residual and multiplying with an arbitrary test function $\phi_t(x_i)$ the problem to be solved can be written in integral form

$$0 \overset{!}{=} \int_\Omega \Big[G(x_i,\boldsymbol{u}(x_i)) - \partial_t \boldsymbol{u}\Big]\cdot\phi_t(x)\mathrm{d}x_i\,. \tag{4.16}$$

This integral corresponds to a weak formulation and the integral has to vanishes. In other words, if Eq. (4.16) is fulfilled for any arbitrary test function $\phi_t(x_i)$, it is equivalent to the nonlinear ODE or PDE. Then, Eq. (4.16) is solved by using Newton method. The time is discretised and the time derivative is approximated by a time-stepping scheme. Hereby, a backward differentiation formula known as BDF scheme of second order is used [44]. In short, a Newton method is used at each time step Δt_i successively, leading towards solution that is approximated more accurately of the next time step t_{i+1}.

In addition, time simulations are used to perform a primitive continuation. At the beginning, steady states or time-periodic states (TPS) are chosen as an initial starting solution. Primarily, these states are obtained from time simulations. Then, another time simulation is performed by changing one of the corresponding parameters λ to $\lambda + \Delta\lambda$. The time simulation is performed until the state is stable or periodic. This allows one to track branches of stable steady states or stable time-periodic states with the aid of time simulations. This primitive continuation method is used to compare results of the different numerical approaches and to identify “true” stable time-periodic states.

In the following section, Eq. (3.50) is treated so that it is implemented in either PDE2PATH and OOMPH-LIB.

4.3 Implementation of the SAW-driven thin-film equation

The derived nondimensional thin-film evolution Eq. (3.50) has to be written in a form that facilitates its solution in PDE2PATH and OOMPH-LIB. The thin-film evolution Eq. (3.50) contains a fourth order derivative term due to the Laplace pressure. However, PDE2PATH as well as OOMPH-LIB are not able to directly handle fourth order derivatives. Both tools use triangle functions as a basis, which allow one to construct only derivatives up to second order. To reduce this problem an additional field is introduced, termed auxiliary field u_{aux}. This field is defined to contain both pressure terms, Laplace and Derjaguin pressure. As a result, only second order derivatives in the first and second (auxiliary) field remain.

As a result, the thin-film evolution Eq. (3.50) in a two-dimensional steady case has to be split for the pseudo-arclength path continuation in PDE2PATH into two equations

$$\begin{aligned}\partial_t h = 0 = &- \mathrm{We_s}(\vec{\nabla} h) \cdot \Big(U_0 + \epsilon_{\mathrm{s}} v_{\mathrm{s}}(h), 0\Big)^T - \mathrm{We_s} h\Big(\epsilon_{\mathrm{s}} \mathrm{d}_h v_{\mathrm{s}}(h), 0\Big)^T \cdot \vec{\nabla} h \\ &+ (\partial_h Q_{\mathrm{m}})\vec{\nabla} h \cdot \vec{\nabla} u_{\mathrm{aux}} + Q_{\mathrm{m}} \Delta u_{\mathrm{aux}} - \mathrm{We_s} G (\partial_h Q_{\mathrm{m}})(\vec{\nabla} h)^2 \\ &- \mathrm{We_s} G Q_{\mathrm{m}} (\vec{\nabla} h) + \mathrm{We_s} G \Big(\alpha, 0\Big)^T \cdot (\partial_h Q_{\mathrm{m}})(\vec{\nabla} h) \end{aligned} \tag{4.17}$$

and

$$0 = - \Delta h - \mathrm{We_s} \Pi(h) + u_{\mathrm{aux}}\,. \tag{4.18}$$

Notice that both expressions are multiplied with the Weber number $\mathrm{We_s}$.

The presented Eqs. (4.17) and (4.18) are further simplified for tracking steady states by the pseudo-arclength path continuation. Eq. (4.17) is multiplied by $Q_{\mathrm{m}}(h)^{-1} = 3/h^3$. Because of its time dependence, the mobility factor in front of the auxiliary field vanishes. This allows one to efficiently obtain steady states. However, this trick is not useful when tracking time-periodic states, because then the film thickness h in the mobility $Q_{\mathrm{m}}(h)$ depends on time.

To compute the branches of TPS a quasi-linear approach is necessary. At first both fields in Eqs. (4.17) and (4.18) are not changed nor multiplied by $Q_{\mathrm{m}}(h)^{-1}$. Therefore, the mobility $Q_{\mathrm{m}}(h)$ needs to be treated separately in PDE2PATH, for more details see [107, 135]. In short, the mobility $Q_{\mathrm{m}}(h)$ is approximated via a quasi-linear approach at each step. Then, this allows one to track branches of TPS accurately.

In the following step, the Jacobian matrix is determined, which allows one to calculate the eigenvalues of the system and to perform Newton iterations. Eq. (4.17) gives $f(h, u_{\mathrm{aux}})$ and Eq. (4.18) gives $g(h, u_{\mathrm{aux}})$. In this way, the Jacobian matrix is

$$J = \partial_{\boldsymbol{u}} G = \begin{pmatrix} \partial_h f(h, u_{\mathrm{aux}}) & \partial_{u_{\mathrm{aux}}} f(h, u_{\mathrm{aux}}) \\ \partial_h g(h, u_{\mathrm{aux}}) & \partial_{u_{\mathrm{aux}}} g(h, u_{\mathrm{aux}}) \end{pmatrix}\,. \tag{4.19}$$

For more information on the implementation, see in App. B.5. In the following, a brief explanation of the necessary implementation is presented, that allows one to follow loci of bifurcations, i.e. Saddle-Node and Hopf bifurcations, in parameter space with path continuation. The method is termed pseudo-spectral method [27].

To track bifurcation points, it is necessary to calculate the eigenfunction of the zero mode at the associated bifurcation point in parameter space. The second derivative of the corresponding Jacobian matrix [Eq. (4.19)] has to be transformed into a tensor of a higher order. Hereby, the toolbox pde2path simplifies the problem. It is sufficient to construct a Hessian Matrix, where the higher order tensor is reduced towards a symmetrical tensor of second order. In the case of tracking a Saddle-Node bifurcation in parameter space, the Hessian Matrix is expressed as

$$H_F = \begin{pmatrix} \partial_h\Big((\partial_h f)\psi_f\Big) + \partial_{u_{\mathrm{aux}}}\Big((\partial_h f)\psi_g\Big) & \partial_h\Big((\partial_{u_{\mathrm{aux}}} f)\psi_f\Big) + \partial_{u_{\mathrm{aux}}}\Big((\partial_{u_{\mathrm{aux}}} f)\psi_g\Big) \\ \partial_h\Big((\partial_h g)\psi_f\Big) + \partial_{u_{\mathrm{aux}}}\Big((\partial_h g)\psi_g\Big) & \partial_h\Big((\partial_h g)\psi_f\Big) + \partial_{u_{\mathrm{aux}}}\Big((\partial_{u_{\mathrm{aux}}} g)\psi_g\Big) \end{pmatrix} . \tag{4.20}$$

With the Hessian matrix in Eq. (4.20), only the real parts ($\mathcal{R}$) of eigenvalues are calculated. Note that in Eq. (4.20), ψ_f and ψ_g are the eigenfunctions of the first and second field at the corresponding bifurcation points, respectively. In this case, they are Saddle-Node bifurcations and the eigenfunctions are provided and calculated automatically with pde2path.

In the second case, a Hopf point continuation is used, which allows one to track Hopf bifurcations. Hereby, it is necessary to calculate the imaginary parts ($\mathcal{I}$) of eigenvalues, so that the expression of the Hessian Matrix in Eq. (4.20) needs to be expanded. Consequently, the number of degrees of freedom are doubled. Eq. (4.20) is simply extended symmetrically where the Hessian matrix then contains real and imaginary parts. Then, it reads

$$H_H = \left[\begin{array}{c|c} H_F & 0 \\ \hline 0 & \mathrm{i}H_F \end{array}\right] . \tag{4.21}$$

Here, in Eq. (4.21), all eigenfunctions of the zero mode for $\mathcal{R}$ and $\mathcal{I}$ are determined, which then allows one to track branches of Hopf bifurcations in the parameter range of interest. Up to here, all important steps are introduced for the bifurcation study in pde2path

In the next part, a brief overview of the necessary implementation of the thin-film evolution Eq. (3.50) is given for oomph-lib, which slightly differs from pde2path. At first, an auxiliary field is introduced, however this is differently treated as in pde2path. Note that for oomph-lib the fields are treated in one dimension in Eq. (3.50) and are not simplified with the Weber number We_{s}. For the time simulation, two arbitrary test functions ϕ_h and ϕ_u are introduced. The evolution equations is multiplied by the two arbitrary test functions ϕ_h (first field) and ϕ_u (second field) so that the residuals vanish. Overall, this leads again to two sets of equations in a weak formulation, which are then solved by oomph-lib with a

Newton method. They are given by

$$0 = \int_\Omega \Big\{\partial_t h - \Big[\epsilon_\mathrm{s} \mathrm{d}_h v_{\mathrm{s}_r}(h) + U_0 + G\alpha(\mathrm{d}_h Q_\mathrm{m})\Big](\vec{\nabla} h)\Big\} \cdot \phi_h \, \mathrm{d}\vec{r}$$

$$- \int_\Omega Q_\mathrm{m}\Big\{(\vec{\nabla} u_\mathrm{aux}) \cdot (\vec{\nabla}\phi_h) + G(\vec{\nabla} h) \cdot (\vec{\nabla}\phi_h)\Big\} \, \mathrm{d}\vec{r} \quad \text{and} \tag{4.22}$$

$$0 = \int_\Omega -(\vec{\nabla} h) \cdot (\vec{\nabla}\phi_u) + \Big\{\mathrm{Ha}\Pi(h) - \frac{1}{\mathrm{We}_\mathrm{s}} u_\mathrm{aux}\Big\} \cdot \phi_u \, \mathrm{d}\vec{r}, \tag{4.23}$$

where u_aux represents the auxiliary field the this time only contains the Laplace pressure Δh. The SAW-term is reduced into $v_{\mathrm{s}_r}(h) = h v_\mathrm{s}(h)$, which allows to simply the formulations.

The domain is given by Ω. Now, all transformed equations are given, which are used either for PDE2PATH [Eqs. (4.17) and (4.18)] or for OOMPH-LIB [Eqs. (4.22) and (4.23)]. The obtained results are presented in Chap. 5 and Chap. 6.

4.4 Linear stability analysis of a flat film in 1D

To determine the linear stability of any given flat one-layer film of height h_0 with respect to infinitesimal perturbations ε in $h_1(x,t)$, a Fourier mode decomposition of h_1 is introduced [125]. The ansatz is $h(x,t) = h_0 + \varepsilon \exp(\beta t + \mathrm{i}kx)$ where $\varepsilon \ll 1$. The growth rate of a perturbation is then obtained as the real part $\mathcal{R}(\beta)$. The imaginary part $\mathcal{I}(\beta)$ determines the phase velocity $v_\mathrm{ph} = \mathcal{I}(\beta)/k$.

Using

$$\partial_x^n h(x,t) = \varepsilon(\mathrm{i}k)^n \mathrm{e}^{\beta t + \mathrm{i}kx} \tag{4.24}$$

and

$$\partial_t h(x,t) = \varepsilon\beta \mathrm{e}^{\beta t + \mathrm{i}kx} \tag{4.25}$$

a linearisation of the equation in ε yields the dispersion relation

$$\beta(k) = -\frac{h_0^3}{3\mathrm{We}_\mathrm{s}} k^2 \left(k^2 - k_c^2\right) - \mathrm{i}k\Big[G\alpha h_0^2 + U_0 + v_\mathrm{s}(h_0) + h_0 \partial_h v_\mathrm{s}(h_0)\Big]. \tag{4.26}$$

Here, the critical wavenumber k_c is introduced with $k_c^2 = \mathrm{We}_\mathrm{s}(\mathrm{Ha}\partial_h \Pi(h_0) - G)$ is introduced. The growth rate is

$$\mathcal{R}[\beta(k)] = -\frac{h_0^3}{3\mathrm{We}_\mathrm{s}} k^2 \Big(k^2 - k_c^2\Big) \tag{4.27}$$

and the phase velocity is

$$\mathcal{I}[\beta(k)]/k = -\Big[G\alpha h_0^2 + U_0 + v_\mathrm{s}(h_0) + h_0 \partial_h v_\mathrm{s}(h_0)\Big]. \tag{4.28}$$

A plot for three different cases for the growth rates behaviour is shown in Fig. 4.2. The flat film is unstable for all wavenumbers k in the interval $k \in [0,k_c]$ as long as $\mathcal{R}[\beta(k)] > 0$, whereas the growth rate at $\mathcal{R}[\beta(0)] = \mathcal{R}[\beta(k_c)] = 0$ is always zero. All other wavenumbers are stable. The red dashed and green dotted line in Fig. 4.2 represent cases, where all wavenumbers k are stable. Hereby, the critical wavenumber is $k = 0$ for the red dashed line, i.e. the curve is shown at onset, so that only the quartic term from Eq. (4.27) remains. For the other critical wavenumbers are $k^2 < 0$ for the green dotted line.

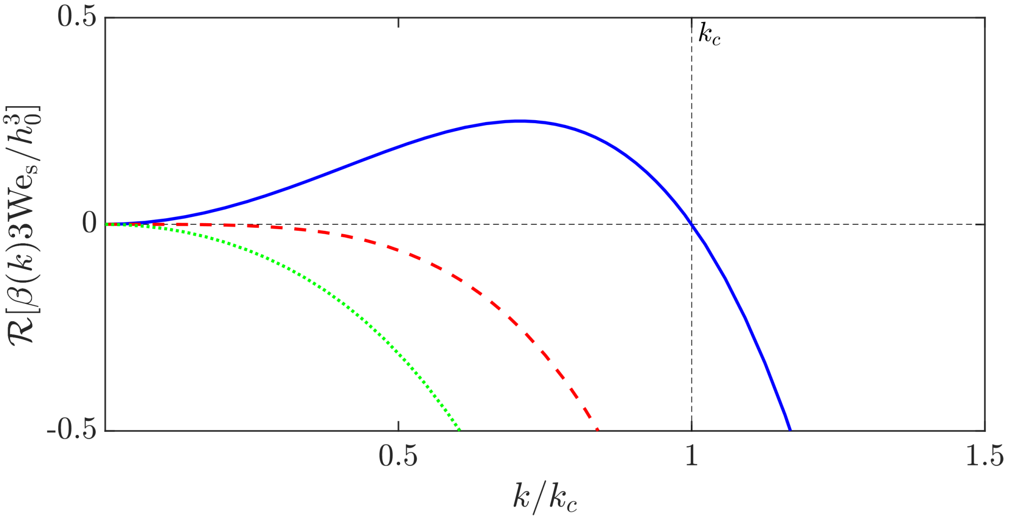

FIGURE 4.2: *Plot for differnt wavenumbers k showing the Dispersion relation (growth rate) for a flat film as a function of the wavenumber k. The solid blue line corresponds to the case where the wavenumbers are unstable at first and get stable at $k \gg k_c = 1$. The dashed red line and the green dotted line corresponds to the stable cases at $k_c = 0$ and $k_c^2 < 0$, where all wavenumbers are stable. Both axes are normalised.*

Notice that in App. A.2 a linear stability analysis for a flat two-layer thin-film system is performed.

CHAPTER FIVE

Behaviour of a thin film driven by SAW

> ”*Discere ne cessa, cura sapientia crescat*“
>
> – DIONYSIUS CATO,
> *Incipit liber Cathonis in vulgares*
> *IV, 27, 3rd/4th AD*

The main goal of this thesis is to theoretically investigate the dynamical behaviour of a thin film driven by surface acoustic waves (SAW). The focus is to find parameter regimes where stable time-periodic states of thin film driven by SAW occur. These theoretical results provide predictions that are useful for experiments to develop advanced coating methods, i.e. thin films driven by SAW.

To investigate and understand the different thin film solutions, which may occur in the SAW-driven case, first the classical Landau-Levich problem is analysed in Sec. 5.1. The derived thin-film evolution Eq. (3.50) is scaled according to (Ae.1). To analyse this partial differential equation (PDE), a numerical treatment is unavoidable. With the numerical analysis, bifurcation diagrams are generated with the pseudo-arclength path continuation in PDE2PATH. It is important to bear in mind, that Eq. (3.50) is split into two Eqs. (4.17) and (4.18) (main- and auxiliary field) for the pseudo-arclength path continuation approach. The main control parameters of interest are the velocity of the plate U_0 withdrawn out a bath and the inclination angle α of the plate, which are commonly varied in experiments. Therefore, three different types of film states are obtained and the occurring transitions of those states are compared to the literature. At first a parameter study is performed for the Landau-Levich case (dragged-case). The classical Landau-Levich case helps to understand and to distinguish occurring types of thin-film solutions [47, 116, 144]. Then, after discussing the classical Landau-Levich case, the main subject is investigated where a thin film is driven by SAW.
In Sec. 5.2 a SAW-driven thin-film model is analysed. In the analysis, the results of Ref. [87] for ideally wetting liquid are reproduced using Eq. (3.43) with scaling (Ae.2). Afterwards the thin-film evolution equation is analysed with the general scaling employed in (3.49) is used. This general scaling facilitates the comparison

of the dragged-case employed in Ref. [47] to the expanded SAW-case of Ref. [87]. The occurring bifurcation diagrams are analysed in detail with a focus on the following control parameters: the SAW strength ϵ_s and the Weber number We_s. In particular, these parameters can also be manipulated in experiments. The computed bifurcation diagrams are examined for parameter ranges where time-periodic states occur. Periodic behaviour of film states are verified by performing time simulations with the software OOMPH-LIB and using phase-plane diagrams. In the case of the classical Landau-Levich problem such time-periodic states have already been found in Ref. [123].

In Sec. 5.3], the problem of a thin film driven by SAW is extended by considering volatile liquids in one-dimension (1D). This results in a thin-film evolution Eq. (3.62) for volatile liquids, where the evaporation rate B is not zero. Then again, the dynamical behaviour of occurring film states is investigated. The computed bifurcation diagrams provide further insight into the behaviour of the liquid film states driven by SAW and allow for comparison to results for non-volatile liquids driven by SAW. To complete the SAW-driven thin-film study, the investigation is extended to a two-dimensional (2D) case, see Sec. 5.4. Hereby, the previously discussed 1D results are expanded by a transversal y-component. The bifurcation diagrams and steady states for 2D are then investigated for different domain sizes L_y. The results are also compared to the dragged-case in 2D, where additional features occur [39]. For this study the main control parameter is the SAW strength ϵ_s.

5.1 Modelling and bifurcation analysis of the classical Landau-Levich system

On the basis of the employed scaling in Sec. 3.2, it is possible to recover different thin-film models from the literature with Eq. (3.49). In the case of the classical Landau-Levich system the scaling Ae.1 is applied to Eq. (3.50). This allows one to reproduce results qualitatively identical according to Refs. [46, 47]. An illustration of the thin-film model, where a plate is withdrawn from a bath is shown in Fig. 5.1. The liquid bath is situated on the right side.

Translating this geometry to the numerical approach as required by pseudo-arclength path continuation, the bath is situated at $x = L/2$, whereas the domain is $\Omega = [-L/2, L/2]$ and the system length is L. For the classical Landau-Levich case a relatively large domain with $L = 500$ is considered for the numerical treatment. The plate is subsequently pulled into the negative x-direction at an angle α, see Fig. 5.1. Furthermore, to solve the thin-film evolution Eq. (3.50), boundary conditions have to be imposed for the corresponding geometry. Here, four boundary conditions are

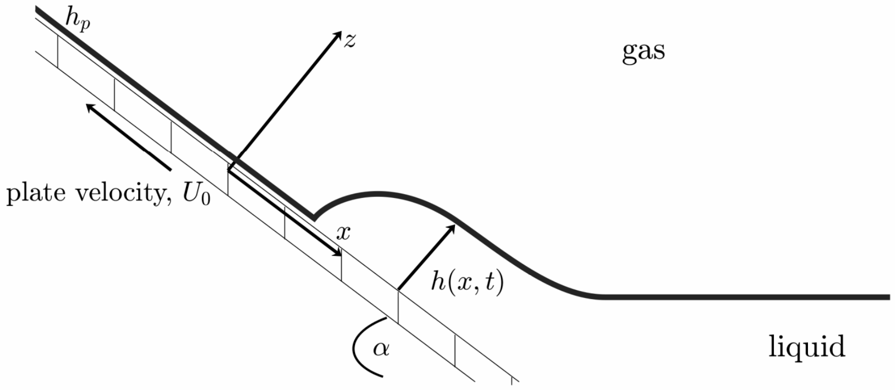

FIGURE 5.1: *Schematic drawing of the one-dimensional (1D) classical Landau-Levich model, in which a liquid film is withdrawn from a bath solution. The geometry is nearly equivalent to the drawn thin film under SAW, see Fig. 3.1, where the bath side is situated at the right boundary. Here, the plate is inclined at an angle α and is moving at velocity U_0 to the negative x-direction. Ahead of the moving contact line of the pultruded film the precursor film with the film height h_p is located.*

applied, namely

$$\begin{aligned} h = h_\mathrm{m} \quad &\text{and} \quad \partial_{xxx} h = 0 \quad \text{at} \quad x = \frac{L}{2} \\ \partial_x h = 0 \quad &\text{and} \quad \partial_{xx} h = 0 \quad \text{at} \quad x = -\frac{L}{2} \,. \end{aligned} \tag{5.1}$$

The film height is pinned with h_m := “height of meniscus” at the bath side ($x = L/2$). This pinning is important to control the translational degree of freedom and the position of the contact line region within the numerical domain Ω. Note that the second boundary condition at $x = L/2$ slightly differs from Refs. [47, 123], instead of using $\partial_x h = \alpha$, here $\partial_{xxx} h = 0$ is used. This allows the solution to adapt at the boundary and the results correspond to qualitatively identical bifurcation diagrams. However, these minor differences of boundary conditions lead to different critical values of parameters where the corresponding film transitions occur. On the other side of the domain at $x = -L/2$, Neumann boundary conditions are used. In this way, the dynamical behaviour of the thin-film system is not geometrically influenced by these boundary conditions at $x = -L/2$. Furthermore, bifurcation diagrams are computed for different angles α, while using the plate velocity U_0 as a main control parameter.

Remember that in front of the contact line, a precursor film of height h_p always exists, due to the Derjaguin pressure. The height of the precursor film is chosen with $h_\mathrm{p} = 1$. Now, all conditions are given to solve the thin-film evolution Eq. (3.50) for the classical Landau-Levich case and to generate bifurcation diagrams. In this section the results of a thin film withdrawn from a bath are presented in analogy to Ref. [47]. The results determine qualitatively different types of steady thin-film solutions. For the measurement of the classical Landau-Levich case, the excess volume $V_\mathrm{ex} = V - V_0$ dynamically extracted from the bath solution is chosen. The volume V is calculated as the integral over the full domain with $V = \int_\Omega h(x)\mathrm{d}x$. Hereby, V_0 is the reference volume without any advection force affecting the thin film solution state. Then, for the path continuation approach the plate velocity U_0 is used as the main control parameter. The plate velocity U_0 is then increased in the numerical approach to generate bifurcation curves. Four bifurcation diagrams are generated, to clarify the difference between thin-film transition states, which occur in the classical Landau-Levich case under different plate inclination angles α [Figs. 5.2-5.4].

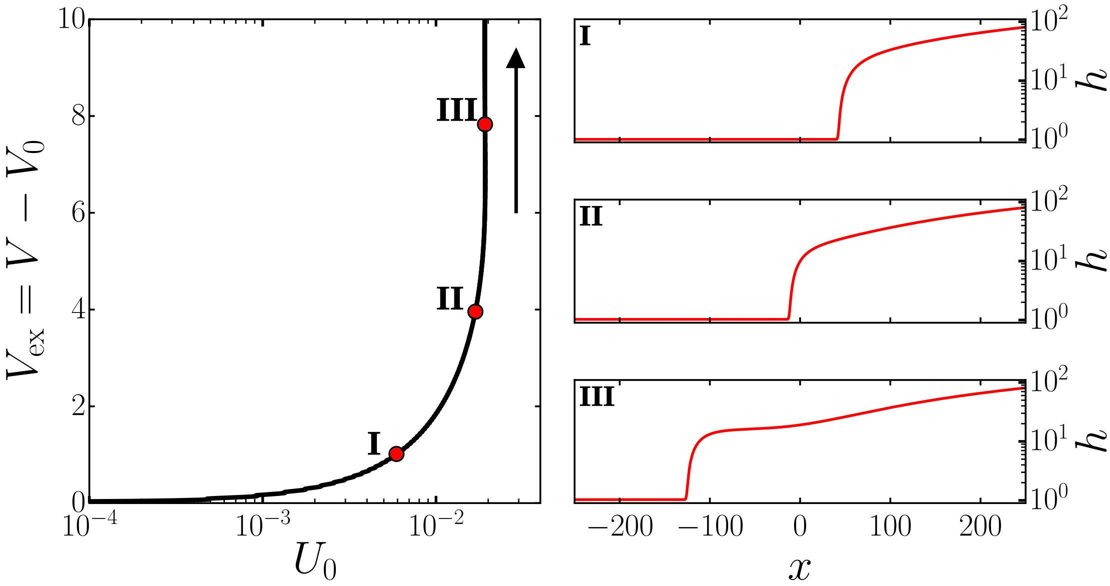

FIGURE 5.2: *The left panel shows a bifurcation diagram with the excess volume V_{ex} as a function of the plate velocity U_0 for the classical Landau-Levich system. The plate is inclined by an angle $\alpha = 0.2$ and the arrow along the bifurcation curve indicates the change of direction. The solid black line represents stable steady states. In addition, three chosen steady state profiles are presented (**I-III**). Note the logarithmic y-axes. The remaining parameters are* $\mathrm{We_s} = 1.0$, $\mathrm{Ha} = 0.001$, $G = 0.001$, $h_\mathrm{p} = 1$, $\epsilon_\mathrm{s} = 0$ *and* $L = 500$.

Fig. 5.2 shows the excess volume which monotonically increases with increasing plate velocity U_0. At first, the excess volume increases slowly and then very rapidly. The excess volume V_{ex} diverges at a critical value $U_{\mathrm{c}_1} \approx 0.21$ of the plate velocity U_0. The presented steady state profiles (panels **I-III**) of the thin film along the branch are all linearly stable. The steady states demonstrate that the excess volume V_{ex} of the thin film increases. Hereby, the steady meniscus profile deforms as the plate velocity increases and a foot-like structure is formed, see panels **I-III**. and thus is termed foot-solution [47, 123]. The foot-length of the foot-solution increases, so that more liquid from the bath is withdrawn. Its length diverges, $U_0 \to U_{\mathrm{c}_1}$. For $U_0 > U_{\mathrm{c}_1}$, the system may settle on a Landau-Levich film state, with a constant film height. The result presented in Fig. 5.2, where the transition occurs at at U_{c_1} is called *dynamic continuous emptying transition*. The transition is analogous to the equilibrium emptying transition state described in Ref. [98].

The first qualitative change in the bifurcation curve occurs at $\alpha = \alpha_{c_1} \approx 0.5$. As an example, a bifurcation diagram is computed with $\alpha = 1 > \alpha_{c_1}$.

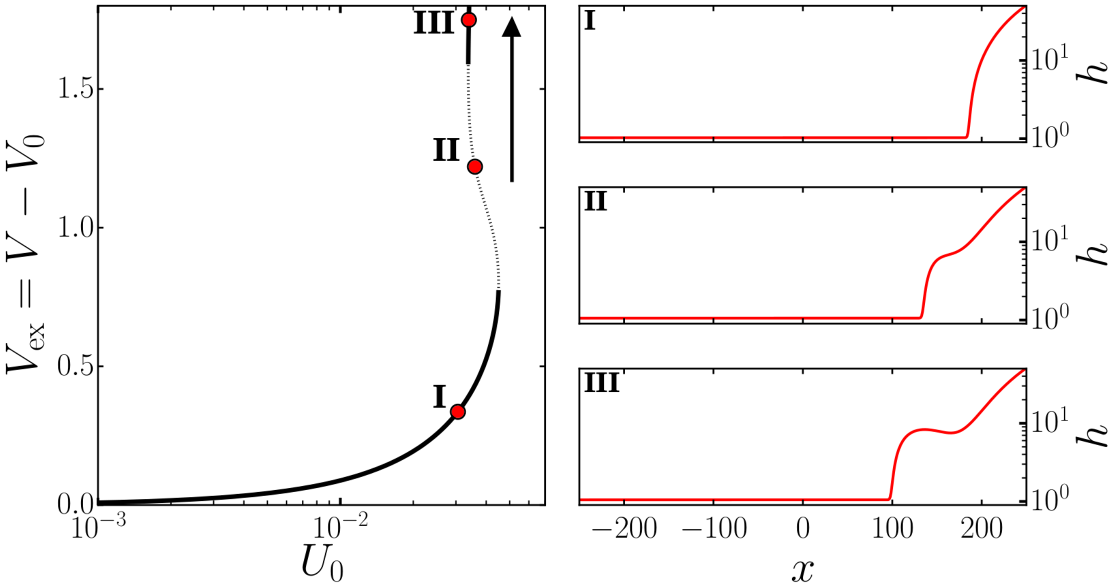

Figure 5.3: *The left panel shows a bifurcation diagram with the excess volume* $V_{\rm ex}$ *in dependence of the plate velocity* U_0 *for the classical Landau-Levich system. The plate is inclined by an angle* $\alpha = 1$ *and the arrow along the bifurcation curve indicates the change of direction. The solid black line represents stable steady states and the dotted line represents unstable steady states. Three selected steady state profiles are shown (**I-III**). There, the film height* h *is scaled logarithmically and only half of the domain* $\Omega_{\rm half} = [0, L/2]$ *is presented. The remaining parameters are* $\mathrm{We_s} = 1.0$, $\mathrm{Ha} = 0.001$, $G = 0.001$, $h_{\rm p} = 1$, $\epsilon_{\rm s} = 0$ *and* $L = 500$.

Again, at small plate velocity U_0 the excess volume $V_{\rm ex}$ increases monotonically. It is similar as the bifurcation curve with $\alpha = 0.2$, see Fig. 5.2. However at $U_0 \approx 0.5$, a Saddle-Node bifurcation occurs and the branch becomes unstable. Then, the branch of steady states continues towards smaller U_0, until a second Saddle-Node bifurcation occurs. At this second Saddle-Node bifurcation at $U_0 \approx 0.3$ the states becomes stable again. Subsequently, the curve folds back. Overall the curve undergoes an exponential or collapsed snaking [80, 132]. This exponential snaking is about a vertical asymptote at a crucial velocity $U_0 = U_{c_2} \approx 0.3$. Hereby at each fold, where a Saddle-Node bifurcation is detected on the branch, the stability of steady states switches between stable and unstable [132]. The steady profiles of Fig. 5.3 show that a liquid protrusion occurs. Once again, the steady film states correspond to a foot-solution, whose span shows undulations. The biggest undulation is situated at the tip of the foot-solution, i.e. see panel **III**. These are directly related to the snaking bifurcation curve, where only some ranges of the foot length correspond to stable steady states. The transition at $U_0 = U_{c_2}$ is termed *dynamic discontinuous emptying transition* [47]. The presented results are thus qualitatively in agreement with previous publications [46, 47]. Remember that this approach, which uses slightly different boundary conditions and scaling, only results in different critical values.

The last two transitions occurring in the classical Landau-Levich system are presented

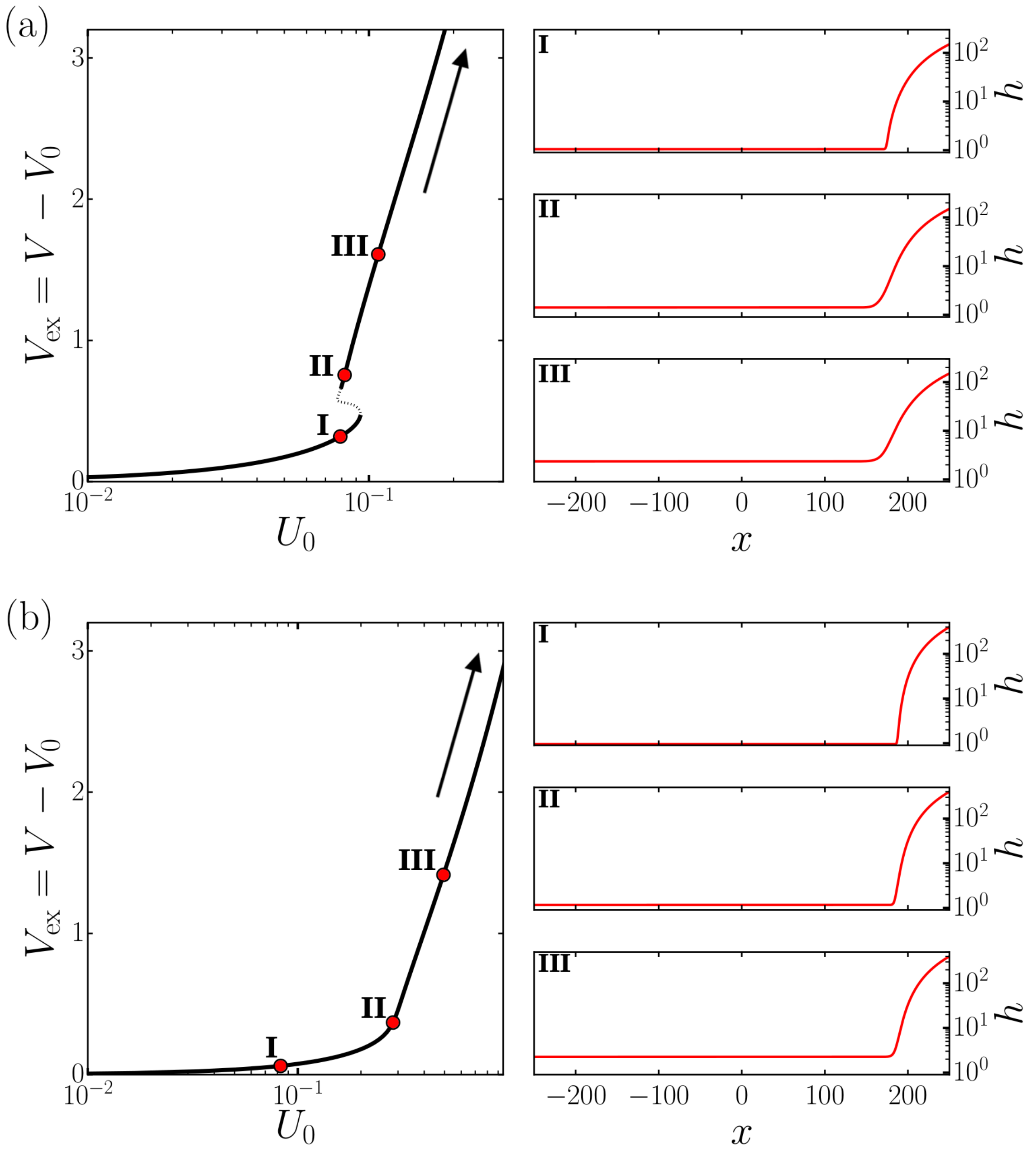

FIGURE 5.4: *Panels on the left show bifurcation diagrams with the excess volume* V_{ex} *in dependence of the plate velocity* U_0 *for the classical Landau-Levich system. In (a) the solution is inclined by an angle* $\alpha = 3$ *and in (b) it is inclined by an angle* $\alpha = 10$*. The arrows along the bifurcation curves indicate the change of direction. For each of the two bifurcation diagrams, three steady states are presented (**I-III**). The lines styles are again, solid and dotted line, corresponding to stable and unstable steady states. The remaining parameters are* $\mathrm{We_s} = 1.0$, $\mathrm{Ha} = 0.001$, $G = 0.001$, $h_{\mathrm{p}} = 1$, $\epsilon_{\mathrm{s}} = 0$ *and* $L = 500$.

in the bifurcation curves with angles $\alpha = 3$ and $\alpha = 10$. The second qualitative change on the bifurcation curve occurs at $\alpha = \alpha_{c_2} \approx 2.45$, when the first and only Hopf bifurcation appears [Fig. 5.5]. Fig. 5.4 (a) shows the bifurcation curve and selected steady states with an angle $\alpha = 3$. Again, at small velocity U_0 the bifurcation curve behaves as described in the latter cases, Fig. 5.2 and 5.3, and undergoes a pair of Saddle-Node bifurcation. Now, however, the difference is the occurrence of a hysteretic transition, where two destabilising Saddle-Node bifurcations appear along the branch. The branch becomes stable again, when following the curve further. The mathematical background behind this observation is that two complex conjugated eigenvalues cross the imaginary axes, which is equivalent to a Hopf bifurcation on the curve. Hopf bifurcations were recently found in the classical Landau-Levich case and are described in Ref. [123]. Then, the branch consisting of stable steady states continues as the velocity U_0 increases following the power law $V_{\mathrm{ex}} \propto U_0^{2/3}$. In contrast to the cases with $\alpha < \alpha_{\mathrm{c}_2}$, the bifurcation curve does note diverge vertically, and the presented steady states in Fig. 5.4 (a) panels **I** to **III** do not develop a foot-like structure. Instead, the coating thickness h_{c} increases homogeneously with the power law. Hereby, the film above the substrate increases similar to an equilibrium wetting transition. This transition is termed *discontinuous dynamic wetting transition* [47]. The last change in the bifurcation curve is determined when all bifurcations, i.e. Hopf and Saddle-Node bifurcations, vanish at $\alpha = \alpha_{\mathrm{c}_3} \approx 5.15$. Here, Fig. 5.4 (b) represents an example of a large angle with $\alpha = 10 > \alpha_{\mathrm{c}_3}$. Comparing the two bifurcation diagrams Fig. 5.4 (a) and (b), it is obvious that all bifurcations have vanished, and the curve increases monotonically. This increasing behaviour is also observed in steady states, as the volume monotonically increases with increasing film height. Here, all steady state profiles correspond to the one of the case at $\alpha = 3$. In contrast, no hysteretic transition occurs, and therefore this case is termed *continuous dynamic wetting transition.* In both panels in Fig. 5.4 (a) and (b) the bifurcation diagrams show a branch, which follows the power law of $V_{\mathrm{ex}} \propto U_0^{2/3}$. These power laws are in agreement with the law determined by Landau and Levich, where the film height follows the power law $\propto \mathrm{Ca}^{2/3}$. Particularly in this case, the plate velocity U_0 is proportional to the Capillary number Ca.

Up to here, the results of the reconstructed bifurcation diagrams and results are governed by the classical Landau-Levich case for different angles α. The three different steady states are outlined and up to four significant transition changes of the bifurcation curve are shown. The determined bifurcation points (Saddle-Node and Hopf bifurcation) are now studied with a Fold- and Hopf-point continuation. These bifurcations are tracked in a parameter space spanned by two control parameters. With this method the loci of the occurring bifurcations can be located. In this process the control parameters are the plate velocity U_0 and the inclination of plate with angle α. Then, the corresponding parameter plane is spanned by U_0 and α.

Fig. 5.5 has two different line styles. One of the lines (black) corresponds to the appearance of the Hopf bifurcation which disappears at an angle of $\alpha \approx 3.83$. The green line represents Saddle-Node bifurcations. Moreover, one can determine that all bifurcations for α greater $\alpha_{\mathrm{c}_3} \approx 5.15$ have disappeared. At this point, the last remaining two Saddle-Node bifurcations meet and vanish. Furthermore, most of the transition information about the classical Landau-Levich case is obtained from Fig. 5.5. No Saddle-Node bifurcation appears on the curve at an angle of $\alpha < 0.5$, so that the determined thin film transition corresponds to a dynamic continuous emptying transition. When two Saddle-Node bifurcations appear on the bifurcation curve at $0.5 \leq \alpha \leq 2.45$ the dynamical behaviour of the thin film changes to a

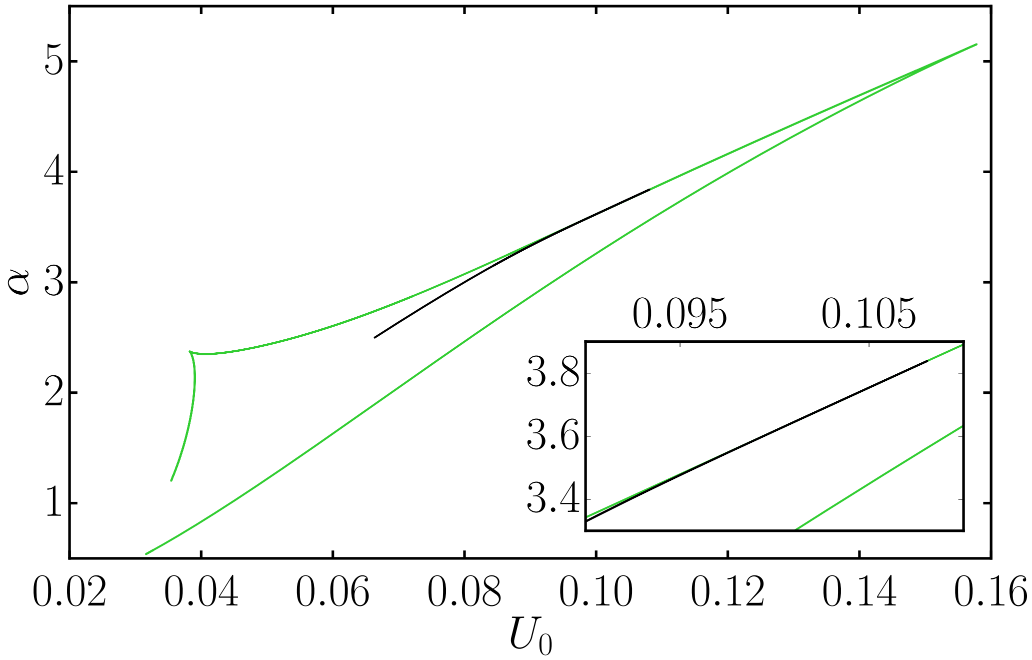

FIGURE 5.5: *Loci of Saddle-Node (green-lines) and Hopf bifurcation (black line) in the parameter plane spanned by plate velocity U_0 and plate angle α. The inset shows a region where the Hopf bifurcation emerges or vanishes from the Saddle-Node bifurcation. The remaining parameters are* $\mathrm{We_s} = 1.0$, $\mathrm{Ha} = 0.001$, $G = 0.001$, $h_\mathrm{p} = 1$, $\epsilon_\mathrm{s} = 0$ *and* $L = 500$.

dynamic discontinuous emptying transition. This dynamic transition of the thin film remains until the cusp, formed by Saddle-Node bifurcations in Fig. 5.5. After the cusp at $2.45 \leq \alpha \leq 5.15$ the transition changes to discontinuous wetting transition. Simultaneously, at the same α a Hopf bifurcation appears for higher plate velocities U_0. In other words, at the cusp formed by two Saddle-Node bifurcations, the second Saddle-Node along the branch switches from stabilising to destabilising. In this case, the stability of the bifurcation curve is double negative (unstable), whereas the tracked Hopf bifurcation is responsible for the branch to become stable again. Following the loci of the Hopf bifurcation further, the numerical investigation reveals that the Hopf bifurcation slowly approaches the fold branch, see inset of Fig. 5.5. It vanishes into a Saddle-Node bifurcation. This indicates that a Bogdanov-Takens bifurcation [122, 145] occurs where the Hopf bifurcation and a global bifurcation emerge or disappear simultaneously at the Saddle-Node bifurcation at $\alpha \approx 3.85$. In summary, when the Hopf bifurcation appears at $\alpha \approx 2.45$ a homoclinic bifurcation has to appear as well, which is, however, not detected by the used path continuation approach. The last transition of the bifurcation diagram occurs, when the hysteretic transition has vanished. This happens at $\alpha > 5.15$ where the two Saddle-Node bifurcations vanish. Then, the transition changes continuous dynamic wetting transition. This spanned map is very similar to the on presented in Ref. [46], however the loci of the Hopf bifurcations were missed. Remember that the results have a different scaled film height (a factor of three) and slightly different boundary conditions.

All results shown in Figs. 5.2-5.5 are produced with the pseudo-arclength path

continuation method. These results of the classical Landau-Levich system indicate significant changes of the different transitions of the bifurcation curve.
Furthermore, they provide the fundamental behaviour of an underlying thin-film model and present different behaviour of bifurcation diagrams and corresponding steady state solutions. Overall, this overview of an 1D, non-volatile and partially wetting liquid provides enough indications that may help to investigate and understand results of thin films driven by SAW. In the final step, the results for the SAW-driven thin-film model are presented and both models are compared with respect to their similarities and differences.

5.2 Analysis of SAW-driven thin-film model

In contrast to the classical Landau-Levich system, the SAW-driven system has a slightly different geometrical approach. An illustration of a SAW-driven thin-film model is shown in Fig. 3.1. To adapt the SAW-driven thin-film model into the numerics, the boundary conditions as well as the domain $\Omega = [-L/2, L/2]$ are adapted accordingly. From Ref. [87] these boundary conditions and the domain are predefined, so that the boundary conditions yield

$$\begin{aligned} h = h_{\mathrm{m}}, \quad \text{and} \quad \partial_{xx}h &= 1 \quad \text{at} \quad x = \frac{L}{2}\,, \\ \partial_x h = 0\,, \quad \text{and} \quad \partial_{xx}h &= 0 \quad \text{at} \quad x = -\frac{L}{2}\,. \end{aligned} \tag{5.2}$$

This geometry of the SAW-driving system is treated equally as in the dragged-case, so that the meniscus is situated at $x = L/2$. In addition, the SAW-driving system has a strong dependency on the meniscus curvature and this is reflected by the boundary condition $\partial_{xx}h = 1$ at $x = L/2$. Moreover, in contrast to the classic Landau-Levich system, the domain of the entire system is much smaller with a domain length of $L = 40$. Roughly speaking, all the considered geometrical aspects of the SAW-driving model lead to a smaller considered thin-film problem. In addition, the film height of the meniscus is also reduced to $h_{\mathrm{m}} = 8.1$ and the precursor film is kept at $h_{\mathrm{p}} = 0.1$. Note that the precursor film has to be very small in comparison to the meniscus film height. These conditions are kept for all computed results of thin films driven by SAW.

First, an ideally wetting liquid is considered for the analysis of a thin film driven by SAW, see the evolution Eq. (3.43) Ref. [87]. Here, the liquid flux induced by SAW is given by the Weber number We_{s}. In this way, the Weber number We_{s} acts as a liquid flow induced by SAW. Subsequently, to generate the first results by using the pseudo-arclength path continuation approach, the Weber number is chosen as the main control parameter.

In the next step the study is expanded towards a more realistic type of thin film problem. This allows one to compare both thin film models, (classical) dragged-case and SAW-driving, in a general case. Therefore, Eq. (3.43) is extended, so that the final Eq. (3.50) is derived. Note that only the general scaling in Eq. (3.49) it is possible to directly compare both models, dragged-case as in Ref. [47] and SAW-driving as in Ref. [87]. In the generalised form [Eq. (3.49)] the SAW strength is represented by ϵ_s, which is then treated equally as the velocity U_0 of the withdrawn plate. In addition, this general scaling allows one to switch between both cases.

To investigate the liquid behaviour even further, different values for the Weber number We_s are chosen, since, the Weber number We_s is a characteristic of the liquid (inverse surface tension). By varying this parameter, the dynamical behaviour of the system may change. Furthermore, bifurcations along the branch are detected by calculating the (exact) eigenvalues of the Jacobian. Subsequently, the identified Hopf bifurcations lead to time-periodic states (TPS). These are analysed, by tracking the Hopf branches which emerge from the Hopf bifurcations. However, as mentioned in Sec. 4.3, the SAW-driving case is then handled with a quasi-linear ansatz. The generate TPS are used for time simulations to identify stable periodic time solution, where ridges are drawn out from the bath.

5.2.1 Ideally wetting liquid

The analysis of the SAW-system starts by investigating the influence of the Weber number We_s. Hereby, the results from Ref. [87] are reproduced with Eq. (3.50) and scaling (Ae.2). In this case, the considered liquid is as an ideally wetting liquid, so that no disjoining pressure acts with $\mathrm{Ha} = 0$ and without influence of gravity. The liquid is placed on a flat horizontal and solid substrate with $G = \alpha = 0$.

The used solution measure is the coating thickness h_c measured at $x = -L/2$ instead of the excess volume V_ex. The presented steady profiles show that the meniscus at $x = L/2$ is smoothly connected to a homogeneous coating layer. Nevertheless, the selected steady states along the bifurcation branch also indicate that the coating layers increase monotonically with increasing We_s. In panels **II** and **III** the presented layer are Landau-Levich films. The power law here is $h_\mathrm{c} \propto \mathrm{We}_\mathrm{s}^{2/3}$, which is expected since the Weber number scales with the Capillary number Ca with $\mathrm{We}_\mathrm{s} \propto \mathrm{Ca}$. This power law is also in agreement with the classical Landau-Levich case. From the gathered information, the transition of the thin film is a discontinuous dynamic wetting transition. Hereby, two Saddle-Node bifurcations appear in a hysteresis on the bifurcation curve. However, the behaviour of the SAW-driving system for ideally wetting liquid changes for very small We_s. A critical threshold in We_s occurs, where the steady states become unstable. This results in a film deposition that collapses abruptly at a finite coating thickness of $h_\mathrm{c} \approx 0.2$.

A more detailed investigation of the bifurcation curves shows that a second Saddle-Node bifurcation occurs on the unstable branch, see Fig. 5.7 black line

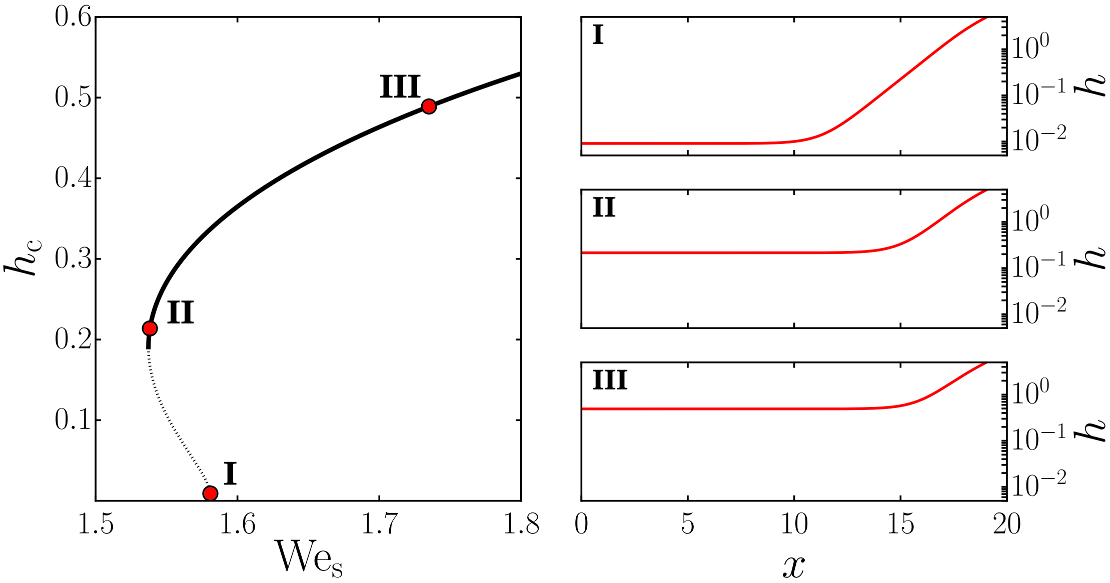

FIGURE 5.6: *On the left panel a bifurcation diagram is shown. The measurement is the coating thickness* h_c *in dependence of the Weber number* $\mathrm{We_s}$ *for a SAW-driven meniscus for an ideally wetting liquid. The solution is resting on a horizontal plate with* $\alpha = 0$. *The solid black line represents stable steady solutions, whereas the dotted line represents unstable steady states. Three selected steady state profiles are shown (**I-III**). There, the film height* h *is scaled logarithmically and only half of the domain* $\Omega_\mathrm{half} = [0, L/2]$ *is presented. The remaining parameters are* $h_\mathrm{m} = 8.1$, $\mathrm{Ha} = 0$, $G = 0$, $h_\mathrm{p} = 0$, $\alpha = 0$, $\epsilon_\mathrm{s} = 1$, $U_0 = 0$ *and* $L = 40$.

and blue line with active gravity ($G = 0.001$). At that Saddle-Node bifurcation (Fold) the stability of the branch does not switch to stable. Instead it gets more unstable by switching the direction towards smaller $\mathrm{We_s}$, see inset of Fig. 5.7. In Ref. [87] this Saddle-Node bifurcation at very low values of h_c was missed. When h_c approaches zero, the subsequent branch ends at a critical value of $\mathrm{We_s}$. Hereby, no bifurcation point is detected with the applied continuation method. The consequence of that critical value is interpreted as meniscus state ending at a true microscopic contact point. This thin film has a different topology than the Landau-Levich film state termed finite-support meniscus state and can not be obtained with the numerical approach employed here.

On the other hand, by incorporating gravity into Eq. (3.50) and using scaling (Ae.2), the bifurcation curve in Fig. 5.7, blue line only shifts to the left so that the Saddle-Node bifurcations appear for smaller values of $\mathrm{We_s}$ at same values of the coating thickness h_c. However, it does not solve the obtained problem state of the meniscus ending at a microscopic contact point.

Next, a wettability is explicitly incorporated into the thin-film model, where this true microscopic contact point is avoided. While adding wettability, a finite inclination of $\alpha = 0.2$ is given during the numerical approach of SAW-driven case. This small angle helps to avoid that numerical problems occur when applying a disjoining pressure with $\mathrm{Ha} > 0$ to the thin-film evolution Eq. (3.50). Note that the scaling (Ae.2) remains while changing from ideally wetting liquid to partially wetting liquid.

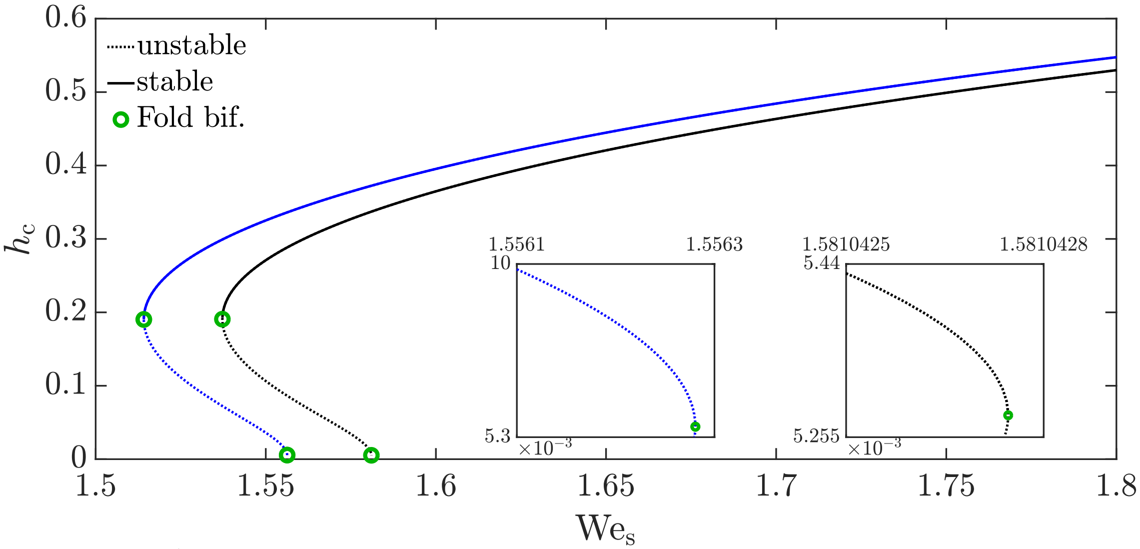

FIGURE 5.7: *A bifurcation diagram showing two bifurcation curves, where the black and blue curve show cases without the contribution of gravity (G = 0) as in Ref. [87] and with the contribution of gravity (G = 10e-3), while dotted and solid lines still represent unstable and stable states, respectively. On both curves Saddle-Node bifurcations (folds) are highlighted by green circles. The inset zooms onto the Saddle-Node bifurcation at very small* h_c. *The remaining parameters are* $h_m = 8.1$, $\mathrm{Ha} = 0$, $h_p = 0$ $\alpha = 0$, $\epsilon_s = 1$, $U_0 = 0$ *and* $L = 40$.

5.2.2 Partially wetting liquid

For a partial wetting liquid the derived thin-film evolution Eq. 3.50 is used. The scaling from Eq. (Ae.2) remains as in the latter case for the ideally wetting liquid. However, the Hamaker number $\mathrm{Ha} = 0.002$ is not zero, which in response consider wettability of the liquid. The Hamaker number is chosen intentionally very small as a very small precursor film of height $h_p = 0.1$ is considered. In this SAW geometry, it is very challenging for the numerics when using big values of the Hamaker number, i.e. $\mathrm{Ha} > 0.01$. The small value of the Hamaker number allow to incorporate and preserve the geometrical consideration of the SAW-driven thin-film model. Remember that the SAW-driving case is considered for a smaller thin film than the one studied in the classical Landau-Levich case. At first, the control parameter, Weber number $\mathrm{We_s}$, remains as in Sec. 5.2.1. This approach leads to expanded results from Ref. [87], so that partial wettability is applied to the SAW-driven case. The result including all detected bifurcations is shown in Fig. 5.8.

The bifurcation diagram of Fig. 5.8, in comparison to Fig. 5.7, has notable changes. In the case of partially wetting liquids, where the substrate is always covered by an adsorption layer of liquid, the incorporation of a wetting energy into the model results in different states. This implies, that the discussed film states, where true contact points of the meniscus state occur are avoided, see Sec. 5.2.1. Furthermore, the branch does not end at a finite value of $\mathrm{We_s}$ as presented in Fig. 5.7. Following the branch further, the coating thickness h_c decreases with a concomitant decrease in $\mathrm{We_s}$. Now, the determined Landau-Levich films state and the finite-support meniscus state are topologically identical, as the former film states transform into

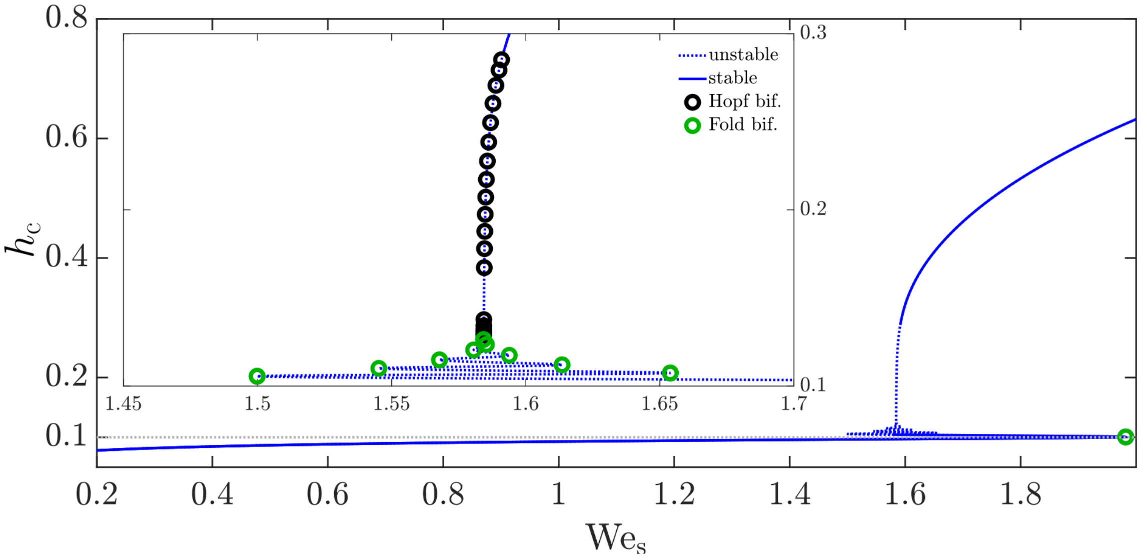

FIGURE 5.8: *Bifurcation diagram for a SAW-driven meniscus for a partially wetting liquid showing the coating thickness* h_c *in dependence of the Weber number* $\mathrm{We_s}$. *The liquid is considered on an inclined substrate with* $\alpha = 0.2$. *Two different line styles show the stability of the steady states, where the solid line corresponds to stable and dotted line represents unstable steady states, respectively. Saddle-Node and Hopf bifurcations are highlighted by green and black circles. The inset zooms onto the region, where the bifurcation curve undergoes a "snaking". The remaining parameters are* $h_\mathrm{m} = 8.1$, $\mathrm{Ha} = 0.002$, $G = 0.001$, $h_\mathrm{p} = 0.1$, $\alpha = 0.2$, $\epsilon_\mathrm{s} = 1$, $U_0 = 0$ *and* $L = 40$.

states with a liquid meniscus smoothly connected to the precursor film. Note that Fig. 5.8 does not show the full branch, as for the Weber number approaches zero ($\mathrm{We_s} \to 0$), subsequently the Laplace pressure diverges. Therefore, the path continuation approach is started at a sufficiently large Weber number, for example $\mathrm{We_s} = 0.3$. By doing so, the coating thickness h_c slowly increases with increasing $\mathrm{We_s}$, while the branch is stable. Until the first Saddle-Node bifurcation occurs at $\mathrm{We_s} \approx 1.93$, a point where the coating thickness h_c passes the equilibrium precursor film height $h_\mathrm{p} = 0.1$, the branch stays stable. At the Saddle-Node bifurcation, the branch folds back and becomes unstable. The coating film thickness h_c increases continuously along the branch. At $\mathrm{We_s} \approx 1.5$ a second Saddle-Node bifurcation appears. Here again, the branch folds back, but instead of that the branch become stable it stays unstable. In other words, a second eigenvalue crosses the imaginary axes, leading to two eigenvalues with positive real parts. This phenomenon of the Saddle-Node bifurcations is already covered for the classical Landau-Levich case in Fig. 5.4 (a). The branch passes through another eight Saddle-Node bifurcations, where at each Saddle-Node bifurcation another eigenvalue crosses the imaginary axes. The steady states along that part remain unstable. Due to the small region where this sequence of Saddle-Node bifurcations are encountered on the branch, it can be translated to a exponential snaking. In exponential snaking the distances of subsequent folds are exponentially decreasing. In this case the snaking stops after the tenth Saddle-Node bifurcation. In the classical Landau-Levich case the snaking behaviour continues ad infinitum with permitting domain L. The stability along the branch changes at each Saddle-Node bifurcation, while in the SAW-driven case, each Saddle-Node bifurcation results in a more unstable branch. However, the finding resembles the behaviour, which is encountered in Langmuir-Blodgett transfer (LB) [67, 68].

At $\mathrm{We_s} \approx 1.56$, the branch nearly diverges. Then, the bifurcation curve bends slightly towards larger values of $\mathrm{We_s}$, see inset of Fig. 5.8. Beyond the tenth Saddle-Node bifurcation, where the branch still remains unstable, a sequence of eight Hopf bifurcation (black circles) occurs in short succession. Each of these bifurcations result in a more unstable state. Following the branch further, another sequence of 13 Hopf bifurcations is detected. These Hopf bifurcations are stabilising, so that finally the branch becomes stable at the last Hopf bifurcation located on the curve. In summary, all 26 eigenvalues that crossed the imaginary axes from the first ten Saddle-Node and eight Hopf bifurcations cross back again due to the 13 Hopf bifurcations.

When following the branch beyond the last Hopf bifurcation, the branch becomes finally stable, while it follows the power law $h_c \propto \mathrm{We_s}^{2/3}$. The power law remains as discussed before in Fig. 5.7 and is accordance with results from the classical Landau-Levich case.

The presented results are expanded with selected steady states, which are shown in Fig. 5.9 **I-IV**.

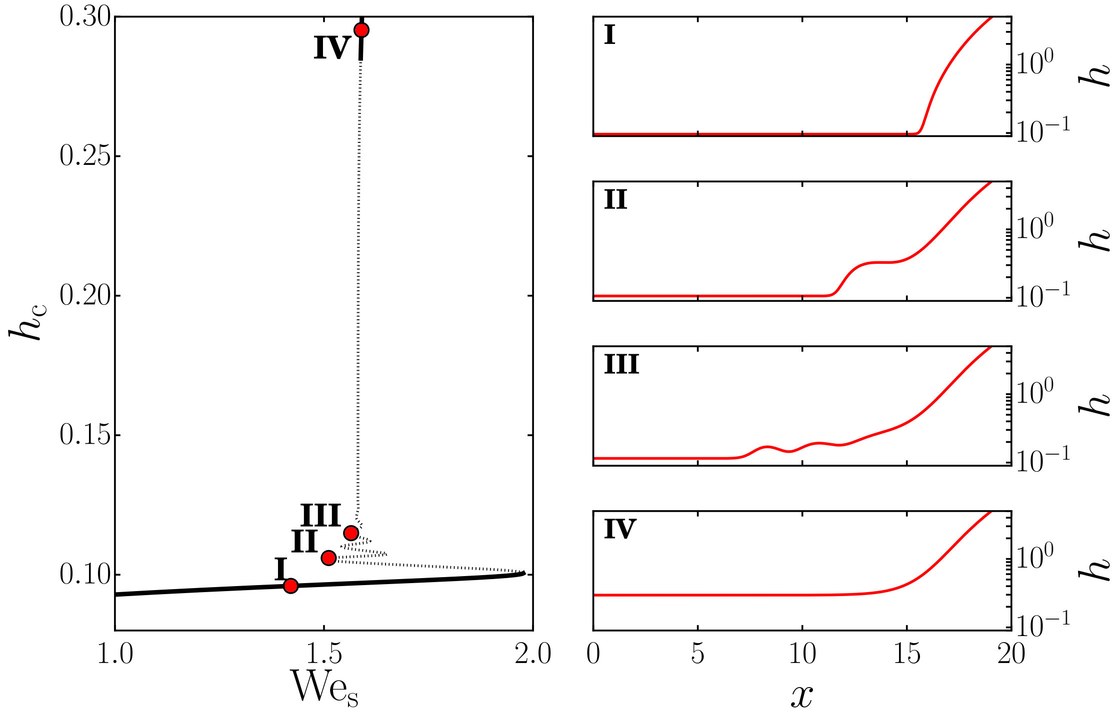

FIGURE 5.9: *On the left panel, a magnification of the bifurcation curve from Fig. 5.8 is shown. The dotted and solid lines represent stable and unstable steady film states. In addition, four chosen steady state profiles are presented (**I-III**). There, the film height h is scaled logarithmically and only half of the domain* $\Omega_{\mathrm{half}} = [0, L/2]$ *is presented. The remaining parameters are* $h_\mathrm{m} = 8.1$, $\mathrm{Ha} = 0.002$, $G = 0.001$, $h_\mathrm{p} = 0.1$, $\alpha = 0.2$, $\epsilon_\mathrm{s} = 1$, $U_0 = 0$ *and* $L = 40$.

Fig. 5.9 shows the steady thickness profiles. The bifurcation diagram on the left panel does not present the complete computational domain but only the range of the selected steady state profiles. The steady state profiles are shown in range of

$0 \leq x \leq 20$, which corresponds to the half of the domain Ω. The focus is only on the transition region from the meniscus to the adsorption layer. Following the branch from point **I** to **IV** in Fig. 5.9, several changes in the profiles are observed. In panel **I** a thin-film state is encountered where an absorption layer thickness $h_\mathrm{p} \approx 0.095$ in front of a meniscus is situated. This steady state profile does not develop a foot with a clearly defined thickness. Following the branch to point **II**, a foot-like structure is growing from the meniscus. The solution shows, that the profile monotonically and smoothly connects the meniscus with the adsorption layer, which is similar to the profiles of the dragged-case (Figs. 5.2-5.4). Note that the steady states **II** and **III** are unstable, whereas steady states in **I** and **IV** are stable states. While advancing along the snaking part of the branch, the foot-like structure starts to develop strong modulations **III** . Notice that the absorption layer thickness h_c only increases slowly in this process. At the last point **IV**, the steady state is stable. The occurring transition in the partially wetting case of SAW-driven meniscus remains as a discontinuous dynamic wetting transition, see Fig. 5.4 (a) and Fig. 5.6.

Up to here, the behaviour of the bifurcation curves for ideally and partially wetting liquid by employing the Weber number We_s have been presented. In the course of the study of partially wetting liquid in a SAW-driving model a numerous number of bifurcations, i.e. Saddle-Node and Hopf bifurcations, appears, see Fig. 5.8. The loci of the determined bifurcations are further investigated by the numerical approach of Fold and Hopf continuation. In this SAW-driven case the corresponding parameter space is spanned by the Weber number We_s and the Hamaker number Ha. This allows to determine parameters, where these bifurcations occur.

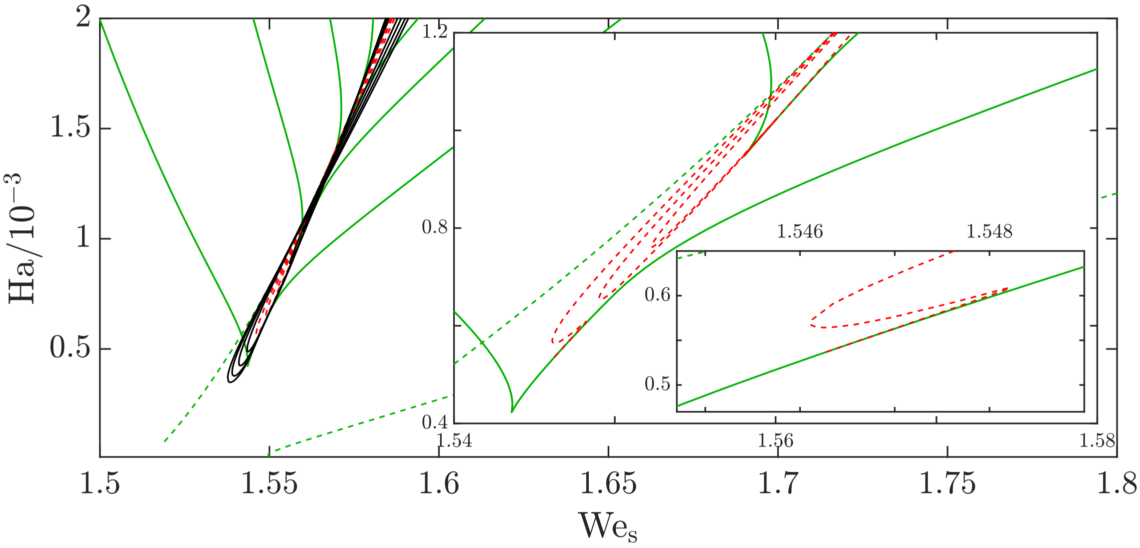

Figure 5.10: *Loci of Saddle-Node (green lines) and Hopf bifurcations (black and red lines) in the parameter plane spanned by the Weber number* We_s *and the Hamaker number* Ha *scaled by a factor with an active propagating SAW-term* $\epsilon_\mathrm{s} = 1$*. The different line styles (solid and dashed) are explained in the main text. The inset highlights the region where the leftmost Hopf bifurcation coloured in red emerges from the Saddle-Node bifurcation, i.e., where a Bogdanov-Takens bifurcation occurs. The remaining parameters are* $h_\mathrm{m} = 8.1$*,* $G = 0.001$*,* $h_\mathrm{p} = 0.1$*,* $\alpha = 0.2$*,* $\epsilon_\mathrm{s} = 1$*,* $U_0 = 0$ *and* $L = 40$*.*

In Fig. 5.10 the loci of Saddle-Node (green lines) and Hopf bifurcation (black solid and red dashed lines) are given. The solid green lines denote Saddle-Node bifurcations, which emerge in pairs at codimension-two hysteresis bifurcations from a cusp in the ($\mathrm{We_s}$, Ha)-plane. The two dashed green lines correspond to the Saddle-Node bifurcations that persist over the entire studied parameter range down to $\mathrm{Ha} = 0$. These two lines correspond to the Saddle-Node bifurcations in Fig. 5.7 with active gravity (black line). In contrast to the other Saddle-Node bifurcations, this pair (dashed green lines) does not emerge from a cusp.
Inspecting the appearance of the Hopf bifurcations in Fig. 5.10 with increasing $\mathrm{We_s}$, notice that the Hopf bifurcations also appear as pairs. The first pair in the codimension-two appears at $\mathrm{We_s} \approx 1.54$ and $\mathrm{Ha} \approx 0.00035$. The subsequent three Hopf pairs follow the same scheme (black lines). However, the next Hopf bifurcation emerges from a line of Saddle-Node bifurcation at $\mathrm{We_s} \approx 1.543$ and $\mathrm{Ha} \approx 0.0005$, see inset of Fig. 5.10. It is a Bogdanov-Takens bifurcation, where a Hopf bifurcation and a global (homoclinic) bifurcation emerge together at a Saddle-Node bifurcation [8, 53, 72]. While following the corresponding line of Hopf bifurcations, it slowly starts to separate from the line of Saddle-Node bifurcations. The trajectory continues until it makes contact with another line of Hopf bifurcation that emerge in a codimension-two double Hopf bifurcation, fifth pair of Hopf bifurcation at $\mathrm{We_s} \approx 1.546$ and $\mathrm{Ha} \approx 0.00055$. These two Hopf bifurcations then vanishes at the meeting point $\mathrm{We_s} \approx 1.549$ and $\mathrm{Ha} \approx 0.0006$. This behaviour is identical for each additionally appearing Hopf bifurcation as with red dashed lines in Fig. 5.10.

In general, the determined number of Saddle-Node and Hopf bifurcations, increases either with the Weber number and/or with the Hamaker number. Keep in mind, that increasing the Weber number corresponds to a decreasing surface tension, whereas the Hamaker number is directly proportional to the wettability strength. The findings for ideally and partially liquids in these sections, thus expand the theoretical results obtained by bifurcation diagrams from Ref. [87]. Different models of thin-film behaviour have been presented in different scaling (Ae.1) and (Ae.2). However, the focus is now switched to comparison of the two models, classical Landau-Levich case and SAW-driving case. Here, the general scaling in Eq. (3.49) is applied, which enables to connect the two models. The Hamaker number is kept constant at $\mathrm{Ha} = 0.001$, while incorporating the strength of the SAW-term ϵ_s. In the previous scaling (Ae.2) of Ref. [87] the latter factor was set to $\epsilon_\mathrm{s} = 1$. The SAW strength ϵ_s is now treated equally as the plate velocity U_0 from the dragged-case, and it is treated as the main control parameter for the upcoming results.

5.2.3 Thin film driven by SAW strength ϵ_s

Up to here, the change of the bifurcation curve as well as the appearance of bifurcations, are thoroughly investigated, while switching from ideally wetting to partially wetting liquid. The Weber number $\mathrm{We_s}$ remains as a main control parameter in this process. In this section the main control parameter is the SAW strength ϵ_s with the general scaling in Eq. (3.49). In addition, the solution measure is switched from coating thickness h_c back to the excess volume V_ex. This allows to directly compare the SAW bifurcation curves to the ones obtained by using the plate velocity U_0 for the classical Landau-Levich system in Sec. 5.1. In the following, four solution paths are presented in a bifurcation diagram for different values of the Weber number We_s.

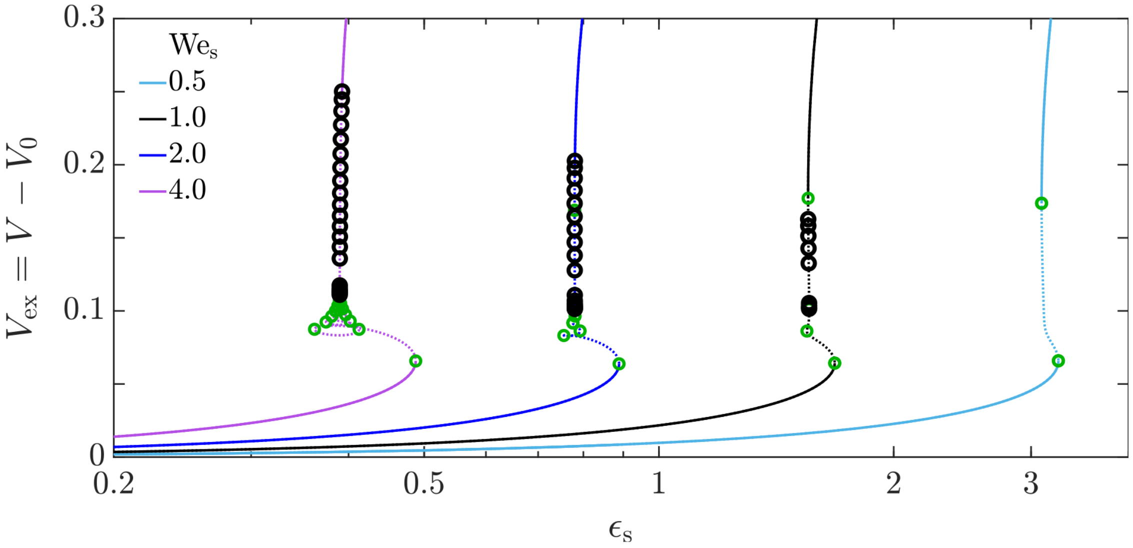

FIGURE 5.11: *Four bifurcation curves showing the excess volume V_ex versus the SAW strength ϵ_s for different Weber numbers We_s. The reference volume V_0 of the thin film is without acting SAW strength ϵ_s. The solid and dotted lines mark stable and unstable steady states, and Saddle-Node and Hopf bifurcation are presented with green and black circles, respectively. With decreasing We_s the number of bifurcation points decreases, whereas all Hopf bifurcations have vanished at $\mathrm{We}_\mathrm{s} = 0.5$, see details in Fig. 5.15. The remaining parameters are $h_\mathrm{m} = 8.1$, $\mathrm{Ha} = 0.001$, $G = 0.001$, $h_\mathrm{p} = 0.1$, $\alpha = 0.2$, $U_0 = 0$ and $L = 40$.*

All bifurcation curves in Fig. 5.11 are similar to the ones in Fig. 5.8, whereas for decreasing We_s the bifurcation curves shift towards smaller SAW strength ϵ_s. This implies, that the system needs less SAW power to spread over the substrate for a smaller ratio of convective stress and capillary stress. Roughly speaking, at larger We_s a lower SAW strength ϵ_s is sufficient to obtain the same exess volume in the meniscus.

Notice that the number of Saddle-Node and Hopf bifurcations increases with the Weber number We_s. For the bifurcation curve with $\mathrm{We}_\mathrm{s} = 0.5$ no Hopf bifurcations are detected. The curve has only two Saddle-Node bifurcations. Inspecting the shape of the bifurcation curves for big values of We_s, for instance $\mathrm{We}_\mathrm{s} = 4.0$, one notices that the exponential snaking region, where all Saddle-Node bifurcations occurred, appears as an exponentially decreasing cycloid, a result of the alternative measure of the excess volume. Changing the measure to the coating thickness h_c, however, will change the appearance back to exponential snaking. It appears that due to the acting SAW, the volume of the drawn out liquid film increases prior to decreases in this sequence. This change of varying volumes occurs only in the cycloid region, until it monotonically increases at the last Saddle-Node bifurcation. The remaining power law of all the curves behaves like the classical Landau-Levich case with $\propto \epsilon_\mathrm{s}^{2/3}$. An example for more complex curve is shown in Fig. 5.12 for $\mathrm{We}_\mathrm{s} = 4.0$. The bifurcation diagram shows a magnification of the snaking region and the inset gives an overview of a the full bifurcation.

In particular, the results of the steady profiles belonging to the exponential snaking region (cycloid region) of the bifurcation curve with $\mathrm{We}_\mathrm{s} = 4.0$ are presented in Fig. 5.13. In addition to the occurring thickness profile, the streamlines within the liquid layer are calculated. These help to better understand, how the occurring modulations are formed. Here, the solution measure of Fig. 5.12 is changed from excess volume V_ex to the coating thickness h_c to make the appearance of the snaking region more visible.

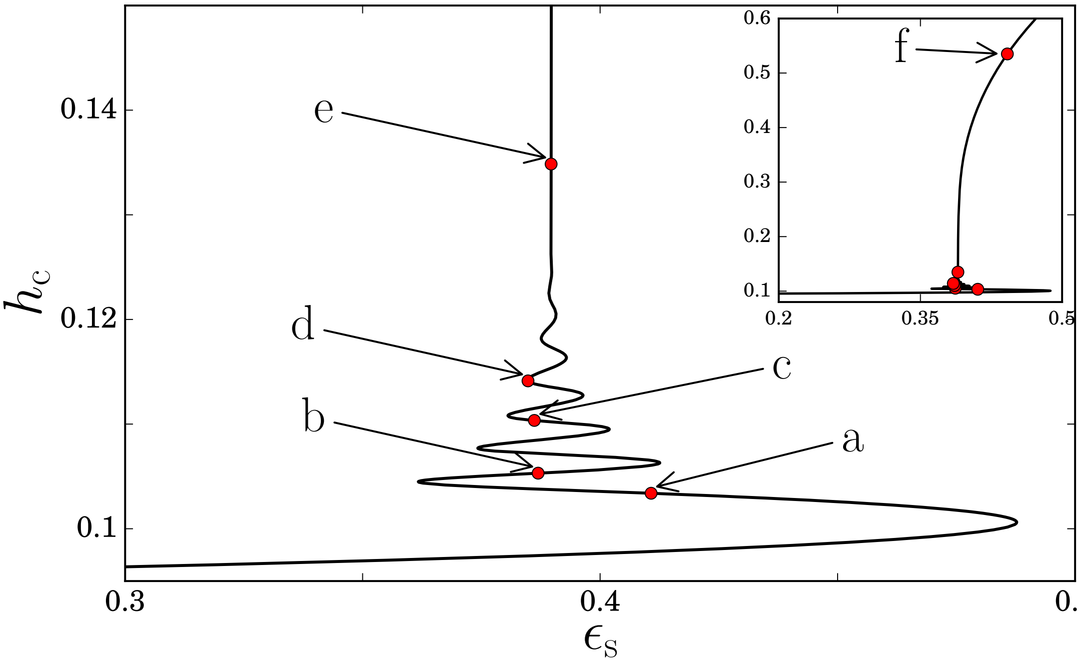

FIGURE 5.12: *Magnification of the snaking area of the bifurcation for* $\mathrm{We}_\mathrm{s} = 4.0$ *in Fig. 5.11, which show the coating thickness* h_c *as function of the SAW strength* ϵ_s. *The red points are marked from "a" to "f" and indicate different loci of steady states, which are presented in Fig. 5.13. The inset shows the complete bifurcation curve harboring the last point "f" on the branch. The remaining parameters are* $h_\mathrm{m} = 8.1$, $\mathrm{Ha} = 0.001$, $G = 0.001$, $h_\mathrm{p} = 0.1$, $\alpha = 0.2$, $U_0 = 0$ *and* $L = 40$.

Note that Fig. 5.12 shows neither the stability nor bifurcations. The magnification indicates the loci of six states which are shown in Fig. 5.13. Furthermore, these profiles only represent the transition region from the meniscus to the absorption layer where the foot-solution structures develop. The only stable steady profile is given with (f), whereas all the remaining points (a) to (e) are located in the exponential snaking region of the bifurcation curve.

In Fig. 5.13 (a), the profile corresponds to a meniscus solution, where the profile is smoothly and monotonically connected to the absorption layer. The bath is always situated on the right side at $x = L/2$ and the coating thickness h_c emerges on the

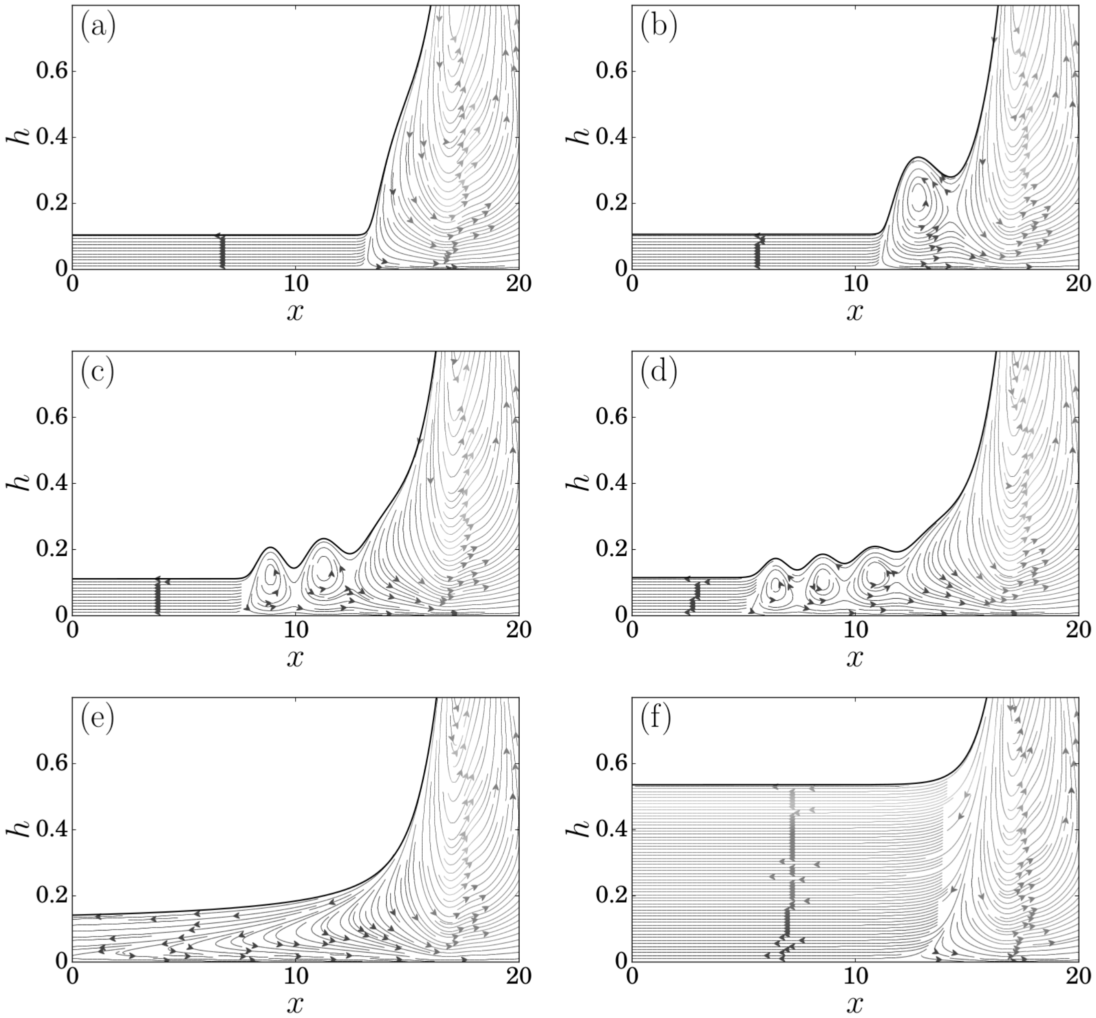

Figure 5.13: *Steady film thickness profiles and the corresponding streamlines within the fluid at parameters are shown, which are indicated by the letters "a" to "f" in Fig. 5.12 along the bifurcation curve, respectively. In (a) a meniscus solution is given, in (b) to (d) modulated foot-solutions are shown, in (e) a transition state between foot and Landau-Levich film state is presented, and in (f) a Landau-Levich film state is represented.*

other side. The presented steady state profiles in Fig. 5.13 show three different types of profiles. In first one is shown in (a), where a thin film solution of a meniscus state is given. This profile shows a thin film state with a close to zero SAW strength ϵ_s. It is similar as in the classical case, where the meniscus states are found at a (very) close to zero plate velocity U_0. The streamlines in Fig. 5.13 reveal that the meniscus exhibits a strong, non-monotonic and large-scaled convection roll developed in all presented steady states. However, a stagnant line appears at the point where the foot-solution is connected to the meniscus down to the solid substrate. Naturally, all streamlines are continuous. The second type of profiles appears, where a foot-structure start to develop in (b) and continuously grow with further strong modulations up to (d). In these foot-structures convection rolls are located. This convection rolls are directly connected to the propagating SAW. The SAW produces strong modulations of the foot thickness, which then corresponds to the convection roll within these structures. However, these foot-solutions are topologically identical to the classical Landau-Levich case, only their modulations are stronger developed and these overall structure starts to fuse with the absorption layer for increasing SAW strength ϵ_s. In contrast to the classical Landau-Levich case, these modulated foot-structures are always unstable. The last profile is a Landau-Levich film state for large ϵ_s, see (f). Note that in (e) the transition of foot-solution and Landau-Levich film state is shown. Here, in parallel, the convection rolls in the liquid layer, seems to weaken and partially fuse and push the stagnant line further away from the meniscus from (d) to (e). So that (f) finally shows a steady state profile of the liquid film which corresponds to a standard Landau-Levich film. The coating thickness h_c grows for continuous SAW strength ϵ_s. This is in line with the expected behaviour of any thin film driven case. The meniscus state in (a) and Landau-Levich film state in (f) are very similar as the one obtained in Sec. 5.1. In summary, the SAW-driven thin film behaves very similar as the classical Landau-Levich case, while providing modulated unstable foot-solutions.

In the presented Figs. 5.8 and 5.11, the obtained bifurcation diagrams demonstrate hysteresis behaviour. Hereby, two stable branches coexists at the same value of SAW strength ϵ_s, while having a different coating thickness h_c or excess volume V_{ex}. This indicates that only one of two outcomes occur depending on the initial state as long as all parameters are maintained. In particular, two time simulations are employed for different initial states, so that two different final steady film states are obtained.

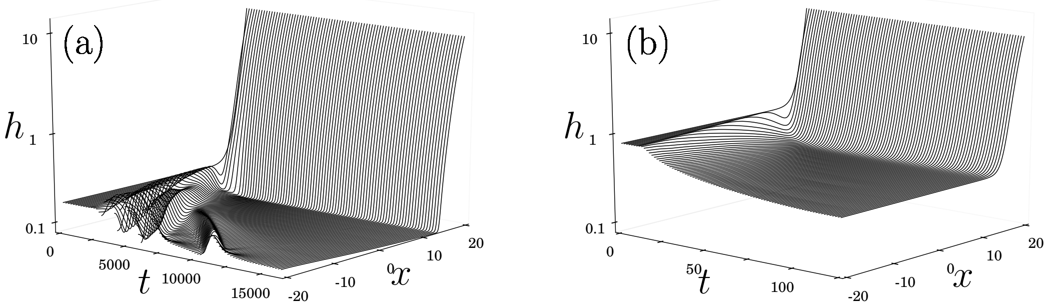

FIGURE 5.14: *Space-time plots of time evolutions demonstating bi-stability of different steady states in a SAW-driven thin film. In both panels, the SAW strength is constant with* $\epsilon_s = 1.6$ *and show two different film states occurring for selected initial condition with* $h_c = 0.2$ *and* $h_c = 0.8$. *Panel (a) shows the thin film relaxing onto a meniscus solution after a long transient time with film height* $h_c = 0.097$, *whereas panel (b) shows that the solution ends into a Landau-Levich film with film height* $h_c = 0.362$. *The film height h is scaled logarithmically. The remaining parameters are* $h_m = 8.1$, $\mathrm{We_s} = 1.0$, $\mathrm{Ha} = 0.001$, $G = 0.001$, $h_p = 0.1$, $\alpha = 0.2$, $\epsilon_s = 1.6$, $U_0 = 0$ *and* $L = 40$.

The time simulations of the SAW-driven thin film shows that two different solutions profiles of thin films are obtained for different initial states. In panel (a) the system requires much more time to become a meniscus state solution. It relaxes on a film height of $h_c = 0.097$. Here, the thicker film is drawn out while showing some modulations or droplets, which vanish over time. In contrast, the thin film in panel (b) indicates that the thicker thin film settles very fast onto a stable Landau-Levich film state with a lower film thickness with $h_c = 0.362$, whereas no modulations or droplets occur.

In the following section, the investigation of the occurring Saddle-Node and Hopf bifurcations is enhanced, to determine the loci where bifurcation occur first. Hereby, the main focus is placed on the appearance of Hopf bifurcations. Hopf bifurcations indicate where time-periodic states (TPS) emerge. As stated, numerically, several Bogdanov-Takens bifurcations are detected, where a Hopf bifurcation emerges from or vanishes at a Saddle-Node bifurcation. To fully understand the appearance of these bifurcations, the investigation is broadened, so that precise statements about individual states can then be proposed.

5.2.4 Appearance of Bogdanov-Takens and Hopf bifurcations

In order to investigate the branches of time-periodic states (TPS) emerging at Hopf bifurcations, the loci of the latter are studied first. The results in the previous sections revealed that many bifurcations are encountered in the SAW-driven thin-film system. However, the main focus is set on two different possibles where Hopf bifurcations appear. On the one hand, Hopf bifurcations appear as a pair (Hopf-pair) on a branch of steady states. On the other hand, presented bifurcation diagrams reveal that Hopf bifurcations appear individually. This is related to Bogdanov-Takens bifurcation. Therefore, in analogy to the dragged-case, an inspection of the loci of occurring bifurcations is performed. Remember that in the case of the SAW-driving, the number of detected Hopf bifurcations depends on either the Weber number $\mathrm{We_s}$ or the Hamaker number Ha. Here, the Hamaker number remains constant at $\mathrm{Ha} = 0.001$.

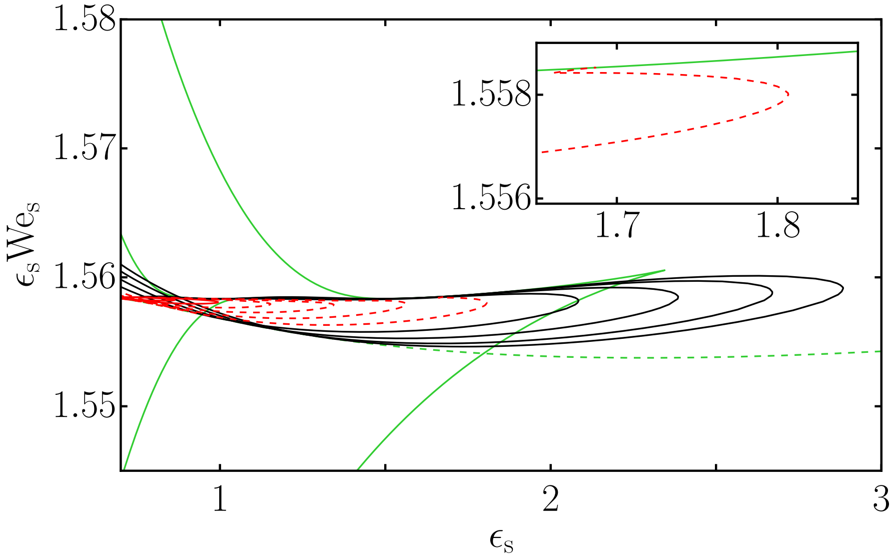

Figure 5.15: *Loci of Saddle-Node and Hopf bifurcations are shown in the parameter plane spanned by SAW strength ϵ_s and its product with the Weber number $\epsilon_s \mathrm{We_s}$. The inset magnifies the parameter region where one of the Bogdanov-Takens bifurcations occurs. The corresponding line styles are as in Fig. 5.10. The remaining parameters are $h_m = 8.1$, $\mathrm{Ha} = 0.001$, $G = 0.001$, $h_p = 0.1$, $\alpha = 0.2$, $U_0 = 0$ and $L = 40$.*

The loci of the bifurcations are not presented in the $(\mathrm{We_s}, \epsilon_\mathrm{s})$-plane, where all curves are nearly coincide. Instead they are shown in the $(\epsilon_\mathrm{s}\mathrm{We_s}, \epsilon_\mathrm{s})$-plane, which provides a well visible picture, see Fig. 5.15.

Fig. 5.15 shows a qualitatively similar behaviour of the loci of bifurcations as in Fig. 5.10. Note that the difference occurs due to the presentation, which is rotated by 90°. The inset of Fig. 5.15 shows, that the first individual Hopf bifurcation appear at $\epsilon_\mathrm{s}\mathrm{We_s} \approx 1.5585$ and $\epsilon_\mathrm{s} \approx 1.686$. This codimension-one Hopf bifurcation emerges from a Bogdanov-Takens bifurcation in codimension-two. This Hopf bifurcation appears simultaneously with a homoclinic bifurcation, as does the entire branch of TPS. Following further the red dashed line in the inset, the branch of Hopf bifurcations separates slowly from the Saddle-Node bifurcations. Then, it collides and vanishes together with another branch of Hopf bifurcation at $\epsilon_\mathrm{s}\mathrm{We_s} \approx 1.5584$ and $\epsilon_\mathrm{s} \approx 1.62$. The latter is one of Hopf-pair emerging at $\epsilon_\mathrm{s}\mathrm{We_s} \approx 1.558$ and $\epsilon_\mathrm{s} \approx 1.8$.

To pinpoint those events, a bifurcation diagrams is plotted showing the coating thickness h_c over the SAW strength ϵ_s for three different values of $\mathrm{We_s}$. In addition, the loci of the Hopf bifurcations are highlighted and the loci of the Bogdanov-Takens bifurcations are marked by red triangles, see Fig. 5.16.

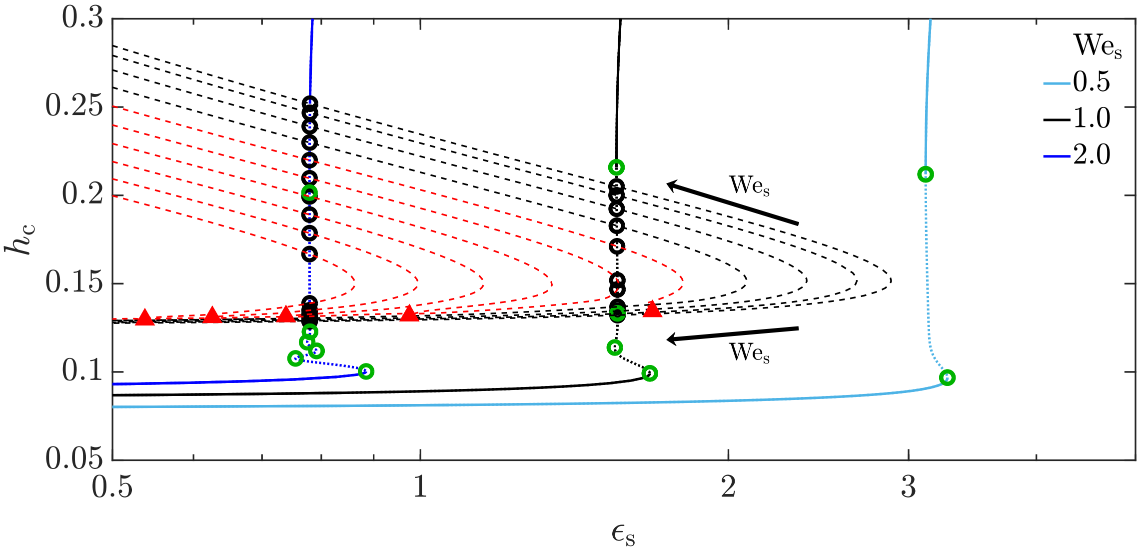

FIGURE 5.16: *Bifurcation diagram showing three bifurcation curves from Fig. 5.11 for different* $\mathrm{We_s} = 2.0, 1.0$ *and* 0.5, *giving the coating thickness* h_c *over SAW strength* ϵ_s. *The loci of the Hopf bifurcation are presented by black and red dashed lines, when changing the parameter* $\mathrm{We_s}$. *Black arrows indicate the direction of increasing* $\mathrm{We_s}$. *The five red triangles mark Bogdanov-Takens bifurcations. The remaining parameters are* $h_\mathrm{m} = 8.1$, $\mathrm{Ha} = 0.001$, $G = 0.001$, $h_\mathrm{p} = 0.1$, $\alpha = 0.2$, $U_0 = 0$ *and* $L = 40$.

The arrows in Fig. 5.16 indicate the direction of increasing $\mathrm{We_s}$. At $\mathrm{We_s} \approx 0.52$ the first Hopf-pair appears. In particular, the first Bodganov-Takens bifurcation appearing at $\epsilon_\mathrm{s} \approx 1.686$ and $\mathrm{We_s} \approx 0.9244$ is investigated. Following the red dashed line beyond the triangle, it bends over towards larger ϵ_s. At that fold at $\epsilon_\mathrm{s} \approx 1.66$ and $\mathrm{We_s} \approx 0.94$, two Hopf bifurcations collide and vanish. The second Hopf bifurcation comes from the Hopf-pair emerging at $\epsilon_\mathrm{s} \approx 1.807$ and $\mathrm{We_s} \approx 0.86$. After this event of annihilation, the Hopf bifurcation from that Hopf-pair remains for increasing $\mathrm{We_s}$. In Fig. 5.17 a magnification of these events is presented.

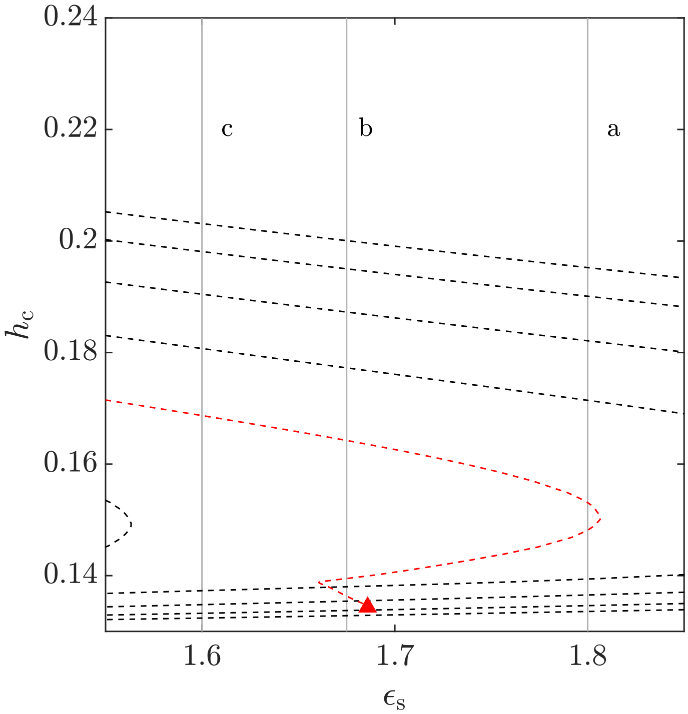

Figure 5.17: *Magnification of Fig. 5.16 focusing on the loci of the Hopf bifurcations (black and red dashed lines). The red triangle marks the Bogdanov-Takens bifurcation and the red dashed line corresponds to the loci of the emerging Hopf bifurcation. At each vertical grey line, which are marked by "a", "b" and "c", show sketches of the related bifurcation diagrams of time-periodic states (TPS) for different parameter ranges in Fig. 5.18.*

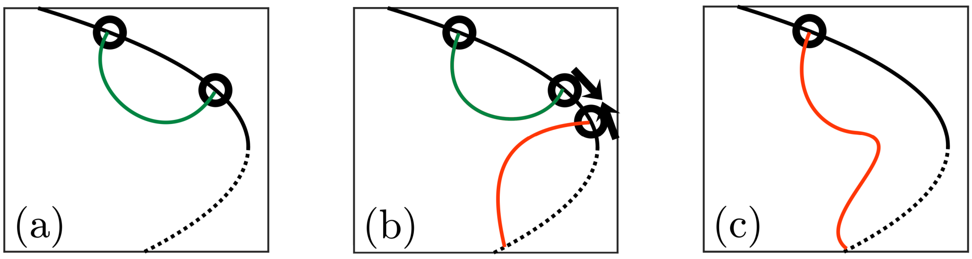

Figure 5.18: *Appearance and annihilation of global homoclinic and local Hopf bifurcations and the connecting branches of time-periodic states (TPS). In (a), a pair of Hopf bifurcations is shown (black circle). These are connected via a TPS branch (green line). For decreasing ϵ_s leads to three Hopf bifurcations one of which emerges from a Bogdanov-Takens bifurcation, shown in (b). It is connected to a global homoclinic bifurcation (red line). Arrows in (b) indicate the movement of the Hopf bifurcation. In panel (c) two Hopf bifurcations have vanished and the remaining Hopf bifurcation is now connected to the homoclinic bifurcation.*

Furthermore, in Fig. 5.17 three vertical grey lines mark different values for We_s. Each of them represents a case, where a different number of Hopf bifurcations occurs at fixed $\mathrm{We}_s = 0.9, 0.925$ and 0.93. At first, qualitative sketches of these cases are given in Fig. 5.18, whereas later, in Sec. 5.2.5, the exact representations are shown in Figs. 5.20-5.25.

In panels (a)-(c) the qualitatively different events of interacting TPS branches are shown for different Weber number We_s with decreasing SAW strength ϵ_s. Fig. 5.18 (a) presents the “bare” state of the bifurcation diagram at the “a”-line of Fig. 5.17. Here, a pair of Hopf bifurcations (black circles) are shown to be connected via a branch of TPS (green line). This pair of Hopf bifurcations appears together in a codimension-two double Hopf bifurcation at $\epsilon_\mathrm{s} \approx 1.807$. When decreasing ϵ_s, a third Hopf bifurcation emerges from a Bogdanov-Takens bifurcation [Fig. 5.18 (b)]. This Hopf bifurcation is connected to a homoclinic bifurcation via a branch of TPS (red line). Decreasing ϵ_s to smaller values, leads to approach of these two Hopf bifurcation indicated by arrows in Fig. 5.18 (b). The two Hopf bifurcations finally collide and vanish at $\epsilon_\mathrm{s} \approx 1.66$ in a reverse double Hopf bifurcation. Subsequently, the two branches of TPS simultaneously fuse together into a single branch of TPS, so that the remaining Hopf bifurcation is connected to the homoclinic bifurcation in (c).

In summary, the parameter study has revealed that Hopf bifurcations in a SAW-driven thin-film model either emerge from a double Hopf bifurcation as a Hopf-pair or from a Bogdanov-Takens bifurcation. In particular, branches of TPS do emerge from Hopf bifurcations and in a recent study branches of TPS in the classical Landau-Levich case are described [123]. To broaden the understanding of these occurring behaviour related to codimension-two bifurcations, they are further discussed and investigated in the following Sec. 5.2.5, where Hopf bifurcations emerge or vanish, i.e. shown in Fig. 5.18. These results will provide detailed information on the occurring behaviour of Hopf bifurcation and the corresponding branches of TPS.

5.2.5 Time-periodic states (TPS)

To examine the variations of the number of Hopf bifurcation appearing in the bifurcation diagram, different bifurcation diagrams are generated at fixed $\mathrm{We}_\mathrm{s} = 0.9, 0.925$ and 0.93. They are then studied with increasing Weber numbers, when the number of Hopf bifurcations increases. In addition, the branches of TPS are investigated to examine the behaviour of corresponding TPS branches.
To start these numerical analyses, two simple cases of bifurcation diagrams are presented for $\mathrm{We}_\mathrm{s} = 0.55$ and $\mathrm{We}_\mathrm{s} = 0.72$, where two and six Hopf bifurcations are detected along the bifurcation curve, respectively. No global homoclinic bifurcation occurs. The branches of TPS are computed with the method presented in Sec. 4.1.2.

The panels (a) and (b) of Fig. 5.19 show a magnification of the region where the Hopf bifurcations are detected. The insets present the overall bifurcation curve. Notice that all occurring Hopf bifurcations (black circles) are connected by branches of TPS (green line). These two results present the basic scenarios of emerging Hopf-pairs connected by branches of TPS.

In the following case, a bifurcation diagram is generated with an increased Weber number $\mathrm{We}_\mathrm{s} = 0.9$. This represents the case of the grey line marked with “a” crossing the red dashed line twice in Fig. 5.17. It also corresponds still to the case presented

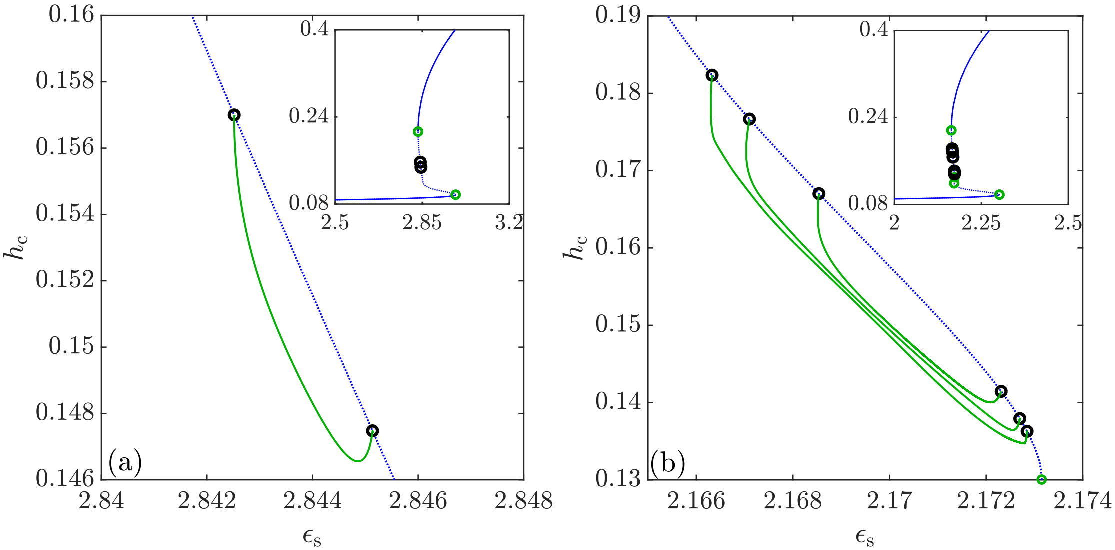

Figure 5.19: *Selected and relevant parts of the bifurcation diagrams are shown, which give the (time-averaged) coating film thickness* h_c *as a function of the SAW strength* ϵ_s *at the fixed Weber number values in (a)* $\mathrm{We_s} = 0.55$ *and in (b)* $\mathrm{We_s} = 0.72$*. Blue (solid and dashed) and green lines represent steady (stable and unstable) and time-periodic states, respectively. Saddle-Node and Hopf bifurcations are marked by green and black circles. The insets magnify the relevant complete bifurcation curve for the steady states. The remaining parameters are* $h_m = 8.1$*,* $\mathrm{Ha} = 0.001$*,* $G = 0.001$*,* $h_p = 0.1$*,* $\alpha = 0.2$*,* $U_0 = 0$ *and* $L = 40$*.*

in Fig. 5.18 (a). Here, an even number of ten Hopf bifurcations is determined and no Bogdanov-Takens bifurcation has emerged.

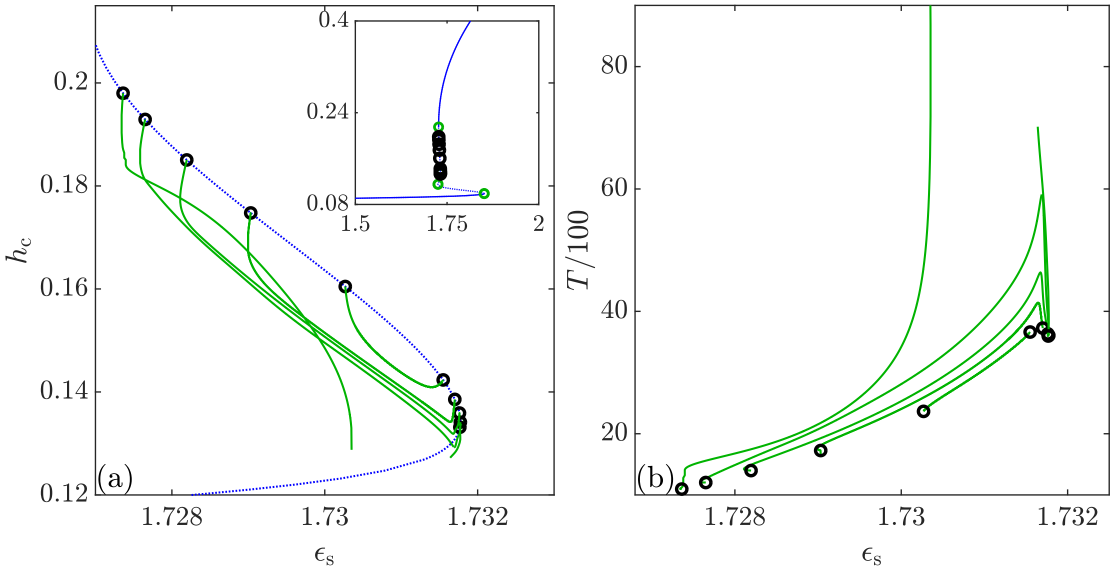

Figure 5.20: *Bifurcation diagrams showing the (time-averaged) coating thickness* h_c *versus the SAW strength* ϵ_s *at fixed Weber number* $\mathrm{We_s} = 0.9$ *in (a). Panel (b) shows the time period* T *as function of* ϵ_s *only for all branches of TPS. Blue (solid and dashed) and green lines represent steady (stable and unstable) and time-periodic states, respectively. Saddle-Node and Hopf bifurcations are marked by green and black circles. The inset in (a) gives the relevant complete bifurcation curve for the steady states. Two branches of TPS from the first and last Hopf bifurcation are not fully tracked due to limits in the numerical resolution. The remaining parameters are* $h_m = 8.1$*,* $\mathrm{Ha} = 0.001$*,* $G = 0.001$*,* $h_p = 0.1$*,* $\alpha = 0.2$*,* $U_0 = 0$ *and* $L = 40$*.*

Fig. 5.20 (a) shows a bifurcation diagram for $\mathrm{We_s} = 0.9$ that has ten Hopf bifurcations along the branch of steady states. All ten are connected pairwise by a branch of TPS (green line). The last branch of TPS, which connects the first and tenth Hopf bifurcation crosses the other branches of TPS. However, this branch could not be fully tracked due to limited numerical resolution. In panel (b) where the time period T as function of ϵ_s is shown, the same reaches the largest T. Overall, the number of occurring Hopf bifurcations will increase for larger Weber number, so that more branches of TPS appear.

In the next bifurcation diagram at $\mathrm{We}_\mathrm{s} = 0.925$, the first odd number of Hopf bifurcations appears. This implies that the first Bogdanov-Takens bifurcation must have occurred and a homoclinic bifurcation must exist [72]. Since the Bogdanov-Takens bifurcation always appears at a Saddle-Node bifurcation, it is possible that further codimension-two events have taken place, e.g. a Fold-Hopf bifurcation. This event, in particular, can be addressed in future simulations. The first Bogdanov-Takens bifurcation appears after the second Hopf bifurcation along the branch of steady states, see Fig. 5.17.

In Fig. 5.21 the third Hopf bifurcation has already emerged from the Bogdanov-Takens bifurcation. All branches of TPS are shown as solid green, dashed-dotted green and dashed red lines. The solid green lines correspond to pairs of Hopf bifurcation connected by branches of TPS. The dashed-dotted green line represents the branch of TPS connecting the Hopf bifurcation, which emerged from the Bogdanov-Takens bifurcation, connected to another Hopf bifurcation. The dashed red line represents the branch connecting a Hopf bifurcation with a homoclinic bifurcation.

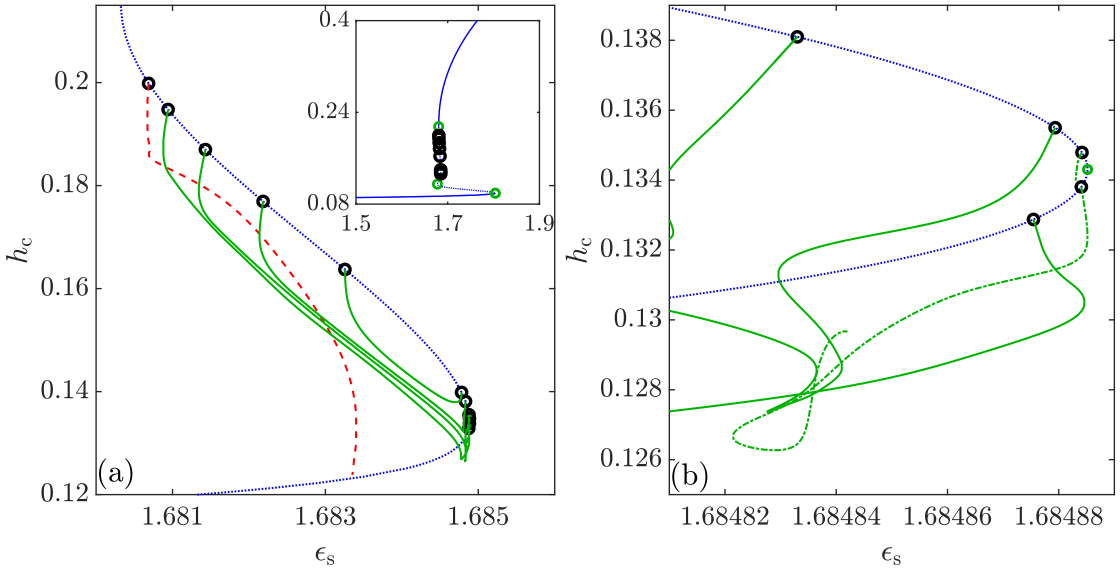

FIGURE 5.21: *Bifurcation diagrams showing the (time-averaged) coating thickness* h_c *versus the SAW strength* ϵ_s *at fixed Weber number* $\mathrm{We}_\mathrm{s} = 0.925$ *in (a). The Hopf branches (TPS, green lines) connect two Hopf bifurcations (black circle). The single branch connecting a Hopf and a global homoclinic bifurcation is indicated by a dashed red line. The Hopf branch connecting the Hopf bifurcation from the Bogdanov-Takens bifurcation with another Hopf bifurcation is indicated by a dashed-dotted green line. Saddle-Node bifurcations are marked with green circles. Panel (a) shows the different TPS in the region where all the Hopf bifurcations occur and panel (b) gives a zoom of the region first Hopf bifurcations. The branch of TPS (green dashed-dotted line) is not completed, which connects the second and third Hopf bifurcation. The corresponding dependencies of the period* T *of the TPS on* ϵ_s *is presented in Fig. 5.22. The remaining parameters are* $h_\mathrm{m} = 8.1$, $\mathrm{Ha} = 0.001$, $G = 0.001$, $h_\mathrm{p} = 0.1$, $\alpha = 0.2$, $U_0 = 0$ *and* $L = 40$.

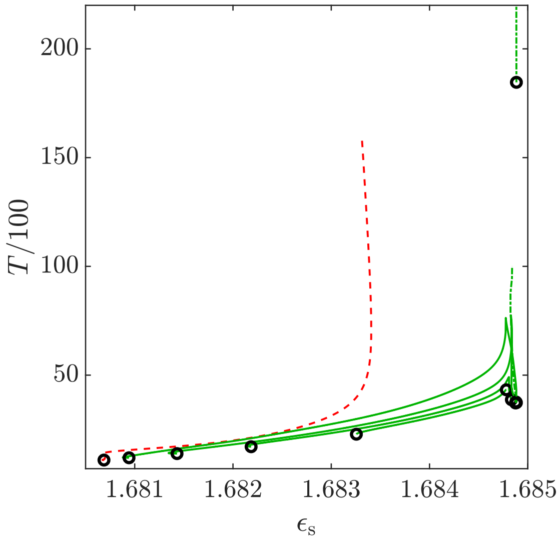

Figure 5.22: *Bifurcation diagram showing the time period T as function of the SAW strength ϵ_s for all branches of TPS in Fig. 5.21. Branches of TPS (solid green lines) connect two Hopf bifurcations (black circle). The single branch connecting a Hopf and a global homoclinic bifurcation is indicated by a dashed red line. The Hopf branch connecting the Hopf bifurcation from the Bogdanov-Takens bifurcation at the top right corner with the second Hopf bifurcation is indicated by a dashed-dotted green line (branch is not completed).*

Note that this branch of TPS is particularly challenging for the numerics, as the period T diverges when approaching a global bifurcation. Therefore, it is not possible to approach the bifurcation closely. This interpretation is supported by the results shown in Fig. 5.22. Inspecting the stability of the branch of steady states with increasing ϵ_s beginning from small values, at first one starts with a stable meniscus state. Then, the branch passes two destabilising Saddle-Node bifurcations and a global bifurcation, which does not affect the stability. Next, two Hopf bifurcations and a Saddle-Node bifurcation occur, which both act destabilising. The third Hopf bifurcation, however, acts stabilising. At this point, five unstable eigenmodes persist, so that the steady states remain unstable, see Fig. 5.21.

Fig. 5.22 shows that the branch related to the global bifurcation (red dashed line) diverges. This T is much larger than all T of the other TPS branches and indicates the approaching global bifurcation. The branch connecting the second and third Hopf bifurcations (green dashed-dotted line) has also a fairly large period T which does not diverge. A possible reason of this large period T is that the Hopf bifurcation was once connected to the global bifurcation for lower Weber numbers. After the reconnection process, the connection switches simultaneously and leads to new connections of all Hopf bifurcations. Hereby, the last Hopf bifurcation inherits the branch connected to the global bifurcation.

Next, the Weber number is further increased to $\mathrm{We_s} = 0.93$ and shows that the Hopf bifurcation emerged from the Bogdanov-Takens bifurcation is the fourth Hopf bifurcation on the branch of steady states. Roughly speaking, this Hopf bifurcation moves along the bifurcation branch, which is indicated within Fig. 5.17.

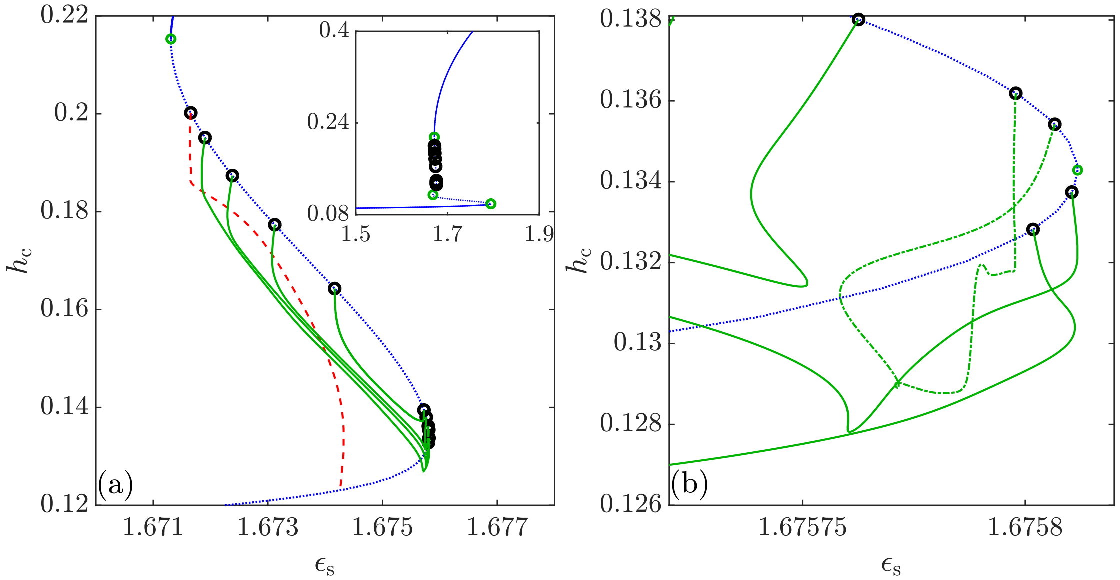

FIGURE 5.23: *Bifurcation diagrams showing the (time-averaged) coating thickness h_c versus the SAW strength ϵ_s at fixed Weber number $\mathrm{We_s} = 0.93$ in (a). The Hopf branches (TPS, green lines) connect two Hopf bifurcations (black circle). The single branch connecting a Hopf and a global homoclinic bifurcation is indicated by a dashed red line. The Hopf branch connecting the Hopf bifurcation from the Bogdanov-Takens bifurcation with another Hopf bifurcation is indicated by a dashed-dotted green line. Saddle-Node bifurcations are marked with green circles. Panel (a) shows the different TPS in the region where all the Hopf bifurcations occur and panel (b) gives a zoom of the region first Hopf bifurcations. The branch of TPS (green dashed-dotted line) is not completed, which connects the second and third Hopf bifurcation. The inset in (a) gives the relevant complete bifurcation curve for the steady states. The corresponding dependencies of the period T of the TPS on ϵ_s is presented in Fig. 5.24. The remaining parameters are* $h_m = 8.1$, $\mathrm{Ha} = 0.001$, $G = 0.001$, $h_p = 0.1$, $\alpha = 0.2$, $U_0 = 0$ *and* $L = 40$.

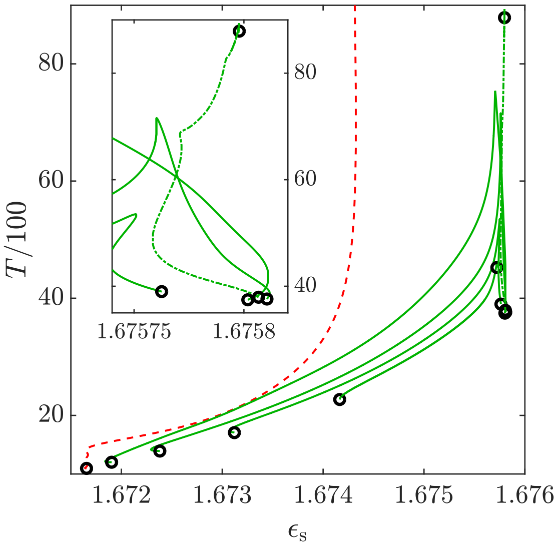

FIGURE 5.24: *Bifurcation diagrams showing the time period T as function of the SAW strength ϵ_s for all branches of TPS in Fig. 5.23. Branches of TPS (solid green lines) connect two Hopf bifurcations (black circle). The single branch connecting a Hopf and a global homoclinic bifurcation is indicated by a dashed red line. The Hopf branch connecting the (moving) Hopf bifurcation from the Bogdanov-Takens bifurcation at the top right corner with the third Hopf bifurcation is indicated by a dashed-dotted green line. The inset gives a magnification of this TPS connected to the moving Hopf bifurcation.*

Fig. 5.23 shows a similar behaviour of the branches of TPS as presented in Fig. 5.21. The case of $\mathrm{We_s} = 0.93$ shows the Hopf bifurcation that emerged from the Bogdanov-

Takens bifurcation has bypassed another Hopf bifurcation. In particular, this Hopf bifurcation is termed "moving Hopf bifurcation". In other words, branches of TPS are connected other Hopf bifurcations when changing the Weber number from 0.925 to 0.93. In Fig. 5.23 the third and fourth Hopf bifurcations are connected by a branch of TPS. In particular, this branch indicated by a dashed-dotted green line correspond to the moving Hopf bifurcation. This also results into a more complicated structure than the other branches of TPS (solid green lines). The second Hopf bifurcation is connected to the ninth Hopf bifurcation, instead it was connected to the Hopf bifurcation, which emerged from Bogdanov-Takens bifurcation, in the latter case. All other branches of TPS remain unchanged. In contrast to the TPS with $\mathrm{We_s} = 0.925$ [Fig. 5.22] the period T decreases drastically for the branch of TPS, which emerges from the moving Hopf bifurcation.

In the next case, for $\mathrm{We_s} = 1.0$ this Hopf bifurcation effectively vanishes at a reverse double Hopf bifurcation. Here, the bifurcation diagram for $\mathrm{We_s} = 1.0$ shows again an odd number of eleven Hopf bifurcations. In particular, the number of Hopf bifurcations decreases, however for $\mathrm{We_s} = 1.0$ another pair of Hopf bifurcation has already appeared.

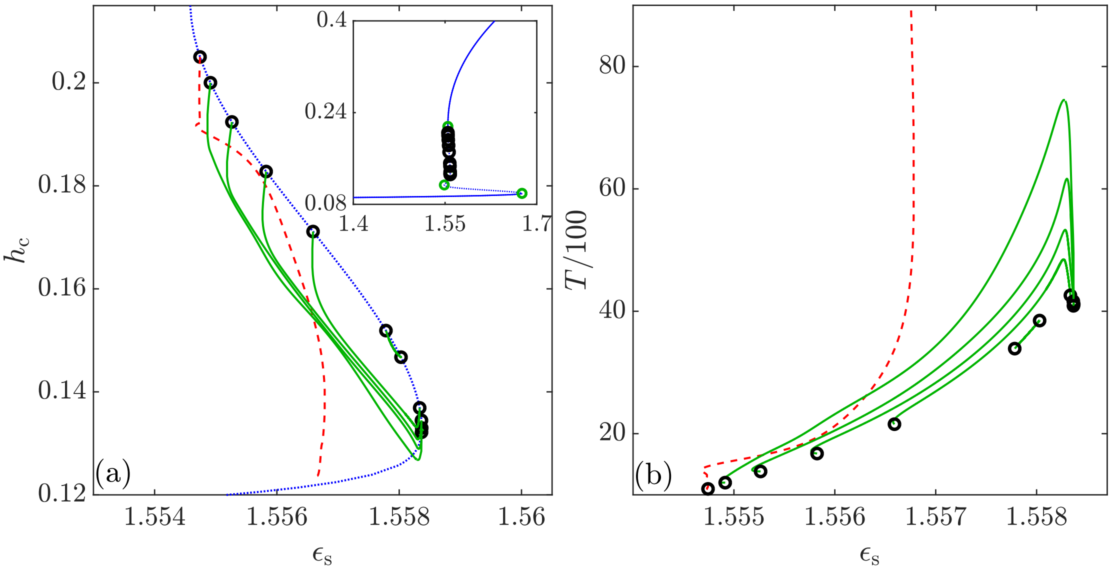

FIGURE 5.25: *Bifurcation diagrams showing the (time-averaged) coating thickness* h_c *versus the SAW strength* ϵ_s *at fixed Weber number* $\mathrm{We_s} = 1.0$ *in (a). Panel (b) shows the time period* T *as function of* ϵ_s *only for all branches of TPS. Blue (solid and dashed) and green lines represent steady (stable and unstable) and time-periodic states, respectively. Saddle-Node and Hopf bifurcations are marked by green and black circles. The inset in (a) gives the relevant complete bifurcation curve for the steady states. Two branches of TPS from the first and last Hopf bifurcation are not fully tracked due to limits in the numerical resolution. The remaining parameters are* $h_m = 8.1$, $\mathrm{Ha} = 0.001$, $G = 0.001$, $h_p = 0.1$, $\alpha = 0.2$, $U_0 = 0$ *and* $L = 40$.

In Fig. 5.25 the reconnection events, caused by the moving Hopf bifurcation, have ended. The remaining branches of TPS are similar as in the latter cases. In addition, the final Hopf bifurcation is connected via a branch of TPS to a global bifurcation, this connection remains unchanged. From the presented results, an illustration of the complex behaviour of reconnecting branches of TPS is presented in Fig. 5.26.

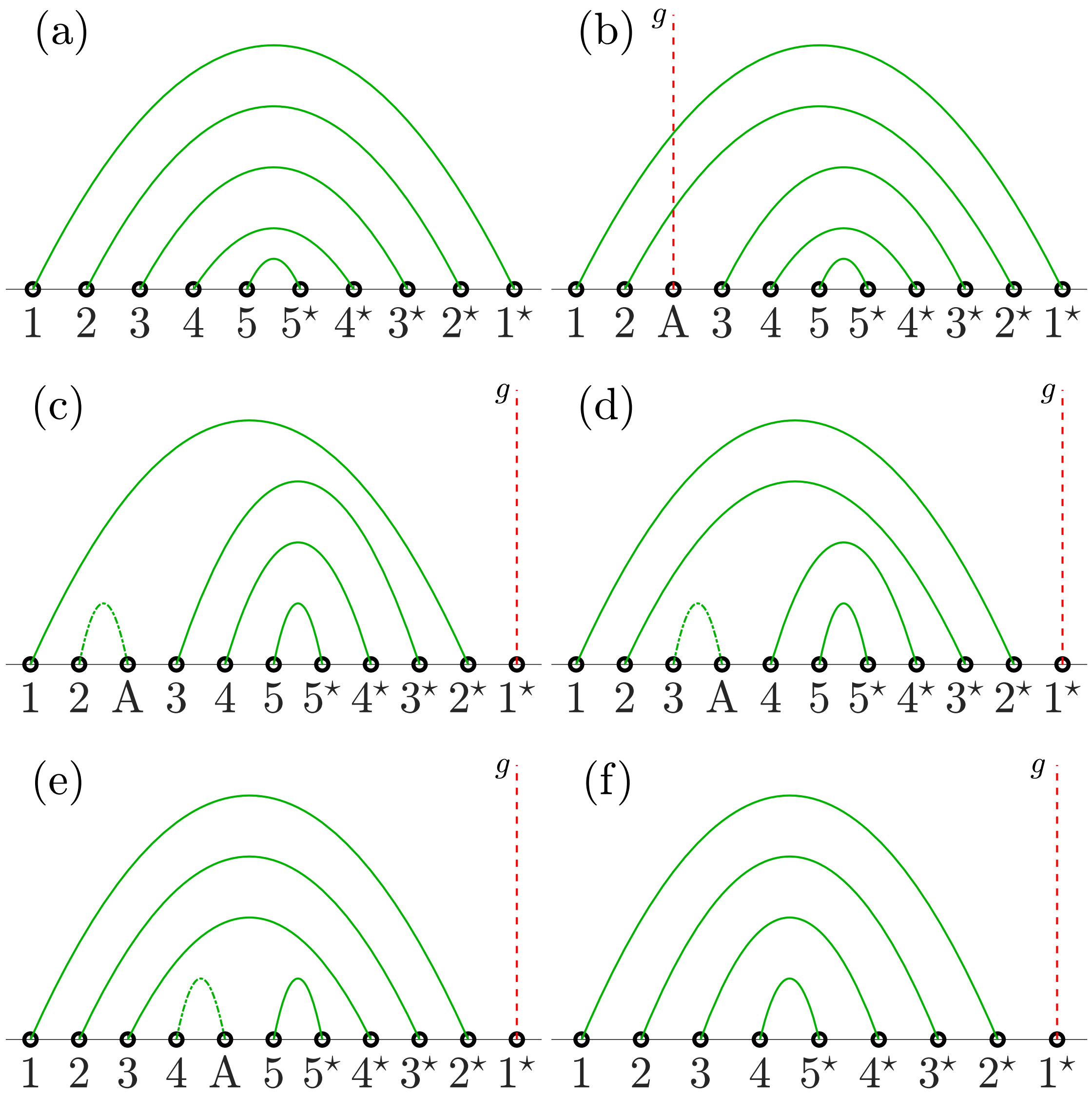

FIGURE 5.26: *Illustration of the motion of Hopf bifurcation "A" and the related reconnections of the branches of TPS during the increasing Weber number are schematically represented in panels (a) to (f). The solid green line connects a pair of Hopf bifurcations, the green dashed-dotted line connects Hopf bifurcation "A" with another Hopf bifurcation and the red dashed line connects Hopf with the global bifurcation "g". All other Hopf bifurcations are also indicated by numbers, e.g., a pair of double Hopf bifurcations "1" and "1⋆". The vertical axes symbolically represents a solution measure, for instance, period T. Note that no bifurcation diagrams are generated for (b) and (e).*

The illustration, Fig. 5.26 (a) starts with the case of the Weber number $\mathrm{We_s} = 0.9$. In panel (a) all ten occurring Hopf bifurcations are shown and the five corresponding branches of TPS (solid green lines) connecting five pairs of Hopf bifurcation indicated by "$1-1^\star$" to "$5-5^\star$". The first topological change occurs when the Hopf bifurcation from the Bogdanov-Takens bifurcation emerges as shown in panel (b). The Hopf bifurcation is marked with "A" and is connected to the global bifurcation "g" (dashed red line). In panel (b) to (c) the connections of branches change. The reconnected branches of TPS are "$1-1^\star$", "$2-2^\star$" and "A-g", which break and immediately reconnect. Panel (c) shows the case of $\mathrm{We_s} = 0.925$ where the connections have switched to “g $-1^\star$”, “2− A” and “$1-2^\star$”, see Fig. 5.21. Increasing the Weber number, the bifurcation “A” moves to the right so that the position of bifurcation “3” and “A” are swapped in Fig. 5.26 (d). This case corresponds to $\mathrm{We_s} = 0.93$ shown in Fig. 5.23. When the bifurcation “A” bypasses the bifurcation “3”, a reconnection is triggered and as a result, the branches “2− A” and “$3-3^\star$“ become ”$2-3^\star$“ and ”3− A“. More reconnections occur as the bifurcation A continues moving to the right from panel (d) to (e). In the final stage, from panel (e) to (f), the branches ”4− A“ and ”$5-5^\star$“ reconnect finally into one branch ”$4-5^\star$“. Thereby, bifurcations ”A“ and ”5“ collide and eliminate. The last panel is aligned to Fig. 5.25, but without the additional pair of Hopf bifurcations. This also corresponds to the simple case shown in Fig. 5.18 (c). Comparing the illustration of Fig. 5.26 (a) with (f), at first the appearances of both states are very similar, however, a additional branch connecting Hopf with global bifurcation at the rightmost position is added. The illustration presented in Fig. 5.26 explains the transition of reconnecting branches of TPS from $\mathrm{We_s} = 0.9$ to $\mathrm{We_s} = 1.0$. The cascade of topological changes of the bifurcation diagram, where all branches of TPS reconnect, is further summarised. The Hopf bifurcation n with $n \in \mathcal{N}_0$, which are initially connected to Hopf bifurcation $n^\star$ (double pair of Hopf bifurcations), is connected to Hopf bifurcation $(n+1)^\star$ at the end of the transition. This sequence of events happens whenever a Hopf bifurcation emerges from a Bogdanov-Takens bifurcation.

As a reminder, the main goal is to determine parameter ranges for the SAW strength ϵ_s in the SAW-system, where stable time-periodic states occur. Therefore, the Weber number is further increased to $\mathrm{We_s} = 2.0$, where the last Hopf bifurcation along the branch of steady states is then responsible for the change in stability. The resulting bifurcation diagram has 18 Hopf bifurcations and is presented in Fig. 5.27.

In the bifurcation diagram at $\mathrm{We_s} = 2.0$, ten branches of TPS exist. However, a large number of these branches have not been fully tracked using PDE2PATH, due to numerical limitations. Fig. 5.16 indicates that two homoclinic bifurcations occur where two moving Hopf bifurcations have already terminated the sequence of reconnections described above. In Fig. 5.27 only the last two Hopf bifurcations ”17“ and ”18“ are connect to the homoclinic bifurcation and the other eight branches are connected as Hopf-pairs, for instance ”1-16“, ”2-15“, up to ”8-9“. Inspecting individual branches in more detail, they acquired a more complex structure and now feature more Saddle-Node bifurcations as some of these branches folds back and forth several times. This behaviour is more common for the outer branches than the inner ones. Also the ranges of periods T of the branches connecting two Hopf bifurcations has increased (not shown). This explains why numerical difficulties occurred, so that several calculated branches of TPS are stopped not showing their full extension.

The most relevant branch of TPS namely the ”outermost“ branch is examined, which emerged from the 18th (last) Hopf bifurcation. For this purpose the L^2-norm is used

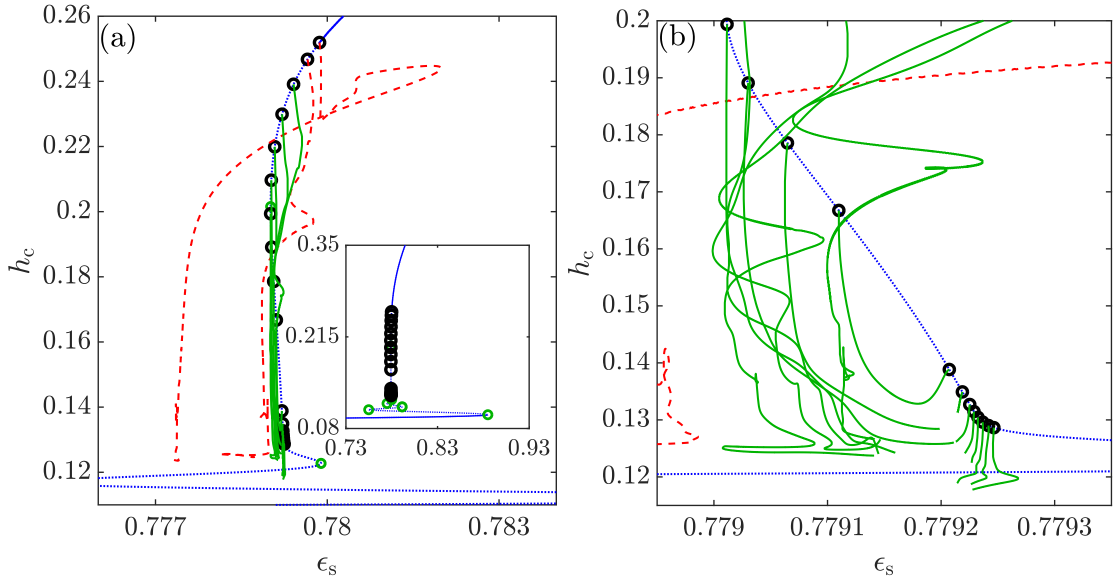

FIGURE 5.27: *Bifurcation diagrams showing the (time-averaged) coating thickness* h_c *versus the SAW strength* ϵ_s *at fixed Weber number* $\mathrm{We}_s = 2.0$ *in (a). The Hopf branches (TPS, green lines) connect two Hopf bifurcations (black circle). The two branches connecting a Hopf and a global homoclinic bifurcation are indicated by a dashed red line. The Hopf branch connecting the Hopf bifurcation from the Bogdanov-Takens bifurcation with another Hopf bifurcation is indicated by a dashed-dotted green line. Saddle-Node bifurcations are marked with green circles. Panel (a) shows the different TPS in the region where all the Hopf bifurcations occur and panel (b) gives a zoom of the region first Hopf bifurcations, where most complex structures of branches appear. The inset in (a) gives the relevant complete bifurcation curve for the steady states. Not all branches of TPS are fully tracked due to numerical limitations. The remaining parameters are* $h_m = 8.1$, $\mathrm{Ha} = 0.001$, $G = 0.001$, $h_p = 0.1$, $\alpha = 0.2$, $U_0 = 0$ *and* $L = 40$.

as solution measure, which allows for a convenient comparison of results obtained by path continuation and time simulations. The L^2-norm is calculated with

$$||h|| = \sqrt{\int_L \left[h^2\right] \mathrm{d}x}\,. \tag{5.3}$$

Note that here a small systematic mismatch between continuation and time simulation results is taken into account. It is caused by different underlying discretization schemes and a different way of implementing the boundary conditions at the meniscus, i.e. the different numerical method is employed with different meshes n_x. In PDE2PATH the mesh n_x is always constant and OOMPH-LIB uses an adaptive mesh so that n_x may change with the solution, which then leads to minor differences when comparing the TPS.

Fig. 5.28 presents the relevant region of the branch of TPS (red line), which emerges from the branch of steads states (black line). It shows that the branch of TPS bifurcates supercritically, and folds back shortly thereafter undergoing another Saddle-Node bifurcation at $\epsilon_s \approx 0.7804$. Along this red branch, four states of TPS are marked by blue points (**I-IV**) and are presented in Fig. 5.29 as space-time plots obtained from the path continuation. The black circles, red triangles and green squares in Fig. 5.28 are obtained by time simulations. These points are employed by a primitive continuation method, namely time simulations starting at various initial states obtained either by path continuation or previous time simulations at

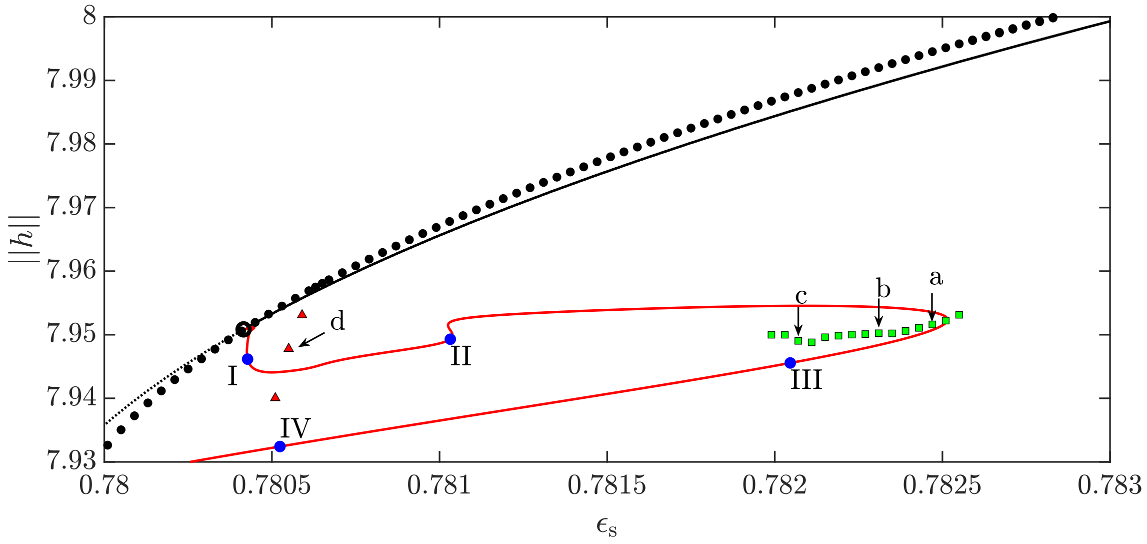

FIGURE 5.28: *Magnification of the bifurcation diagram showing the (time-averaged) L^2-norm as a function of the SAW strength ϵ_s at the fixed Weber number $\mathrm{We_s} = 2.0$ in the region where the last (18th) Hopf bifurcation occurs. The full bifurcation diagram can be found in Fig. 5.27. The blue circles (**I-IV**) are time-periodic states obtained by continuation and shown in Fig. 5.29. The black circles represent states of Landau-Levich film solutions, the red triangle are quasi-chaotic states and the green squares are true time-periodic states obtained by a primitive continuation method. The points indicated with "a" to "d" are presented in space-time plots in Fig. 5.30. The remaining parameters are $h_\mathrm{m} = 8.1$, $\mathrm{Ha} = 0.001$, $G = 0.001$, $h_\mathrm{p} = 0.1$, $\alpha = 0.2$, $U_0 = 0$, $n_x = 300$ and $L = 40$.*

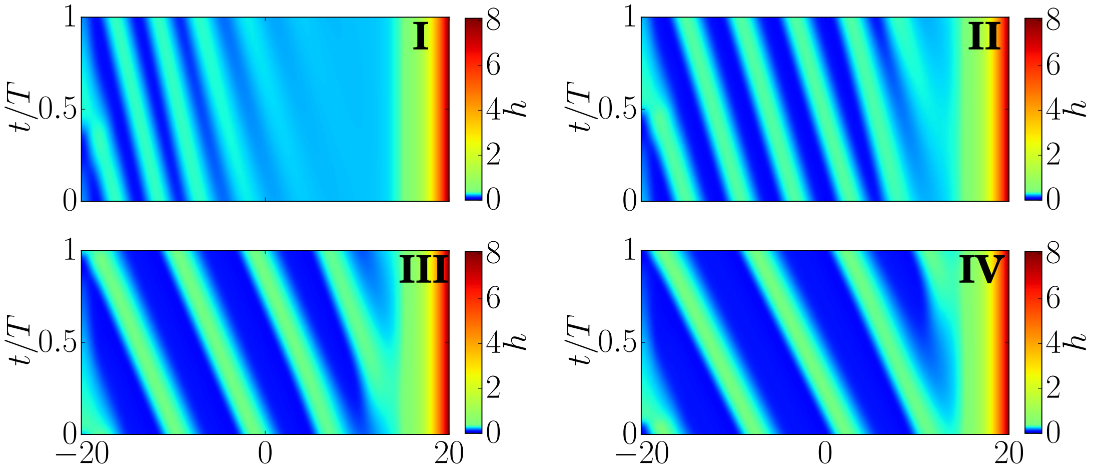

FIGURE 5.29: *Space-time plots (**I-IV**) showing TPS obtained by path continuation in Fig. 5.28. Here, the time period T for each panel is **I**: $T = 1238$, **II**: $T = 1407$, **III**: $T = 1747$ and **IV**: $T = 2030$.*

neighboring parameter values. After the transients have settled, the obtained states are indicated by different symbols in Fig. 5.28. The symbols are representing Landau-Levich states (black circles), regular TPS (green squares) and irregular TPS that are seemingly chaotic (red triangles). Selected TPS indicated by arrows are shown in Fig. 5.30. Note that the black points nearly coincide with the branch of steady states. This method does not allow to track unstable states and therefore information of unstable steady states and bifurcations are missed. However, it allows to compare the results obtained by path continuation with the ones obtained by time simulations.

In the four presented time-periodic states in Fig. 5.29 **I-IV**, the drops are shed regularly from the foot-structure and then move at about constant speed along the substrate until they reach the boundary at $L = -x/2$. At the boundary, the drops get slightly deformed due to Neumann boundary conditions. However, this does not influence the main course of their trajectory. Moving along the branch of TPS, the number of drops in the domain becomes smaller as the shedding events become less frequent, i.e. the period T becomes longer. The foot-like structure formed by the emerged drops does not change along the branch. The difference between the various branches of TPS here mainly lies in the details of the length of the foot-structures and the number of visible undulations.

The obtained states by path continuation are confirmed with time simulations to determine the corresponding stability. The results of the time simulations in Fig. 5.28 are given by black circles, red triangles and green squares. In particular, they correspond to three different categories: (i) black circles are Landau-Levich film states, (ii) red triangles correspond to a chaotic behaviour and (iii) green square are states of truly periodic behaviour. Selected states "a" to "d" are presented as space-time plots in Fig. 5.30.

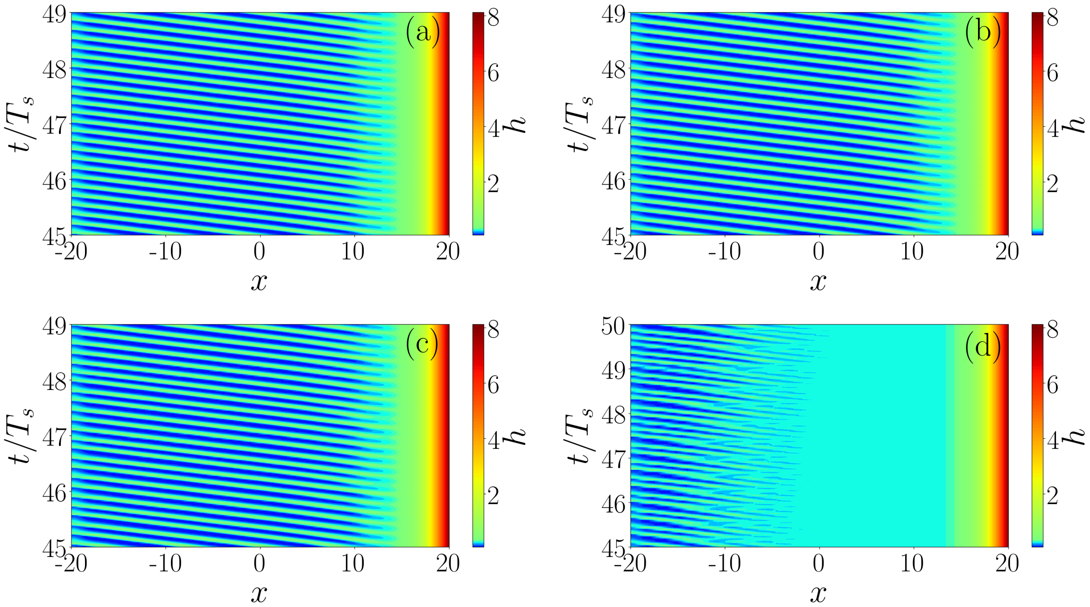

FIGURE 5.30: *Space-time plots of time simulations starting with TPS "a" to "d" in Fig. 5.28, respectively. They are at (a) $\epsilon_s = 0.78247$, (b) $\epsilon_s = 0.78231$, (c) $\epsilon_s = 0.78207$ and (d) $\epsilon_s = 0.78055$. The time is scaled with $T_s = 10^4$. These states present periodic or chaotic behaviour as illustrated in the phase-plane plots (a) - (c) and the return map (d) in Fig. 5.31.*

In Fig. 5.30 (a), (b) and (c) show very similar patterns, where a train of regularly spaced drops is shed from the foot-structure in front of the meniscus, whereas in panel (d) a more irregular pattern is shown. To determine the stability of these states, phase-planes plots and a return map for (d) are employed [64, 121]. The phase-planes are generated by plotting the time derivative of the L^2-norm $\mathrm{d}_t||h||$ versus the L^2-norm $||h||$, whereas the return is map uses max $||h_{i+1}||$ versus max $||h_i||$. This allows one to accurately identify the corresponding trajectory, which is used to confirm the stability of the TPS.

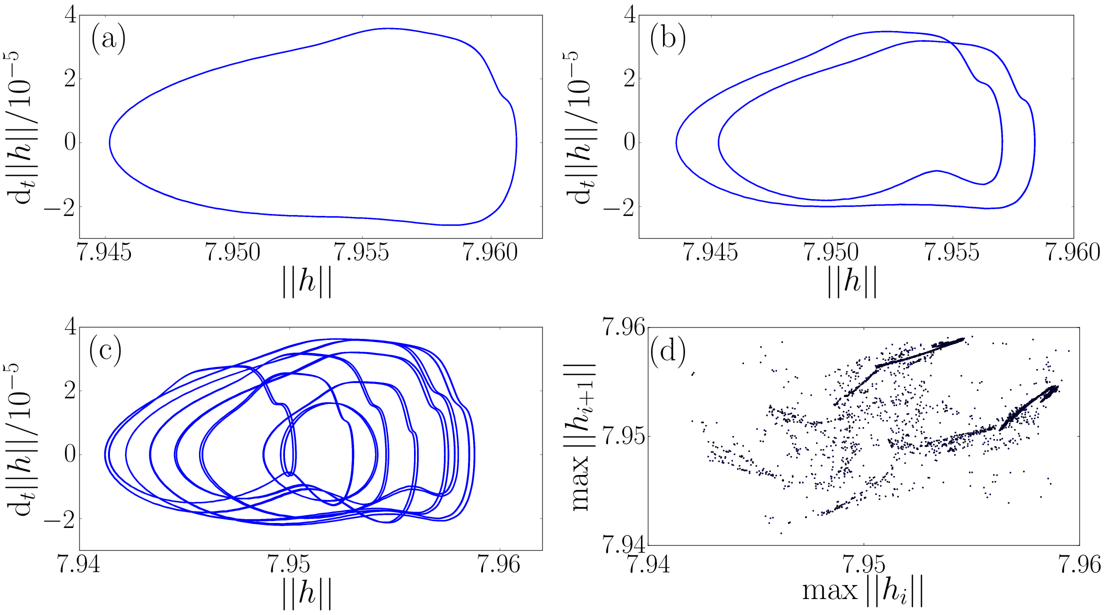

Figure 5.31: *Phase-plane plots in (a), (b) and (c) showing the time derivative of the L^2-norm ($\mathrm{d}_t||h||$) versus the L^2-norm ($||h||$) along the attractor for the TPS obtained in Figs. 5.28 and 5.30. The trajectories are on a closed orbit, (a) has one-loop, (b) has two loops and (c) has multiple loops. In (d) a return map is shown, where the max $||h_{i+1}||$ is plotted versus the max $||h_i||$ for the corresponding trajectory. Here, a chaotic behaviour is given.*

In Fig. 5.31 panel (a) shows a trajectory corresponding to a one-loop closed orbit (point ”a“ from Fig. 5.28). It shows that this TPS is stable and contains one period. Then, continuing from right to left, green squares in Fig. 5.28, panels (b) and (c) of Fig. 5.30 are obtained. The corresponding phase-plane plots are given in Fig. 5.31 (b) and (c). Here, both trajectories again correspond to closed orbits, however, (b) consists of two loops, i.e. a period-doubling must have taken place. The third panel (c) shows a trajectory, which contains multiple loops. The results of path continuation in Fig. 5.28 and space-time plots in Fig. 5.30 hide the facts of period-doubling. This explains that only the green squares close to ”a“ in Fig. 5.28 closely coincide with the continuation results while bend-like deviations occur when going to ”b“, and again before ”c“. It corresponds to steps of a period-doubling cascades, which may explain why most TPS obtained by continuation are unstable. Therefore, all TPS along the green squares are interpreted as states of truly periodic behaviour.

In Fig. 5.31 (d), a return map is extracted from time series of the norms at each maximum $||h_{i+1}||$ in the series and plotted over the previous maximum $||h_i||$. Note that this can not be well represented in the ($\mathrm{d}_t||h||$,$||h||$)-plane as density fills it. The resulting cloud of points in Fig. 5.31 (d) indicates that the the ridges shedding is chaotic as it resembles a strange attractor. This applies to all states marked by the red triangles. They can not be discerned by the pseudo-arclength path continuation and it shows further that multi-stability of chaotic shedding and stable Landau-Levich film deposition exists. This is further supported by the fact that in the simulations resulting in the black dots in Fig. 5.28 sometimes intermittent bursts of chaotic shedding are observed close to the downstream boundary (not shown).

In summary, the detailed bifurcation study of a SAW-driven thin-film model reveals that several features occur. First, a global homoclinic and a Hopf bifurcation emerge from Bodganov-Takens bifurcation, which leads to an odd number of Hopf bifurcations encountered in bifurcation diagrams. Thereby, branches of TPS emerge at Hopf bifurcations, and many reconnections of those branches related to the emerged Hopf bifurcations from Bodganov-Takens bifurcations appear. Furthermore, the SAW-driving shows that states of truly periodic behaviour occur. The stability of theses states are confirmed with time simulations and furthermore, both continuation methods of path continuation and primitive continuation are in agreement. Hereby, multi-stability of different states, Landau-Levich solutions, meniscus states, time-periodic states and chaotic shedding are revealed. In the next section, the corresponding model of a SAW-driven meniscus is considered for volatile liquids.

5.3 Influence of evaporation

This section focuses on the behaviour of volatile liquid thin films for SAW-driving. The investigation results in a different behaviour of steady states leading to a change in bifurcation diagrams. The case for volatile thin film is described by Eq. (3.62) with scaling (3.49). Hereby, the term j_{evap} is introduced to account for the evaporation or condensation flux.

For the investigation a bifurcation study is performed using the numerical methods described in previous sections. In particular, the bifurcation diagrams and occurring steady states are determined and compared to the ones obtained for the latter case of non-volatile liquids. The solution measure is the excess volume V_{ex} and the SAW strength ϵ_{s} remains as a main control parameter. In the following, the computed bifurcation diagrams of volatile liquids (evaporation rate $\beta_{\mathrm{s}} > 0$) and non-volatile liquids ($\beta_{\mathrm{s}} = 0$) are compared.

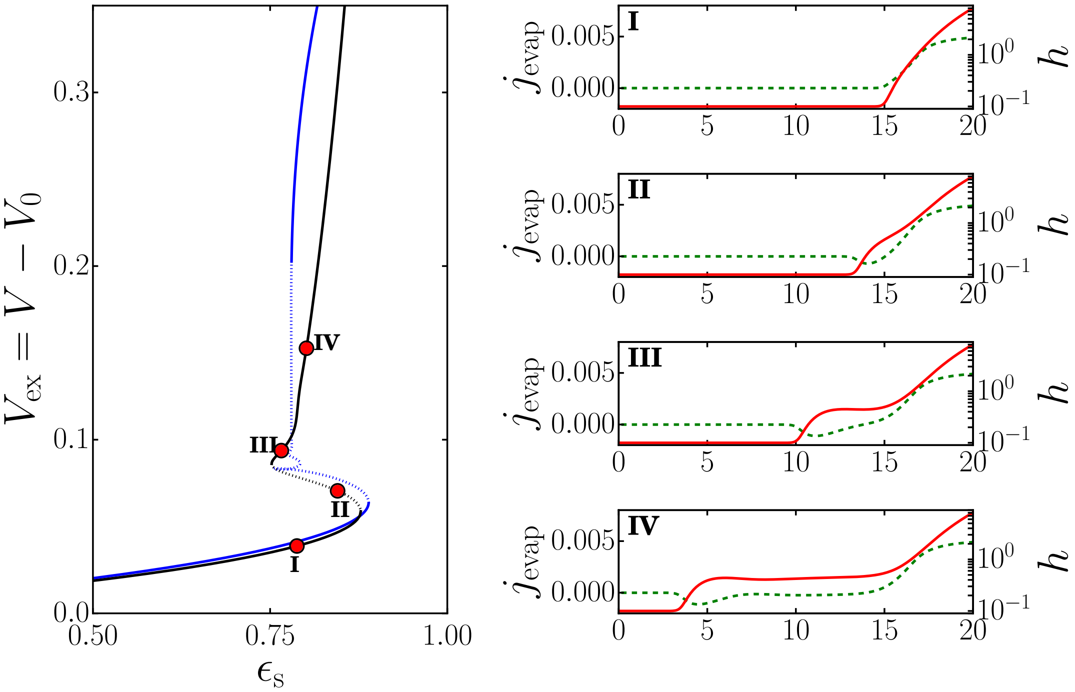

FIGURE 5.32: *On the left panel a bifurcation diagram showing two cases: a non-volatile (solid blue line) and a volatile liquid (solid black line) driven by SAW. The measurement is the excess volume V_{ex} in dependence of the SAW strength ϵ_{s}. Linearly stable and unstable states are indicated by solid and dashed lines, respectively. The red points (**I-IV**) indicate the loci of selected steady state profiles. There, the film height h is scaled logarithmically and only half of the domain $\Omega_{\mathrm{half}} = [0, L/2]$ is presented. The corresponding non-conserved flux $j_{\mathrm{evap}}(x)$ is plotted as a dashed green line in the panels of the steady states (**I-IV**). The remaining parameters are $h_m = 8.1$, $\mathrm{We_s} = 2.0$, $\mathrm{Ha} = 0.001$, $G = 0.001$, $h_{\mathrm{p}} = 0.1$, $\alpha = 0.2$, $U_0 = 0$, $\beta_{\mathrm{s}} = 0.01$, $\mu_{\mathrm{s}} = 0.01$ and $L = 40$.*

In Fig. 5.32 two cases, one for a volatile (black line) liquid and one for non-volatile liquid (blue line), are shown. The non-volatile case is already discussed in previous Sec. 5.2. In the volatile case, the bifurcation curve loses nearly all bifurcations and only two Saddle-Node bifurcations remain. At the first Saddle-Node bifurcation, the steady states of volatile liquid become unstable and then stable at the second Saddle-Node bifurcation. Here, no Hopf bifurcations are encountered. The flux describing the evaporation seems to prevent the signature structures of the SAW-driven bifurcation curve. As a result, the two sequences of Hopf bifurcations and the exponential snaking are not developed compared to the non-volatile case. Taking a look at the steady state profiles along the branch, one notices that the strongly modulated foot-solutions do not exist. Only foot-solutions, where no modulations appear, are identified. Along the steady states presented in **I** up to **IV**, the foot-solution increases in length. The flux j_{evap} corresponding to the steady state profiles is plotted in Fig. 5.32. It indicates the rate of evaporation and condensation at any position along the profile. At the precursor film height h_{p} the flux j_{evap} vanishes and at the meniscus it shows that $j_{\mathrm{evap}} > 0$ (evaporation). However, along the full length of the foot the flux becomes negative (condensation), giving the foot-solution its structure. The obtained steady states are very similar to non-volatile liquids in the dragged-case shown in Fig. 5.3. In contrast, the bifurcation curve in Fig. 5.32 does not contain any snaking behaviour. The dynamical transition behaviour is classified as a discontinuous dynamic emptying transition. The behaviour of the stable branch for higher values of the SAW strength ϵ_{s} has a power law of $V_{\mathrm{ex}} \propto \epsilon_{\mathrm{s}}^{2/3}$ and is in agreement with the classical Landau-Levich system.

The influence of evaporation rate β_{s} and chemical potential μ_{s} for the volatile liquid are further explored in Fig. 5.33. The first bifurcation diagram (a) shows the case of an evaporation rate $\beta_{\mathrm{s}} = 0.1$, which is higher than in Fig. 5.32 while keeping the chemical potential μ_{s} constant. In the second bifurcation diagram (b) the evaporation rate remains unchanged and only the chemical potential is increased to $\mu_{\mathrm{s}} = 0.05$. All other parameters remain the same.

In the first case, [Fig. 5.33 (a)] the bifurcation curve is qualitatively similar to Fig. 5.32, but at the beginning of the curve, the excess volume increases faster with increasing SAW strength ϵ_{s}. This leads to a higher value of excess volume V_{ex} until the first Saddle-Node bifurcation. Therefore, the thin film problem needs less SAW strength ϵ_{s} for the same amount of excess volume V_{ex}. Again, this bifurcation only contains two Saddle-Node bifurcations.

In contrast, the other bifurcation diagram in Fig. 5.33 (b) shows the appearance of a single Hopf bifurcation beyond the second Saddle-Node bifurcation. The results show that both Saddle-Node bifurcations act destabilising. The steady states along the curve remain unstable even after the second Saddle-Node bifurcation. However, the determined Hopf bifurcation acts stabilising, so that the steady states become stable. As a side note, the power law is identical as discussed the latter case.

Comparing the bifurcation curve in Fig. 5.33 (b) to one of the dragged-case, one observes a similar appearance of the bifurcation curve. In particular, at first sight it looks identical to the bifurcation diagram obtained at angle $\alpha = 3$, see Fig. 5.4 (a). However, the steady states of this volatile case correspond qualitatively to another case at angle $\alpha = 1$, see Fig. 5.3.

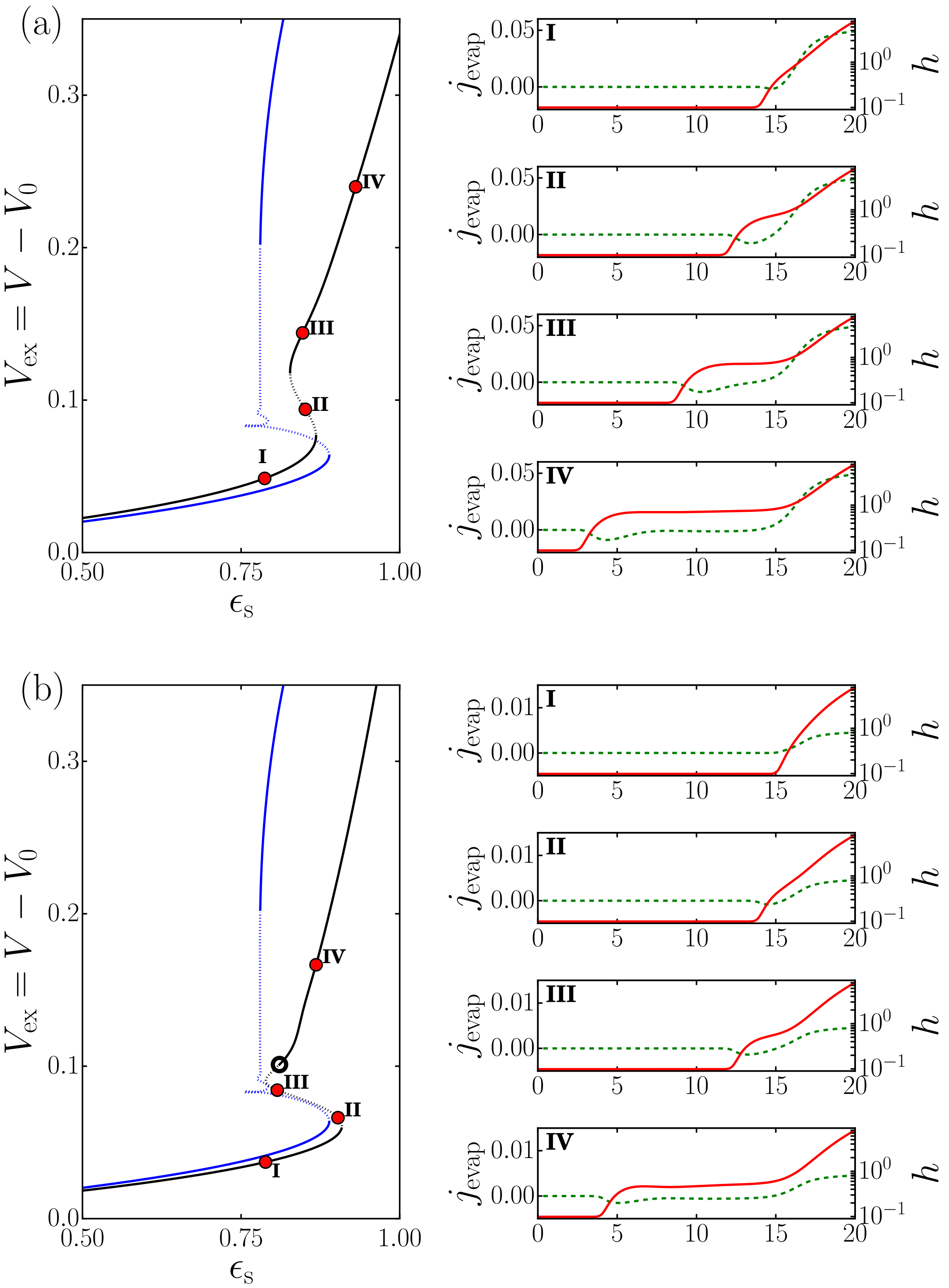

FIGURE 5.33: *On the left panels bifurcation diagrams showing two cases: a non-volatile (solid blue line) and a volatile liquid (solid black line) driven by SAW. Both measurements are the excess volume* $V_{\rm ex}$ *in dependence of the SAW strength* $\epsilon_{\rm s}$*. Linearly stable and unstable states are indicated by solid and dashed lines, respectively. The red points (**I-IV**) in each bifurcation diagram (a) and (b) indicate loci of selected steady state profiles. There, the film height* h *is scaled logarithmically and only half of the domain* $\Omega_{\rm half} = [0, L/2]$ *is presented. The corresponding non-conserved flux* $j_{\rm evap}(x)$ *is plotted as a dashed green line in the panels of the steady states (**I-IV**). The black circle represents a Hopf bifurcation, which is only shown for the volatile liquid case. In panel (a) the parameters are* $\beta_{\rm s} = 0.1$ *and* $\mu_{\rm s} = 0.01$ *and in panel (b) they are* $\beta_{\rm s} = 0.01$ *and* $\mu_{\rm s} = 0.05$*. The remaining parameters are* $h_m = 8.1$, $\mathrm{We}_{\rm s} = 2.0$, $\mathrm{Ha} = 0.001$, $G = 0.001$, $h_{\rm p} = 0.1$, $\alpha = 0.2$, $U_0 = 0$ *and* $L = 40$*.*

The presented results show that volatile liquids driven by SAW have a very similar behaviour as to the ones obtained for the classical Landau-Levich system for non-volatile liquids. The characteristics found in the case of a SAW-driven meniscus for non-volatile liquids are completely suppressed by the non-conserved flux j_{evap}. Consequently, very few bifurcations are determined. The investigation of a SAW-driven meniscus for volatile liquids revealed only one Hopf bifurcation at $\mu_{\mathrm{s}} = 0.05$, see Fig. 5.33 (b). In all cases, there are always two Saddle-Node bifurcations. The steady state profiles show that a foot-solution without modulations emerges from the bath. The determined transitions of all results are discontinuous dynamic emptying transitions. Next, the corresponding model of a (non-volatile) SAW-driven meniscus is investigated in two-dimensions.

5.4 Meniscus states in 2D

In this section, the study focuses on the 2D SAW-driven meniscus. This requires an expansion of the thin-film evolution Eq. (3.50) into the y-direction. Therefore, the domain is extended to $\Omega = L_x \times L_y$ with $L_x = 40$ and $L_y = 30$. Again, the SAW propagates towards the negative x-direction, and the inclination of the solid substrate is also in the x-direction, see Eq. (3.50).

The investigation will only cover non-volatile liquids and the computed bifurcation curves in 2D are compared to the 1D case. In the 2D system, additional boundary conditions in the lateral direction have to be set. Here, Neumann boundary conditions are used for both sides, yielding

$$\partial_y h = \partial_{yyy} h = 0 \quad \text{at} \quad y = \pm \frac{L_y}{2}\,. \tag{5.4}$$

These boundary conditions guarantee that the 2D steady states are nearly unaffected by boundaries at $y = \pm L_y/2$, i.e. that the computed domain shows part of a laterally periodic structure. For the 2D case, the solutions are characterised by their L^2-norm, which is a typical solution measure when comparing 1D and 2D results. The L^2-norm is calculated with respect to the domain Ω and is defined as

$$||h|| = \frac{1}{L_y}\sqrt{\int_\Omega \left[h^2\right] \mathrm{d}\vec{r}}. \tag{5.5}$$

The resulting bifurcation diagrams for both cases are presented in Fig. 5.34 (a).

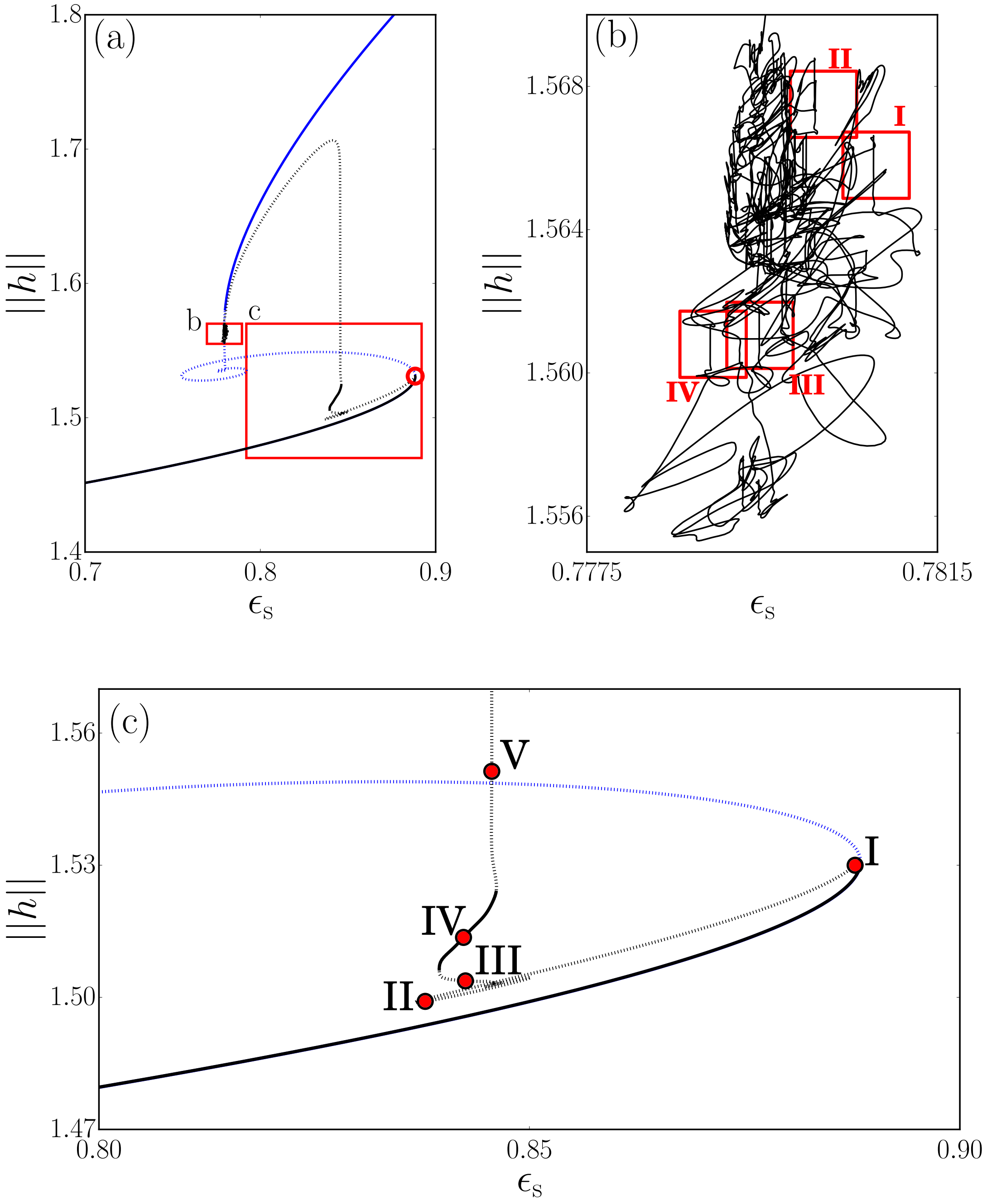

FIGURE 5.34: *Three bifurcation diagrams showing a 1D (blue line) and a 2D (black line) thin film driven by SAW. In panel (a) two bifurcation diagrams for a 1D and a 2D thin film driven by SAW are shown. In both cases the line styles indicates stability, where a solid line represents stable and a dotted line represents unstable states. A Pitchfork bifurcation (red circle) is detected, where the 2D solutions undergo a symmetry break and diverges from the 1D curve. Two (red) frames "b" and "c" are presented in panel (b) and (c). In panel (b) additional four (red coloured) frames (**I-IV**) highlight regions, where exponential snaking structures occur as known from the 1D case, see Fig. 5.36. Panel (c) magnifies the part of the bifurcation diagram, where the Pitchfork bifurcation appears. In addition, the region where the branch gets stable after the first snaking region is shown for the 2D case. The red points **I-V** are selected steady state profiles and are shown in Fig. 5.35. The remaining parameters are* $h_m = 8.1$, $\mathrm{We_s} = 2.0$, $\mathrm{Ha} = 0.001$, $G = 0.001$, $h_\mathrm{p} = 0.1$, $\alpha = 0.2$, $U_0 = 0$, $L_x = 40$ *and* $L_y = 30$.

In Fig. 5.34 the results for the 2D case are identical with the 1D curve for small ϵ_s. The occurring solutions are invariant with respect to translation in y-direction.

Following the bifurcation curve in the 2D case, closely after the first Saddle-Node bifurcation a Pitchfork bifurcation (red circle) occurs. This region is magnified in panel (c). There, a branch of states with broken y-translation symmetry emerges. The branch continues towards smaller ϵ_s and shows a small region of exponential snaking, similar to the 1D case. Remember that due to the different measures the exponential snaking takes a different form than the solution measure excess volume. The steady states on this part of the 2D curve are all unstable. However, after the first snaking segment two Saddle-Node bifurcations occur, so that the branch becomes stable. Then, after the next Saddle-Node bifurcation along the bifurcation curve, the branch becomes unstable again. The entire branch stays unstable along the tracked bifurcation curve. Note that in the present result of the 2D SAW-driven meniscus, the computed bifurcation curve does not include all determined bifurcations, i.e. Saddle-Node and Hopf bifurcations. Most of the bifurcations appear in the clustered region shown in Fig. 5.34 (b).

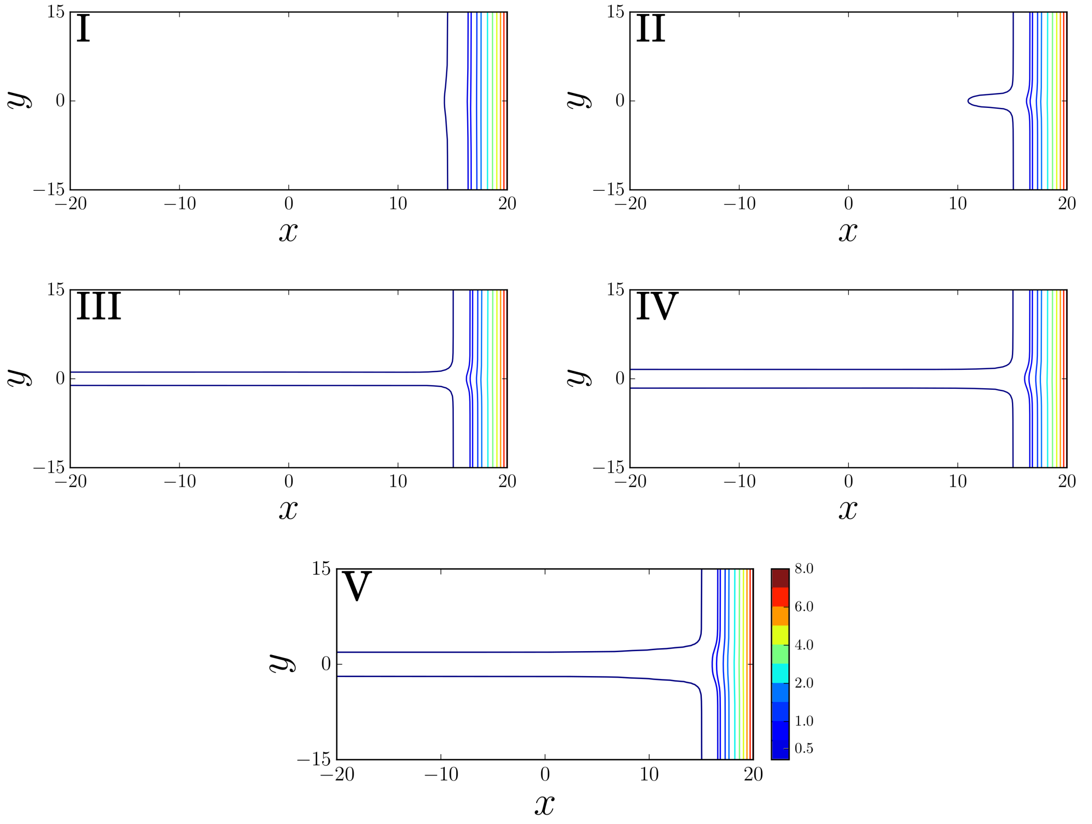

Figure 5.35: *Contour plots* ***I-V*** *showing selected steady state profiles for the 2D SAW-driven meniscus from Fig. 5.34 (c) after the Pitchfork bifurcation appears. All presented steady states are unstable with exception of the steady state at point* ***IV****. The colourbar for all states is presesnted in panel* ***V****.*

Taking a closer look at the corresponding steady states in the snaking region, one notices that a central finger structure is prolonged until it reaches the boundary at $x = -L_x/2$, see Fig. 5.35 **I** to **III**. Fig. 5.35 **I** shows that the y-translation symmetry is already broken and a small finger starts to emerge at the center of the meniscus. Following the curve further between states in **II** and **III**, a sequence of

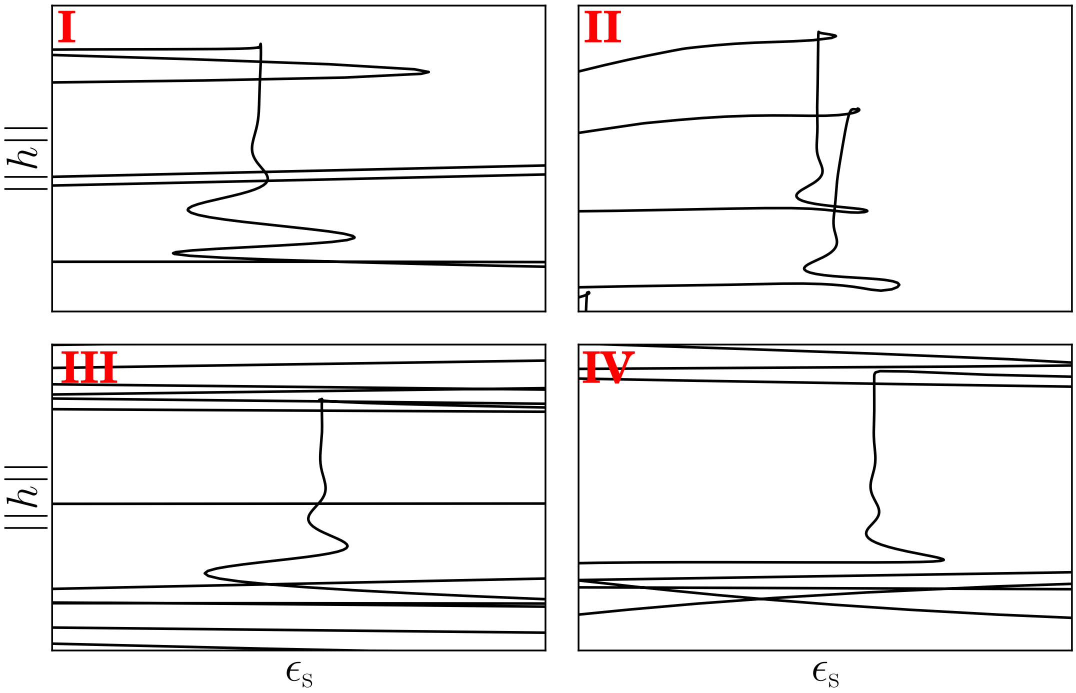

Figure 5.36: *Four regions are highlighted by red frames in Fig. 5.34 (b). They are magnified showing in particular examples of repeating exponential snaking structures. In each panel **I**, **III** and **IV** one structure of exponential snaking is presented and in **II** two structures of exponential snaking are given.*

Hopf bifurcations appears (not shown). Subsequently, the finger length increases until it reaches the boundary at $x = -L_x/2$. Then, two Saddle-Node bifurcations are detected. At the first of these Saddle-Node bifurcations, the branch folds back towards larger ϵ_s and becomes stable. Inspecting the steady state profile **IV**, the rivulet that is shown in **III** has slightly widened. The difference between both profiles are the increasing width of the central finger structure (rivulet) and the stability. At the next Saddle-Node bifurcation, the branch becomes again unstable. The profile in Fig. 5.35 **V** indicates that the central finger broadens. The broadening takes place at the transition of finger and meniscus, and then further along the rivulet.
Then, the bifurcation curve in Fig. 5.34 follows a large excursion and turns back towards the branch of 1D states. Here, the curve starts to become wildly criss-crossed and forms an extremely dense cluster of many subbranches, see magnification in Fig. 5.34 (b). Additional magnifications are presented in Fig. 5.36. Note that all detected steady states in this dense cluster are unstable. The process was manually ended as the 2D branch did not reconnect to the 1D branch after a long continuation time (many weeks). In Fig. 5.36 several repeating structures are highlighted. They consist of a few Saddle-Node bifurcations ending in a short vertical lines. These regular structures commonly appear in the criss-cross region. They resemble exponential snaking [80, 116, 132] as already discussed for the 1D SAW-driven thin-film system. In Fig. 5.37 selected steady states along the branch of 2D states are presented.

Similarly, while following the branch from the beginning of transversally invariant steady states, i.e. see Fig. 5.37 panel (1.1). Soon after the first Saddle-Node bifur-

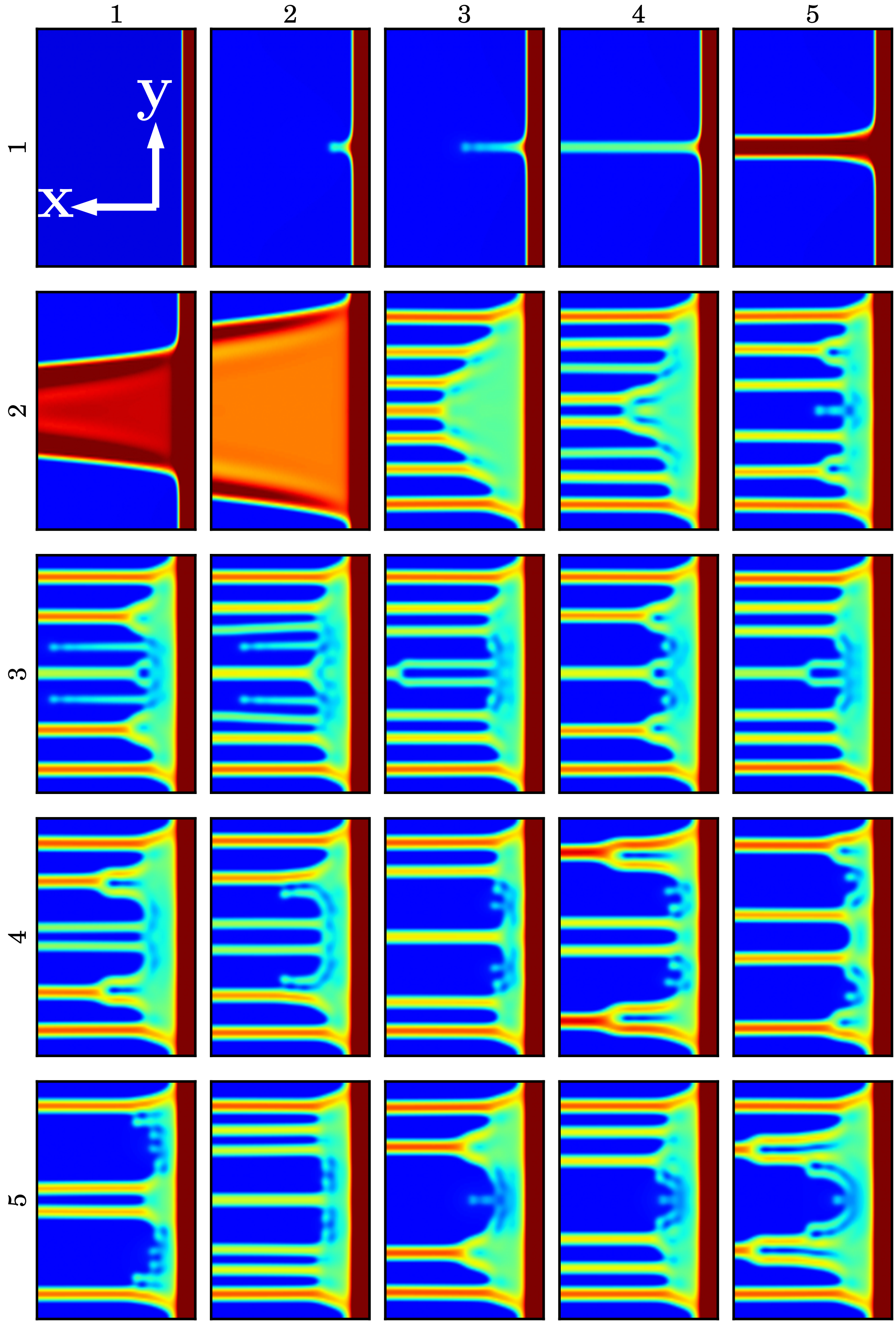

FIGURE 5.37: *Selected film height profiles are presented from the 2D bifurcation curve in Fig. 5.34. The corresponding colour bar is shown in Fig. 5.38. From the top left corner panel (1.1) to the bottom right corner panel (5.5) steady states are shown beginning with small* ϵ_s *following the transversally invariant states. Here, only panel (1.1) is stable. For visibility the y-domain is stretched by a factor of* 2.4 *as compared to the x-axis.*

cation appears, a Pitchfork bifurcation is detected. Then, the branch switches to another branch where only invariant steady states occur, see Fig. 5.37 panel (1.2). Here, ϵ_s decreases and a very short centered finger emerges from the meniscus. This finger becomes longer and finally meets the boundary at $x = -L/2$, see Fig. 5.37 (1.2) to (1.4). Between the panels (1.4) and (1.5), the only stable steady states are determined. Following the branch beyond this point, it continues in a rather long and nearly vertical part. Along this part, the finger structures widen as the L^2-norm $||h||$ increases and the branch remains unstable.
The finger structure further widens and nearly fills the entire domain, so that the steady state is similar to a stretched pyramid. In parallel, the pyramid-like structure flattens and consists of a broad plateau with higher rims at its lateral edges. Hereby, the curve rises nearly vertical up to $||h|| \approx 1.7$, while the pyramid structure is widened, see Fig. 5.34, and then it bends over and decreases to smaller norm values and smaller ϵ_s.
Subsequently, while the L^2-norm starts to drastically decrease, the extended pyramid-like structure laterally decays into seven narrow fingers. The space between these fingers slightly increases from the center to the boundary, see panel (2.3). Then, the bifurcation curve enters the criss-cross region, see Fig. 5.34 (b). In this region the steady state profiles reveal a multiplicity of occurring states, for instance, one finger breaks into two smaller fingers, neighboring fingers start to coalesce. Long fingers get shorter and recede from the downstream boundary or get longer until they finally reach the boundary. In addition, fingers fuse with their neighboring fingers, resulting in a root-like structure in the transition region between meniscus and fingers [e.g. Fig. 5.37 panels (4.1) and (4.2)]. These different interactions of the fingers in the criss-cross region is named “dance of fingers” [79]. The number of fingers changes between three and nine. It is important to point out, that throughout the criss-cross region, certain bifurcation structures repeatedly appear as the magnified in the highlighted regions in Fig. 5.36.

In the following, the dance of fingers behaviour is further investigated: First, a new type of plot is introduced in order to obtain a more readily discernible result. Here, the solution measure is changed from the L^2-norm to the arclength s used in each continuation step. In addition to the plot of the arclength, an additional plot giving the height profile $h(y)$ at boundary at $x = -L_x/2$. This allows to determine the behaviour of fingers, which reach the boundary. This leads to a more transparent visualisation presented in Fig. 5.38. This helps to investigate the changes in the criss-cross region of the bifurcation curve. The behaviour of the steady state profiles where the dance of the fingers occurs, become more transparent.

These arclength plots are shown in Fig. 5.38 and reveal several features. After the pyramid-like structure decays into seven fingers at arclength $s \approx 0.5$, only the two outermost fingers always remain. The location of these fingers is nearly unchanged.

At $s \approx 2.65$, another pair of coexisting fingers fuses with the outermost fingers.

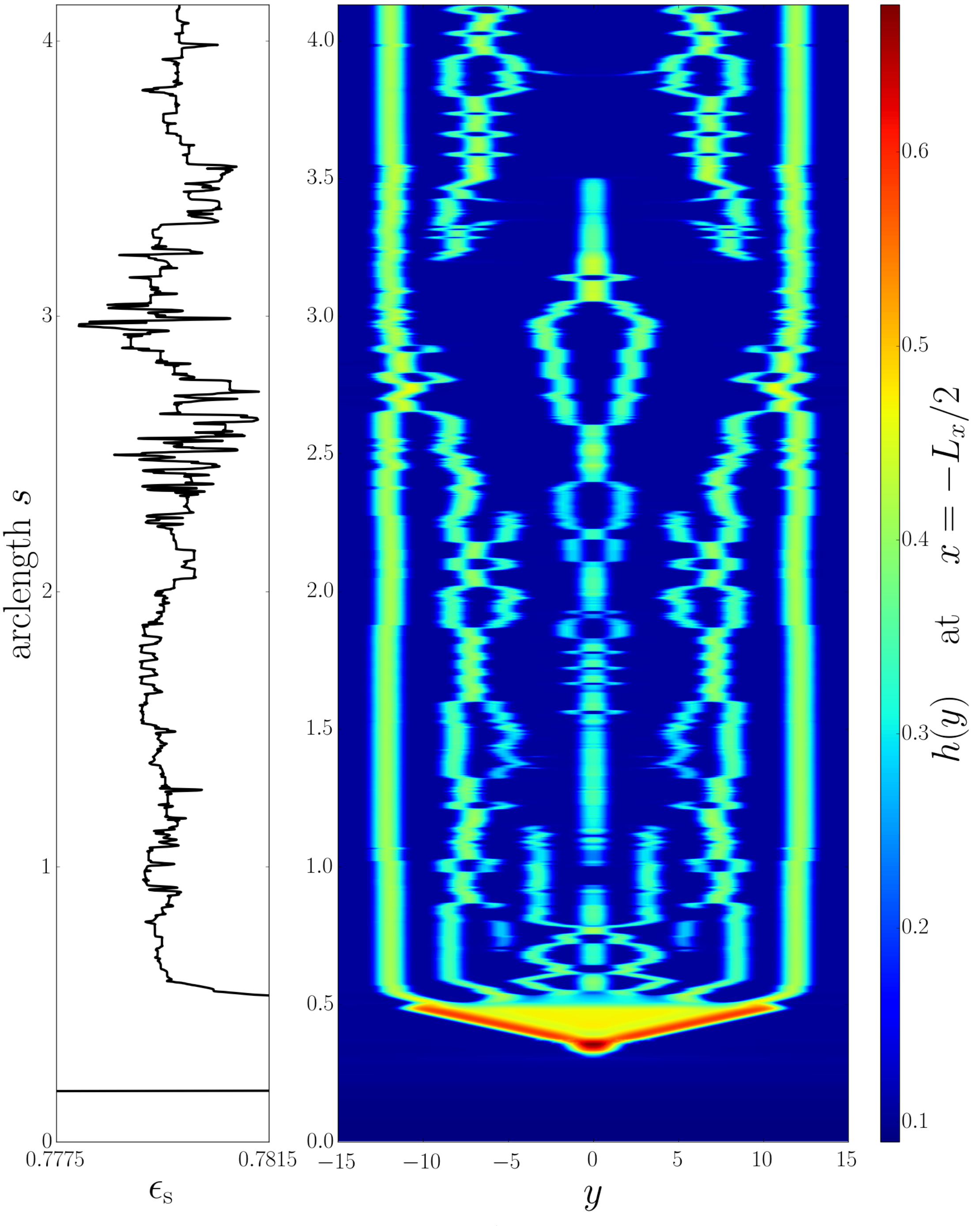

Figure 5.38: *Space-arclength plots for a 2D SAW-driven meniscus showing the film height profile $h(x = -L_x/2, y)$ on the downstream boundary function of arclength s following the full bifurcation curve of 2D states shown in Fig. 5.34 (a). The left panel shows, as a reference, the arclength s versus the SAW strength ϵ_s and the right panel gives the corresponding film height profile at $h(x = -L_x/2, y)$.*

After these fingers fuse, the outermost fingers split-up and fuse again. At $s \approx 3.22$, the vanished fingers next to the outermost ones start to reappear. Here, a small number of splits and fusions occurs. The central finger splits into two fingers. These fingers exist until they fuse back into the central finger. In a short range of the arclength at $s \approx 0.9$ to $s \approx 1.0$ the central finger vanishes and then reappears. Events of splitting and fusing fingers occur until the fully centered finger vanishes again at arclength $s \approx 3.5$. In ranges of the arclength $1.7 \leq s \leq 1.9$ and $3.55 \leq s \leq 3.76$, repeating oscillations between five and six fingers occur.

The presented results of the 2D SAW-driven meniscus in a domain $\Omega = L_x \times L_y$ with $L_x = 40$ and $L_y = 30$ are very complex. To simplify the results, the lateral domain is reduced. The simplest case is found for a domain of $\Omega = L_x \times L_y$ with $L_x = 40$ and $L_y = 1$ and corresponds to an identical bifurcation curve as in the 1D case as all states remain transversally invariant.

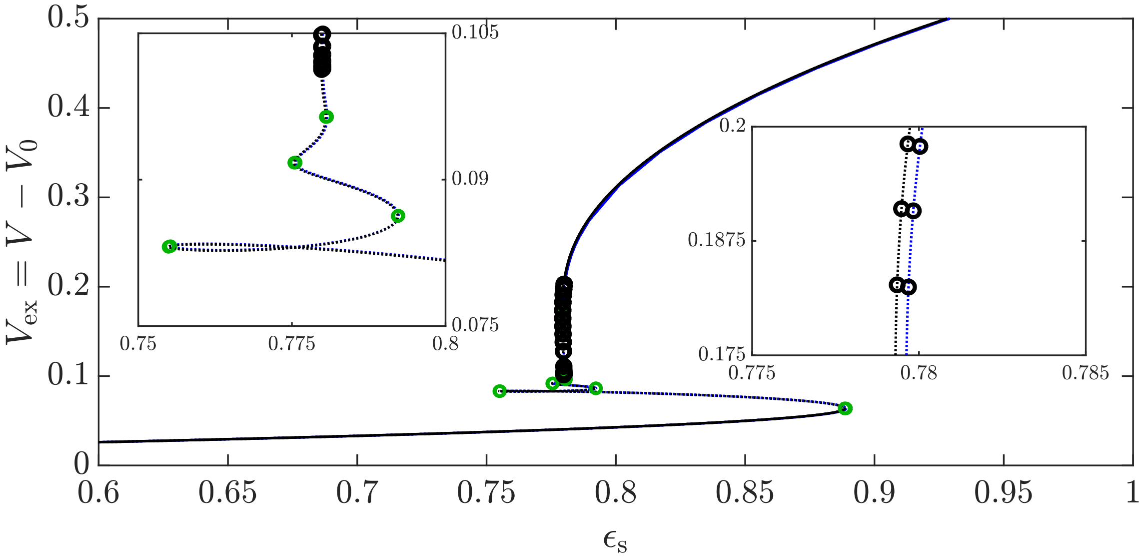

FIGURE 5.39: *Two bifurcation diagrams are presented for a SAW-driven meniscus in 1D (blue line) and 2D (black line), which shows the excess volume V_{ex} in dependence of the SAW strength ϵ_{s}. The domain of the 2D case is $\Omega = L_x \times L_y$ with $L_x = 40$ and $L_y = 1$, where the 1D case has $L_y = 0$. The different line styles correspond to the stability of the steady states, where the solid line indicates stable and the dotted line represents unstable steady states, respectively. Saddle-Node and Hopf bifurcations are highlighted with green and black circles. The two insets magnify regions, where bifurcations undergo snaking and a sequence of Hopf bifurcations appears. Both bifurcation curves are transversally invariant. The remaining parameters are $h_m = 8.1$, $\text{We}_{\text{s}} = 2.0$, $\text{Ha} = 0.001$, $G = 0.001$, $h_{\text{p}} = 0.1$, $\alpha = 0.2$, $U_0 = 0$, $L_x = 40$ and $L_y = 1$.*

In Fig. 5.39 two magnifications show that the curves are slightly shifted to the right. This small qualitative difference is due to the different numerical approaches in 1D and 2D and has no further effect on the curve. In particular, both bifurcation curves have the same number of Saddle-Node and Hopf bifurcations at nearly identical positions along the curve.
Next, the domain is slightly increased to $L_y = 2$, while keeping all other parameters at the same values. In addition, the solution measure is changed to the L^2-norm $||h||$ instead of the excess volume V_{ex}.

Fig. 5.40 shows that all states are transversally invariant until the third Saddle-Node bifurcation of the curve is approached. Here at $\epsilon_{\text{s}} \approx 0.792$, a Pitchfork bifurcation corresponding to a Saddle-Node bifurcation is detected. The symmetry of the 2D bifurcation breaks in y-translation at each Pitchfork bifurcations (red circles). Thereby, the curve bends towards decreasing SAW strength ϵ_{s} as a branch of states with broken

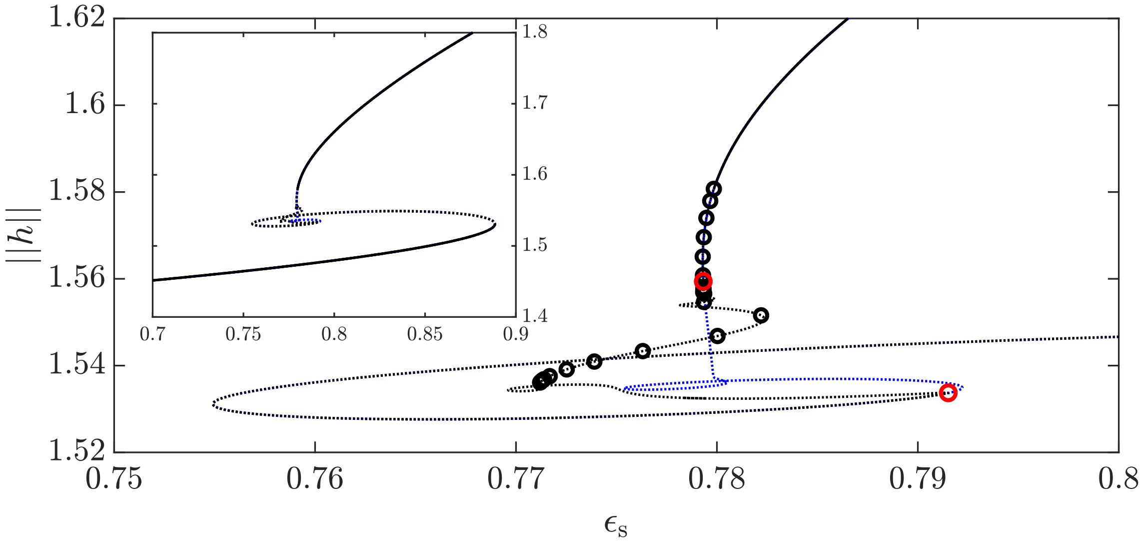

FIGURE 5.40: *Two bifurcation diagrams are presented for a SAW-driven meniscus in 1D (blue line) and 2D (black line), which shows the L^2-norm $||h||$ in dependence of the SAW strength ϵ_s. The domain of the 2D case is $\Omega = L_x \times L_y$ with $L_x = 40$ and $L_y = 2$. The different line styles correspond to the stability of the steady states, where the solid line indicates stable and the dotted line represents unstable steady states, respectively. Up to 26 Hopf bifurcations (black circles) are marked only on the 2D curve. Also, Pitchfork bifurcations (red circles) are shown. The inset shows the full bifurcation curves. In the main panel the region where the 2D solution breaks in the y-translation symmetry. The remaining parameters are* $h_m = 8.1$, $\mathrm{We_s} = 2.0$, $\mathrm{Ha} = 0.001$, $G = 0.001$, $h_\mathrm{p} = 0.1$, $\alpha = 0.2$, $U_0 = 0$, $L_x = 40$ *and* $L_y = 2$.

y-translation symmetry. Following this branch, three Saddle-Node bifurcations occur in form of a loop. Subsequently, a sequence of Hopf bifurcations appears while the SAW strength is increased. At $\epsilon_\mathrm{s} \approx 0.783$ the curve bends towards decreasing SAW strength at a Saddle-Node bifurcation and undergoes an exponential decreasing snaking. This snaking is around the nearly vertical 1D curve. At the second Pitchfork bifurcation (red circle) the 2D curve undergoes another transition in symmetry and gets invariant to the 1D case. After the transition, seven Hopf bifurcations are detected on the 2D branch. These seven Hopf bifurcations are qualitatively at the same position located as the last seven Hopf bifurcations of the 1D case. Finally the 2D curve becomes stable at the last Hopf bifurcation and follow the same power law as in the 1D case, namely $h_\mathrm{c} \propto \epsilon_\mathrm{s}^{2/3}$.

In Fig. 5.41, 50 selected steady state profiles are presented. At first, where the 2D case is transversally invariant with the 1D case, only meniscus states occur. Then, while the SAW strength increases the contact line of the meniscus advances. Here, only panels (1.1) to (1.4) present stable steady states. The states become unstable identical to the 1D case. The 2D case behaves similar as the 1D case, however in the steady state profile, in panel (4.5) of Fig. 5.41, the symmetry break occurs. At that moment the branch of 2D has already bypassed the Pitchfork bifurcation, where the curve diverges from 1D. Then, a finger structure increases in length and advances through the domain until it reaches the boundary at $x = -L_x/2$. This phenomenon is identical to the case with domain length of $L_y = 30$, where a centered finger advances along the x-direction. In contrast to case where the domain is larger in y-direction, the finger directly emerges before the third Saddle-Node bifurcation on the bifurcation

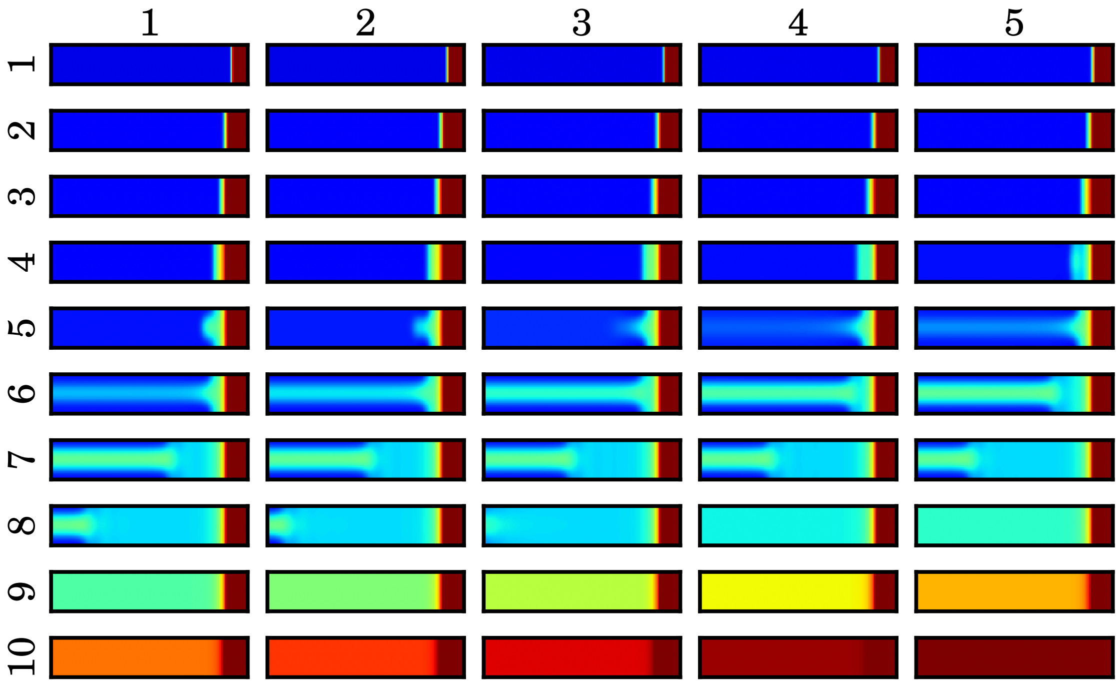

FIGURE 5.41: *Selected film height profiles in equidistant continuation points along the bifurcation of Fig. 5.40 are shown. The corresponding colour bar is given in Fig. 5.38. From the top left corner panel (1.1) to the bottom right corner panel (10.5) steady states are shown beginning with small ϵ_s following the transversally invariant states. The profiles (1.1) to (3.2) and (9.1) to (10.5) are stable steady states. For visibility the y-domain is stretched by a factor of four as compared to the x-axis.*

curve. In addition, the presented steady states of a finger structure remain unstable. Following the branch further, a uniform film advances in x-direction, until it reaches the boundary at $x = -L_x/2$. Subsequently, the finger structure vanishes and a Landau-Levich solution emerges, so that the full domain is covered by a thin film of coating thickness h_c. The coating thickness then further increases. When it reaches $h_c \approx 0.25$, see panel (8.1), the shown Landau-Levich film becomes stable as the last Hopf bifurcation is bypassed. Hereby, only stable states occur. Although the results for $L_y = 2$ has shown a single finger solution and two Pitchfork bifurcation and therefore, is more different than the simplest case for $L_y = 1$ presented in Fig. 5.39. The case for $L_y = 2$ resemebles more the features obtained in the case of $L_y = 30$. In the last part of this section, the lateral domain is increased once more to $L_y = 4$. In order to fit two finger structures into the domain.

Fig. 5.42 shows the resulting bifurcation curve and Fig. 5.43 shows 50 selected steady states along the 2D curve. The bifurcation curve has up to 86 Hopf bifurcations, but are not shown here. Comparing both the 1D and the 2D curve, at first the 2D curve is invariant to the 1D. Between the first and second Saddle-Node bifurcation of the 1D curve, the 2D curve diverges at a Pitchfork bifurcation at $\epsilon_s \approx 0.839$ (red circle). This Pitchfork bifurcation is similar to the case with the domain length $L_y = 30$, but it appears not directly after the first Saddle-Node bifurcation. Inspecting the steady states in Fig. 5.43 at that locus, it shows the symmetry breaks in Fig. 5.43 panel (1.5). Here, a central finger structure appears. At $\epsilon_s \approx 0.84$ the L^2-norm decreases. At the second occurring Saddle-Node bifurcation the L^2-norm increases again, followed by

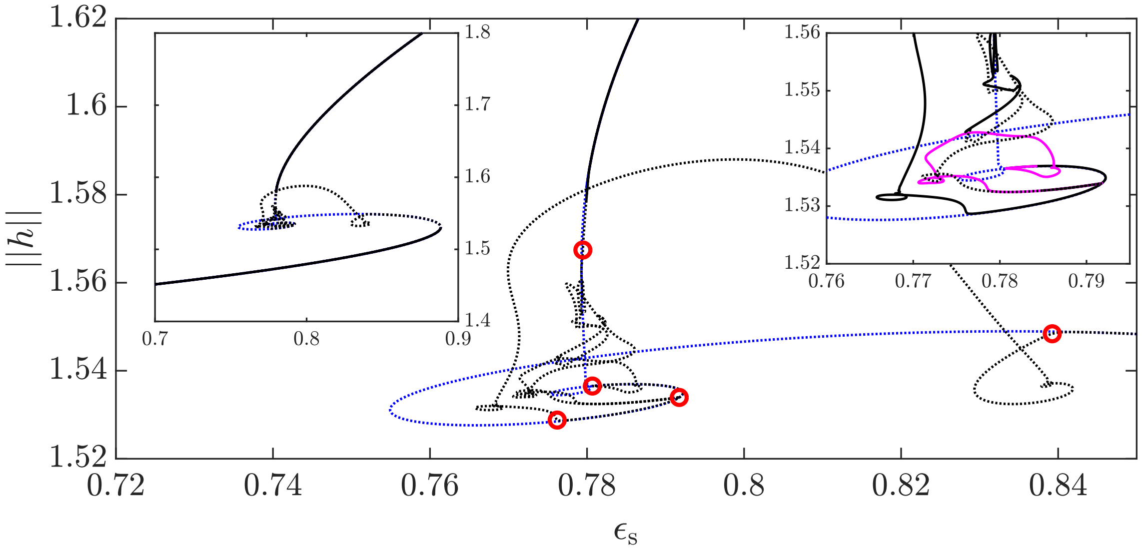

FIGURE 5.42: *Two bifurcation diagrams are presented for a SAW-driven meniscus in 1D (blue line) and 2D (black line), which shows the* L^2*-norm* $||h||$ *in dependence of the SAW strength* ϵ_s*. The domain of the 2D case is* $\Omega = L_x \times L_y$ *with* $L_x = 40$ *and* $L_y = 4$*. The different line styles correspond to the stability of the steady states, where the solid line indicates stable and the dotted line represents unstable steady states, respectively. Five Pitchfork bifurcations (red circles) are shown. Inset on the left shows the full bifurcation curves and the other inset magnifies the region where Pitchfork bifurcations occur. The colour schemes indicate the path of the curve and begins with solid black, magenta, dotted black and ends in solid back. These colour schemes do not correspond to stabilities on the branch, they are all unstable. A detail explaination is in the main text. The main panel magnifies the region where the 2D steady state breaks the y-translation symmetry. The remaining parameters are* $h_m = 8.1$*,* $\mathrm{We_s} = 2.0$*,* $\mathrm{Ha} = 0.001$*,* $G = 0.001$*,* $h_\mathrm{p} = 0.1$*,* $\alpha = 0.2$*,* $U_0 = 0$*,* $L_x = 40$ *and* $L_y = 2$*.*

sequences of Saddle-Node and Hopf bifurcations (not shown). In this region the 2D curve for $L_y = 4$ appears to be very similar as for $L_y = 30$ shown in Fig. 5.34 (c) and resembles the snaking region of the 1D case. While the SAW strength of the 2D curve decreases with increasing L^2-norm, the finger structure widens until the curve reaches a maximum in L^2-norm at $\epsilon_\mathrm{s} \approx 0.795$. Then, the L^2-norm decreases and the 2D curve bypasses the nearly vertical part of the 1D curve and the width of the finger decreases and no stable steady state of a finger structure occurs. At $\epsilon_\mathrm{s} \approx 0.771$ the L^2-norm drastically decreases (the curve goes "down") and two Saddle-Node bifurcations appear. The 2D curve approaches the 1D curve at a second Pitchfork bifurcation (red circle) and becomes indistinguishable from the 1D case. This is seen in the magnification in Fig. 5.42 solid black line. The corresponding steady state profile is presented in Fig. 5.43 panel (4.2). Then, following this solid black line, where the 2D states remain identical to the 1D case, the line colour scheme changes to a solid magenta, see magnification in Fig. 5.42. Another Pitchfork bifurcation occurs at $\epsilon_\mathrm{s} \approx 0.781$ and $||h|| \approx 1.535$. Here, the curve drastically bends towards increasing SAW strength and the steady states reveal that a central finger structure appears, see Fig. 5.43 panels (4.3) to (4.5). This central finger is connected to the meniscus by two smaller fingers (root-structure). Following the the magenta curve further, several bifurcations occur. At $\epsilon_\mathrm{s} \approx 0.788$ a very small exponential snaking occurs. This is very similar to the repeating structure determined in 2D for $L_y = 30$, see Fig. 5.36. Then, the line changes its scheme to a dashed black at a Pitchfork

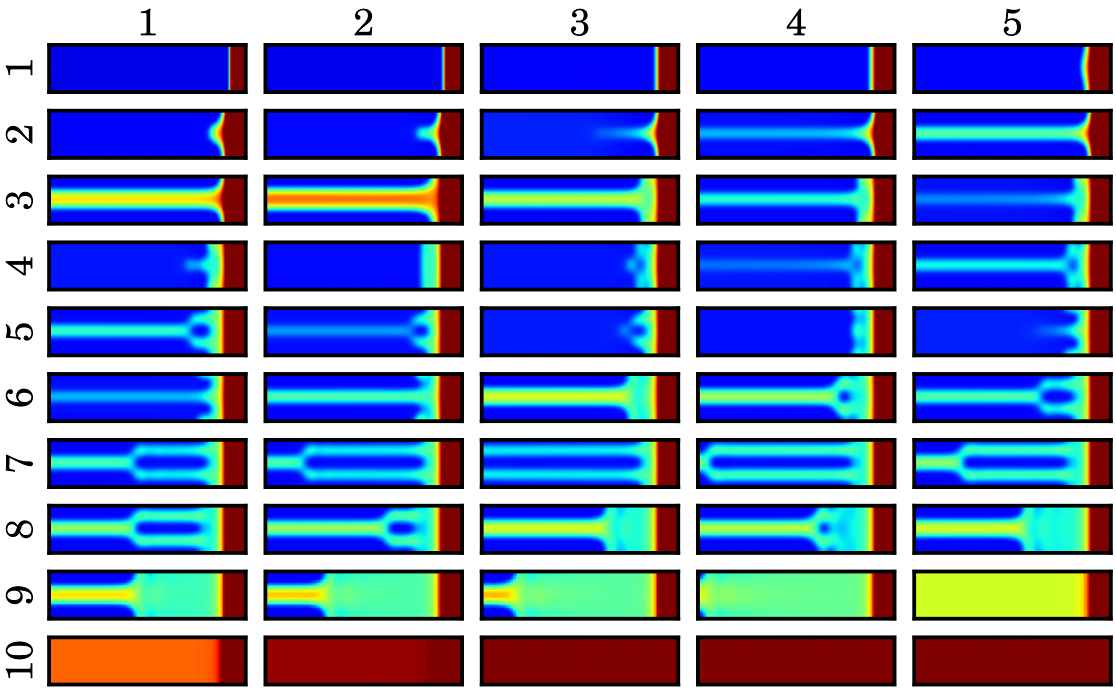

Figure 5.43: *Selected film height profiles in equidistant continuation points along the bifurcation curve of Fig. 5.42 are shown. The corresponding colour bar is shown in Fig. 5.38. From the top left corner panel (1.1) to the bottom right corner panel (10.5) steady states are shown beginning with small ϵ_s following the transversally invariant states. The profiles (1.1) to (1.4) and (9.4) to (10.5) are stable steady states. For visibility the y-domain is stretched by a factor of 2.4 as compared to the x-axis.*

bifurcation located at $\epsilon_s \approx 0.791$ and $||h|| \approx 1.534$. This Pitchfork bifurcation is the same as the one found on the 2D curve with $L_y = 2$. At the Pitchfork bifurcation the branch folds back. The occurring steady state is shown in Fig. 5.43 panel (5.4). Further following the curve, the central finger reappears and advances until it reaches the boundary at $x = -L_x/2$. However, at the lateral boundaries $\pm L_y/2$ two very small finger structure remain. Taking a look on the steady states Fig. 5.43 panels (5.5) to (6.3), the two outer fingers fuse into the central finger and the central finger widens occurring along the dashed black line. Following the curve further, the dashed black line changes into a solid black line. Here, the profiles in panels (6.4) to (8.2) show that the root-structure built by two fingers push the central finger out of the boundaries, so that in Fig. 5.41 panel (7.3) only two finger structures remain. Then, the central finger comes back and pushes the two fingers into the meniscus until they vanish, see panels (7.4) to (8.3). This events happen in the more complex region of the branch (criss-cross section). Inspecting the steady state profiles from panel (8.4), one sees that a flat film advanes and pushes the central finger beyond the domain boundary, see panel (9.5). Here, the full domain is covered by a Landau-Levich film solution. At $\epsilon_s \approx 0.78$ and $||h|| \approx 1.57$ another Pitchfork bifurcation (red circle) occurs [Fig. 5.42] and the 2D curve is invariant with 1D. Then, the 2D curve behaves identical for increasing SAW strength ϵ_s and has the same power law. The steady states shown in row 10 are all stable and present only Landau-Levich solutions.

In summary, when the domain Ω is increased in the lateral y-direction a numerous additional bifurcations occur. The observed behaviour of the bifurcation curve becomes more complex, so that a dense cluster occurs, e.g. in first case with a domain $L_y = 30$. In this dense cluster of overlapping branches, many variations of finger structures occur and they are interacting as a "dance of fingers", i.e. see Fig. 5.34. For the simplest case with domain $L_y = 1$ no finger structure is observed and the bifurcation curve is identical with the 1D case. In the cases with $L_y = 2$ and with $L_y = 4$ one and two finger structures are possible, whereas in the biggest case with $L_y = 30$ up to nine finger structures are determined. In other words, the number of finger structures increases as the lateral y-direction gets larger as more finger structure fit in. All the presented results in the 2D case show transitions of discontinuous dynamic wetting transitions similar to the 1D SAW-driven thin film case.

CHAPTER SIX

Two-layer thin-film models

> ” *Gutta cavat lapidem non vi sed saepe cadendo* “
>
> – PUBLIUS OVIDIUS NASO,
> *Pistulae ex Ponto IV, X, V*
> *12.-17. AD*

Up to this point the classical Landau-Levich model, where a film is withdrawn from a liquid bath or is spread due to the propagating surface acoustic waves (SAW) within the substrate, has been thoroughly studied. Both of these models are categorised as a “one-layer” thin-film model. The entire system is now extended by including an additional layer. These two-layer films consist of an upper and a lower layer of immiscible liquids, leading to an interface exist between the two-layers, referred to as a liquid-liquid interface. A number of studies has been conducted on two-layer models in theory and experiments. They investigated structure and pattern formation of flat two-layer polymer films under the influence of temperature gradient [52, 92, 99, 129]. Other studies use external vertical vibrations, which leads to Faraday instabilities encountered in the upper layers [14, 104] and also film ruptures in both layers [138]. In this work, however, temperature gradient, evaporation or external vibrations are not investigated. Instead, the focus lies on final states of occurring droplet constellations encountered after the coarsening process. This underlying dynamics always correspond to dewetting dynamics of a two-layer liquid films [23, 69, 106] and are theoretically investigated by performing time simulations.

In the course of this work the isothermal case of the already established model of Ref. [106] is used. In Ref. [106] evolution equations of a two-layer thin-film model are already derived. These equations describe a problem of a two-layer model of flat and horizontal oriented films on a solid substrate. The first step is to consider at a flat film system where the lower layer has different wettabilities, either completely wetting or partially wetting, whereas the upper layer is always partially wetting. The wettability is controlled via the Derjaguin disjoining pressure. A simple illustration of a two-layer flat film is presented in Fig. 6.1 (a). After studying the different wettabilities of the lower layer, further parameters are varied to examine the temporal evolution of dewetting. In particular, the relative energies per length of the states are evaluated during the dewetting process and then compared between different cases.

Furthermore, the two-layer system is extended by consideration of a Landau-Levich geometry. Therefore, additional lateral forces from gravitation and an inclination as in Eq. (3.47) are included into the two-layer model. This directly leads to an expansion of the Landau-Levich model. This model is then examined using time simulations and compared with previous findings for the two-layer and one-layer model. A sketch is illustrated in Fig. 6.1 (b).

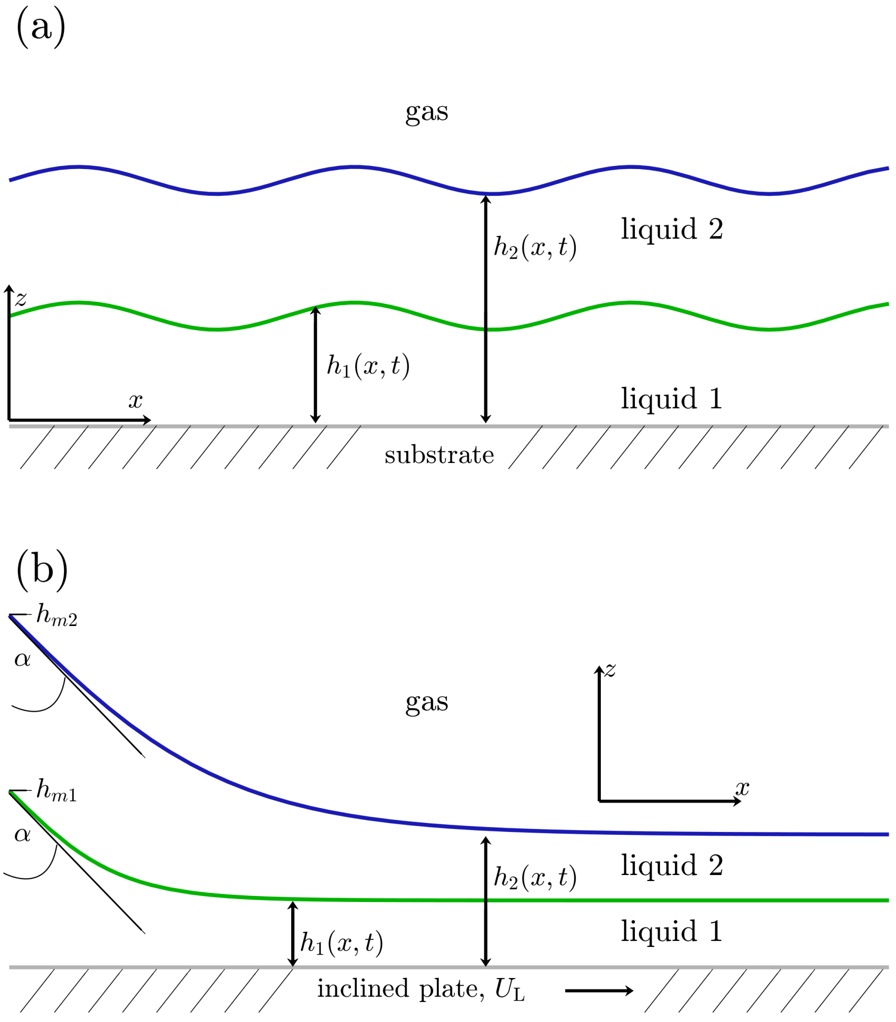

FIGURE 6.1: *Schematic drawings of two different one-dimensional (1D) two-layer thin-film models. In (a) a flat two-layer film on a horizontal substrate is shown. The total film height is* h_2 *and the film height of the liquids is* h_1 *and* $h_2 - h_1$*. In (b) a two-layer thin-film model with the Landau-Levich geometry is illustrated. Both liquid film heights are identical as defined in (a) and a bath is located at the left boundary with corresponding meniscus film heights* h_m2 *and* h_m1*. The plate is inclined by angle* α *and moving at velocity* U_L *towards the positive* x*-direction.*

6.1 Modelling and scaling of two-layer thin-film system

In the two-layer thin-film model the liquid layers are considered to be immiscible. However, the derived equations of Ref. [106] do not contain all properties relevant for the Landau-Levich geometry. In order to examine these evolution equations, they are expanded by substrate withdrawal, velocity U (towards the positive x-direction) and lateral force, gravitation g. The investigation of the two liquids is restricted to non-volatile liquids. The expanded evolution equations read

$$\begin{aligned} \partial_t h_1 &= -\,\partial_x\left[\mathcal{Q}_{11}\partial_x\frac{\delta F}{\delta h_1} + \mathcal{Q}_{12}\partial_x\frac{\delta F}{\delta h_2}\right] - \partial_x\Big[h_1 U\Big] \\ \partial_t h_2 &= -\,\partial_x\left[\mathcal{Q}_{21}\partial_x\frac{\delta F}{\delta h_1} + \mathcal{Q}_{22}\partial_x\frac{\delta F}{\delta h_2}\right] - \partial_x\Big[h_2 U\Big]\,. \end{aligned} \tag{6.1}$$

Following Ref. [106], mobilities are written as a 2 × 2−Matrix,

$$\mu_1\boldsymbol{\mathcal{Q}}(h_1,h_2) = \begin{pmatrix} \mathcal{Q}_{11} & \mathcal{Q}_{12} \\ \mathcal{Q}_{21} & \mathcal{Q}_{22} \end{pmatrix} = \begin{pmatrix} \dfrac{h_1^3}{3} & \dfrac{h_1^2}{2}\left(h_2 - \dfrac{h_1}{3}\right) \\ \dfrac{h_1^2}{2}\left(h_2 - \dfrac{h_1}{3}\right) & \dfrac{(h_2-h_1)^3}{3}\left(\dfrac{\mu_1}{\mu_2} - 1\right) + \dfrac{h_2^3}{3} \end{pmatrix}. \tag{6.2}$$

The model introduces two different film thicknesses h_1 and h_2 and also two different viscosities μ_1 and μ_2 corresponding to the two films. The function h_1 represents the film thickness of the lower layer and μ_1 its viscosity, whereas h_2 represents the total film thickness by adding both films thicknesses. The given Eqs. (6.1) may be reduced to a one-layer model. In order to do this, the film height of the lower layer must vanish with $h_1 = 0$ so that only the total film height h_2 remains. Subsequently, the equation for h_2 becomes the usual one-layer model.

Note that the lateral force, as well as the Derjaguin disjoining pressure are contained in the free energy F. The wettability is introduced for both liquid films in an analogous manner. The Derjaguin disjoining pressure is adapted to the respective interfaces, one at the solid-liquid and the other at the liquid-liquid interface, according to geometric considerations of the film thicknesses h_1 and h_2. Then, the lateral force caused by the gravitation g in combination with inclination angle α are implemented. The free energy functional reads

$$\begin{aligned} F = \int\Bigg[&\frac{\sigma_1}{2}(\partial_x h_1)^2 + \frac{\sigma_2}{2}(\partial_x h_2)^2 + \frac{h_1^2}{2}\rho_1 g + \frac{h_2^2 - h_1^2}{2}\rho_2 g \\ &- \alpha\rho_2 g(h_2 - h_1)x - \alpha\rho_1 g h_1 x + f(h_1,h_2 - h_1)\Bigg]\mathrm{d}^2x \end{aligned} \tag{6.3}$$

The interfacial tensions are given by σ_1 (liquid-liquid interface) and σ_2 (liquid-gas interface). The different densities of the liquids are given by ρ_1 and ρ_2, respectively.

In addition, the wetting energy $f(h_1,h_2-h_1)$ is defined as

$$f(h_1,h_2-h_1)=\kappa_2\left(\frac{h_{\mathrm{p2}}^3}{5(h_2-h_1)^5}-\frac{1}{2(h_2-h_1)^2}\right)+\kappa_1\left(\frac{h_{\mathrm{p1}}^3}{5h_1^5}-\frac{1}{2h_1^2}\right). \tag{6.4}$$

The first term of Eq. (6.4) corresponds to the wetting properties of the upper layer, and the second part to the one of the lower layer). In this case, it is convenient to use two different strengths of wetting energy given by κ_1 and κ_2. They are directly related to the two equilibrium contact angles. In this study, both precursor film heights are identical $h_{\mathrm{p1}}=h_{\mathrm{p2}}$.

Next, the dimensional equations have to be rescaled to obtain nondimensional equations. To simplify those steps, the presented equations are handled separately. First, the following dimensionless quantities indicated as tildes are introduced

$$h=\delta_{\mathrm{L}}\tilde{h}\,,\quad (x,z)^T=L(\tilde{x},\tilde{z})^T\,,\quad \delta_{\mathrm{L}}=\epsilon L\quad\text{and}\quad t=\tau\tilde{t}\,. \tag{6.5}$$

Including the scalings of Eq. (6.5) into the wetting energy [Eq. (6.4)]. It yields

$$\begin{aligned}f(h_1,h_2-h_1)&=\frac{\kappa_2}{\delta_{\mathrm{L}}^2}\tilde{f}(\tilde{h}_1,\tilde{h}_2-\tilde{h}_1)\\&=\left(\frac{\tilde{h}_{\mathrm{p2}}^3}{5(\tilde{h}_2-\tilde{h}_1)^5}-\frac{1}{2(\tilde{h}_2-\tilde{h}_1)^2}\right)+D_1\left(\frac{\tilde{h}_{\mathrm{p1}}^3}{5\tilde{h}_1^5}-\frac{1}{2\tilde{h}_1^2}\right).\end{aligned} \tag{6.6}$$

Here, the dimensionless ratio of wetting strengths for the both layers is introduced as

$$D_1=\frac{\kappa_1}{\kappa_2}\,. \tag{6.7}$$

Next, the free energy in Eq. (6.3) is scaled by using scalings Eq. (6.5) which gives

$$\begin{aligned}F=\sigma_2\delta_{\mathrm{L}}^2\tilde{F}=\int\Bigg[&D_2\frac{1}{2}(\partial_{\tilde{x}}\tilde{h}_1)^2+\frac{1}{2}(\partial_{\tilde{x}}\tilde{h}_2)^2+D_3D_4\frac{\tilde{h}_1^2}{2}+D_4\frac{\tilde{h}_2^2-\tilde{h}_1^2}{2}\\&-D_4\frac{\alpha}{\epsilon}(\tilde{h}_2-\tilde{h}_1)\tilde{x}-D_3D_4\frac{\alpha}{\epsilon}\tilde{h}_1\tilde{x}+D_5\tilde{f}(\tilde{h}_1,\tilde{h}_2-\tilde{h}_1)\Bigg]\mathrm{d}\tilde{x}\,.\end{aligned} \tag{6.8}$$

Hereby, five dimensionless parameters are introduced

$$D_2=\frac{\sigma_1}{\sigma_2}\,,\quad D_3=\frac{\rho_1}{\rho_2}\,,\quad D_4=\frac{\delta_{\mathrm{L}}^2\rho_2 g}{\epsilon^2\sigma_2}\quad\text{and}\quad D_5=\frac{\kappa_2}{\epsilon^2\sigma_2\delta_{\mathrm{L}}^2}\,. \tag{6.9}$$

Next, the mobility matrix (6.2) is scaled

$$\boldsymbol{Q}(h_1,h_2) = \frac{\delta_{\mathrm{L}}^3}{\mu_1}\tilde{Q}(\tilde{h}_1,\tilde{h}_2) = \frac{\delta_{\mathrm{L}}^3}{\mu_1}\begin{pmatrix} \dfrac{\tilde{h}_1^3}{3} & \dfrac{\tilde{h}_1^2}{2}\left(\tilde{h}_2 - \dfrac{\tilde{h}_1}{3}\right) \\ \dfrac{\tilde{h}_1^2}{2}\left(\tilde{h}_2 - \dfrac{\tilde{h}_1}{3}\right) & \dfrac{(\tilde{h}_2 - \tilde{h}_1)^3}{3}\left(D_6 - 1\right) + \dfrac{\tilde{h}_2^3}{3} \end{pmatrix}. \tag{6.10}$$

One additional dimensionless parameter is introduced, which corresponds to the ratio of viscosities of the two layers

$$D_6 = \frac{\mu_1}{\mu_2}. \tag{6.11}$$

Furthermore, the variational derivative is rescaled:

$$\frac{\delta}{\delta h} = \frac{1}{\delta_{\mathrm{L}}^3}\frac{\delta}{\delta \tilde{h}}\,. \tag{6.12}$$

The long-wave inclination angle is defined as $\tilde{\alpha} = \alpha/\epsilon$. Now, all of the quantities are dimensionless and are incorporated into the two-layer thin-films evolution Eqs. (6.1). The corresponding time scale τ is chosen as

$$\tau = \frac{\delta\mu_1}{\epsilon\sigma_2}. \tag{6.13}$$

The dimensionless parameter for the plate velocity reads

$$D_7 = \frac{\tilde{U}\mu_1}{\sigma_2}\,. \tag{6.14}$$

Then, σ_2 is further specified, which allows to reduce one of the dimensionless quantities. Using $\sigma_2 = \kappa_2/\delta_{\mathrm{L}}^2\epsilon^2$ yields

$$\begin{aligned} &D_1 = \frac{\kappa_1\sigma_2}{\epsilon^2\delta_{\mathrm{L}}^2} = \kappa\,, \quad D_2 = \frac{\sigma_1}{\sigma_2} = \sigma\,, \quad D_3 = \rho\,, \quad D_4 = \frac{\delta_{\mathrm{L}}^4\rho_2 g}{\kappa_2} = G\,, \\ &D_5 = 1\,, \quad D_6 = \mu\,, \quad \text{and} \quad D_7 = \frac{\epsilon^2\tilde{U}\mu_1\delta_{\mathrm{L}}^2}{\kappa_2} = U_{\mathrm{L}}\,. \end{aligned} \tag{6.15}$$

Scaling (6.15) is the parametrisation for the investigation of the two-layer thin-film model. Note that D_2 is interpreted as ratio of surface tensions of both layers. In the next step, all tildes are dropped and the scaling is applied for the set of equations and yields

$$
\begin{aligned}
\partial_t h_1 &= -\,\partial_x\left[\mathcal{Q}_{11}\partial_x\frac{\delta F}{\delta h_1} + \mathcal{Q}_{12}\partial_x\frac{\delta F}{\delta h_2}\right] - \partial_x\left[h_1 U_\mathrm{L}\right],\\
\partial_t h_2 &= -\,\partial_x\left[\mathcal{Q}_{21}\partial_x\frac{\delta F}{\delta h_1} + \mathcal{Q}_{22}\partial_x\frac{\delta F}{\delta h_2}\right] - \partial_x\left[h_2 U_\mathrm{L}\right].
\end{aligned}
\tag{6.16}
$$

The dimensionless two-layer thin-film evolution Eqs. (6.1) contain six dimensionless parameters and are expressed as

$$
\begin{aligned}
\partial_t h_1 = -\partial_x\Big\{ & h_1 U_L + \mathcal{Q}_{11}\partial_x\Big[\sigma\partial_{xx}h_1 + \Pi_1(h_1,h_2-h_1)\Big]\\
& + \mathcal{Q}_{11}(1-\rho)G\Big[\partial_x h_1 - \alpha\Big]\\
& + \mathcal{Q}_{12}\partial_x\Big[\partial_{xx}h_2 + \Pi_2(h_1,h_2-h_1)\Big] - \mathcal{Q}_{12}G\Big[\partial_x h_2 - \alpha\Big]\Big\}
\end{aligned}
\tag{6.17}
$$

and

$$
\begin{aligned}
\partial_t h_2 = -\partial_x\Big\{ & h_2 U_\mathrm{L} + \mathcal{Q}_{21}\partial_x\Big[\sigma\partial_{xx}h_1 + \Pi_1(h_1,h_2-h_1)\Big]\\
& + \mathcal{Q}_{21}(1-\rho)G\Big[\partial_x h_1 - \alpha\Big]\\
& + \mathcal{Q}_{22}\partial_x\Big[\partial_{xx}h_2 + \Pi_2(h_1,h_2-h_1)\Big] - \mathcal{Q}_{22}G\Big[\partial_x h_2 - \alpha\Big]\Big\}
\end{aligned}
\tag{6.18}
$$

with

$$
\begin{aligned}
\Pi_1(h_1,h_2-h_1) = -\partial_{h_1} f(h_1,h_2) = -&\left(\frac{h_{\mathrm{p2}}^3}{(h_2-h_1)^6} - \frac{1}{(h_2-h_1)^3}\right)\\
&+\kappa\left(\frac{h_{\mathrm{p1}}^3}{h_1^6} - \frac{1}{h_1^3}\right)
\end{aligned}
\tag{6.19}
$$

and

$$
\Pi_2(h_1,h_2) = -\partial_{h_2} f(h_1,h_2) = \left(\frac{h_{\mathrm{p2}}^3}{(h_2-h_1)^6} - \frac{1}{(h_2-h_1)^3}\right). \tag{6.20}
$$

Note that Eqs. (6.17) and (6.18) combine the two-layer thin-film model of Ref. [106] with terms known from the classical one-layer Landau-Levich problem [47, 116, 144].

6.2 Dewetting of flat films and coarsening

The derived thin-film evolution Eqs. (6.17) and (6.18) are examined by performing time simulations and provided bifurcation diagrams. [1] The first aspect is to study the dewetting dynamics of the liquid layers for different wetting properties of the lower layer. Two different cases are considered where the liquid of the lower layer is either fully or partially wetting the solid substrate. The liquid of the upper layer is always partially wetting the lower layer liquid. The dewetting and coarsening process for flat films is investigated with Eqs. (6.17) and (6.18). In particular, the lateral force and plate velocity are set to zero, i.e. $G = U_\mathrm{L} = 0$, and periodic boundary conditions are applied.

First, a fully wetting lower liquid is considered. The disjoining pressure in Eq. (6.19) is correspondingly changed, i.e. the sign is adjusted to $+1/h_1^3$ similar to the disjoining pressure shown in Fig. 2.4. Both layers are chosen to have equal film thickness with $h_1 = 4$ and $h_2 = 8$. The first set of parameters is given by $\sigma = \kappa = \mu = 1$. A flat two-layer film is a steady state. The linear stability analysis reveals that the flat two-layer film is either stable or unstable depending on the chosen parameters, see App. A.2. A flat film can become unstable in a stationary large scale instability similar to a flat film in a one-layer system, see Fig. 4.2. However, in order to observe morphological changes during time simulations in the form of dewetting, noise is added to the initial solution of a flat film [125]. This allows to investigate the corresponding coarsening behaviour of the flat two-layer film. Space-time plots of thickness profiles of both layers are presented in Fig. 6.2.

Notice that Fig. 6.2 (a) only shows the lower layer, and the changes are readily seen in the upper layer, panel (b). This rupture is caused by long and short-range interactions encoded by the disjoining pressure in the partially wetting upper layer. The number of droplets is in calculated with the linear stability analysis, see App. A.2. Due to maximal growth rate $\beta_\mathrm{max}(k)$ at $k = k_\mathrm{max} = 0.056 \approx 2\Pi/L \cdot N_\mathrm{drop}$ with $N_\mathrm{drop} = 4.5 \approx 5$, the fifth unstable eigenmode is expected as the dominant one, which corresponds to a film breaking into five droplets. This result of the time simulation is in agreement with the linear stability analysis. At the same time, the lower layer develops two small wetting ridges in the contact line regions of each formed droplet of the upper layer. The space-time plot of the film height h_1, Fig. 6.3 (a) shows the evolution of wetting ridges beneath the coarsening droplets of the upper layer.

---

[1] All bifurcation diagrams shown in Sec. 6.2 have been created by U. Thiele employing the code package `auto07p` [33].

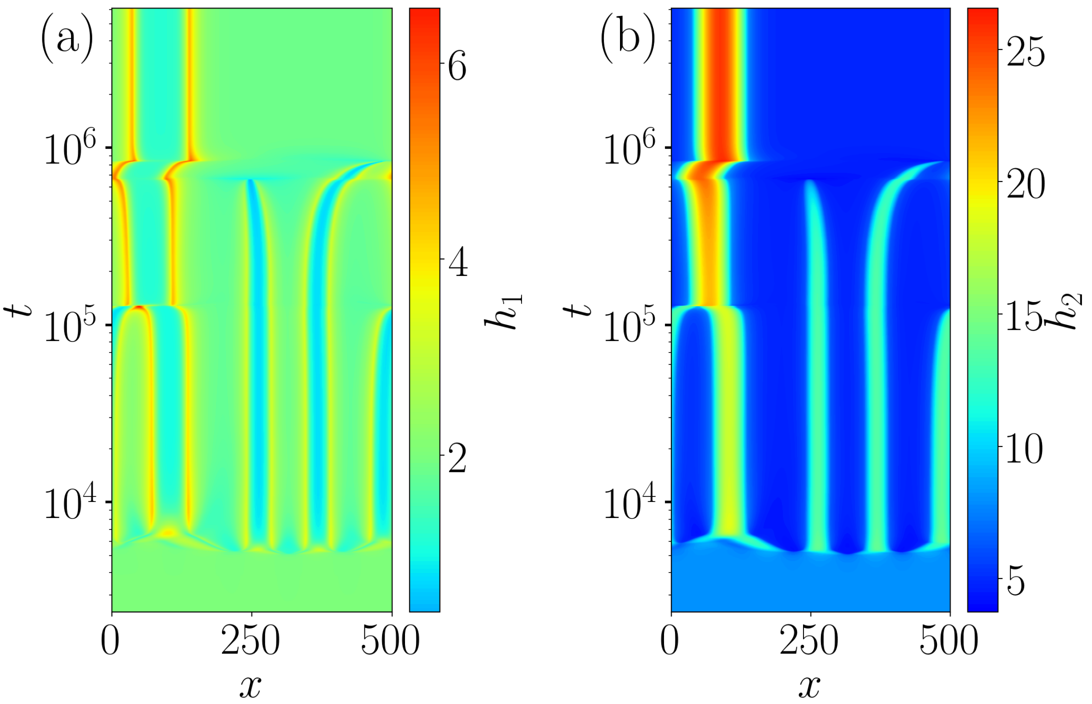

FIGURE 6.2: *Space-time plots of thickness profiles h_1 (a) and h_2 (b) illustrate the dewetting dynamics of two-layer films. The lower layer is completely wetting and the upper layer is partially wetting. The start solution is a flat film with added noise of an amplitude $A_n = 0.001$. The time is scaled logarithmically and the colour bar is adapted for the corresponding film heights. Selected states obtained in the time simulation are presented in Fig. 6.3. The remaining parameters are $h_1 = 4$, $h_2 = 8$, $h_{\mathrm{p1}} = h_{\mathrm{p2}} = 1$, $\kappa = 1$, $\sigma = 1$, $\rho = 0$, $G = 0$, $\mu = 1.5$, $U_{\mathrm{L}} = 0$ and $L = 500$.*

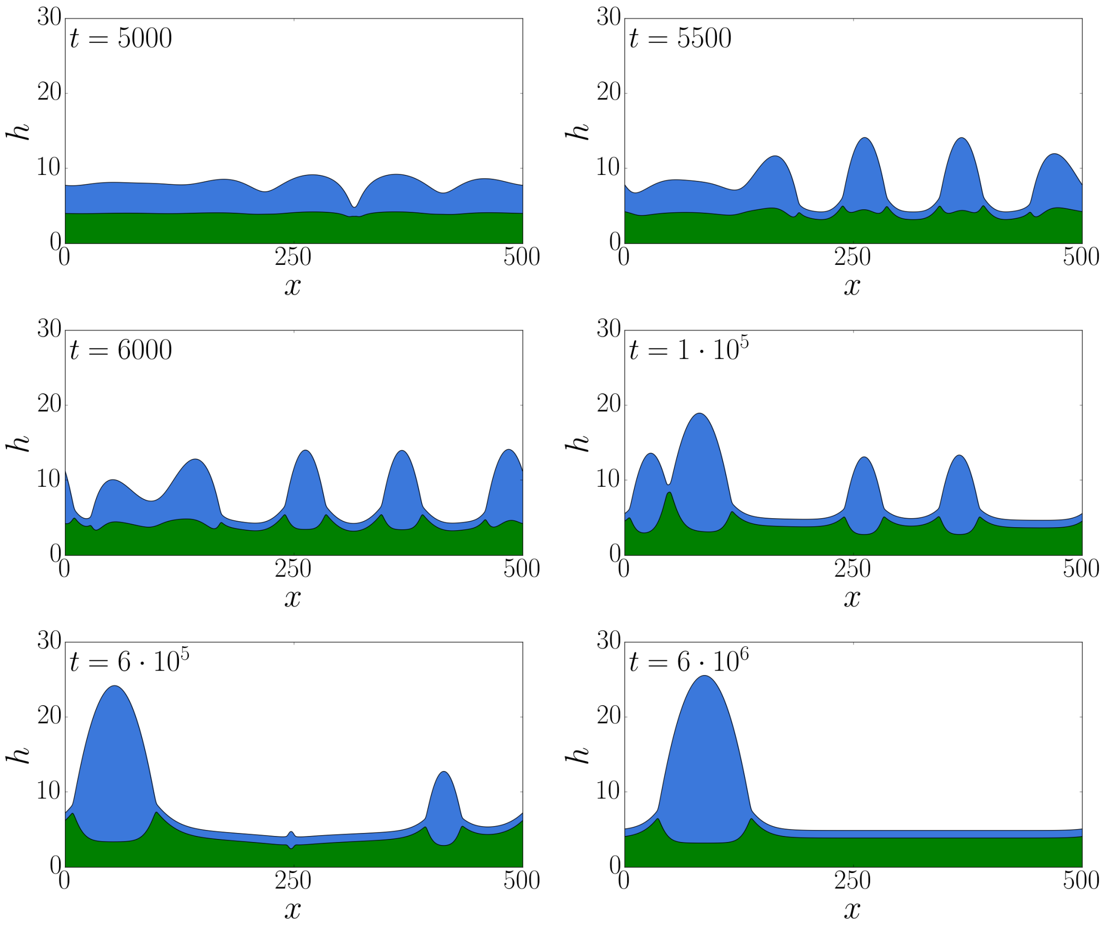

FIGURE 6.3: *Snapshots from a time simulation corresponding to time evolution of a two-layer flat film system in Fig. 6.2. The lower layer is fully wetting. The time t of the states are given in the top-left corner. The green coloured film is h_1 (lower layer) and the blue coloured film is $h_2 - h_1$ (upper layer).*

At $t \approx 5000$ the first rupture in the upper layer appears. Then, slowly more ruptures occur in the upper layer, so that finally five droplets remain. At $t \approx 6000$, a coarsening step occurs where two droplets fuses together, see Fig. 6.3. The newly formed larger droplet has a maximal film height of $h_2 \approx 20$, while the other droplets have a smaller height of $h_2 \approx 15$. Until $t \approx 10^5$, the four remaining droplets remain unchanged. Then another coarsening step occurs, where the larger droplet coalesces with the rightmost droplet at $x \approx 480$. After this process, the big droplet absorbs all remaining volumes of all small droplets with increasing time and grows to a maximum of $h \approx 28$. Hereby, mass of all the smaller droplets is slowly transfered to the large droplet and finally they collapse. The transitions of every coarsening step occur on a very fast time scale, which is noticeable in the space-time plot [Fig. 6.2] by sudden transitions. Ultimately, a single droplet remains.

Due to partial wetting, a precursor film of $h_{\mathrm{p}2} = 1$ remains around the major droplet. In contrast, the film thickness of the lower layer remains nearly unchanged with $h_1 = 4$ due to the full wetting property. Only two small wetting ridges remain in the contact line regions. During this full coarsening process two different coarsening mechanisms occur, where either two droplets collide and coalesce or mass (volume of liquid) is transferred through the precursor film until a droplet collapses completely. These translation and volume instabilities have also been observed for a one-layer film model, e.g. [50]. The full dynamics are known as coarsening and/or dewetting of a liquid layer. In other studies, similar dynamics of dewetting and coarsening in a bilayer (two-layer) liquids have been observed [17, 43, 51, 52, 58, 81].

To investigate the gradient dynamic, the relative energy per length, $(F - F_0)/L$, obtained from the time simulations is calculated with Eq. (6.8). Then, the time evolution of the energy is plotted, where the reference energy F_0 is the one of the initial flat film. Due to the gradient dynamic's character of the model, the energy monotonously decreases in time converging to a local minimum.

Fig. 6.4 shows that the relative energy decreases stepwise during each coarsening step. At the end, the system has a minimum energy of $(F - F_0)/L \approx -0.19$.

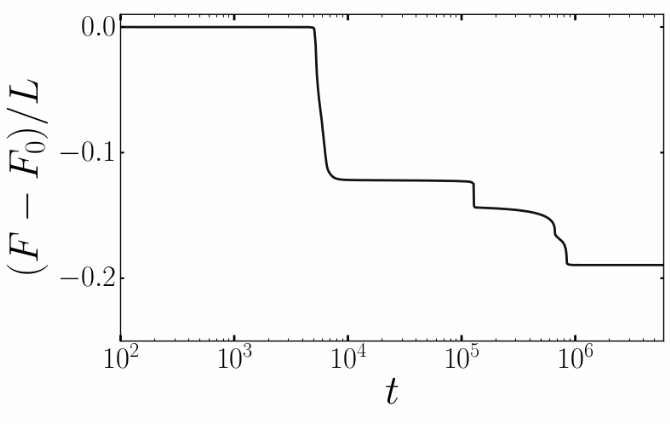

FIGURE 6.4: *Time evolution of the relative energy per length $(F - F_0)/L$ showing the case presented in Fig. 6.2.*

In the following scenarios, both liquid layers are assumed to be partially wetting [105, 106]. In contrast to the previous case, where the lower layer is fully wetting, the disjoining pressure from Eq. (6.19) is used. For otherwise identical parameters, starting solution and boundary conditions, a time simulation is performed. The space-time plots for both film heights are given in Fig. 6.5 and snapshots are presented in Fig. 6.6.

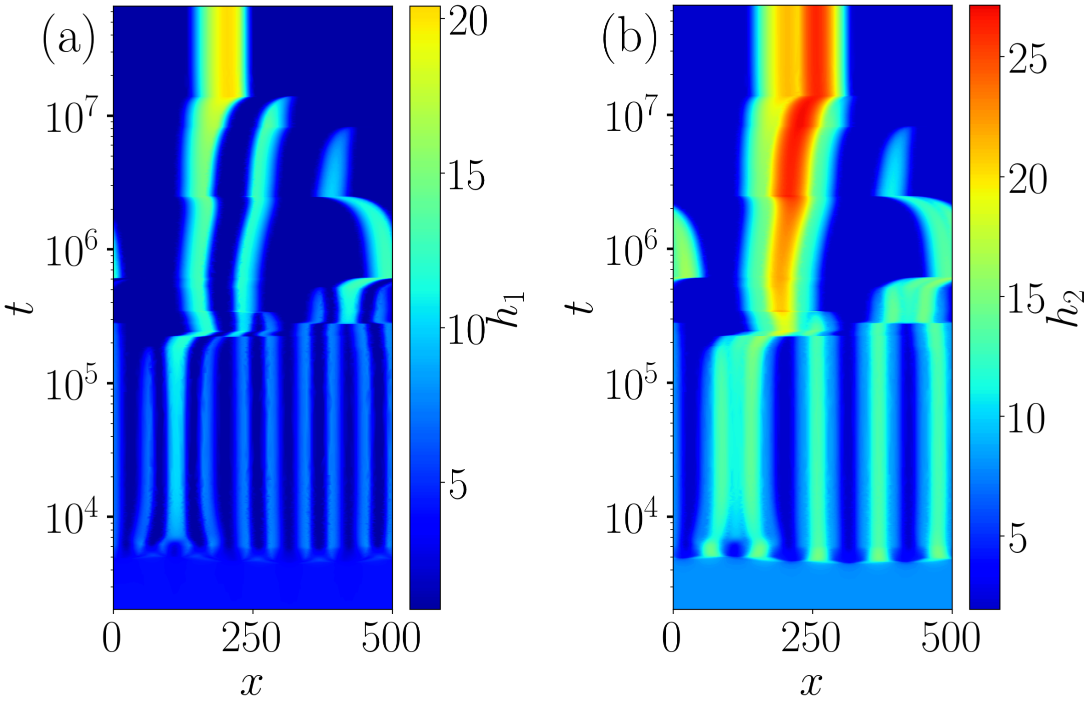

FIGURE 6.5: *Space-time plots of the (a) h_1 and (b) h_2 profile illustrate the dewetting dynamics of two-layer films, where both layers are partial wetting. The start solution is a flat film with added noise of an amplitude $A_n = 0.001$. The time is scaled logarithmically and the colour bar is adapted for the corresponding film heights, respectively. Selected states obtained in the time simulation are presented in Fig. 6.6. The remaining parameters are $h_1 = 4$, $h_2 = 8$, $h_{\mathrm{p}1} = h_{\mathrm{p}2} = 1$, $\kappa = 1$, $\sigma = 1$, $\rho = 0$, $G = 0$, $\mu = 1.5$, $U_{\mathrm{L}} = 0$ and $L = 500$.*

Fig. 6.5 shows that new features and a different final state is obtained. At the beginning of the time simulation, again the upper layer ruptures forming five droplets. The development of the five droplets influences the lower layer, so that two wetting ridges form under each droplet until $t = 5000$ with equal contact angles arises, see Fig. 6.6. In contrast to the fully wetting case considered before, the wetting ridges are more pronounced. Here, the wetting ridges actually correspond to droplets. Due to the partially wetting behaviour, a precursor film forms on the substrate. Inspecting Fig. 6.5 (a) shows that the first coarsening step in the lower layer occurs at $t = 6000$. The first coarsening step in the upper layer, in contrast, does not occur until $t \approx 10^4$, see Fig. 6.5 (b). Additionally, multiple coarsening steps also occur in the partially wetting lower liquid, where either mass is transfered or different droplets coalesce, which is different to the previous case in Fig. 6.2. At the end of the time simulation, an asymmetric droplet remains. It corresponds to a compound droplet consisting of each layer. In addition, the complete domain is coated with both precursor films $h_{\mathrm{p}1}$ and $h_{\mathrm{p}2}$. This asymmetric droplet is termed asymmetric bi-droplet constellation. It appears, that this type of asymmetric bi-droplet constellation is strongly related to the gradient dynamics of partially wetting liquids, where the energy of the system has a local minimum. In consequence, both liquid layers form a compound asymmetric bi-droplet. Next, the time evolution of the relative energy per length is investigated to determine the differences to the previous case.

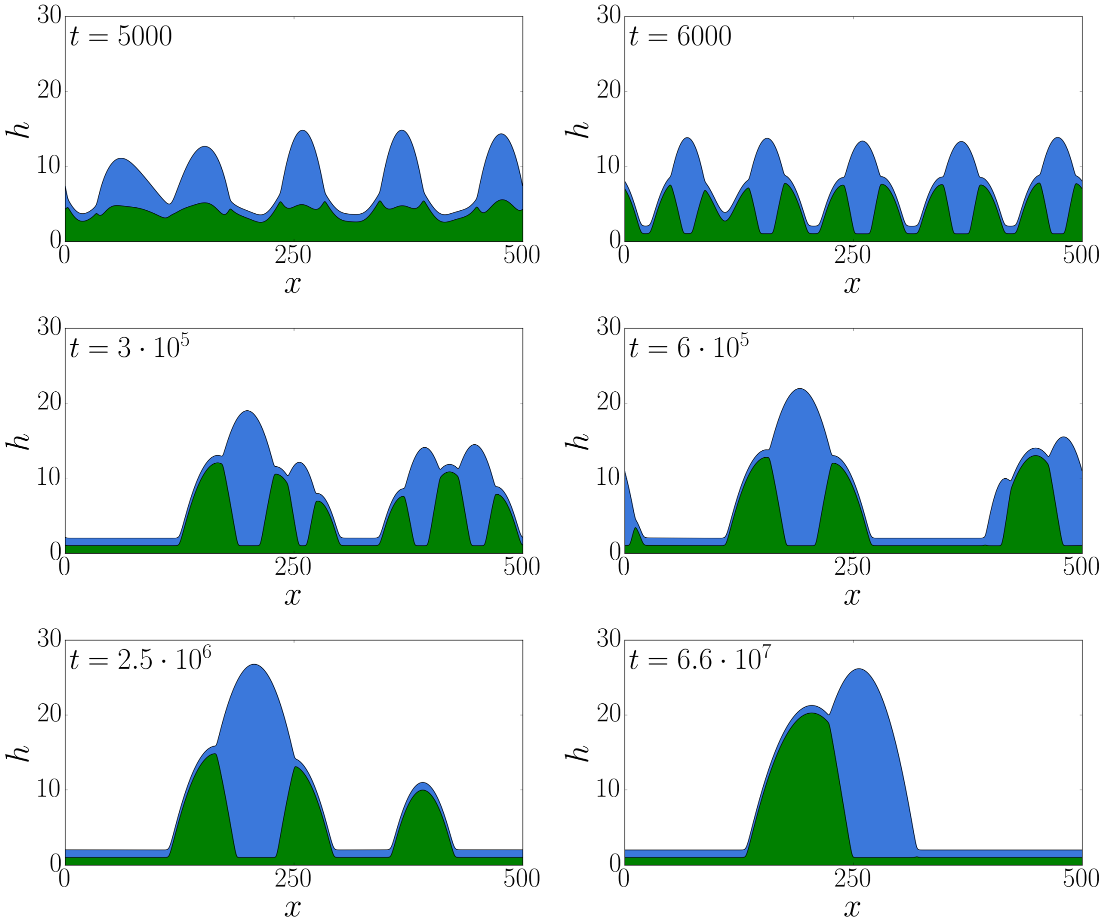

FIGURE 6.6: *Snapshots from a time simulation corresponding to time evolution of two-layer flat film system in Fig. 6.5. Both layers are partially wetting. The time t of the states are given in the top-left corner. The green coloured film is h_1 (lower layer) and the blue coloured film is $h_2 - h_1$ (upper layer).*

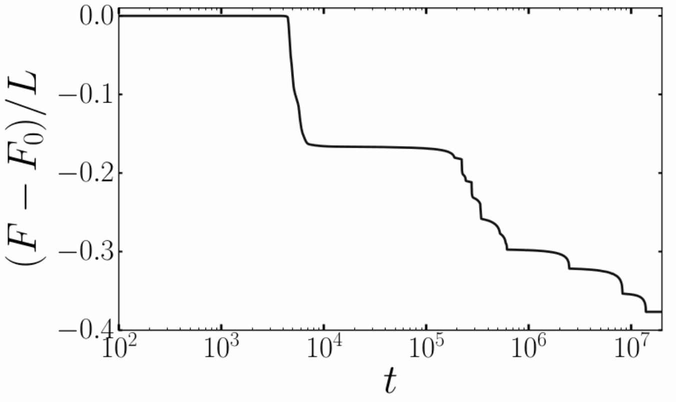

FIGURE 6.7: *Time evolution of the relative energy per length $(F - F_0)/L$ showing the case for both films are partially wetting from Fig. 6.5.*

The relative energy per length of this system develops in a very similar way as in the previous case, see Fig. 6.4. The different wetting property of the lower layer changes the coarsening process and more coarsening steps occur. Each step can be easily detected in the relative energy in Fig. 6.7. The minimum of the relative energy is $(F - F_0)/L \approx -0.37$, which is significantly lower than the previous case of the wetting lower layer, see Fig. 6.4.

The final states of time simulations reveal that two different types of droplet constellations are encountered: a symmetrical and an asymmetrical one. Here, the focus is solely placed on the different ratios of either surface tension σ or wetting strength κ, where other droplet constellations are anticipated. Furthermore, the relative energy is dependent on either ratio. The ratios of liquid layer characteristics provide further information on different dewetting and coarsening processes.

In case of the surface tension, two different cases are considered. In the first case, the ratio of surface tension is very low with $\sigma = 0.2$ and in the second one it is high with $\sigma = 100$ and $\sigma = 200$. These values are further examined with a bifurcation study. From the time simulations only the final states are presented, see Fig. 6.8.

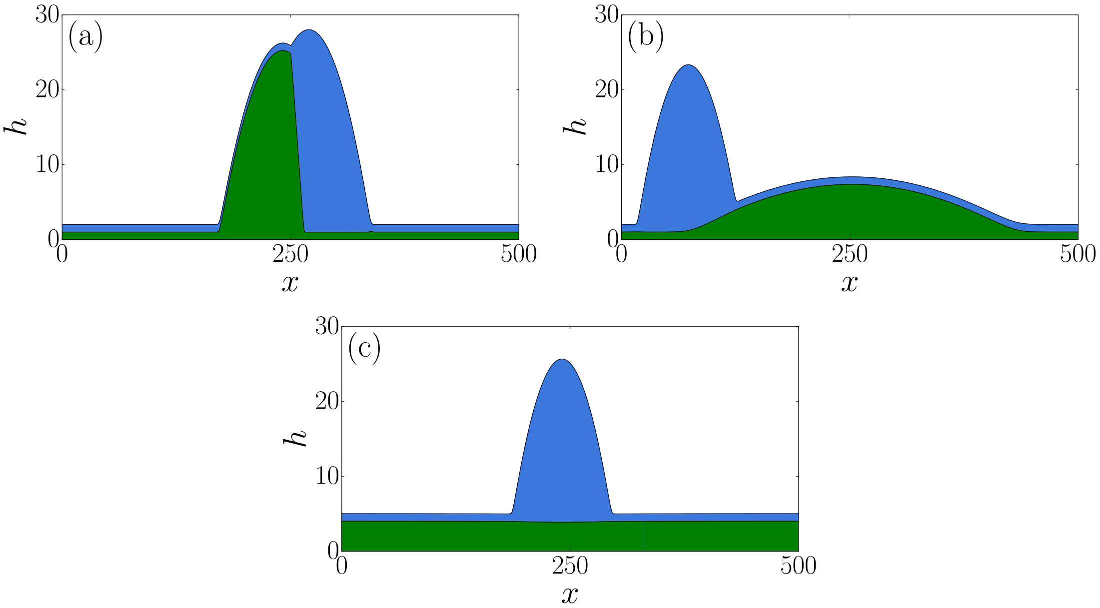

FIGURE 6.8: *Three different and final converged states obtained from dewetting dynamics of two-layer films for (a) a small ($\sigma = 0.2$), and for (b) and (c) larger ($\sigma = 100, 200$) ratio of surface tensions. The remaining parameters are $h_1 = 4$, $h_2 = 8$, $h_{\mathrm{p1}} = h_{\mathrm{p2}} = 1$, $\kappa = 1$, $\rho = 0$, $G = 0$, $\mu = 1.0$, $U_{\mathrm{L}} = 0$ and $L = 500$.*

In panels (a) and (b) asymmetric bi-droplets are obtained for $\sigma = 0.2$ and $\sigma = 100$. The relation between the surface tension and the dewetting process becomes readily visible. Fig. 6.8 (b) with $\sigma = 0.2$ show a very similar droplet constellation as obtained in Fig. 6.6 (final panel). In the case of $\sigma = 100$, shown in Fig. 6.8 (b), the droplet from the lower layer widens and flattens, whereas the upper layer develops into a large droplet. Increasing σ further to $\sigma = 200$, the lower layer remains nearly unaffected and has kept a constant film thickness of $h_1 = 4$ on the entire domain. Hereby, no wetting ridges are formed, and only one large droplet emerges from the upper layer. This phenomenon depends on the ratio of surface tension σ. Inspecting the corresponding relative energy values per length in Fig. 6.9, it becomes obvious that the relative energy per length of the final state increases for decreasing ratio of surface tension.

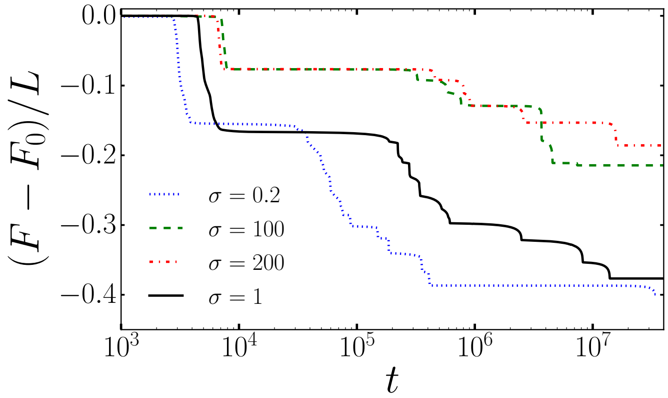

FIGURE 6.9: *Time evolution of the relative energy per length* $(F - F_0)/L$ *showing for different ratio of surface tension* $\sigma = 0.2, 1, 100$ *and* 200.

Fig. 6.9 allows to identify, without having to refer to the space-time plots, the number of undergone coarsening steps indicated by stepwise decrease in the energy level. For $\sigma = 200$ six and for $\sigma = 100$ seven coarsening steps are detected. In the case of a lower ratio of surface tension $\sigma = 1$ and $\sigma = 0.2$ the number of coarsening steps is much higher than for $\sigma = 100$ and $\sigma = 200$. This result demonstrates that for smaller ratio of surface tension σ, multiple coarsening processes occur during the dewetting of the liquid layers.

From the results of the time simulations for different ratio of surface tension σ, only one symmetric constellation is found. This is in contrast to previous studies, which did not observe asymmetric droplet constellations of bi-droplets [17, 43, 51, 52, 58, 81, 106].

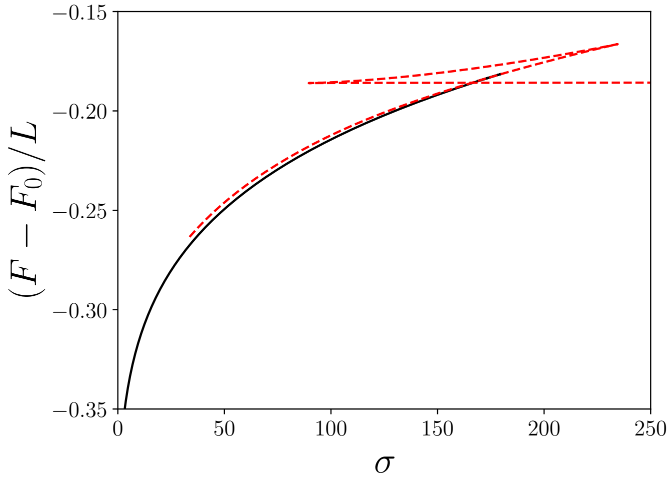

FIGURE 6.10: *Bifurcation diagram showing the relative energy* $(F - F_0)/L$ *versus the ratio of surface tension* σ. *The two different branches represent symmetric and asymmetric droplet constellations as dashed red and solid black, respectively. The remaining parameters are* $h_1 = 4$, $h_2 = 8$, $h_{\mathrm{p}1} = h_{\mathrm{p}2} = 1$, $\kappa = 1$, $\rho = 0$, $G = 0$, $U_{\mathrm{L}} = 0$ *and* $L = 500$. *The bifurcation diagram has been obtained by U. Thiele.*

The results from the time simulations in Fig. 6.9 for the relative energy per length $(F-F_0)/L$ to the respective σ are in agreement with the result from the continuation in Fig. 6.10. In Fig. 6.10 the ratio of the surface tension σ is employed as main control parameter and the relative energy $(F-F_0)/L$ is chosen as a measurement. Inspecting the branch of steady states with increasing σ, only asymmetric droplet constellations exist. At $\sigma \approx 190$ the branch of symmetric steady states emerges subcritically from the branch of asymmetric steady states. This emerging branch of symmetric steady states is tracked for increasing σ. Hereby, two Saddle-Node bifurcations appear (not shown). At the first Saddle-Node bifurcation the relative energy per length $(F-F_0)/L$ continuously decreases. At second Saddle-Node bifurcation, where the branch folds towards larger σ again, the relative energy per length $(F-F_0)/L$ decreases at a lower rate. Tracking the branch of symmetric steady states for decreasing σ, it ends at $\sigma \approx 30$ seemingly in a bifurcation on another branch (not further discussed).

Fig. 6.10 reveals that the two-layer thin film system for flat film has multi-stability. Hereby, the bifurcation diagram shows that steady symmetric and asymmetric states of droplet constellations coexist at identical parameter values. Inspecting the relative energy levels per length of both types of constellations, one notices, that they have a very similar local energy minimum at same parameters. The energy of asymmetric bi-droplet constellations is always lower compared to the symmetric ones.

Next, the ratio of the wetting strength κ is analysed similar to the ratio of surface tension σ. Here, only two different values $\kappa = 0.05$ and $\kappa = 10$ are considered. In addition, the dewetting dynamics are illustrated with space-time plots, see Fig. 6.11. In contrast to the previous time simulations [Figs. 6.2 and 6.5], these thin films are disturbed sinusoidally to produce exactly five undulations in the domain. Therefore, in both space-time plots across a relatively long time interval $\Delta t \approx 10^6$, five droplets of constant height are identified by means of the height profile h_2. After $t \approx 10^6$, the first coarsening steps begin simultaneously in both simulations. At the end of the time simulations, two different symmetrical constellations are obtained after the coarsening process.

At the small $\kappa = 0.05$, there is a large droplet of the upper liquid on a droplet of the lower liquid, Fig. 6.12 (a). This final structure resembles a lens on a sessile drop [91]. Such a constellation has also occurred during the coarsening process in Fig. 6.6, where up to five of smaller droplets have emerged.

The symmetrical constellation at $\kappa = 10$ shows a different final structure. Here, a droplet from the lower layer is formed and surrounded by two droplets of a similar large height of the upper liquid. As a result, the droplet from the lower layer is at the center of other droplets. The low ratio of κ means that the wetting strength of the upper liquid is higher than of the lower one. Then, the lower liquid is more likely to get shaped by the wetting strength from the upper liquid. In the other case for large ratio of κ the reversed scenario appears, where the lower layer (partially

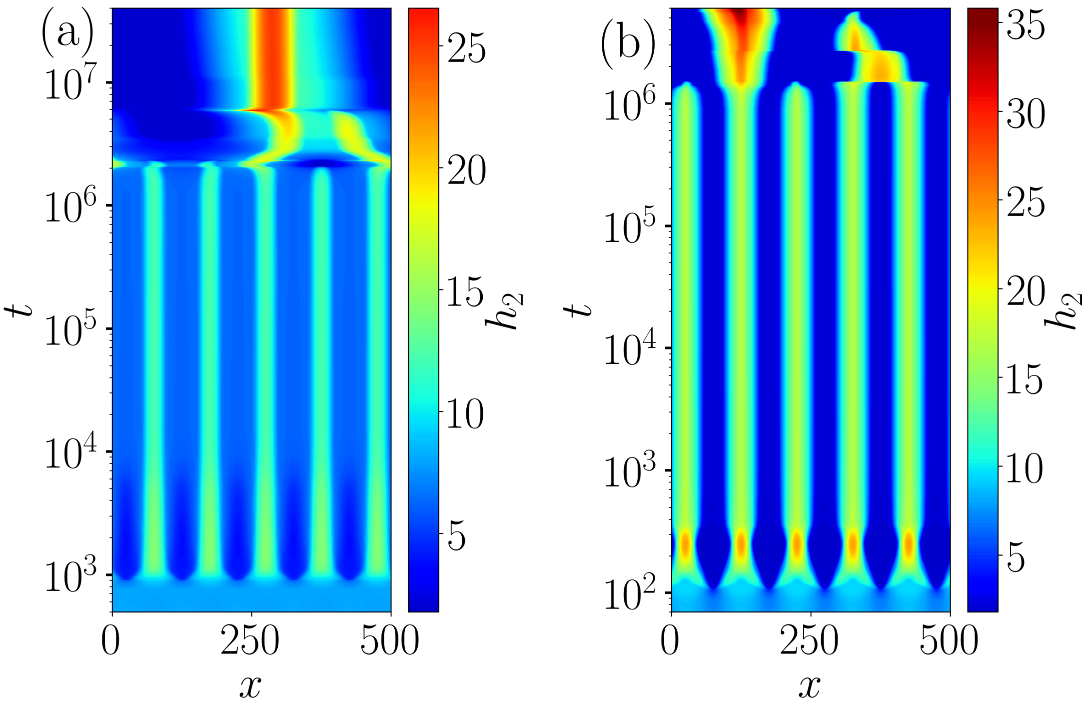

Figure 6.11: *Space-time plots of the h_2 profile illustrate the dewetting dynamics of two-layer films for a (a) small ($\kappa = 0.05$) and (b) large ($\kappa = 10$) dimensionless ratio of wetting strength. The final converged states obtained when the coarsening process is completed are presented in Figs. 6.11. The remaining parameters are $h_1 = 4$, $h_2 = 8$, $h_{\mathrm{p1}} = h_{\mathrm{p2}} = 1$, $\sigma = 1$, $\rho = 0$, $G = 0$, $\mu = 1.0$, $U_{\mathrm{L}} = 0$ and $L = 500$.*

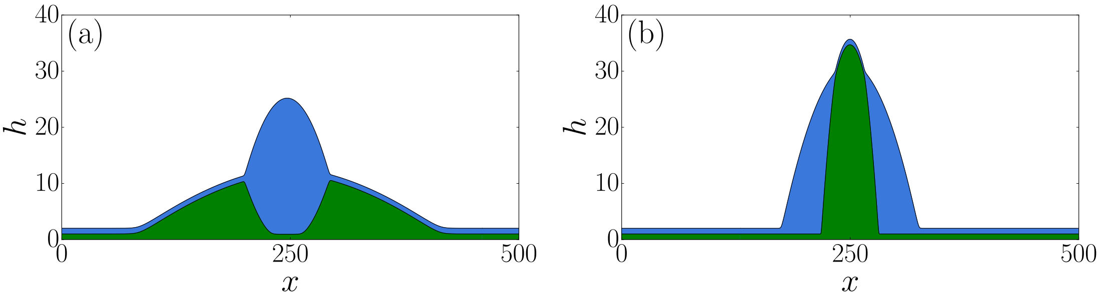

Figure 6.12: *Panels (a) and (b) show the final converged states of the time simulations shown in Figs. 6.11 (a) and (b), respectively.*

wetting) forms a droplet and the upper layer is shaped around that droplet, see Fig. 6.12 (b). Again, the relative energy of the dewetting dynamics is considered. For a large ratio of κ the energy of the final state is much smaller than for smaller κ, as more pronounced droplet shapes are formed.

In contrast to the relation of the relative energy in the case of the surface tension σ [Fig. 6.9], the ratio of wetting strengths, has more influence during a dewetting process. This leads to much lower relative energies for larger ratio of wetting strength κ. Note that for $\kappa = 1$ an asymmetric droplet constellation is obtained in Fig. 6.6 (last panel), whereas both droplet constellations presented in Fig. 6.12 are symmetric. The difference in droplet constellations is further investigated with a bifurcation diagram.

Fig. 6.14 shows two different branches of asymmetric steady states. Both asymmetric droplet constellations (dashed lines) emerge from the branch of the symmetric (black solid line) one. The obtained results of the relative energies per length$(F - F_0)/L$

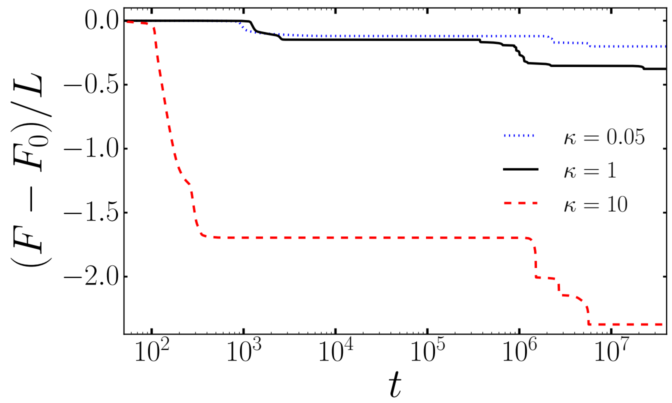

FIGURE 6.13: *Time evolution of the relative energy per length $(F - F_0)/L$ showing for different ratio of wetting strength $\kappa = 0.05, 1$ and 10.*

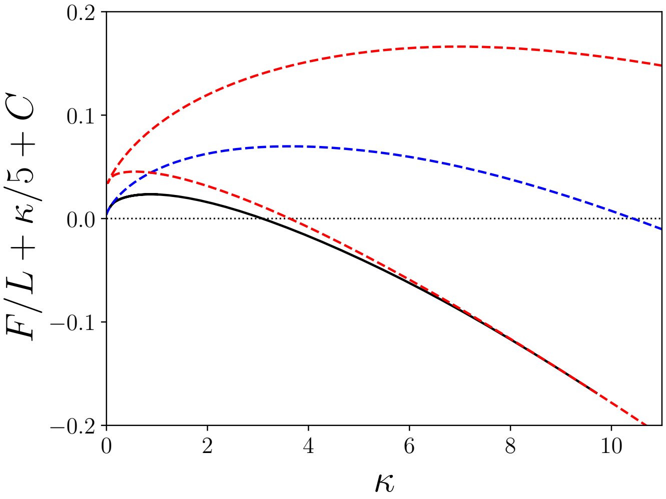

FIGURE 6.14: *Bifurcation diagram showing a shifted energy F versus the ratio of wetting strength κ. Three different branches represent symmetric and asymmetric droplet constellations. The black solid line corresponds to symmetric steady states, and the dashed lines, red and blue, represent two different asymmetric states. The relative energy per length F/L is conveniently shifted with an arbitrary function of $\kappa/5$ and some constant C. This scaled y-axis allows to provide to improve visibility of the three branches. The raw (not scaled) bifurcation diagram is shown in the appendix, see Fig. Af.2. The remaining parameters are $h_1 = 4$, $h_2 = 8$, $h_{\mathrm{p}1} = h_{\mathrm{p}2} = 1$, $\sigma = 1$, $\rho = 0$, $G = 0$, $U_{\mathrm{L}} = 0$ and $L = 500$. The bifurcation diagram has been obtained by U. Thiele.*

from the time simulations are consistent with those from the path continuation. Inspecting the branch of the symmetric droplets indicates that it connects the different asymmetric branches, see Fig. 6.14. The branches show, that the system always contains multi-stability of different possible states for $\kappa > 0$, where symmetric and asymmetric droplets coexist. The bifurcation diagrams in Fig. 6.10 and Fig. 6.14 show that the flat two-layer thin film system has multi-stable states.

Next, multi-stability is further investigated. For this purpose, an example of two different time simulations with identical parameters are performed to obtain either a symmetric or an asymmetric droplet constellation as a final state. Both final droplet states are obtained by different disturbances. The symmetric constellation is obtained by added noise, whereas the asymmetric constellation is obtained by a flat film disturbed sinusoidally. The final states of symmetric and asymmetric droplets are presented for a domain of $L = 96$ in Fig. 6.15.

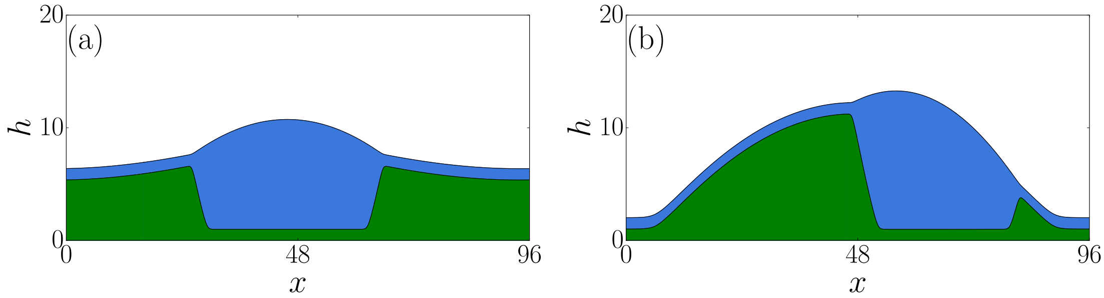

FIGURE 6.15: *Panels (a) and (b) show the final converged states, symmetric and asymmetric, which coexist for identical parameters. The remaining parameters are* $h_1 = 4$, $h_2 = 8$, $h_{\mathrm{p}1} = h_{\mathrm{p}2} = 1$, $\sigma = 0.1$, $\kappa = 0.5$, $\mu = 0.1$, $\rho = 0$, $G = 0$, $U_{\mathrm{L}} = 0$ *and* $L = 96$.

In Fig. 6.15, panel (a) shows a symmetric droplet constellation. Here, a droplet of the upper layer lies in a basin formed by the lower layer. The structure of the symmetric droplet constellation seems like a "crock"-like structure, whereas the domain is always covered by a film of total film thicknesses of $h_2 > 6.5$. It is very similar as a lens on a sessile drop. In Fig. 6.15, panel (b) shows an asymmetric bi-droplet constellation. The film height of the asymmetric droplet is slightly higher than the symmetric droplet constellation and only a very short range of the domain is covered by the precursor film height. The corresponding relative energy plot is given in Fig. 6.16.

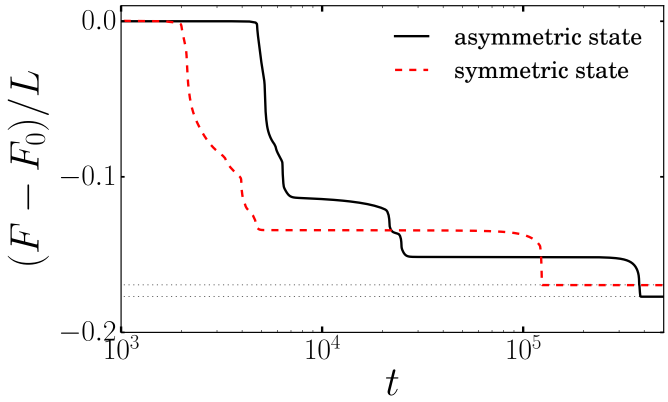

FIGURE 6.16: *Time evolution of the relative energies per length* $(F - F_0)/L$ *showing multi-stability, symmetric and asymmetric, of Fig. 6.15. The black solid line corresponds to the relative energy of the symmetric state and the dashed red line to the asymmetric state. The dotted lines represent the relative energies obtained by continuation at* $(F - F_0)/L = -0.177$ *and* $(F - F_0)/L = -0.169$.

The relative energy $(F - F_0)/L$ in both cases is very similar with $(F - F_0)/L = -0.177$ (asymmetric) and $(F - F_0)/L = -0.169$ (symmetric). The symmetric state of the droplet lying in the basin of the lower layer has a slightly higher relative energy than the asymmetric case. The results are compared with the bifurcation diagram obtained. The bifurcation diagram, where the domain L is the main control parameter, is provided to study the behaviour of multi-stability, symmetric and asymmetric.

Fig. 6.17 shows only the relevant region of the bifurcation diagram where multi-stability occurs. The bifurcation diagram in Fig. 6.17 is qualitatively similar to the one presented in Fig. 6.10. Tracing the branch of asymmetric states (black

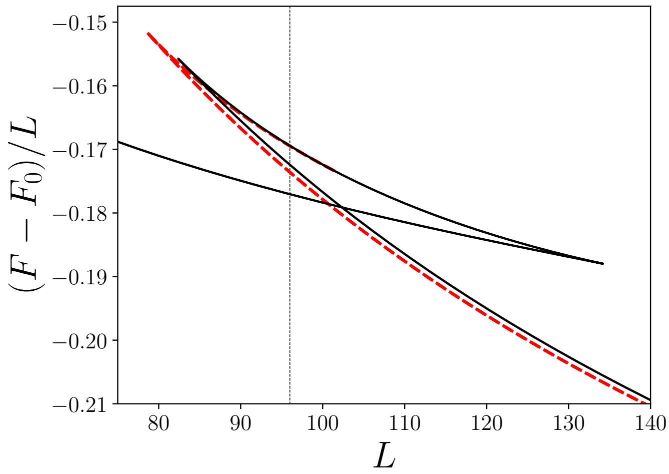

Figure 6.17: *Magnification of the bifurcation diagram presented in Fig. Af.3 showing the relevant region of the relative energy $(F - F_0)/L$ versus domain L. The black solid line corresponds to asymmetric steady states and the red dashed line represents the symmetric states. At $L = 96$ a vertical dashed line is shown. The corresponding film states are shown in Fig. 6.15 and the time evolution of the relative energy per length is shown in Fig. 6.16. The complete bifurcation diagram is presented in Fig. Af.3. The remaining parameters are $h_1 = 4$, $h_2 = 8$, $h_{\mathrm{p1}} = h_{\mathrm{p2}} = 1$, $\sigma = 0.1$, $\kappa = 0.5$, $\rho = 0.1$, $G = 0$ and $U_{\mathrm{L}} = 0$. The bifurcation diagram has been obtained by U. Thiele.*

line) for increasing domain size L, a Saddle-Node bifurcation (not shown) occurs at $L \approx 135$. Along this branch of steady states, the relative energy per length decreases. The branch folds back at that Saddle-Node bifurcation and then, the relative energy per length increases. At $L \approx 105$ a branch of symmetric states (dashed red) emerges subcritically from the branch of asymmetric states. Both branches of steady states follow the same path and are nearly parallel. Then, another Saddle-Node bifurcation (not shown) occurs at both branches for different values. The Saddle-Node bifurcation on the symmetric branch appears at a lower domain L and at higher relative energy per length $(F - F_0)/L$. Following the branches further, the relative energy per length decreases for increasing domain size L. In Fig. 6.17 a vertical line at $L = 96$ is given. It crosses the branches of symmetric and asymmetric steady states. The performed time simulations are in agreement with the results obtained by the bifurcation diagram. Both methods show that the same relative energies per length $(F - F_0)/L = -0.177$ for the asymmetric and $(F - F_0)/L = -0.169$ for symmetric constellation are determined. Next, the dynamical behaviour of a two-layer model in a Landau-Levich geometry is investigated.

6.3 Two-layer thin films in a Landau-Levich geometry

The two-layer system is examined considering the Landau-Levich geometry. As a reminder, the classic Landau-Levich model considers a liquid film remaining on a plate that is withdrawn from a bath at certain velocity. Hereby, a meniscus forms at the transition from the bath to the substrate. This geometry is already incorporated into the governing evolution equation of a two-layer, see Eqs. (6.17)-(6.18). The following set of boundary conditions are

$$h_1 = h_{\mathrm{m}1}\,, \quad h_2 = h_{\mathrm{m}2}\,, \quad \partial_x h_1 = -\alpha \qquad \text{and} \quad \partial_x h_2 = -\alpha \qquad \text{at} \quad x = 0\,, \tag{6.21}$$

and

$$\partial_x h_1 = 0\,, \quad \partial_x h_2 = 0\,, \quad \partial_{xx} h_1 = 0 \qquad \text{and} \quad \partial_{xx} h_2 = 0 \qquad \text{at} \quad x = L\,. \tag{6.22}$$

The bath is situated at $x = 0$ (left boundary) and the plate is withdrawn towards the positive x-direction. The film heights of the meniscus of both liquid layers are fixed at $h_{\mathrm{m}1}$ and $h_{\mathrm{m}2}$, see Fig. 6.1 (b). In addition, the plate is inclined by an angle α and the gravitation is set to $G = 0.001$. On the other side, at $x = L$ Neumann boundary conditions are chosen. The boundary conditions are identical as for the classical Landau-Levich model as in Ref.[47, 116] and different from the previous ones used in Sec. 5.1.

A parameter study is performed with the aid of time simulations using the existing results of the classical Landau-Levich and the two-layer flat film system as references. Remember that in the one-layer system (classical Landau-Levich system), three different states namely, meniscus state, foot-solution and Landau-Levich film are obtained, see Figs. 5.2-5.4. Thus, similar solutions are to be expected for layer thin films in a Landau-Levich geometry.

Fig. 6.18 shows the four possible main configurations of steady meniscus states and Landau-Levich films. In panel (a) both layers are in a meniscus state for very low velocity $U_{\mathrm{L}} = 0.001$. Panel (b) has the upper layer in a Landau-Levich film state while the lower layer is in a meniscus state. This is due to the stronger surface tension of lower layer indicated by $\sigma = 10$. Panel (c) and (d) share parameters $\sigma = 1$ and $\kappa = 0.05$. They differ in velocity $U_L = 0.015$ and $U_L = 0.09$. Hereby, panel (c) represents the reversed case of panel (b), where the lower layer is in a Landau-Levich film state and the upper layer is in a meniscus state. In addition, a wetting ridge-like elevation appears in the lower film at the transition from the meniscus to the film. This elevation is formed due the ratio of wetting strength $\kappa = 0.05$, which aligns the contact angle of the lower layer with the upper layer, preventing it to advance further. The velocity $U_{\mathrm{L}} = 0.015$ is not large enough to pull the upper layer. In panel (d), where the velocity is $U_{\mathrm{L}} = 0.09$, both layers are Landau-Levich films. I.e,

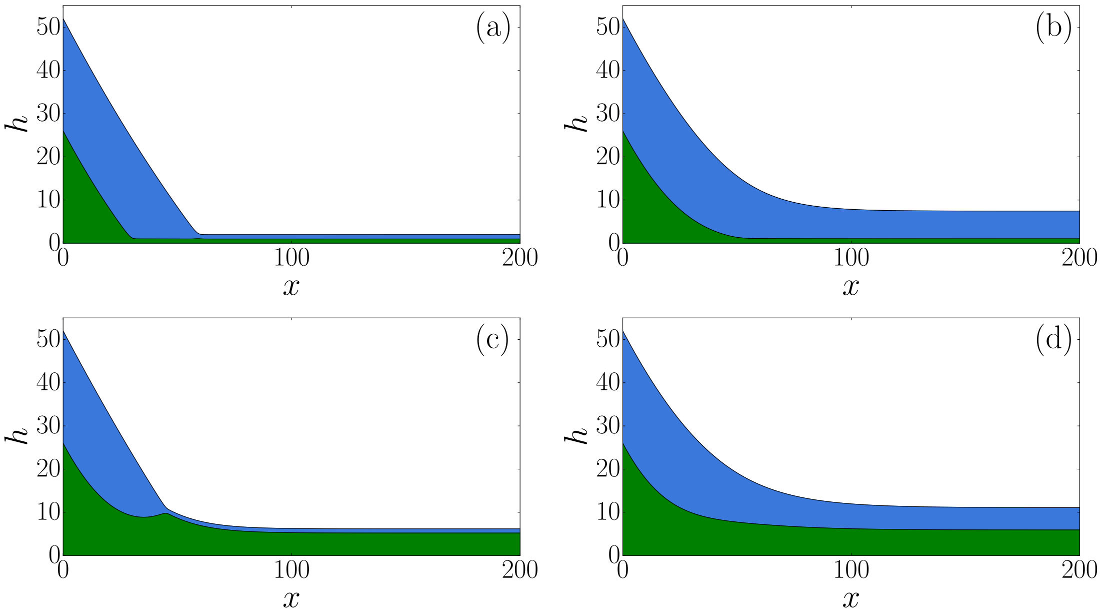

FIGURE 6.18: *Four different steady film states obtained from time simulations of the two-layer system in the Landau-Levich geometry. In (a), both layers are in a meniscus state with* $\sigma = 1$, $\kappa = 1$ *and* $U_{\mathrm{L}} = 0.001$, *in (b) the upper layer is a Landau-Levich film and the lower layer is a meniscus state with* $\sigma = 10$, $\kappa = 1$ *and* $U_{\mathrm{L}} = 0.05$, *(c) the upper layer is in a meniscus state and lower layer is a Landau-Levich film with* $\sigma = 1$, $\kappa = 0.05$ *and* $U_{\mathrm{L}} = 0.015$, *and (d) both layers are a Landau-Levich film with* $\sigma = 1$, $\kappa = 0.05$ *and* $U_{\mathrm{L}} = 0.09$. *Note that only the relevant part of the domain is shown. The remaining parameters are* $h_{\mathrm{m1}} = 26$, $h_{\mathrm{m2}} = 52$, $h_{\mathrm{p1}} = h_{\mathrm{p2}} = 1$, $\rho = 1$, $G = 0.001$, $\alpha = 1$ *and* $L = 500$.

a transition from panel (c) to (d) has occurred, which leads to those different steady states.

Now, this information about the four main configurations is used to determine possible transitions between these different steady states. The main idea is to perform

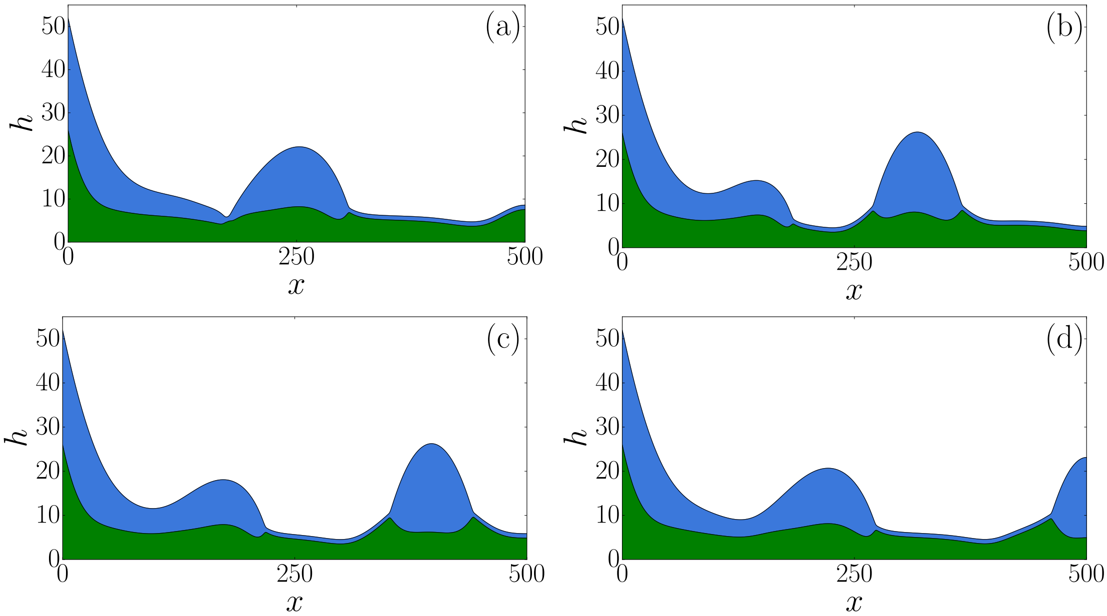

FIGURE 6.19: *Snapshots from a time simulation are presented corresponding to time evolution in Fig. 6.20 (a). The snapshots illustrate a sequence of time-periodic behaviour, where a droplet from the upper layer is withdrawn. The remaining parameters are* $h_{\mathrm{m1}} = 26$, $h_{\mathrm{m2}} = 52$, $h_{\mathrm{p1}} = h_{\mathrm{p2}} = 1$, $\sigma = 1$, $\kappa = 0.05$, $\rho = 1$, $G = 0.001$, $\alpha = 1$, $U_{\mathrm{L}} = 0.08$ *and* $L = 500$.

further time simulations for values of the plate velocity U_L, which are between these occurring states. At first, the main focus is on the parameters used in Fig. 6.18 (c) and (d).

The first results of states are time-periodic states, which are determined for the velocity $U_\mathrm{L} = 0.08$ with $\sigma = 1$ and $\kappa = 0.05$. To obtain an overview of the time-periodic behaviour snapshots from the corresponding time simulation are shown first, see Fig. 6.19.

In Fig. 6.19, panel (a)-(d), snapshots of a periodic sequence are illustrated. The lower layer is a Landau-Levich film on which a foot-solution of the upper layer has developed. Droplets are then repeatedly pulled out of this foot-structure. In panel (a), the droplet is formed at the tip of the foot. Panel (b) shows a state where the droplet has already detached from the foot and is withdrawn. The droplet is deposited on an elevation of the lower layer. In panel (c) this elevation flattens in the center of the droplet and the droplet looks similar to the steady drop in Fig. 6.12 (a). Notice that surface tension ratio σ and ratio of wetting strengths κ are identical. Furthermore in Fig. 6.19 (c), the tip of the foot-structure is growing again leading to the formation of a new droplet that detaches from the meniscus, as apparent in (d).

At this time, the moving droplet has already reached the edge of the domain and starts to disappear. Small distortions in the droplet shape at the boundary conditions are due to Neumann boundary conditions. Meanwhile, the tip of the foot is growing, so that the next droplet breaks off and detaches. This process is then repeated beginning with the state in panel (a).

In Fig. 6.20 space-time plots for four different sets of parameters of such a process are shown. All four panels present one-dimensional TPS, where depositions of a periodic array are formed by 1D droplets. These structures of TPS, where trains of regularly spaced drops are shed, are very similar to the results obtained in the SAW-driven system, see Fig. 5.30. In panels (a) and (b) deposition of the upper liquid is drawn out in form of droplets, while they remain on an elevation of the lower layer, see Fig. 6.19. The differences between the TPS in (a) and (b) of Fig. 6.20 are the variation of the ratio of wetting strengths κ and the different velocities U_L. This results into different frequencies of shedding droplets, as well as different volumes of the emerging droplets. Panel (c) in Fig. 6.20 shows that a droplet with a long tail of the lower liquid is drawn out. Hereby, the droplet moves beyond the boundary at $x = 500$, so that the lower liquid fully covers the domain. Subsequently, the upper layer "cuts off" the tails of the lower layer, which is readily seen by the dips in panel (c). Two snapshots for this case are presented in Fig. 6.21.

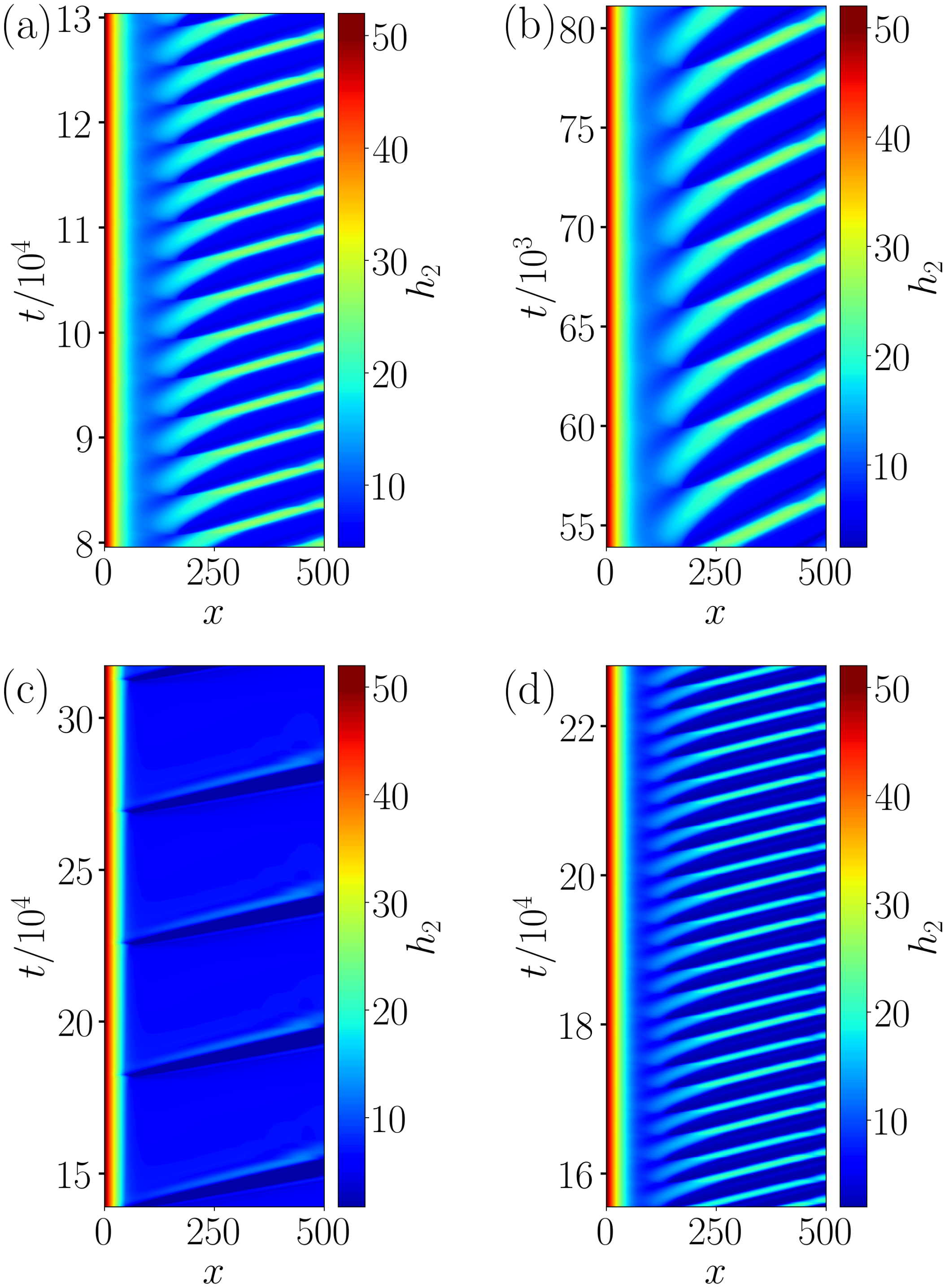

FIGURE 6.20: *Space-time plots for different parameters: (a)* $\sigma = 1$, $\kappa = 0.05$ *and* $U_\mathrm{L} = 0.08$*, (b)* $\sigma = 1$, $\kappa = 1$ *and* $U_\mathrm{L} = 0.09$*, (c)* $\sigma = 0.9$, $\kappa = 1$ *and* $U_\mathrm{L} = 0.034$ *and (d)* $\sigma = 10$, $\kappa = 1$ *and* $U_\mathrm{L} = 0.07$*. Panels (a), (b) and (d) show droplets, which are drawn out from the upper liquid. In panel (c) droplets with a large tail from the lower layer are drawn out. The remaining parameters are* $h_\mathrm{m1} = 26$, $h_\mathrm{m2} = 52$, $h_\mathrm{p1} = h_\mathrm{p2} = 1$, $\rho = 1$, $G = 0.001$, $\alpha = 1$ *and* $L = 500$.

Panel (d) shows the time evolution of the sequence of four subsequent droplets of the upper liquid. Here, two large and two small droplets of different heights are pulled out from the bath, see Fig. 6.22. In the space-time plot Fig. 6.20 (d) these small droplets are not quite visible, only the two successive large droplets are discernible. Each of these space-time plots is confirmed to show a TPS with the aid of phase-plane plots.

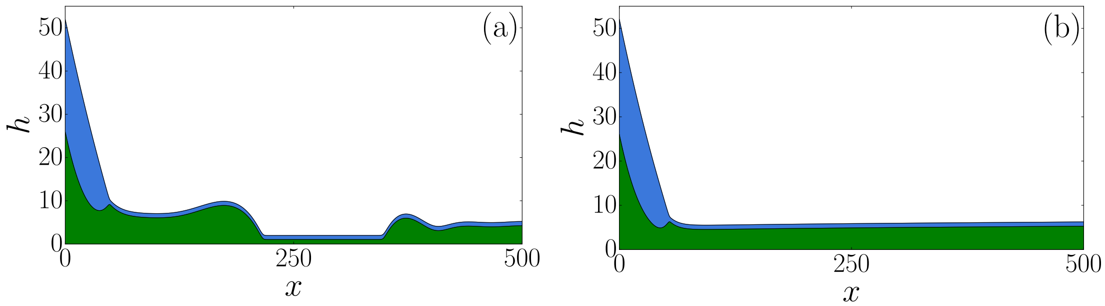

FIGURE 6.21: *Two snapshots from a time simulation are presented corresponding to time evolution in Fig. 6.20 (c). In (a), the lower layer forms a foot-structure which is pulled from the bath and the upper layer is in a meniscus state. The last part of the dragged tail from a droplet, which has already withdrawn. In (b), the droplet has moved beyond the right boundary at $L = 500$ and a large tail of the droplet is dragged behind. The remaining parameters are $h_{\mathrm{m1}} = 26$, $h_{\mathrm{m2}} = 52$, $h_{\mathrm{p1}} = h_{\mathrm{p2}} = 1$, $\sigma = 0.9$, $\kappa = 1$, $\rho = 1$, $G = 0.001$, $\alpha = 1$, $U_{\mathrm{L}} = 0.034$ and $L = 500$.*

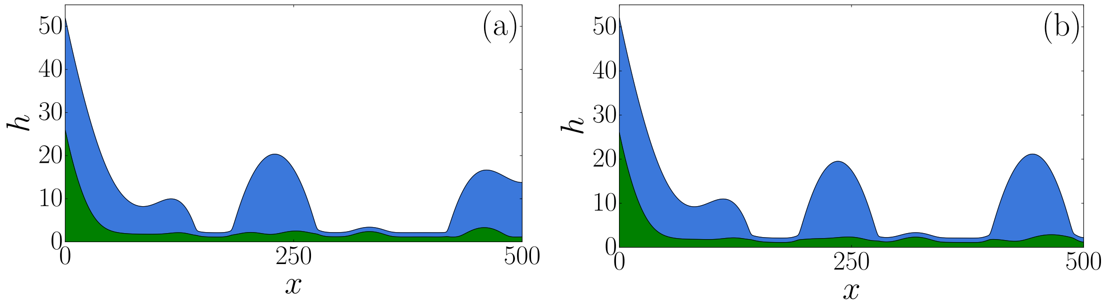

FIGURE 6.22: *Two snapshots from a time simulation are presented corresponding to time evolution Fig. 6.20 (d). In (a), the upper layer forms a foot-structure, where two droplets with different film heights are shown. The first droplet is slightly larger, whereas the other droplet has already reached the boundary at $L = 500$. The lower layer has several small wetting ridges, where a very small droplet is seen between these large droplets. In (b) the position of these droplet from the upper layer is swapped. Now, the larger droplet is further moved from the bath and the smaller has detached from the foot-structure. A very small droplet of the lower layer is seen between both large ones. The snapshots illustrate the two successive large droplets of a time-periodic behaviour. The remaining parameters are $h_{\mathrm{m1}} = 26$, $h_{\mathrm{m2}} = 52$, $h_{\mathrm{p1}} = h_{\mathrm{p2}} = 1$, $\sigma = 10$, $\kappa = 1$, $\rho = 1$, $G = 0.001$, $\alpha = 1$, $U_{\mathrm{L}} = 0.07$ and $L = 500$.*

As in Sec. 5.2.5, phase-plane plots are employed to determine true time-periodic behaviour. In the case of the two-layer thin film system, two different film heights h_1 and h_2 have to be considered. Therefore, instead of the time derivative of $\mathrm{d}/\mathrm{d}t||h_i||$ versus $||h_i||$, now the L^2-norm $||h_2||$ versus L^2-norm $||h_1||$ is plotted. Using this method, the number of phase-plane plots is reduced by one for each case and the information of the corresponding space-time plots in Fig. 6.20 remains.

Fig. 6.23 (a) shows that the trajectory corresponds to a closed orbit. It confirms that the corresponding space-time plot in Fig. 6.20 (a) shows a time-periodic state. In panel (a) the trajectory crosses once, giving the impression of a single loop. This indicates that the trajectory shows no period-doubling. The trajectories in Fig. 6.23 (b) and (c) are similar to the one in panel (a). Both are also periodic. The trajectory of the closed orbit in Fig. 6.23 (d) is periodic but more complex. The space-time plot

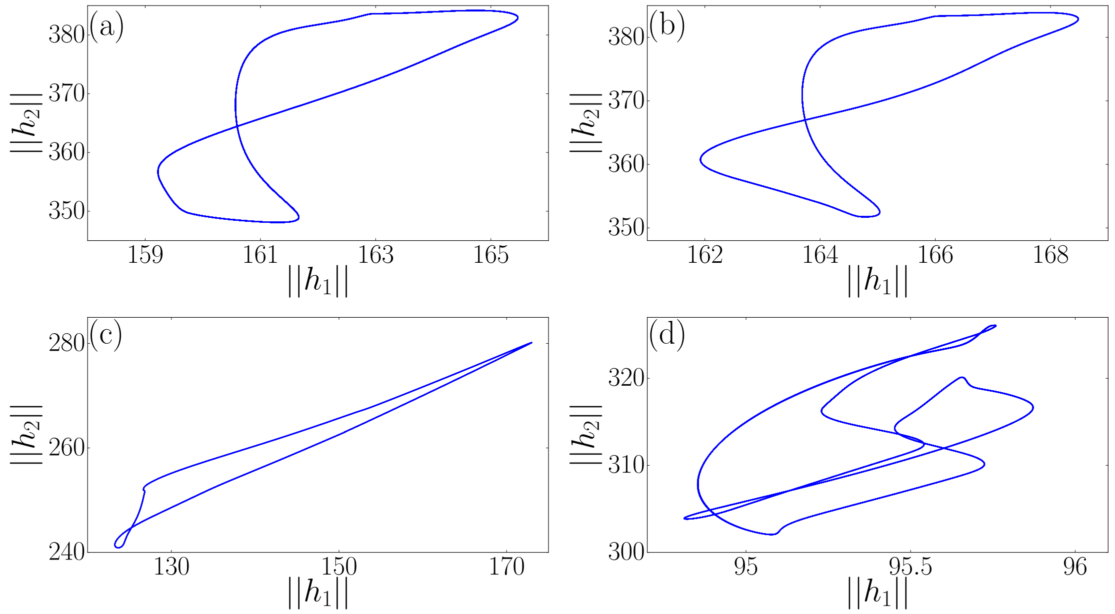

FIGURE 6.23: *Four phase-plane plots showing the L^2-norm $||h_2||$ versus L^2-norm $||h_1||$ along the attractor of the TPS obtained in Fig. 6.20. All four panels (a)-(d) show trajectories on a closed orbit.*

in Fig. 6.20 (d) shows that the droplets of different film heights are drawn out in an alternating pattern. This leads to the more complex trajectory in Fig. 6.23 (d) indicating that a period-doubling must have taken place. In general, Figs. 6.20 and 6.23 demonstrate that the two-layer thin-film system in a Landau-Levich geometry shows many different possible TPS.

To gain deeper insight into the solution behaviour of the system, a primitive continuation is performed. It only allows to track branches of (linearly) stable states. Therefore, the results mainly focus on the transition between different steady states, multi-stability and TPS obtained at fixed $\sigma = 1$ and $\kappa = 0.05$. For this purpose, a new L^2-norm is introduced as

$$||h|| = \sqrt{\frac{1}{L}\int_L (h_1^2 + h_2^2)\mathrm{d}x}\,, \tag{6.23}$$

which combines both film thicknesses h_1 and h_2.

In Fig. 6.24 four different states are identified. At velocity $U_\mathrm{L} = 0.001$, the red diamond represents a steady state, where both layers are in a meniscus film state. The velocity of the withdrawn plate is very low and does not affect the two-layer system.

Increasing the velocity U_L changes the steady states resulting in a lower layer corresponding to a Landau-Levich film, while the upper layer remains in a meniscus state. This steady state corresponds to the one presented in Fig. 6.18 (c). At velocity $U_\mathrm{L} = 0.025$ the L^2-norm $||h||$ has a local maximum. The film thickness of the lower layer is $h_1 \approx 5.9$ at the right boundary at $x = 500$. Following the branch further, h_2 decreases and the corresponding L^2-norm $||h||$ decreases until reaching a local minimum at velocity $U_\mathrm{L} = 0.055$. There, the film thickness of the lower layer

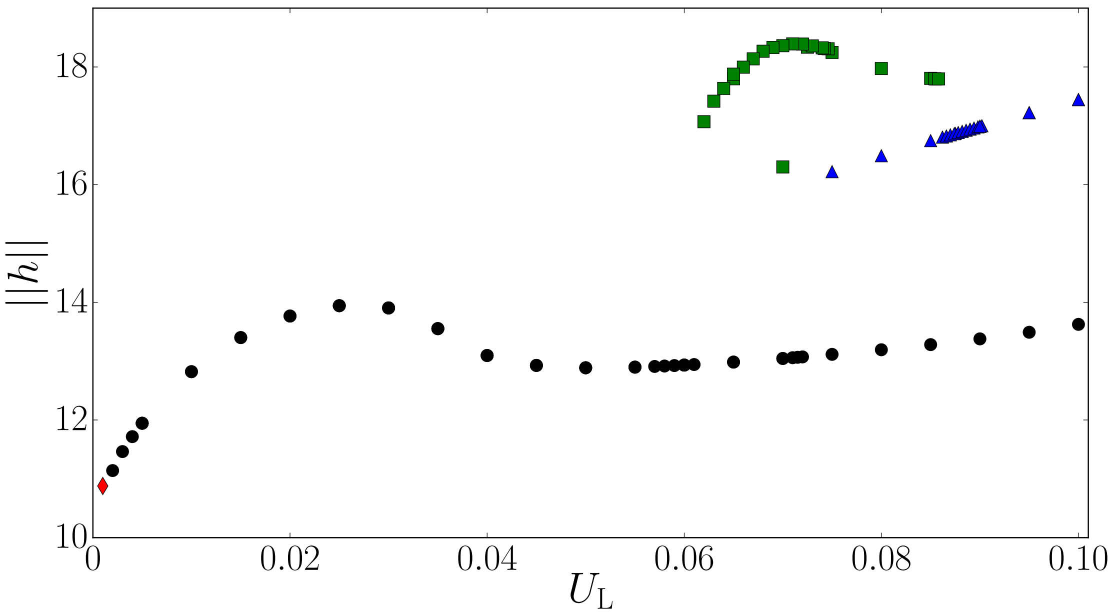

FIGURE 6.24: *Bifurcation diagram for a two-layer film in a Landau-Levich geometry showing the (time-averaged) L^2-norm $||h||$ as a function of plate velocity U_L. It is obtained by time simulations employed in a primitive continuation scheme. The different symbols indicate different types of states: red diamond: both layers are in a meniscus state; black circles: the lower layer is in a Landau-Levich film state and the upper layer is in a meniscus state; blue triangles: both layers are in Landau-Levich film state; and green squares: time-periodic states, i.e., deposition of a periodic array of ridges. The remaining parameters are* $h_\mathrm{m1} = 26$, $h_\mathrm{m2} = 52$, $h_\mathrm{p1} = h_\mathrm{p2} = 1$, $\sigma = 1$, $\kappa = 0.05$, $\rho = 1$, $G = 0.001$, $\alpha = 1$ *and* $L = 500$.

is $h_1 \approx 4.3$. This transition depends on the ratio of wetting strengths $\kappa = 0.05$, where the film thickness h_1 decreases for increasing velocity U_L. Between the local maximum and the local minimum, the meniscus of the upper layer advances and forces the lower layer further down due to the increasing velocity U_L. In other words, it slightly suppresses the withdrawal of the lower layer, which has consequently a more reduced film thickness h_1 and a concomitant decrease of the total film thickness h_2. Following the branch of black circles further, the L^2-norm $||h||$ continuously increases at a constant rate with velocity U_L. Along this branch, the steady states show that the domain is mainly covered by a the increasing film thickness of the lower layer h_1. The upper layer thickness stays constant at precursor film height of $h_2 - h_1 \approx 1$, i.e. in a meniscus state.

The branch of blue triangles represents steady states, where both layers correspond to a Landau-Levich film solution. In particular, following this branch from $U_\mathrm{L} = 0.1$ to lower velocities, the L^2-norm $||h||$ decreases at a constant rate. This behaviour is expected, as less force acts on both layers due to the drawn plate. While the velocity decreases further to $U_\mathrm{L} \approx 0.07$, the steady states transition into time-periodic states, marked by green triangles. Here, deposition of equally formed droplets are withdrawn from the foot-structure of the upper layer. The branch of TPS (green squares) has a hysteretic transition behaviour to the branch of blue triangles. Decreasing the velocity below $U_\mathrm{L} = 0.06$, the system falls back onto the branch of black circles.

The primitive bifurcation diagram in Fig. 6.24 shows that for the parameters $\sigma = 1$ and $\kappa = 0.05$ in a two-layer system in a Landau-Levich geometry, four different (steady) state classes are obtained. They are: (i) both layers in a meniscus state, (ii) lower layer in a Landau-Levich film solution and upper in a meniscus states,(iii) both layers in a Landau-Levich film solution and (iv) time-periodic states. In addition, it shows that up to three branches, which show different linearly stable states, exist at the same parameters and thus confirms multi-stability. For the range of the velocities in $0.075 \leq U_\mathrm{L} \leq 0.0858$ three different steady states are encountered: the lower layer is a Landau-Levich film solution and the upper layer is a meniscus state, both layers are a Landau-Levich film solution and time-periodic states. Furthermore, it reveals that two branches, one of time-periodic states and the other of a lower layer in a Landau-Levich film solution and upper in a meniscus states, coexist for the velocity range between $0.062 \leq U_\mathrm{L} < 0.075$.

However, the primitive continuation approach does not reveal the complete branches and misses all unstable steady states. Therefore, several transitions of different solutions branches and bifurcations can not be obtained.

Chapter Seven

Conclusion and outlook

> ” *Prudentia [...] est rerum expetendarum fugiendarumque scientia!* “
>
> – Marcus Tullius Cicero,
> *De Officiis*
> *I,43,153, 44 BC*

In this thesis, three different models of thin film system were analysed theoretically. These models are in turn subdivided into two types of thin films, namely a one-layer and two-layer film. The model for the one-layer case is further classified into the classical Landau-Levich model, where a plate is withdrawn from a bath [73] and into a thin film driven by surface acoustic waves (SAW) [87]. The latter is the first main subject of this work. In general, results obtained in the one-layer model of a thin film driven by SAW, mainly focuses on parameter regimes where patterned thin film depositions occur. The other type is a two-layer thin-film model, which is studied for flat thin films [106] and this model is further expanded into a Landau-Levich geometry. The results obtained in this theoretical work are predictions of ideal thin film behaviour and shall be used in suitable experiments to recover possible and similar phenomena of film states. The theoretical framework allows to provide extensive information for experiments for the development of more precise strategies to obtain, for instance patterned deposits (time-periodic states). Together, this provides an overall understanding of the fundamental dynamic behaviour occurring in thin-film models, either in the SAW-driven meniscus, or in a two-layer system.

In Chap. 2, the theoretical foundations for liquid films and droplets, i.e. gradient dynamics of partially wetting liquid are presented. These are used to approximate the Navier-Stokes equations in a lubrication approach to derive a nonlinear partial differential equation (PDE), which describes the temporal behaviour of a thin film profile driven by SAW. The corresponding equation is based on the work of Ref. [87] and is expanded by further influences such as gravitation, substrate inclination and Derjaguin (disjoining) pressure [30]. In Chap. 3 additionally, different scalings are introduced allowing one to describe and combine the classical Landau-Levich system of Ref. [47, 116, 123, 132, 144] and the SAW-driven thin film of Ref. [87]. The scaling established in Eq. (3.49) corresponds to a case, which allows to directly compare both models from the literature in a case of partially wetting liquids. Hereby, a new parameter ϵ_s is introduced, which corresponds to the SAW strength playing a similar role as the withdrawal plate velocity U_0 in the Landau-Levich case. The parameter ϵ_s facilitates the direct comparison of the extended SAW-driven thin-film system with the classical Landau-Levich system. To analyse the governing equation, numerical methods such as pseudo-arclength continuation using PDE2PATH [136] and time simulations using OOMPH-LIB [54] are employed, see Chap. 4. Both methods allows one to determine the full bifurcation behaviour of steady and time-periodic states. In particular, time simulations are used to identify the stability of the time-periodic states.

First, the governing Eq. (3.50) is used to reconstruct the bifurcation diagrams in the Landau-Levich case [47], where the main control parameter is the plate velocity U_0 at various fixed plate inclinations α. The results in Sec. 5.1 show a good agreement with previous works [46, 47] despite the slightly different boundary conditions. The analysis of this classical Landau-Levich case is required to properly categorise and interpret possible transitions that also occur in a SAW-driven system.

Then, the results of Ref. [87] for a SAW-driven thin film of an ideal fully wetting liquid are reproduced in Sec. 5.2.1. Here, the main control parameter is the Weber number We_s, the inverse of a Capillary number (surface tensions). The analysis has shown that a second Saddle-Node bifurcation is detected, which was missed in Ref. [87]. The completed bifurcation diagram reveals that a steady state is obtained where the coating thickness h_c approaches zero for the film thickness h at a critical value of We_s. However, this result is interpreted as a film state where a meniscus ends at a true microscopic contact point. This thin film has a different topology than the Landau-Levich film state termed finite-support meniscus state. These states can not be obtained with the employed numerical approach. Inspecting the steady states in general, the coating thickness increases homogeneously with the power law $h_\mathrm{c} \propto {\mathrm{We}_\mathrm{s}}^{2/3}$. This power law is identical to the ones obtained for the classical Landau-Levich system, because the We_s is scaled with the Capillary number [73].

In the next step, the model of Ref. [87] is expanded by incorporating a disjoining pressure and inclination. This leads to significant changes in the bifurcation diagrams. The bifurcation curve has a short sequence of exponential snaking and furthermore, the study reveals numerous Hopf and Saddle-Node bifurcations. At each fold (Saddle-Node bifurcation) the branch of steady states becomes more unstable and the solution profiles show foot-structures with strong modulations. This snaking closely resembles the behaviour encountered in Langmuir-Blodgett transfer [67, 68], but not in the Landau-Levich system. In the latter, however, the stability changes at each Saddle-Node bifurcation in the snaking region and continues without limit. This feature observed in the SAW-driven case has not been discovered for a dragged-plate case. Furthermore, notice that very small and centered modulations on a well defined foot thickness may occur in the classical Landau-Levich case [132]. The streamlines in the SAW-driven case reveal that strong convection rolls are responsible for these modulations and they depend on the SAW function $v_\mathrm{s}(h)$. In addition, a more continuous transition towards the precursor film at the tip of the strong modulated foot-structures occurs.

The transitions encountered in the SAW-driven cases are all discontinuous dynamic wetting transitions and the results also reveal that bi-stability occurs. The observed hysteretic behaviour shows that at the same parameters two different steady states, namely Landau-Levich film solution and meniscus states, exists. These results were corroborated by performing time simulations. From an extensive bifurcation study of SAW-driven thin film with the main control parameter SAW strength ϵ_s, a qualitatively similar behaviour to the previous control parameter We_s is observed. Here, for increasing values of the Weber number and also for increasing wettability more bifurcations appear. Noteworthy are the complexity of reconnections observed of the occurring Hopf branches emerging from Hopf bifurcations. Basically, Hopf bifurcations appear in pairs and they are connected by a branch of TPS. However, for increasing values of the Weber number, an odd number of Hopf bifurcations is encountered. This odd number comes from an additional Hopf bifurcation, which emerges from a Bogdanov-Takens bifurcation. At this Bogdanov-Takens bifurcation a Hopf and homoclinic (global) bifurcation emerge at a Saddle-Node bifurcation [8, 53, 72]. The bifurcation study further reveals, that in particular, this Hopf bifurcation moves along the branch of steady states for increasing Weber number. It is shown that this moving Hopf bifurcation is responsible for the different Hopf branch interactions. Therefore, a simple model is developed, where all important reconnections of Hopf branches are visualised caused by the moving Hopf bifurcation. In the final event, this moving Hopf bifurcation disappears in a reverse double Hopf bifurcation. After increasing the Weber number further, i.e. to $\mathrm{We}_\mathrm{s} = 2.0$, the very last (18th) Hopf bifurcation causes the branch of steady states to become stable. Therefore, the stability of the occurring time-periodic states are investigated by performing time simulations and primitive continuations. Time simulations show that ridges of liquid move from a bath at equidistant times. These results are checked with phase-plane diagrams and reveal that the corresponding attractors are closed orbits. This theoretical investigation confirms that stable time-periodic states occur in a very short parameter range of SAW strength ϵ_s. The results of a very finely tuned SAW could possibly be used to alternate between the deposition of a homogeneous film and the deposition of lines or a droplet pattern. The control by SAW could be used together with other means of control, for instance prestructured substrates [140, 143] or variable plate velocity [78].

In the classical Landau-Levich system, time-periodic states have already been confirmed [123] and they are also encountered in a SAW-driven thin-film system. In other experiments, for instance (i) water droplets sliding on an oil film, which are destabilised by voltage so that they transform into small oil droplets underneath the water droplets [117], (ii) gas bubbles that moves along a tube filled with partially wetting liquid where between bubbles and the tube-wall a liquid film may undergoes related instabilities [71], and (iii) a relatively thick viscous liquid films flowing down a cylindrical fiber [63], are related qualitative transitions encountered. Here, an employed SAW may be used to stabilise the occurring Landau-Levich(-Bretherton) films [18].

Furthermore, dynamic and wetting behaviour of thin liquid films are often studied for volatile liquids where an additional flux is considered, i.e. evaporation, [45, 89, 115, 128, 131, 139]. For this purpose, a non-conserved flux is added to the SAW-driving system in Eq. (3.62) to explore the alteration of the bifurcation diagrams. Hereby, it is shown that all new features encountered in a SAW-driving system vanish and the obtained bifurcation diagrams resemble qualitatively the ones obtained for the classical Landau-Levich system. Therefore, the underlying transition changes to a dynamic discontinuous emptying transition, caused by the non-conserved flux and suppresses SAW relevant component.

Further, the SAW-driven thin-film system in two dimensions (2D) is investigated, see Sec. 5.4. The behaviour of the bifurcation diagram depending on the transversal system size is examined and related to the 1D results. This analysis show that the symmetry breaks at a Pitchfork bifurcation. At that point, the 2D branch of steady states becomes transversally invariant to the 1D ones. A similar phenomenon is also seen for the classical Landau-Levich problem in 2D [39]. The obtained steady states show stripes or finger solutions. The corresponding number of fingers is directly correlated to the transversal domain size L_y. By tracking the solution branch, it is further discovered that many interactions between such fingers occur. This phenomenon is interpreted as a 'dance of fingers' [79]. However, the bifurcation study shows that only one particular a finger state is stable, namely a single centered prolonged finger. It has been already experimentally shown that such stripe solutions of a thin-film system exist [48, 57, 65, 83, 108]. The study of the 2D bifurcations gives a rough overview of possible film transitions and will encourage further investigations of the behaviour of SAW-driven or classical Landau-Levich systems to determine possible time-periodic states in 2D. In a brief outlook, it might be possible that through a new method – the deflated continuation – so that further insights into this bifurcation behaviour may be reached [41, 42, 56]. The main concept of this method is to jump from a known bifurcation branch towards another neighbouring branch by the use of a deflated operator. Hereby, the equations is transformed by adding a deflation operator [41]. With the help of this deflated operater the already known solution $\boldsymbol{u}^k$ can be changed, so that the known solution is not a solution of the transformed equation anymore. Then, a newton method is applied, which should converge to another solution if it exists. The new solution is possibly located on a new branch, which is not connected to the previous branch and therefore not identified yet.

In the second part of this thesis, a two-layer thin-film system is studied, see Chap. 6. The approach is based on Ref. [106] for non-volatile liquid films (isothermal) and is primarily concerned with the derivation of a model of a two-layer film in Landau-Levich geometry based on results obtained earlier in this thesis, see Sec. 5.1. First, the dynamic behaviour for thin flat films is studied by using time simulations of the derived Eqs. (6.17) and (6.18) for the parameters, in particular the ratio of surface tension σ and the ratio of wetting strengths κ. During the investigation of time simulations, it is observed that for the two-layer system the coarsening process contains different time scales and has two different coarsening events. In particular, the overall dynamic behaviour of the full system reacts very slowly, whereas the coarsening events, mass transfer and coalescence of droplets occur very quickly. During the mass transfer event, the mass of small droplets is transferred to a larger droplet, so that small droplets collapse. In the other event, two droplets collide and coalesce [50]. The results show that four symmetric droplet constellations are discovered after the coarsening process, which are (i) a large droplet formed by the upper layer between two wetting ridges of the lower layer at each contact line, (ii) a large droplet formed by the upper layer and the lower layer with a constant film thickness, (iii) a large droplet formed by the lower layer with the upper layer shaped around that droplet and (iv) a droplet of the upper layer lying in a hole formed by the lower layer. These symmetric droplet constellations are also confirmed in various literature [17, 43, 58, 81], for instance a symmetric structure of a lens on a sessile drop [91]. In addition to the symmetric constellations, this study also encountered asymmetric droplet constellations after the coarsening process, but only when both liquids are partially wetting. These asymmetric droplet constellations consist of two droplets, namely one droplet from each liquid, and were only studied in very few experiments [91]. In their study these droplet constellations are termed Janus droplets. With the influence of evaporation these Janus droplets turn to a symmetric compound droplet with a collar.

The bifurcation study reveals that the relative energy of the different droplet constellation, symmetric and asymmetric, are very close to each other. In addition, various bifurcation diagrams uncover multi-stability of those different solution branches of either symmetric and asymmetric droplet constellations. In particular, multi-stability of droplet constellations of either symmetric and asymmetric droplet are observed. In time simulations, these are governed by different initial starting solutions while keeping identical parameter values. The combination of results obtained by bifurcation diagrams and time simulations confirms that stable asymmetric droplet constellations have to exist. Based on these facts, it is suspected that many previous theoretical studies in an isothermal model have missed asymmetric droplet constellations [105, 106].

For all performed time simulations of a two-layer flat film system, only adaptive time steps are used, which either result into symmetric and asymmetric droplet constellations. Consequently, this proposes that the presented results of this thesis may be used to reconsider previous theoretical studies of two-layer model in isothermal and non-isothermal systems. The use of adaptive time steps provides new motivation to investigate two-layer thin-film models in the future.

In the final part of this thesis, the two-layer system in a Landau-Levich geometry (expanded Landau-Levich system) for partially wetting liquid layers is examined by using time simulations. Here, it is shown that two immiscible layers, which are withdrawn by a plate from a bath, are given by a combination of different solution types encountered in the classical Landau-Levich system, namely meniscus state and Landau-Levich film solutions. This extended Landau-Levich model has not been studied yet. Multiple regimes of solutions are discovered, in which pattern formation of two partially wetting liquids are observed. The detailed analysis of these depositions reveals that those states are stable time-periodic states. These TPS show that droplets formed by the upper layer are deposited in hollows of the lower layer and are transferred with a constant velocity U_L from the bath. Then, the occurring transitions are examined at a fixed set of parameters. For $\sigma = 1$ and $\kappa = 0.05$ a primitive continuation is performed using the withdrawal velocity U_L as main control parameter. The result demonstrates that the expanded Landau-Levich system contains multi-stable states of at least three different possible states. These states are: (i) time-periodic, (ii) a layered Landau-Levich film state and lastly (iii) a combination of a Landau-Levich film state (lower layer) and a meniscus state (upper layer). However, information of the full branches of steady states is missing, because the primitive continuation does not allow one to track unstable states. To uncover missing information and unstable steady states, a pseudo-arclength continuation needs to be performed.

In summary, the investigation of the two-layer system reveals a promising model to demonstrate droplet depositions. Comparing the results of the one-layer system of SAW-driving and classical Landau-Levich to the new model of an expanded Landau-Levich model with two-layers, it becomes clear, that the two-layer system provides yet undiscovered variations of droplet depositions leading to pattern formation than the one-layer systems. This new model of two liquid layers shall be further investigated to reveal more details of the dynamical behaviour. However, more accurate bifurcation studies are necessary to provide deeper understanding of the corresponding steady states and occurring transitions. Therefore, the presented results of a two-layer system in a Landau-Landau geometry shall encourage further studies in the future. Note that a PDE2PATH tutorial in this work is available in a data repository `https://doi.org/10.5281/zenodo.5595985`.

Appendix

A Details of calculations

A.1 Different scaling for thin-film models

In Eq. (3.49) a general scaling is employed to study a thin film problem for two cases: (i) a thin film withdrawn by a plate or (ii) driven by SAW. All quantities in Eq. (3.49) depend on ν. If ν is specified based on particular physical effects, it is possible to recover various scalings employed in the literature, for instance:

(i) By using $\nu = \epsilon^3\gamma/\mu$, the quantities yield

$$\begin{gathered} U_0 = \frac{\mu U_\mathrm{drag}}{\epsilon^3\gamma} \quad \epsilon_\mathrm{s} = \frac{\mu U_\mathrm{w}}{\epsilon^3\gamma}, \quad \mathrm{We}_\mathrm{s} = 1\,, \\ \mathrm{Ha} = \frac{\kappa\delta}{\epsilon^2\gamma} \quad \text{and} \quad G = \frac{gL^2}{\gamma}. \end{gathered} \tag{Ae.1}$$

Here, $\mathrm{Ha} = 1$ is fixed by choosing $L \equiv \gamma\epsilon/\kappa$ and $\epsilon_\mathrm{s} = 0$ so that one recovers the scaling employed for a plate withdrawn out of bath [47]. This scaling corresponds to the so-called dragged-case of a classical Landau-Levich system. Note that the film height is not scaled by three, which only results in the qualitative change of stretched bifurcation curve by a factor of three, while using the same main control parameter U_0.

(ii) Alternatively, the use of $\nu = U_\mathrm{w}$ yields

$$\begin{gathered} U_0 = \frac{U_\mathrm{drag}}{U_\mathrm{w}}, \quad \epsilon_\mathrm{s} = 1\,, \quad \frac{1}{\mathrm{We}_\mathrm{s}} = \frac{\epsilon^3\gamma}{\mu U_\mathrm{w}}, \\ \mathrm{Ha} = \frac{\delta\mu\epsilon\kappa}{U_\mathrm{w}} \quad \text{and} \quad G = \frac{\epsilon\rho g\delta^2}{\mu U_\mathrm{w}}. \end{gathered} \tag{Ae.2}$$

With $\mathrm{Ha} = 0$, $G = 0$ and $U_0 = 0$ the scaling corresponds to the case in Ref. [87] for a SAW-driven thin film. Note that in this case, both L and δ are chosen by geometry and the SAW-intrinsic length.

A.2 Linear stability analysis of a two-layer flat film

The linear stability analysis for the two-layer thin-film system in Chap. 6 is realised in the same way as in Sec. 4.4 for a one-layer system. The two-layer thin-film evolution Eqs. (6.17) and (6.18) are considered for a horizontal and flat film and yield

$$\partial_t h_1 = -\partial_x \left\{ \mathcal{Q}_{11} \partial_x \Big[\sigma \partial_{xx} h_1 + \Pi_1(h_1,h_2) \Big] + \mathcal{Q}_{12} \partial_x \Big[\partial_{xx} h_2 + \Pi_2(h_1,h_2) \Big] \right\} \tag{Ae.3}$$

and

$$\partial_t h_2 = -\partial_x \left\{ \mathcal{Q}_{21} \partial_x \Big[\sigma \partial_{xx} h_1 + \Pi_1(h_1,h_2) \Big] + \mathcal{Q}_{22} \partial_x \Big[\partial_{xx} h_2 + \Pi_2(h_1,h_2) \Big] \right\}. \tag{Ae.4}$$

Then, the homogeneous states h_{i_0} with $i = 1,2$ are perturbed. The perturbations are decomposed into Fourier modes (& Laplace modes) up to the first order in ϵ:

$$h_i(x,t) = h_{i_0} + \varepsilon h_{i_1} \mathrm{e}^{\beta t + \mathrm{i} k x} \quad \text{with} \quad i = 1,2\,. \tag{Ae.5}$$

Plugging the ansatz into Eqs. (Ae.3) and (Ae.4) gives

$$\begin{aligned} \beta h_{1_1} =& - k^2 [\mathcal{Q}_{11}(\sigma k^2 + \partial_{h_1} \Pi_1(h_{1_0},h_{2_0})) + \mathcal{Q}_{12} \partial_{h_1} \Pi_2(h_{1_0},h_{2_0}))] h_{1_1} \\ & - k^2 [\mathcal{Q}_{12}(k^2 + \partial_{h_2} \Pi_2(h_{1_0},h_{2_0})) + \mathcal{Q}_{11} \partial_{h_2} \Pi_1(h_{1_0},h_{2_0}))] h_{2_1} \end{aligned} \tag{Ae.6}$$

$$\begin{aligned} \beta h_{2_1} =& - k^2 [\mathcal{Q}_{21}(\sigma k^2 + \partial_{h_1} \Pi_1(h_{1_0},h_{2_0})) + \mathcal{Q}_{22} \partial_{h_1} \Pi_2(h_{1_0},h_{2_0}))] h_{1_1} \\ & - k^2 [\mathcal{Q}_{22}(k^2 + \partial_{h_2} \Pi_2(h_{1_0},h_{2_0})) + \mathcal{Q}_{21} \partial_{h_2} \Pi_1(h_{1_0},h_{2_0}))] h_{2_1}\,. \end{aligned} \tag{Ae.7}$$

The mobilities are written as a 2 × 2−Matrix, see Eq. (6.2). The determined expressions are written as

$$\beta \begin{pmatrix} h_{1_1} \\ h_{2_1} \end{pmatrix} = \boldsymbol{\mathcal{Q}} \boldsymbol{J} \begin{pmatrix} h_{1_1} \\ h_{2_1} \end{pmatrix} \tag{Ae.8}$$

with

$$\boldsymbol{J} = \begin{pmatrix} -k^2(\sigma k^2 + \partial_{h_1} \Pi_1) & -k^2 \partial_{h_2} \Pi_1 \\ -k^2 \partial_{h_2} \Pi_2 & -k^2(k^2 + \partial_{h_1} \Pi_2) \end{pmatrix}. \tag{Ae.9}$$

The eigenvalues are

$$\beta_{\pm} = \frac{\mathrm{Tr}(\boldsymbol{\mathcal{Q}} \boldsymbol{J})}{2} \pm \sqrt{\left(\frac{\mathrm{Tr}(\boldsymbol{\mathcal{Q}} \boldsymbol{J})}{2} \right)^2 - \det(\boldsymbol{\mathcal{Q}} \boldsymbol{J})}\,. \tag{Ae.10}$$

The stability thresholds are obtained from $\boldsymbol{J}$ as

$$\mathcal{Q}^{-1}\beta \begin{pmatrix} h_{1_1} \\ h_{2_1} \end{pmatrix} = \boldsymbol{J} \begin{pmatrix} h_{1_1} \\ h_{2_1} \end{pmatrix}. \tag{Ae.11}$$

Then, it is only necessary to calculate $\det(\boldsymbol{J}) = 0$. The growth rates $\beta_{\pm}(k)$ are plotted and shown in Fig. Af.1.

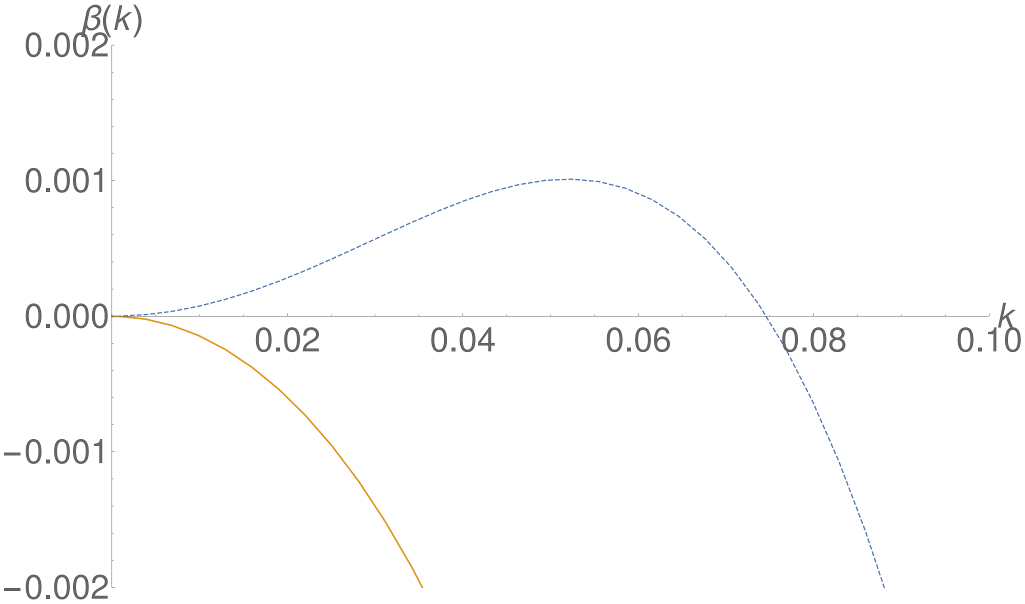

FIGURE Af.1: *Plot showing the Dispersion relations (growth rates) $\beta_{\pm}(k)$ for a flat two-layer film as a function of the wavenumber k. The dashed blue line corresponds to the case where the wavenumber are unstable first and gets stable at $k \approx 0.74$. The solid orange line is always stable for all wavenumbers. The remaining parameters are $h_1 = 4$, $h_2 = 8$, $h_{\mathrm{p1}} = h_{\mathrm{p2}} = 1$, $\kappa = 1$, $\sigma = 1$, $\rho = 0$, $G = 0$, $\mu = 1$ and $U_{\mathrm{L}} = 0$.*

The growth rate β_- is positive for $k \in \{0, k_0\}$ where $k_0 \approx 0.074$. The maximal growth rate $\beta_-(k_{\max})$ is at $k = k_{\max} = 0.055$. Furthermore, for a given domain this gives N unstable eigenmodes with $N = N_{\mathrm{drop}} \approx k_{\max}L/2\pi$. For the time simulations the domain of $\Omega = L$ with $L = 500$ is used, so that up to five unstable eigenmodes occur during the growth processes, see Sec. 6.2.

A.3 Weak formulations for continuation and time simulations

The two-layer thin-film evolution Eqs. (6.17) and (6.18) are brought into a weak formulation yielding

$$\begin{aligned}0 = &\int_\Omega -\Big\{\partial_t h_1 + U_\mathrm{L}\nabla h_1 + G\Big[\nabla_h \mathcal{Q}_{11}(\rho-1) + \nabla_h \mathcal{Q}_{12}\Big]\cdot \phi_1\Big\}\,\mathrm{d}x\\ &-\int_\Omega \mathcal{Q}_{11}\Big[u_1 + (\rho-1)G\nabla h_1\Big]\cdot\phi_1\,\mathrm{d}x\\ &-\int_\Omega \mathcal{Q}_{12}\Big[u_2 + (\rho-1)G\nabla h_2\Big]\cdot\phi_1\,\mathrm{d}x\end{aligned} \qquad \text{(Ae.12)}$$

$$0 = \int_\Omega (\nabla h)\cdot\nabla\phi_2 - \Pi_1(h_1,h_2)\cdot\phi_2 - \sigma u_1\cdot\phi_2 \mathrm{d}x \qquad \text{(Ae.13)}$$

and

$$\begin{aligned}0 = &\int_\Omega -\Big\{\partial_t h_2 + U_\mathrm{L}\nabla h_2 + G\Big[\nabla_h \mathcal{Q}_{21}(\rho-1) + \nabla_h \mathcal{Q}_{22}\Big]\cdot \phi_3\Big\}\,\mathrm{d}x\\ &-\int_\Omega \mathcal{Q}_{21}\Big[u_1 + (\rho-1)G\nabla h_2\Big]\cdot\phi_3\,\mathrm{d}x\\ &-\int_\Omega \mathcal{Q}_{22}\Big[u_2 + (\rho-1)G\nabla h_2\Big]\cdot\phi_3\,\mathrm{d}x\end{aligned} \qquad \text{(Ae.14)}$$

$$0 = \int_\Omega (\nabla h)\cdot\nabla\phi_4 - \Pi_2(h_1,h_2)\cdot\phi_4 - u_2\cdot\phi_4 \mathrm{d}x \qquad \text{(Ae.15)}$$

with the test functions ϕ_k with $k = 1,2,3,4$. The auxilliary fields are given by $u_1 = \partial_{xx}h_1$ and $u_2 = \partial_{xx}h_2$, respectively. The derivation $\nabla_h = \partial_{h_1} + \partial_{h_2}$ and the mobility matrix is represented as $\mathcal{Q}_{ij}$ with $i,j = 1,2$.

A.4 Dewetting and coarsening of two-layer flat films

A bifurcation diagram of the relative energy per length $(F - F_0)/L$ versus the ratio of wetting strengths κ is given. The bifurcation diagram is showing the full bifurcation curves of Fig. 6.17.

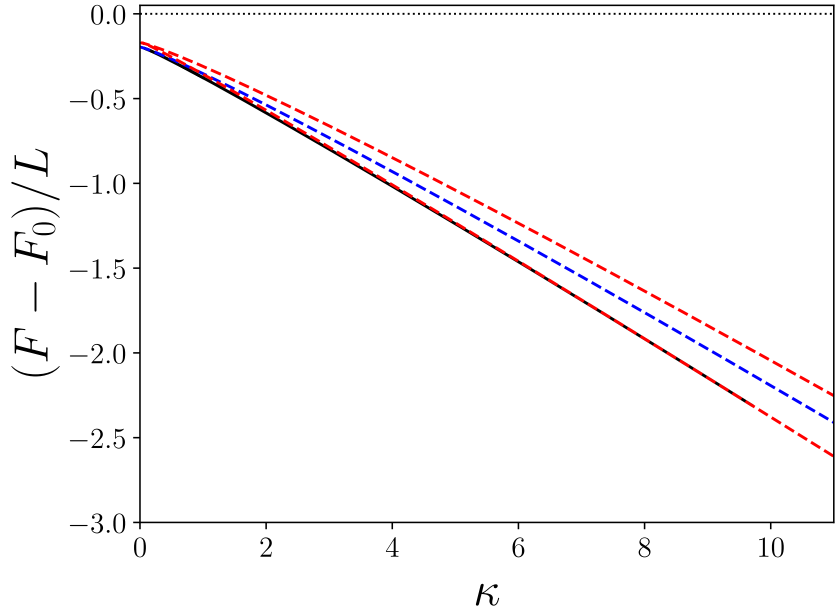

FIGURE AF.2: *Bifurcation diagram showing the relative energy F plotted versus the ratio of wetting strengths κ. The black solid line corresponds to symmetric steady states, and both dashed lines red and blue represent two different asymmetric states. The remaining parameters are $h_1 = 4$, $h_2 = 8$, $h_{\mathrm{p1}} = h_{\mathrm{p2}} = 1$, $\sigma = 1$, $\rho = 0$, $G = 0$, $U_{\mathrm{L}} = 0$ and $L = 500$. The bifurcation diagram has been obtained by U. Thiele.*

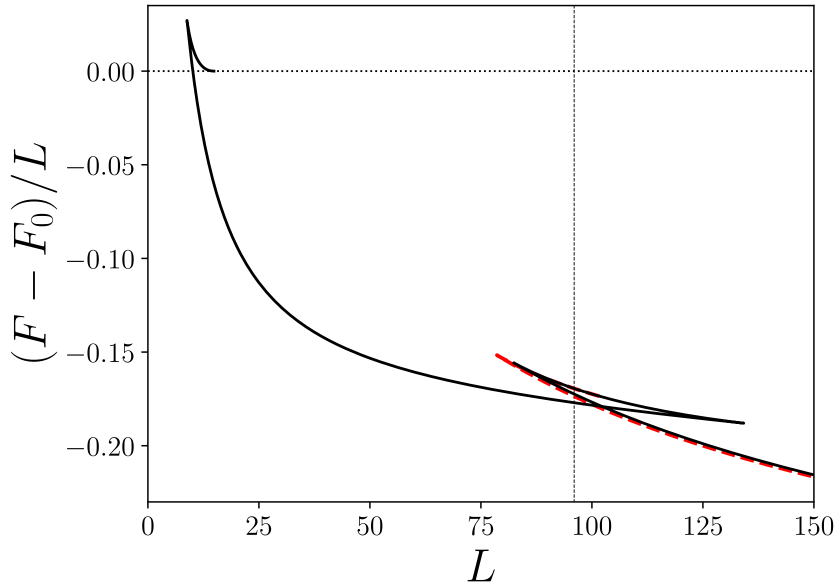

FIGURE AF.3: *Bifurcation diagram showing the relative energy per length $(F - F_0)/L$ versus domain L. The dashed red line corresponds to symmetric steady states and the solid black line represents asymmetric states. At $L = 96$ a vertical dashed line is shown. The corresponding film states are shown in Fig. 6.15 and the time evolution of the relative energy per length is shown in Fig. 6.16. The remaining parameters are $h_1 = 4$, $h_2 = 8$, $h_{\mathrm{p1}} = h_{\mathrm{p2}} = 1$, $\sigma = 0.1$, $\kappa = 0.5$, $\rho = 0.1$, $G = 0$ and $U_{\mathrm{L}} = 0$. The bifurcation diagram has been obtained by U. Thiele.*

B A pde2path tutorial for SAW-driven meniscus

B.5 SAW-driving meniscus – pde2path Tutorial

A common approach in nonlinear physics is to investigate the given PDEs and ODEs using nonlinear analysis techniques. In many cases, direct numerical analysis of time simulations is sufficient to observe the dynamics of the system as time evolves. However, it is important to note that time simulations cannot always extract all the information from systems. To collect all more information from a given system, tools, for instance PDE2PATH, a Matlab package, are used to track steady, time-periodic states and bifurcations in parameter space [34, 134, 135, 136]. PDE2PATH makes use of the pseudo-arclength continuation, a method typically used in numerical bifurcation analysis, where the full branches of these steady states are traced, see Chap. 4 for more details. By tracking steady states with a path continuation, it is possible to detect also linear unstable states, whereas time simulations can only reveal stable states. The stability of states are determined in PDE2PATH, where an approximative calculation of the Jacobian is provided, which is sufficient for the investigation. Then, the gathered results are displayed in a bifurcation diagrams, employing the parameter of interest as control paramater. The library of PDE2PATH also allows one to track bifurcations in paramater space [27, 107, 133], for instance the loci of Saddle-Node and Hopf bifurcations. Furthermore, PDE2PATH is able to track branches emerging from bifurcations, including branches of time-periodic states (TPS), which emerge from Hopf bifurcations. The numerical investigation with PDE2PATH covers all the branches in a bifurcation diagram and the corresponding steady states.

This tutorial is primarily intended to give a short overview for intermediate PDE2PATH users. Therefore, the main focus is set on dealing with the implementation and analysis of the corresponding SAW-driven thin-film model. The equations implemented in PDE2PATH are obtained in Eqs. (4.17) and (4.18).

In the simplest case of studying any problem only three files are needed in PDE2PATH. These are namely: (i) an initial function (*_init.m), (ii) a problem function (*_sG.m) and (iii) a starting function (startcont_⋆). In this tutorial the "*" symbol represents the name of the problem, i.e. **SAWDRM** (**S**urface **A**coustic **W**ave **DR**agged **M**eniscus) and the ⋆-symbol represents information of the start solution and main control parameter for the continuation. The file names are composed of the analysed system and they include the dimension of system, domain size, fixed parameters, control parameter and, if the control parameter is increased or decreased. Roughly speaking, the main control parameter approaches larger values (f = forward) or lower values (b = backwards), so that the final name is set to: 1D_Lx40_fix_We1_Ha1_alpha020_cp_eps_f. However, it is advisable to have a detailed look at the files `https://doi.org/10.5281/zenodo.5595985`, where additional information are provided.

To use the attached files, first one needs to install pde2path. In very short it can be downloaded at `http://www.staff.uni-oldenburg.de/hannes.uecker/pde2path/` and then it is recommended to define a startup.m file, so that the all required packages are loaded. Additionally, note that Matlab version 2019b (17 Sep. 2019) is a minimum requirement.

Next, the three important pde2path files with their relevant content are explained. The first step of any implementation in pde2path is to create an initial file *_init.m. Hereby, information of the given parameters, the necessary switches, a suitable start solution, the boundary conditions, the calculation of norms and many more are defined.

The considered problem is built in the *_sG.m file. Here, the right-hand-side (rhs) of the main PDE or ODE is handled. pde2path uses finite element method (FEM) operators.

The third file is the starting script named startcont_⋆.m. In this file all start values of paramaters, boundary conditions and the chosen main control parameter are set. It is recommended to take a close look at the file named startcont_1D_Lx40_fix_We1_Ha1_alpha020_cp_eps_f.m. In this case, the parameters are

$$\Omega = 40\,, \qquad \mathrm{We_s} = 1\,, \qquad \mathrm{Ha} = 0.001\,, \qquad \alpha = 0.2\,.$$

Hereby, the SAW strength ϵ_s is chosen as the main continuation parameter. All important parameters are denoted with fixed (fix), main control parameter (cp) and in which direction, positive “f” (forward) or negativ “b” (backwards), the control parameter is increased or decreased. The remaining parameters, gravity $G = 0.001$, plate velocity $U_0 = 0$ and precursor film height $h_\mathrm{p} = 0.1$ are not changed. The starting script is further seperated into five parts.

In the first part, all start values and boundary conditions are set. The script starts from a given solution, which is initiated in the SAWDRM_init.m file. This solution converges onto an exact solution of the rhs which is determined by Newton method. Notice that this solution, in particular, has a plate velocity $U_0 > 0$ and SAW strength $\epsilon_\mathrm{s} = 0.2$. This allows to determine a solution very fast and also avoids numerical problems.

After this “start” solution is calculated and it is loaded in the second part, where the first continuation starts. In this case, the first control parameter is U_0 and decreased to $U_0 = 0$. Notice that in the SAW model the velocity speed of the plate has to vanish.

Then, the third part of the script begins. At the beginning, the very last solution is loaded with $U_0 = 0$. Then, the SAW strength ϵ_s is set as a control parameter. The solution branch is tracked again, until ϵ_s approaches zero (decreased). The last calculated steady state solution corresponds to a thin film solution without any advection, so that plate velocity $U_0 = 0$ and SAW $\epsilon_\mathrm{s} = 0$ is zero.

In the fourth part of the starting script, a similar procedure is repeated. The main

control parameter remains the SAW strength ϵ_s and it is continuated towards $\epsilon_\mathrm{s} = 2$ (increased). Notice that the step size is chosen intentionally large with p.sol.ds = 0.01. This allows to track a rough bifurcation curve very fast. However, for a more accurate tracking and detection of different bifurcations, it is recommended to use a smaller step size. Therefore, in this tutorial a point from this generated branch is loaded, i.e. a well-chosen point for instance right before the first Saddle-Node bifurcation (fold) is loaded.
Then, the last part of the starting script is performed. Hereby, the point 'pt95' is chosen. Then, a smaller step size of p.sol.ds = 0.0005 is used. This should be sufficient to detect all the Hopf- and Saddle-Node bifurcations. In other step, a steady state at the point 'pt455', when no significant changes of the bifurcation curve occurs, is loaded and the step size is increased to p.sol.ds=0.005. After this, all important information are obtained and can be displayed Ãn a bifurcation diagram.
In addition, this tutorial provides some further starting script files. These are, e.g. a complete Fold- and Hopf bifurcation continuations and a script to track branches of TPS. They allow to follow the corresponding bifurcations. Some details of the numerical implementation are discussed in Chap. 4. The three files are named:
startcontfold_1D_Lx40_fix_Ha1_alpha020_cp_eps_We_f (Fold),
startconthopf_1D_Lx40_fix_Ha1_alpha020_cp_eps_We_f (Hopf) continuation and startcontTPS_1D_Lx40_fix_We1_Ha1_alpha020_cp_eps_f_Hopf_pt4 (TPS).
For the Fold continuation, the third Saddle-Node bifurcation 'fpt3' is loaded, whereas for the case of the Hopf continuation the first Hopf bifurcation with ('hpt1') is used and tracked. Hereby, an additional free parameter is chosen, that allows the corresponding solution to converge onto the next solution during each continuation step. In this tutorial the Weber number We_s is choosen as a second free parameter. The script, which tracks the branch of TPS, starts from the fourth Hopf bifurcation ('hpt4').
After all these scripts are started, the user may use a predefined plot script by running SAWDRM_plot_branches.m, and it should result into the following Fig. Bf.4.

In addition, the following scripts are included: SAWDRM_sGjac.m, SAWDRM_bra.m, SAWDRM_v.m, SAWDRM_oosetfemops.m and SAWDRM_ufu.m . In short: the script *_sGjac.m calculates the eigenvalues of the Jacobian Matrix to determine the stability of the steady states of the tracked branch. Overall, it is highly recommended to implement an analytically computed Jacobian, so that the calculation time is greatly reduced during each continuation step. During each continuation step, additional measurements are calculated and saved with the script SAWDRM_bra.m . The user may add other measurements, which are saved, e.g. a excess volume V_ex or a L^2-norm. In particular, the SAWDRM_bra.m file includes excess volume V_ex, reference volume V_0, coating thickness $h_c(x)$ at $x = -L/2$, flux at $x = -L/2$ and mean pressure p_0. In the file SAWDRM_v.m the dimensionless SAW-term $v_\mathrm{s}(h)$ is implemented, see Eq. (3.42). Here, the derivatives up to the third order are analytically derived. This file can be expanded by introducing other acting forces

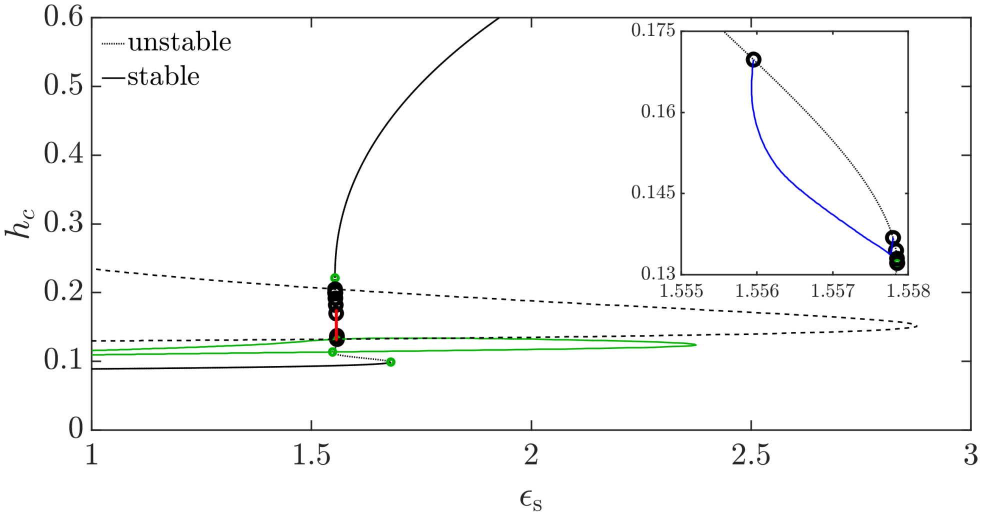

FIGURE BF.4: *Bifurcation diagram including all calculated branches of this tutorial, where coating thickness h_c is plotted vs. SAW strength ϵ_s. The black solid line corresponds to the stable states of the bifurcation of steady states with the control parameter ϵ_s. The dotted line represents unstable states, the black circles present Hopf bifurcations and the green circles are Saddle-Node bifurcations. The green solid line represents the branch corresponding of the Saddle-Node (fold) continuation method and the black dashed line corresponds to the Hopf continuation. The inset gives a magnification into the red marked region. The branch of TPS is presented by the blue solid line. This Hopf branch connects the two Hopf bifurcations.*

that are equally treated as plate velocity U_0 and SAW $v_s(h)$ in Eq. (3.50).

The preassembled FEM operators are given in SAWDRM_oosetfemops.m. Here, two matrices, the mass matrix M, which is time independent, and a stiffness matrix K (spatial derivative), which is anti-diagonal, are defined. Furthermore, the boundary conditions for each field are implemented in this file, i.e. Neumann and Dirichlet boundary conditions. In addition, a user specific function, named SAWDRM_ufu.m, is given, which checks if a breaking condition is fullfilled after each continuation step, so that the continuation stops. A basic PDE2PATH abrupt criterium is here defined for the main control parameter, i.e. it checks if the control parameter λ is within the range defined by p.nc.lammin (λ_{min}) and p.nc.lammax (λ_{max}).

In the files SAWDRM_spjac.m and SAWDRM_hpjac.m the spectral continuation is implement, which allows to track branches of Saddle-Node and Hopf bifurcations. In these files, the Jacobian matrix in a form of a reduced Hessian matrix are implemented, see Sec. 4.3.

The branch continuation of TPS, starts with the file named:
startconthopf_1D_Lx40_fix_Ha1_alpha020_cp_eps_We_f.m . The output script here is SAWDRM_hobra.m and specific measurements for TPS. Now, the user should be able to create new starting scripts to analyse different parameter ranges and investigate the diversity of the SAW-driven meniscus case or classical Landau-Levich problem of a plate withdrawn out of a bath.

Bibliography

[1] M. Abo Jabal, A. Egbaria, A. Zigelman, U. Thiele, and O. Manor. Connecting monotonic and oscillatory motions of the meniscus of a volatile polymer solution to the transport of polymer coils and deposit morphology. *Langmuir*, 34:11784–11794, 2018. `doi:10.1021/acs.Langmuir.8b02268`.

[2] C. Acott. The diving "law-ers": A brief resume of their lives. *SPUMS*, 29: 39–42. URL `https://citeseerx.ist.psu.edu/viewdoc/download?doi=10.1.1.738.9225&rep=rep1&type=pdf`.

[3] K. Albers and B. Wilmanski. *Continuum Thermodynamics – Part II: Applications and Examples*, volume 85. World Scientific, 2014. `doi:10.1142/8523`.

[4] E. L. Allgower and K. Georg. *Introduction to numerical continuation methods*, volume 45. Colorado State University, 2003. ISBN 978-0-89871-544-6. `doi:10.1137/1.9780898719154.bm`.

[5] G. Altshuler and O. Manor. Spreading dynamics of a partially wetting water film atop a MHz substrate vibration. *Phys. Fluids*, 27:102103, 2015. `doi:10.1063/1.4932086`.

[6] G. Altshuler and O. Manor. Free films of a partially wetting liquid under the influence of a propagating MHz surface acoustic wave. *Phys. Fluids*, 28:072102, 2016. `doi:10.1063/1.4955414`.

[7] S. Alzuaga, J.-F. Manceau, and F. Bastien. Motion of droplets on solid surface using acoustic radiation pressure. *J. Sound Vib.*, 282:151–162, 2005. `doi:10.1016/j.jsv.2004.02.020`.

[8] V. I. Arnold. *Geometrical methods in the theory of ordinary differential equations*, volume 250. Springer Science & Business Media, New York, 2012. ISBN 978-1-4612-1037-5. `doi:10.1007/978-1-4612-1037-5`.

[9] P. Bahadur, P. S. Yadav, K. Chaurasia, A. Leh, and R. Tadmor. Chasing drops: Following escaper and pursuer drop couple system. *J. Colloid Interf. Sci.*, 332:455–460, 2009. `doi:10.1016/j.jcis.2008.12.050`.

[10] D. H. Bangham and Z. Saweris. The behaviour of liquid drops and adsorbed films at cleavage surfaces of mica. *Trans. Faraday Soc.*, 34:554–569, 1938. `doi:10.1039/TF9383400554`.

[11] G. K. Batchelor. *An introduction to fluid dynamics*. Cambridge Mathematical Library. Cambridge University Press, Cambridge, 2000. `doi:10.1017/CBO9780511800955`.

[12] P. Beltrame, E. Knobloch, P. Hänggi, and U. Thiele. Rayleigh and depinning instabilities of forced liquid ridges on heterogeneous substrates. *Phys. Rev. E*, 83:016305, 2011. `doi:10.1103/PhysRevE.83.016305`.

[13] A. L. Bertozzi, A. Münch, X. Fanton, and A. M. Cazabat. Contact line stability and ”undercompressive shocks” in driven thin film flow. *Phys. Rev. Lett.*, 81: 5169–5173, 1998. `doi:10.1103/PhysRevLett.81.5169`.

[14] M. Bestehorn and A. Pototsky. Faraday instability and nonlinear pattern formation of a two-layer system: A reduced model. *Phys. Rev. Fluids*, 1:063905, 2016. `doi:10.1103/PhysRevFluids.1.063905`.

[15] M. Bestehorn, A. Pototsky, and U. Thiele. 3D large scale Marangoni convection in liquid films. *Eur. Phys. J. B*, 33:457–467. `doi:10.1140/epjb/e2003-00186-3`.

[16] S. Biwersi, J. Manceau, and F. Bastien. Displacement of droplets and deformation of thin liquid layers using flexural vibrations of structures. influence of acoustic radiation pressure. *J. Acoust. Soc. Am.*, 107:661–664, 2000. `doi:10.1121/1.428566`.

[17] S. Bommer, F. Cartellier, S. Jachalski, D. Peschka, R. Seemann, and B. Wagner. Droplets on liquids and their journey into equilibrium. *Eur. Phys. J. E*, 36:87, 2013. `doi:10.1140/epje/i2013-13087-x`.

[18] F. P. Bretherton. The motion of long bubbles in tubes. *J. Fluid Mech.*, 10: 166–188, 1961. `doi:10.1017/S0022112061000160`.

[19] P. Carles and A. M. Cazabat. The thickness of surface-tension-gradient-driven spreading films. *J. Colloid Interf. Sci.*, 157:196–201, 1993. `doi:10.1006/jcis.1993.1176`.

[20] A. M. Cazabat, F. Heslot, S. M. Troian, and P. Carles. Fingering instability of thin spreading films driven by temperature gradients. *Nature*, 346:824–826, 1990. `doi:10.1038/346824a0`.

[21] A. Chakrabarti, S. Mora, F. Richard, T. Phou, J.-M. Fromental, Y. Pomeau, and B. Audoly. Selection of hexagonal buckling patterns by the elastic Rayleigh-Taylor instability. *J. Mech. Phys. Solids*, 121:234–257, 2018. `doi:10.1016/j.jmps.2018.07.024`.

[22] E. F. F. Chladni. *Entdeckungen uber die Theorie des Klanges.* Weidmanns erben und Reich, 1787. ISBN 978-1-1660-1705-7.

[23] R. V. Craster and O. K. Matar. Dynamics and stability of thin liquid films. *Rev. Mod. Phys.*, 81:1131–1198, 2009. `doi:10.1103/RevModPhys.81.1131`.

[24] M. C. Cross and P. C. Hohenberg. Pattern formation out of equilibrium. *Rev. Mod. Phys.*, 65:851–1112, 1993. `doi:10.1103/RevModPhys.65.851`.

[25] P. G. de Gennes. Wetting: statics and dynamics. *Rev. Mod. Phys.*, 57:827, 1985. `doi:10.1103/RevModPhys.57.827`.

[26] P. G. de Gennes, F. Brochard-Wyart, and D. Quéré. *Capillarity and Wetting Phenomena: Drops, Bubbles, Pearls, Waves.* Springer Science & Business Media, New York, 2004. ISBN 978-0-387-21656-0. `doi:10.1007/978-0-387-21656-0`.

[27] H. de Witt. Fold and branch point continuation in a Schnakenberg system and details of branch plotting–a pde2path tutorial. 2017. `http://www.staff.uni-oldenburg.de/hannes.uecker/pde2path/tuts/schnakfoldtut.pdf`, last accessed on 05.05.2021.

[28] B. V. Derjaguin. On the thickness of the liquid film adhering to the walls of a vessel after emptying. *Acta Physicochim. URSS*, 20:349–352, 1945. `doi:10.1016/0079-6816(93)90022-n`.

[29] B. V. Derjaguin. Untersuchungen des Spaltdruckes dünner Filme, deren Entwicklung, Ergebnisse und zu lösende aktuelle Probleme. *Colloid Polym. Sci.*, 253:492–499, 1975. `doi:10.1007/BF01491828`.

[30] B. V. Derjaguin, N. V. Churaev, and V. M. Muller. *Surface Forces.* Springer, New York, 1987. ISBN 978-1-4757-6639-4. `doi:10.1007/978-1-4757-6639-4`.

[31] H. A. Dijkstra, F. W. Wubs, A. K. Cliffe, E. Doedel, I. F. Dragomirescu, B. Eckhardt, A. Y. Gelfgat, A. Hazel, V. Lucarini, A. G. Salinger, E. T. Phipps, J. Sanchez-Umbria, H. Schuttelaars, L. S. Tuckerman, and U. Thiele. Numerical bifurcation methods and their application to fluid dynamics: Analysis beyond simulation. *Commun. Comput. Phys.*, 15:1–45, 2014. `doi:10.4208/cicp.240912.180613a`.

[32] E. J. Doedel. Lecture notes on numerical analysis of nonlinear equations. In *Numerical Continuation Methods for dynamical systems*, pages 1–49. Springer, New York, 2007. ISBN 978-1-4020-6356-5. `doi:10.1007/978-1-4020-6356-5`.

[33] E. J. Doedel, A. R. Champneys, T. F. Fairgrieve, Y. A. Kuznetsov, B. Sandstede, and X. Wang. Continuation and bifurcation software for ordinary differential equations (with homcont). *AUTO07, Concordia University, Canada*, 1997. URL `http://citeseerx.ist.psu.edu/viewdoc/summary?doi=10.1.1.44.9955`.

[34] T. Dohnal, J. D. M. Rademacher, H. Uecker, and D. Wetzel. pde2path - version 2.0: faster FEM, multi-parameter continuation and periodic domains. In H. Ecker, A. Steindl, and S. Jakubek, editors, *Proceedings of 8th European Nonlinear Dynamics Conference*, 2014. `https://www.staff.uni-oldenburg.de/hannes.uecker/p2p2.pdf`, last accessed on 05.05.2021.

[35] F. Doumenc and B. Guerrier. Self-patterning induced by a solutal Marangoni effect in a receding drying meniscus. *Europhys. Lett.*, 103:14001, 2013. `doi:10.1209/0295-5075/103/14001`.

[36] I. E. Dzyaloshinskii, E. M. Levich, and L. P. Pitaevskii. Van der Waals forces in liquid films. *Perspectives in Theoretical Physics: The Collected Papers of E. M. Levich*, pages 425–441, 1992. `doi:10.1016/B978-0-08-036364-6.50038-7`.

[37] C. Eckart. Vortices and streams caused by sound waves. *Phys. Rev.*, 73:68, 1948. `doi:10.1103/PhysRev.73.68`.

[38] S. Engelnkemper, M. Wilczek, S. V. Gurevich, and U. Thiele. Morphological transitions of sliding drops: Dynamics and bifurcations. *Phys. Rev. Fluids*, 1: 073901, 2016. `doi:10.1103/PhysRevFluids.1.073901`.

[39] S. Engelnkemper, S. V. Gurevich, H. Uecker, D. Wetzel, and U. Thiele. *Computational Modeling of Bifurcations and Instabilities in Fluid Mechanics*, chapter Continuation for thin film hydrodynamics and related scalar problems, pages 459–501. Computational Methods in Applied Sciences, vol 50. Springer International Publishing, 2018. ISBN 978-3-319-91494-7. `doi:10.1007/978-3-319-91494-7`$_1$3.

[40] M. Faraday. On a peculiar class of acoustical figures; and on certain forms assumed by groups of particles upon vibrating elastic surfaces. *Phil. Trans. R. Soc. Lond.*, pages 299–340, 1831. `doi:10.1098/rstl.1831.0018`.

[41] P. E. Farrell, A. Birkisson, and S. W. Funke. Deflation techniques for finding distinct solutions of nonlinear partial differential equations. *SIAM J. Sci. Comp.*, 37:A2026–A2045, 2015. `doi:10.1137/140984798`.

[42] P. E. Farrell, C. H. Beentjes, and Á. Birkisson. The computation of disconnected bifurcation diagrams. *Submitted, preprint available on arXiv/160300809*, 2016. URL `https://arxiv.org/pdf/1603.00809.pdf`.

[43] L. S. Fisher and A. A. Golovin. Nonlinear stability analysis of a two-layer thin liquid film: Dewetting and autophobic behavior. *J. Colloid Interf. Sci.*, 291: 515–528, 2005. `doi:10.1016/j.jcis.2005.05.024`.

[44] S. A. Forth. A second order accurate, space-time limited, BDF scheme for the linear advection equation. In *Godunov Methods*, pages 335–342. Springer, Boston, 2001. ISBN 978-1-4613-5183-2. `doi:10.1007/978-1-4615-0663-8`$_3$5.

[45] L. Fraštia, A. J. Archer, and U. Thiele. Modelling the formation of structured deposits at receding contact lines of evaporating solutions and suspensions. *Soft Matter*, 8:11363–11386, 2012. `doi:10.1039/C2SM26574E`.

[46] M. Galvagno. *Modelling of driven free surface liquid films.* PhD thesis, Loughborough University, 2015. URL `https://hdl.handle.net/2134/16574`.

[47] M. Galvagno, D. Tseluiko, H. Lopez, and U. Thiele. Continuous and discontinuous dynamic unbinding transitions in drawn film flow. *Phys. Rev. Lett.*, 112: 137803, 2014. `doi:10.1103/PhysRevLett.112.137803`.

[48] P. Gao, L. Li, J. J. Feng, H. Ding, and X. Y. Lu. Film deposition and transition on a partially wetting plate in dip coating. *J. Fluid Mech.*, 791:358–383, 2016. `doi:10.1017/jfm.2016.64`.

[49] A. V. Getling. *Rayleigh-Bénard Convection: Structures and Dynamics*. Advanced series in nonlinear dynamics. World Scientific, London, 1998. ISBN 978-981-02-2657-2. `doi:10.1142/3097`.

[50] K. B. Glasner and T. Witelski. Collision versus collapse of droplets in coarsening of dewetting thin films. *Physica D*, 209(1-4):80–104, 2005. `doi:10.1016/j.physd.2005.06.010`.

[51] L. V. Govor, G. Reiter, G. H. Bauer, and J. Parisi. Bilayer formation in thin films of a binary solution. *Phys. Lett. A*, 353:198–204, 2006. `doi:10.1016/j.physleta.2005.11.088`.

[52] L. V. Govor, J. Parisi, G. H. Bauer, and G. Reiter. Self-assembled patterns from evaporating layered fluids. *J. Phys. Condens. Matter*, 21:264015, 2009. `doi:10.1088/0953-8984/21/26/264015`.

[53] J. Guckenheimer and P. Holmes. *Nonlinear oscillations, dynamical systems, and bifurcations of vector fields*, volume 42 of *Applied Mathematical Sciences*. Springer Science & Business Media, Berlin, 1993. `doi:10.1007/978-1-4612-1140-2`.

[54] M. Heil and A. L. Hazel. Oomph-lib - an object-oriented multi-physics finite-element library. In H.-J. Bungartz and M. Schäfer, editors, *Fluid-Structure Interaction: Modelling, Simulation, Optimisation*, volume 53, pages 19–49. Springer, Berlin, 2006. ISBN 978-3-540-34596-1. `doi:10.1007/3-540-34596-5`$_2$.

[55] F. Heslot, N. Fraysse, and A.-M. Cazabat. Molecular layering in the spreading of wetting liquid drops. *Nature*, 338:640–642, 1989. `doi:10.1038/338640a0`.

[56] M. Höffmann. Deflated continuation in pde2path. 2018. `https://www.feb.uni-bremen.de/branch_switching_pde2path.pdf`, last accessed on 05.05.2021.

[57] C. Honisch, T.-S. Lin, A. Heuer, U. Thiele, and S. V. Gurevich. Instabilities of layers of deposited molecules on chemically stripe patterned substrates: Ridges versus drops. *Langmuir*, 31:10618–10631, 2015. `doi:10.1021/acs.langmuir.5b02407`.

[58] R. Huth, S. Jachalski, G. Kitavtsev, and D. Peschka. Gradient flow perspective on thin-film bilayer flows. *J. Eng. Math.*, 94:43–61, 2015. `doi:10.1007/s10665-014-9698-1`.

[59] R. E. Isele-Holder and A. E. Ismail. Requirements for the formation and shape of microscopic precursors in droplet spreading. *Langmuir*, 32:4472–4478, 2016. `doi:10.1021/acs.langmuir.6b00807`.

[60] A. J. M. Spencer. The static theory of finite elasticity. *IMA J. Appl. Math.*, 6: 164–200, 1970. `doi:10.1093/imamat/6.2.164`.

[61] J. W. Jacobs and I. Catton. Three-dimensional Rayleigh-Taylor instability Part 1. weakly nonlinear theory. *J. Fluid Mech.*, 187:329–352, 1988. `doi:10.1017/S002211208800045X`.

[62] T. Jacobsen and S. Lloyd. *Sennacherib's Aqueduct at Jerwan.* University of Chicago Press, Chicago. `https://oi.uchicago.edu/sites/oi.uchicago.edu/files/uploads/shared/docs/oip24.pdf`, last accessed on 05.05.2021.

[63] H. Ji, C. Falcon, A. Sadeghpour, Z. Zeng, Y. S. Ju, and A. L. Bertozzi. Dynamics of thin liquid films on vertical cylindrical fibres. *J. Fluid Mech.*, 865: 303–327, 2019. `doi:10.1017/jfm.2019.33`.

[64] C. Jung. Poincaré map for scattering states. *J. Phys. A: Math. Gen.*, 19:1345, 1986. `doi:10.1088/0305-4470/19/8/016`.

[65] K. Kargupta and A. Sharma. Mesopatterning of thin liquid films by templating on chemically patterned complex substrates. *Langmuir*, 19:5153–5163, 2003. `doi:10.1021/la026634w`.

[66] H. B. Keller. Lectures on numerical methods in bifurcation problems. *J. Appl. Math.*, 217:50, 1987. URL `http://www.math.tifr.res.in/~publ/ln/tifr79.pdf`.

[67] M. H. Köpf and U. Thiele. Emergence of the bifurcation structure of a Langmuir-Blodgett transfer model. *Nonlinearity*, 27:2711–2734, 2014. `doi:10.1088/0951-7715/27/11/2711`.

[68] M. H. Köpf, S. V. Gurevich, R. Friedrich, and U. Thiele. Substrate-mediated pattern formation in monolayer transfer: a reduced model. *New J. Phys.*, 14: 023016, 2012. `doi:10.1088/1367-2630/14/2/023016`.

[69] K. Kostourou, D. Peschka, A. Münch, B. Wagner, S. Herminghaus, and R. Seemann. Interface morphologies in liquid/liquid dewetting. *Chem. Eng. Process.*, 50:531–536, 2011. `doi:10.1016/j.cep.2010.10.006`.

[70] B. Krauskopf, H. M. Osinga, and J. Galan-Vioque, editors. *Numerical Continuation Methods for Dynamical Systems.* Springer, Dordrecht, 2007. `doi:10.1007/978-1-4020-6356-5`.

[71] M. T. Kreutzer, M. S. Shah, P. Parthiban, and S. A. Khan. Evolution of nonconformal Landau-Levich-Bretherton films of partially wetting liquids. *Phys. Rev. Fluids*, 3:014203, 2018. `doi:10.1103/PhysRevFluids.3.014203`.

[72] Y. A. Kuznetsov. *Elements of Applied Bifurcation Theory*, volume 112. Springer, New York, 3rd edition, 2010. `doi:10.1007/978-1-4757-3978-7`.

[73] L. Landau and B. Levich. Dragging of a liquid by a moving plane. *Acta Physicochimica URSS*, 17:42, 1942. `doi:10.1016/b978-0-08-092523-3.50016-2`. reprinted in [101], p. 141–151.

[74] L. Landau and E. M. Levich. Fluid mechanics. 2nd english ed. vol. 6. *Course of Theoretical Physics (Pergamon Press, Oxford)*. `doi:10.1016/C2013-0-03799-1`.

[75] P. Li, W. Liao, L. Yue, Z. Fan, and F. Rao. Key factors affecting rayleigh instability of ultrathin 4h hexagonal gold nanoribbons. *Nanoscale Adv.*, 2: 3027–3032, 2020. `doi:10.1039/D0NA00186D`.

[76] D. L. Logan. *A First Course in the Finite Element Method*. Thomson, 2007. ISBN 978-0-534-38068-7. URL `https://dl.acm.org/doi/10.5555/517316`.

[77] R. Lüdtge. Ueber die Ausbreitung der Flüssigkeiten auf einander. *Ann. Phys. (Poggendorf)*, 137:362–377, 1869. `doi:10.1002/andp.18692130703`.

[78] P. M. T. Ly, U. Thiele, L. Chi, and S. V. Gurevich. Effects of time-periodic forcing in a Cahn-Hilliard model for Langmuir-Blodgett transfer. *Phys. Rev. E*, 99:062212, 2019. `doi:10.1103/PhysRevE.99.062212`.

[79] P. M. T. Ly, K. D. J. Mitas, U. Thiele, and S. V. Gurevich. Two-dimensional patterns in dip coating - first steps on the continuation path. *Physica D*, 409: 132485, 2020. `doi:10.1016/j.physd.2020.132485`.

[80] Y.-P. Ma, J. Burke, and E. Knobloch. Defect-mediated snaking: A new growth mechanism for localized structures. *Physica D*, 239:1867–1883, 2010. `doi:10.1016/j.physd.2010.06.014`.

[81] L. Mahadevan, M. Adda-Bedia, and Y. Pomeau. Four-phase merging in sessile compound drops. *J. Fluid Mech.*, 451:411–420, 2002. `doi:10.1017/S0022112001007108`.

[82] C. Marangoni. *Sull'espansione delle goccie d'un liquido galleggianti sulla superfice di altro liquido*. Fratelli Fusi, 1865.

[83] S. Mechkov, M. Rauscher, and S. Dietrich. Stability of liquid ridges on chemical micro- and nanostripes. *Phys. Rev. E*, 77:061605, 2008. `doi:10.1103/PhysRevE.77.061605`.

[84] G. K. Mikhailov. *Daniel Bernoulli, Hydrodynamica (1738)*, chapter 9. Elsevier Science, Amsterdam, 2005. `doi:10.1016/B978-044450871-3/50090-5`.

[85] H. D. Mittelmann. A pseudo-arclength continuation method for nonlinear eigenvalue problems. *SIAM J. Num. Ana.*, 23:1007–1016, 1986. `doi:10.1137/0723068`.

[86] R. H. Moore. Approximations to nonlinear operator equations and newton's method. *Numer. Math.*, 12:23–34, 1968. `doi:10.1007/BF02170993`.

[87] M. Morozov and O. Manor. An extended Landau-Levich model for the dragging of a thin liquid film with a propagating surface acoustic wave. *J. Fluid Mech.*, 810:307–322, 2017. `doi:10.1017/jfm.2016.728`.

[88] M. Morozov and O. Manor. Vibration-driven mass transfer and dynamic wetting. *Curr. Opin. Colloid Interface Sci.*, 36:37–45, 2018. `doi:10.1016/j.cocis.2017.12.002`.

[89] A. P. Mouat, C. E. Wood, J. E. Pye, and J. C. Burton. Tuning contact line dynamics and deposition patterns in volatile liquid mixtures. *Phys. Rev. Lett.*, 124, 2020. `doi:10.1103/physrevlett.124.064502`.

[90] A. Münch and P. L. Evans. Marangoni-driven liquid films rising out of a meniscus onto a nearly-horizontal substrate. *Physica D*, 209:164–177, 2005. `doi:10.1016/j.physd.2005.06.025`.

[91] M. J. Neeson, R. F. Tabor, F. Grieser, R. R. Dagastine, and D. Y. C. Chan. Compound sessile drops. *Soft Matter*, 8:11042–11050, 2012. `doi:10.1039/c2sm26637g`.

[92] A. A. Nepomnyashchy and I. B. Simanovskii. Marangoni instability in ultrathin two-layer films. *Phys. Fluids*, 19:122103, 2007. `doi:10.1063/1.2819748`.

[93] W. L. Nyborg. Acoustic streaming due to attenuated plane waves. *J. Acoust. Soc. Am.*, 25:68–75, 1953. `doi:10.1121/1.1907010`.

[94] W. L. Nyborg. Acoustic streaming near a boundary. *J. Acoust. Soc. Am.*, 30: 329–339, 1958. `doi:10.1121/1.1909587`.

[95] A. Oron, S. H. Davis, and S. G. Bankoff. Long-scale evolution of thin liquid films. *Rev. Mod. Phys.*, 69:931–980, 1997. `doi:10.1103/RevModPhys.69.931`.

[96] R. L. Panton. *Incompressible Flow.* Wiley, New Jersey, 2013. ISBN 978-1-118-01343-4. `doi:10.1002/9781118713075`.

[97] D. F. Parker. Stratification effects on nonlinear elastic surface waves. *Phys. Earth Planet. Inter.*, 50:16–25, 1988. `doi:10.1016/0031-9201(88)90086-6`.

[98] A. O. Parry, C. Rascon, E. A. G. Jamie, and D. G. A. L. Aarts. Capillary emptying and short-range wetting. *Phys. Rev. Lett.*, 108:246101, 2012. `doi:10.1103/PhysRevLett.108.246101`.

[99] V. N. Paunov, K. D. Danov, N. Alleborn, H. Raszillier, and F. Durst. Stability of evaporating two-layered liquid film in the presence of surfactant - III. Non-linear stability analysis. *Chem. Eng. Sci.*, 53:2839–2857, 1998. `doi:10.1016/S0009-2509(98)00100-6`.

[100] J. Peiró and S. Sherwin. Finite difference, finite element and finite volume methods for partial differential equations. In *Handbook of materials modeling*, pages 2415–2446. Springer, Dordrecht, 2005. ISBN 978-1-4020-3287-5. `doi:10.1007/978-1-4020-3286-8`$_1$27.

[101] P. Pelce. *Dynamics of curved fronts*. Academic Press, London, 1988. `doi:10.1016/C2009-0-22180-5`.

[102] L. M. Pismen. Nonlocal diffuse interface theory of thin films and the moving contact line. *Phys. Rev. E*, 64:021603, 2001. `doi:10.1103/PhysRevE.64.021603`.

[103] L. M. Pismen and Y. Pomeau. Disjoining potential and spreading of thin liquid layers in the diffuse-interface model coupled to hydrodynamics. *Phys. Rev. E*, 62:2480–2492, Aug 2000. `doi:10.1103/PhysRevE.62.2480`.

[104] A. Pototsky and M. Bestehorn. Faraday instability of a two-layer liquid film with a free upper surface. *Phys. Rev. Fluids*, 1:023901, Jun 2016. `doi:10.1103/PhysRevFluids.1.023901`.

[105] A. Pototsky, M. Bestehorn, D. Merkt, and U. Thiele. Morphology changes in the evolution of liquid two-layer films. *J. Chem. Phys.*, 122:224711, 2005. `doi:10.1063/1.1927512`.

[106] A. Pototsky, M. Bestehorn, D. Merkt, and U. Thiele. Evolution of three-dimensional interface patterns in dewetting two-layer liquid films. *Europhys. Lett.*, 74:665–671, 2006. `doi:10.1209/epl/i2006-10026-8`.

[107] J. D. Rademacher and H. Uecker. The OOPDE setting of pde2path - A tutorial via some Allen-Cahn models, 2018. `https://www.staff.uni-oldenburg.de/hannes.uecker/pde2path/tuts/actut.pdf`, last accessed on 05.05.2021.

[108] S. Raupp, M. Schmitt, A.-L. Walz, R. Diehm, H. Hummel, P. Scharfer, and W. Schabel. Slot die stripe coating of low viscous fluids. *J. Coat. Tech. Res.*, 15, 2018. `doi:10.1007/s11998-017-0039-y`.

[109] L. Rayleigh. On the circulation of air observed in Kundt's tubes, and on some allied acoustical problems. *Phil. Trans. R. Soc. Lond.*, 175:1–21, 1884. `doi:10.1098/rstl.1884.0002`.

[110] L. Rayleigh. On waves propagated along the plane surface of an elastic solid. *Proc. Lon. Math. Soc.*, 1:4–11, 1885. `doi:10.1112/plms/s1-17.1.4`.

[111] L. Rayleigh. On convection currents in a horizontal layer of fluid, when the higher temperature is on the under side. *Philos. Mag.*, 32:529–546, 1916. `doi:10.1080/14786441608635602`.

[112] A. R. Rezk, O. Manor, J. R. Friend, and L. Y. Yeo. Unique fingering instabilities and soliton-like wave propagation in thin acoustowetting films. *Nat. Commun.*, 3:1167, 2012. `doi:10.1038/ncomms2168`.

[113] A. R. Rezk, O. Manor, L. Y. Yeo, and J. R. Friend. Double flow reversal in thin liquid films driven by megahertz-order surface vibration. *Proc. R. Soc. A*, 470:20130765, 2014. `doi:10.1098/rspa.2013.0765`.

[114] H. Schlichting and K. Gersten. *Grenzschicht-Theorie*. Springer, Berlin, 2006. `doi:10.1007/3-540-32985-4`.

[115] M. Schneemilch and A. M. Cazabat. Wetting films in thermal gradients. *Langmuir*, 16:8796–8801, 2000. `doi:10.1021/la0002785`.

[116] J. H. Snoeijer, B. Andreotti, G. Delon, and M. Fermigier. Relaxation of a dewetting contact line. part 1. a full-scale hydrodynamic calculation. *J. Fluid Mech.*, 579:63–83, 2007. `doi:10.1017/S0022112007005216`.

[117] A. Staicu and F. Mugele. Electrowetting-induced oil film entrapment and instability. *Phys. Rev. Lett.*, 97:167801, 2006. `doi:10.1103/PhysRevLett.97.167801`.

[118] V. M. Starov and M. G. Velarde. Surface forces and wetting phenomena. *J. Phys. Condens. Matter*, 21(46):464121, 2009. `doi:10.1088/0953-8984/21/46/464121`.

[119] S. Stein. *Archimedes: What Did He Do Besides Cry Eureka?* Classroom Resource Materials. Mathematical Association of America, 2015. ISBN 978-0-88385-718-2. `doi:10.33137/aestimatio.v2i0.25737`.

[120] K. Stoev, E. Ramé, T. Leonhardt, and S. Garoff. The effects of thin films on the hydrodynamics near moving contact lines. *Phys. Fluids*, 10:1793–1803, 1998. `doi:10.1063/1.869700`.

[121] S. Strogatz. *Nonlinear Dynamics And Chaos: With Applications to Physics, Biology, Chemistry and Engineering*. Studies in nonlinearity. Westview Press, New York, 2000. `doi:10.1201/9780429492563`.

[122] F. Takens, H. Broer, B. Krauskopf, and G. Vegter. Global analysis of dynamical systems festschrift dedicated to floris takens for his 60th birthday. 2001. `doi:10.1201/9781420034288`.

[123] W. Tewes, M. Wilczek, S. V. Gurevich, and U. Thiele. Self-organised dip-coating patterns of simple, partially wetting, nonvolatile liquids. *Phys. Rev. Fludip-coids*, 4:123903, 2019. `doi:10.1103/PhysRevFluids.4.123903`.

[124] A. Thess and M. Bestehorn. Planform selection in Bénard-Marangoni convection: l hexagons versus g hexagons. *Phys. Rev. E*, 52:6358–6367, 1995. `doi:10.1103/PhysRevE.52.6358`.

[125] U. Thiele. *Structure Formation in Thin Liquid Films*, pages 25–93. Springer, Wien, 2007. `doi:10.1007/978-3-211-69808-2`$_2$.

[126] U. Thiele, K. Neuffer, Y. Pomeau, and M. G. Velarde. On the importance of nucleation solutions for the rupture of thin liquid films. *Colloids Surf. A*, 206: 135–155, 2002. `doi:10.1016/S0927-7757(02)00069-9`.

[127] U. Thiele, J. M. Vega, and E. Knobloch. Long-wave Marangoni instability with vibration. *J. Fluid Mech.*, 546:61–87, 2006. `doi:10.1017/S0022112005007007`.

[128] U. Thiele, A. Archer, and L. Pismen. Gradient dynamics models for liquid films with soluble surfactant. *Phys. Rev. Fluids*, 1:083903, 2016. `doi:10.1103/PhysRevFluids.1.083903`.

[129] K. R. Thomas, N. Clarke, R. Poetes, M. Morariu, and U. Steiner. Wetting induced instabilities in miscible polymer blends. *Soft Matter*, 6:3517–3523, 2010. `doi:10.1039/c0sm00046a`.

[130] J. Thomson. On certain curious motions observable at the surfaces of wine and other alcoholic liquors. *Philos. Mag.*, 10:330–333, 1855. `doi:10.1080/14786445508641982`.

[131] D. Todorova, U. Thiele, and L. M. Pismen. The relation of steady evaporating drops fed by an influx and freely evaporating drops. *J. Eng. Math.*, 73:17–30. `doi:10.1007/s10665-011-9485-1`.

[132] D. Tseluiko, M. Galvagno, and U. Thiele. Collapsed heteroclinic snaking near a heteroclinic chain in dragged meniscus problems. *Eur. Phys. J. E*, 37:1–17, 2014. `doi:10.1140/epje/i2014-14033-2`.

[133] H. Uecker. Hopf bifurcation and time-periodic orbits with pde2path - Algorithms and Applications. *Commun. Comput. Phys.*, 25:812–852, 2017. `doi:10.4208/cicp.OA-2017-0181`.

[134] H. Uecker. Steady bifurcations of higher multiplicity in pde2path. 2018. `https://www.staff.uni-oldenburg.de/hannes.uecker/pre/061-mbif.pdf`, last accessed on 05.05.2021.

[135] H. Uecker and D. Wetzel. Linear system solvers in pde2path–a tutorial. 2017. `https://www.staff.uni-oldenburg.de/hannes.uecker/pde2path/tuts/lsstut.pdf`, last accessed on 05.05.2021.

[136] H. Uecker, D. Wetzel, and J. D. M. Rademacher. pde2path - A matlab package for continuation and bifurcation in 2d elliptic systems. *Numer. Math. Theory, Methods Appl.*, 7:58–106, 2014. `doi:10.4208/nmtma.2014.1231nm`.

[137] C. Ward. Boat-building and its social context in early egypt: interpretations from the first dynasty boat-grave cemetery at abydos. *Antiquity*, 80, 2006. `doi:10.1017/s0003598x00093303`.

[138] M. H. Ward. Interfacial thin films rupture and self-similarity. *Phys. Fluids*, 23: 062105, 2011. `doi:10.1063/1.3604003`.

[139] M. R. E. Warner, R. V. Craster, and O. K. Matar. Surface patterning via evaporation of ultrathin films containing nanoparticles. *J. Colloid Interf. Sci.*, 267:92–110, 2003. `doi:10.1016/S0021-9797(03)00640-4`.

[140] M. Wilczek, J. Zhu, L. Chi, U. Thiele, and S. V. Gurevich. Dip-coating with prestructured substrates: transfer of simple liquids and Langmuir–blodgett monolayers. *J. Phys. Condens. Matter*, 29:014002, 2016. `doi:10.1088/0953-8984/29/1/014002`.

[141] S. K. Wilson. The effect of an axial temperature-gradient on the steady motion of a large droplet in a tube. *J. Eng. Math.*, 29:205–217, 1995. `doi:10.1007/BF00042854`.

[142] T. Young. An essay on the cohesion of fluids. *Phil. Trans. R. Soc. Lond.*, 95: 65–87, 1805. `doi:10.1098/rstl.1805.0005`.

[143] J. Zhu, M. Wilczek, M. Hirtz, J. Hao, W. Wang, H. Fuchs, S. V. Gurevich, and L. Chi. Branch suppression and orientation control of Langmuir–Blodgett patterning on prestructured surfaces. *Adv. Mater. Interf.*, 3:1600478, 2016. `doi:10.1002/admi.201600478`.

[144] J. Ziegler, J. H. Snoeijer, and J. Eggers. Film transitions of receding contact lines. *Eur. Phys. J.-Spec. Top.*, 166:177–180, 2009. `doi:10.1140/epjst/e2009-00902-3`.

[145] H. Żołdek. Bifurcations of certain family of planar vector fields tangent to axes. *J. Differ. Equ.*, 67:1–55, 1987. `doi:10.1016/0022-0396(87)90138-0`.

List of Figures

Introduction **1**

Fundamentals of hydrodynamics **5**

Derivation of a thin-film equation driven by surface acoustic waves (SAW) **15**

Numerical and analytical techniques **31**

Behaviour of a thin film driven by SAW **42**

Danksagung

Am Ende dieser Arbeit möchte ich noch meinen ganz besonderen Dank an allen Personen aussprechen, die mir beim vollenden dieses Werkes beiseite gestanden und geholfen haben.

Dazu möchte ich mich zu aller erst bei meiner Mutter *Romualda Maria Mitas* bedanken. Sie hat mir während der gesamten Zeit, von Beginn des Studiums bis zu diesem Ende hin, immer Mut und Kraft gegeben. Die mentale Stütze, die sie mir gegeben hat, hat mir geholfen, dass ich während einiger schwere Phasen dieser Zeit, metaphorisch gesprochen nicht den Boden unter meinen Füßen verliere.

Weiterhin möchte ich mich ganz besonders bei meinem Doktorvater *Prof. Dr. Uwe Thiele* bedanken. Er hat mir bei vielen Problemstellungen geholfen, mir sehr viele Denkanstößen gegeben und hatte immer einen sehr hilfreichen und fachlichen Rat, den er mir geben konnte. Die vielen Gespräche, die wir geführt haben, sorgten dafür, dass – die Saat der Arbeit neue Nährstoffe erhält –.

An weiterer Stelle möchte ich mich auch bei *Dr. Ofer Manor* aus Isreal bedanken. Nicht nur für die Gastfreundschaft bei der er Zeit und Mühen investiert hat, während des Aufenthalts in Israel, sondern auch für die interessanten und neue Ideenvorschläge, die diesem Thema zugrunde liegen.

An letzter Stelle, möchte ich mich vorallem bei meinem Korrekturlesern aus dem Freundeskreis als auch einigen aus der Arbeitsgruppe Thiele, *Dr. Sebastian Engelnkemper*, *Simon Hartmann*, *Tobias Frohoff-Hülsmann*, *Dr. Mariano Galvagno*, *Dr. Kaspar Gierke*, *Phong-Minh Timmy Ly*, *Agnieszka Paruzel* und *Dr. Paul Repgen* bedanken. Die Reihenfolge ist alphabetisch und impliziert keine Wertung. Eure Zeit, Bemühung und Anmerkungen haben dieser Arbeit ihren letzten feinen Schliff gegeben und deswegen soll eure Hilfe nicht umsonst(!) gewesen sein.